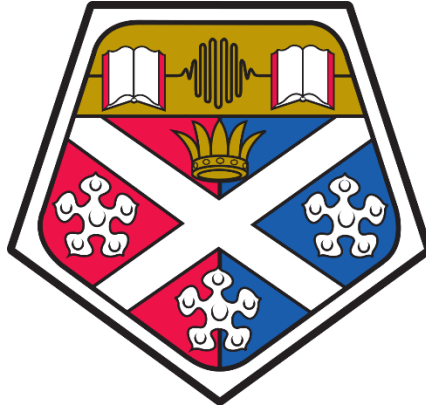# University of Strathclyde

Department of Physics

Design of a High-Power 48GHz Gyroklystron Amplifier for Accelerator Applications

Laurence J. R. Nix

(B.Sc. (Hons), M.Phys. (Hons), University of Strathclyde)

A thesis presented in fulfilment of the requirements for

the degree of Doctor of Philosophy.

2021

Copyright

This thesis is the result of the author's original research. It has been composed by the author and has not been previously submitted for examination which has led to the award of a degree. The copyright of this thesis belongs to the author under the terms of the United Kingdom Copyright Acts as qualified by University of Strathclyde Regulation 3.50. Due acknowledgement must always be made of the use of any material contained in, or derived from, this thesis.

Contents

Abstract

As the technology of radiofrequency linear accelerators (RF linacs) continues to improve, higher frequency acceleration systems become of interest as the achievable acceleration gradient has a dependence on frequency. Using a high driving frequency requires the consideration of many technological challenges. One such challenge is mitigating the effect of nonlinearities introduced during the electron acceleration and bunching process. To counteract the nonlinearity, an additional cavity at a harmonic of the main driving frequency can be included. This technique is known as harmonic linearisation. In existing C-band systems, harmonic linearisation can be achieved with an X-band structure, but if the main frequency is X-band, the lineariser must be Ka-band or higher. Linear klystrons are a well-developed technology and can reliably deliver tens of MW at X-band, but they are subject to a steep drop-off in achievable output power toward the Ka-band. The different interaction mechanism in a gyroklystron, based on phase-modulation of a helical beam, allows it to deliver multi-MW output power at significantly higher frequencies. The gyroklystron is therefore a strong candidate for delivering power to high-frequency linearising cavities.

The international collaboration, CompactLight, is developing a design for a sophisticated X-ray Free Electron Laser (XFEL) with wide ranging research applications [1, 2]. The project required the consideration of both a 36GHz and 48GHz lineariser options. In each case, the development of new amplifiers was required to deliver sufficient power for the application. This thesis presents the design and analysis of a gyroklystron appropriate to drive a 48GHz linearising cavity. While the research presented in this thesis was performed with direct consideration of the CompactLight XFEL, its relevance is not exclusive to this project. With the performance of the microwave amplifier presented in this thesis, a lineariser at 48GHz could be a viable option for other C-band or X-band accelerator applications.

Gyroklystron research was historically focused on radar applications. Since 48GHz lies in a frequency band unfavourable for atmospheric transmission, the development of components in this band has been lacking. The design presented in this thesis is the first published work on a MW-level amplifier at 48GHz and marks a step toward this frequency becoming a desirable choice for linearisation systems in future linacs. A gyroklystron design, including the electron source, vacuum windows, and input coupler has been designed through detailed simulation work. A triode-type magnetron injection gun compatible with a 2.02T axial guide magnetic field was designed and simulated. Applying -140kV to the cathode and -107.5kV to the modulating anode resulted in a gyrating electron beam with a current of 37A, guiding centre radius of 1.77mm, and velocity ratio spread of 8.9%. This resulted in a predicted gyroklystron output power of 2.0MW with a gain of 35dB at an efficiency of 38.6%.

Acknowledgements

Publications

Journal Papers

[1] – L. J. R. Nix, L. Zhang, W. He, C. R. Donaldson, K. Ronald, A. W. Cross, and C. G. Whyte, "Demonstration of Efficient Beam-wave Interaction for a MW-level 48 GHz Gyroklystron Amplifier", Physics of Plasmas, 27, 053101. March 2020.

[2] – L. Zhang, L. J. R. Nix, and A. W. Cross, "Magnetron Injection Gun for High-Power Gyroklystron", IEEE Transactions on Electron Devices, 67, no. 11, November 2020.

[3] – L. J. R. Nix, L. Zhang, and A. W. Cross, "Design of a 48GHz Gyroklystron Amplifier", Accepted for IEEE Transactions on Electron Devices, August 2021

Conference Papers

[1] – L. J. R. Nix, L. Zhang, and A. W. Cross, "Design and Simulation of a High-Power 48GHz Gyroklystron Amplifier for Accelerator Applications", Proceedings of 22nd International Vacuum Electronics Conference (IVEC), April 2021.

[2] – L. Zhang, L. J. R. Nix, W. He, and A. W. Cross, "MW-level Gyroklystron for Driving a Harmonic Lineariser for an X-ray FEL", International Workshop on Breakdown Science and High Gradient Technology (HG2021), April 2021

Other Presentations

Material presented in this thesis has also been presented at:

- CompactLight Annual Conference and Mid-year Reviews in Helsinki, 2019, Athens, 2020, and Glasgow (Virtual), 2020
- National Vacuum Electronics Conference (NVEC) at the University of Strathclyde, Glasgow, 2019

Role of the Author

Throughout this PhD study, the author gained experience in the theory, design, and simulation of gyro-devices including the interaction circuit, the beam source, and the input components. The main simulation results on the beam-wave interaction were obtained using the MAGIC simulation package, with other design work taking place in MATLAB, CST Microwave Studio, and CST Particle Studio.

Chapter 4: The author studied the theory and outlined the required parameters of the Magnetron Injection Gun (MIG) based on parallel consideration of the interaction circuit. The author performed preliminary work with a MIG model in MAGIC, and then ran thorough an optimisation routine using TRAK.

Chapter 5 and 6: The author played the central role in the design and simulation of the gyroklystron interaction circuit, which forms the bulk of this thesis. Several MATLAB scripts were written by the author based on existing theory from the literature to study the cavities and obtain linear theory results, while the MATLAB model for non-linear analysis was written by Dr. L. Zhang. Particle-in-Cell (PIC) simulation in MAGIC made up the bulk of the computational time required in the project. The author performed the bulk of the required simulation work on the interaction circuit, while Dr. L. Zhang played a vital role in troubleshooting the simulation input files and carrying out additional simulations to assess the impact of velocity spread.

Chapter 7: The author performed the simulation work on the input coupler, vacuum windows, and collector. The author calculated the initial dimensions and optimised them using CST microwave studio to create designs with appropriate operating parameters.

Clarification of Terminology

There is no universally applied standard for some of the terms in this field, and the reader should be aware of differences that may be found between this thesis and some of the cited publications. Here the terms *"gyroklystron"* and *"gyroklystron amplifier"* are used. Some references may instead hyphenate to *"gyro-klystron"* or use the term *"gyrotron klystron".* These terms interchangeably refer to the same type of device. The related device, the *"gyrotron,"* or *"gyrotron oscillator"* in full, is discussed in the background section. This name is used in the majority of literature, though a small number of the cited works may instead call it a *"gyromonotron."* Finally, the "*Cyclotron Resonance Maser (CRM) Mechanism"* is referred to as the *"Electron Cyclotron Maser (ECM)"* in some literature. In broader definitions, the term CRM describes a phenomenon involving any charged particle beam, while ECM is the same phenomenon specifically applied to electrons. As electron beam devices are the only widely used CRM technology, the terms are often used interchangeably in publications on gyro-devices, which are also commonly referred to as the *"CRM family"* of devices, which includes gyrotrons, gyroklystrons, gyro-TWAs, and CARMs.

Throughout this thesis and in much of the cited literature, frequencies are categorised by the IEEE bands, defined as shown in table 0.1. The naming of these bands began during the second world war to classify frequencies used in radar, but many modern publications use these band designations regardless of whether the device in question is related to radar systems.

In discussion of free-electron lasers operating regimes, the terms *"soft X-ray"* and *"hard X-ray"* are often used. X-rays are in the wavelength range from 10nm down to 0.1nm, and hard X-rays are those with a wavelength close to the low end of this band, i.e. wavelengths between 0.2nm and 0.1nm.

Table 0.1: Frequency band labels

Frequency (GHz)	Band
1 to 2	L
2 to 4	S
4 to 8	C
8 to 12	X
12 to 18	Ku
18 to 27	K
27 to 40	Ka
40 to 75	V
75 to 110	W
110 to 300	G or mm

List of Figures

List of Tables

List of Abbreviations

CERN – The European Organisation for Nuclear Research

CLARA – Compact Linear Accelerator for Research Applications

CLIC – Compact Linear Collider

CARM – Cyclotron Auto-Resonant Maser

CRM – Cyclotron Resonance Maser

CVD – Chemical Vapour Deposition

CW – Continuous Wave

ECM – Electron Cyclotron Maser

ECRH – Electron Cyclotron Resonance Heating

EM – Electromagnetic

EUV – Extreme Ultraviolet (wavelength of 124 to 10nm)

FEL – Free Electron Laser

   XFEL – X-ray FEL

FEM – Finite Element Method

Linac – Linear Accelerator

MIG – Magnetron Injection Gun

   CMIG – Coaxial MIG

   IMIG – Inverted MIG

MBK – Multiple Beam Klystron

MOGA – Multi-objective Genetic Algorithm

NRL – Naval Research Laboratory (USA)

(FDTD-)PIC – (Finite-Difference Time-Domain) Particle-in-Cell (simulation)

RF – Radiofrequency (around 20kHz to 300GHz)

SLAC – Stanford Linear Accelerator Centre

TE & TM – Transverse Electric and Transverse Magnetic (modes)

TWA – Travelling Wave Amplifier

TWT – Travelling Wave Tube

VUV – Vacuum Ultraviolet (wavelength of 300 to 100nm)

Chapter 1: Introduction and Background

This thesis presents the first study into the development of a MW-level 48GHz gyroklystron amplifier. While the theory and design of gyroklystron amplifiers have been studied for many years, the frequency band around 48GHz has received little to no attention. This is because historically radar systems have been the most common application of the gyroklystron, and due to atmospheric propagation windows, Ka and W-band frequencies have been a much larger focus. This chapter presents the broad background required to explain the application that motivated this research.

Section 1.1 covers the essential background on free electron lasers (FELs) and RF acceleration. The concepts of the gyrotron, klystron, and gyroklystron and then introduced in section 1.2. Section 1.3 then presents the history and current state-of-the-art in the field of gyroklystron development, and details how the gyroklystron relates to accelerator design. Section 1.4 then presents the conclusions of the literature review which demonstrate a gap in the available technology and the necessity of the 48GHz gyroklystron that is presented in this thesis.

1.1: Free Electron Lasers and Electron Bunch Linearisation

1.1.1: General Principles of Free-Electron Lasers

A free electron laser (FEL) [3, 4] is an extremely adaptable light source that can produce high-power coherent radiation across a large range in the electromagnetic (EM) spectrum. Conventional lasers operate at distinctly defined wavelengths based on energy transitions within the lasing medium involving electrons bound to discrete energy levels. In contrast, in an FEL laser emission of light comes from electrons freely streaming through a vacuum. This allows for much greater tuneability of the

wavelength than a conventional solid lasing medium. The operational process of the FEL can be described by classical electromagnetic theory without considering the quantum mechanisms of electrons. Conventional lasers have energy conversion efficiencies of only a few percent, while FELs have been demonstrated with 40%, and could theoretically reach as high as 65% [3].
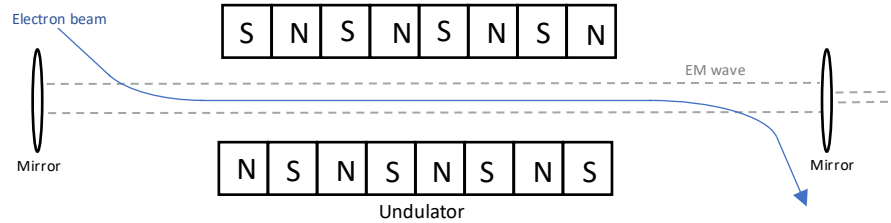
Figure 1.1
Simple schematic of an FEL

The radiation from an FEL is produced by an interaction of three elements, depicted in figure 1.1: the electron beam, an electromagnetic wave traveling in the same direction as the beam, and an undulatory magnetic field produced by a wiggler or an undulator. The difference in usage of these two terms is arbitrary and usage may vary between different publications, but in general "undulator" is used for the periodic magnets in FELs and "wiggler" is used for incoherent synchrotron light sources. The electrons follow an undulatory motion under the effect of the undulator field. In the process, electrons lose energy due to Bremsstrahlung radiation to the electromagnetic wave that is amplified and emitted by the laser. The photon wavelength generated from the interaction depends on the undulator field and the beam energy, each of which can be varied, allowing for excellent tuneability of the system. The radiated wavelength is given by

$$\lambda_r = \frac{\lambda_u}{2\gamma^2}\left(1 + \frac{K^2}{2}\right) \tag{1.1}$$

where λ_u is the undulator period, γ is the relativistic factor, and K is the undulator strength parameter defined as

$$K = \frac{eB_0\lambda_u}{2\pi mc} \tag{1.2}$$

where B_0 is the undulator's magnetic field strength, m is electron mass, and e is electron charge, and c is the speed of light. An electron beam passing through an undulatory magnetic field emits incoherent radiation. To generate the coherent radiation, the electron beam must form coherent bunches. When a light wave traverses the wiggler field, the combined effect of its field and the wiggler field produce a beat wave. The interaction between the beat wave and the electrons gives rise to the stimulated emission in an FEL. Because the beat wave travels slower than light, electrons can move in synchronism with it and experience a constant field, to achieve a strong interaction. The tunability, power, and high photon energy achievable make the free-electron laser very useful, but the benefits come at the cost of requiring a large facility to house it. Compared with synchrotrons, FELs are able to reach lower wavelengths and higher peak brightness which makes them a desirable light source for applications that require such properties, several examples of which are discussed in the following section. The following section discusses the development of FEL technology and its recent expansion into the X-ray region of the wavelength spectrum.

1.1.2 Free Electron Lasers: History, Advances, and Applications

The idea of radiation emission from an electron beam in an undulatory magnetic field was studied as early as 1951 [5]. This work and other independent discoveries [6] soon demonstrated coherent emission and several orders of magnitude's increase in the achievable power, but the true potential was not realised at the time. After the program was terminated, it was around a decade later before interest in the field grew again. A range of emission experiments were performed at Stanford University, and the term free-electron laser (FEL) was coined [4, 7-9]. Storage-rings instead of linacs were explored, leading to the development of FELs in France and Russia [10-12], but soon the effectiveness of RF linear accelerators as the beam source was realised. Several facilities were developed around the world [13-15] and many papers

were published at this time, marking rapid and focused progress in the field of FELs. Further detail on this history may be found in several reviews and textbooks [3, 16-18] but is not presented here as it is more relevant to this thesis to focus on the recent advances, specifically regarding the extension of FEL technology into the X-ray region of the electromagnetic spectrum.

Several advances were made, pushing toward shorter wavelength ultraviolet FELs in the vacuum ultraviolet (VUV) range (300nm to 100nm), and extreme UV (EUV or XUV) range (100nm to 10nm) [19, 20]. Following these significant leaps, the FLASH FEL at DESY, Germany, which had been operational for several years underwent a series of upgrades, achieving a wavelength tuneable down to 6.5nm in 2007, making it the first operational XFEL in the world [21]. FLASH has since continued to be an important and relevant XFEL facility with further improvements. The minimum wavelength has since been reduced to 4.1nm, among other achievements as described in an extensive review and the references therein [22]. Several other XFELs have also come into operation since then. The Linac Coherent Light Source at SLAC, USA, was the first XFEL to produce pulses in the hard X-ray range, achieving 0.12nm radiation and beginning to serve various users in 2009 [23]. In Japan, SACLA began operation in 2011 as the world's first sub-ångström wavelength FEL, with emission at 0.06nm [24, 25]. Elettra Sincrotrone Trieste in Italy is home to FERMI, a UV and soft X-ray FEL which can produce extremely short pulses with exceptional peak brightness [26, 27] which opened to users in 2016. In 2016 at the Pohang Accelerator Laboratory in South Korea, the PAL-XFEL came into operation as the third hard X-ray facility in the world [28, 29]. The European XFEL in Hamburg was first opened for users in 2017 and achieved a new world record wavelength in 2020 with emission at 0.05nm [30, 31]. Several more XFEL projects around the world exist in various stages of development between conceptual design stages and construction. The development of China's first XFEL at SINAP, Shanghai, is underway and expected to be in a user-ready state in the near future [32, 33]. PSI in Switzerland is working on a facility called SwissFEL [34-36]. Its hard X-ray beamline, Aramis, has been in operation since early 2019 and has seen some experimental use, but optimisation is an ongoing process and the facility is not

yet in its final state. In addition to further work on Aramis, a second beamline, Athos, which will serve soft X-ray applications is under construction. The first lasing was recently reported, and the next milestone for the beamline will be the delivery of laser power to the experimental station. Figure 1.2 shows the layout of the SwissFEL facility as an example of an XFEL layout. While the precise layout can vary significantly between different facilities, the SwissFEL is a good example of a typical facility, featuring a series of linear accelerators and bunch compressors prior to the undulator.

At SLAC, the LCLS-II XFEL is under construction, with the first operation likely to begin in the second half of 2021 [37, 38]. The operating parameters of each of these facilities are shown in figure 1.3 (compiled from many of the citations in this section, especially reference [17] which provides a detailed review of XFEL facilities). Since most FELs are tuneable over a range of parameters, in each case the minimum wavelength and the highest electron beam energy are shown.
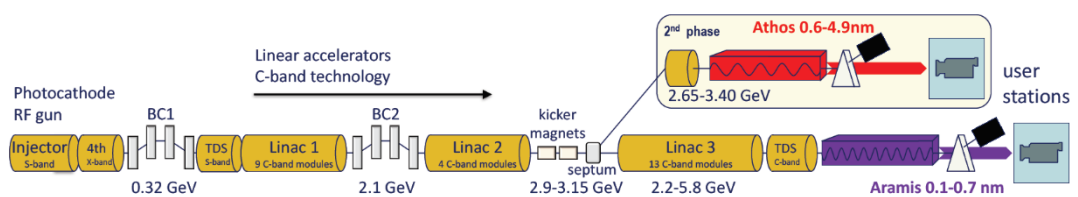
Figure 1.2
Layout of SwissFEL as an example FEL facility
Image from Ref. 35
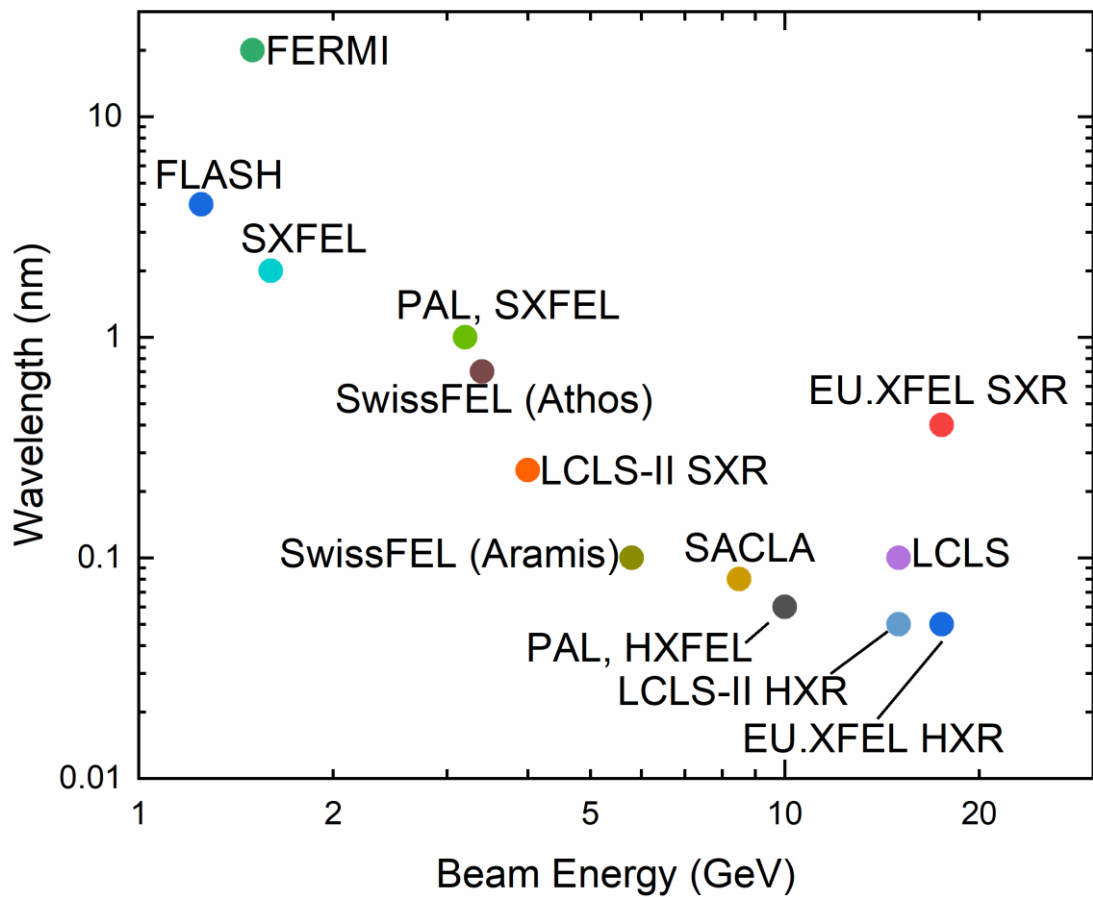
Figure 1.3
Parameters of present and future XFEL facilities

The operational XFELs around the world have each served a range of researchers who require the unique properties only offered by such a facility [2, 17, 18, 39, 40]. Imaging applications are dependent on the wavelength, so the ability to generate hard X-rays allows for very high spatial resolution, and the very short pulse duration allows ultrafast shutter speeds capable of freezing individual atomic motion. This can be used for pump-probe experiments, in which an optical laser is used to instigate some process or reaction, and then after a delay, an FEL beam is used to capture the image. The optical resolution is on an atomic scale, and hence this process can be used to study the steps in the formation and break of bonds in chemical reactions, mechanisms of matter at extreme conditions, and nanoparticle chemistry. The application of X-rays for the study of soft and biological material has been limited due to the damage they can cause to a sample, but the much shorter exposure time from an XFEL pulse can allow imaging to be completed more quickly than it takes for the effects of radiation damage to become apparent. Images of X-ray diffraction can be

recorded before the molecules under investigation are destroyed. The high coherence is also beneficial to imaging applications. FELs have also been used in industrial applications, such as material experiments by Rolls-Royce at LCLS to study pressure-induced phase transformations and high-velocity dislocation motion in titanium and zirconium foils [39]. Pharmaceutical companies have extensively used synchrotron sources. As technology improves with new FEL facilities, the purchasing of beamtime at FELs is likely to become cost-effective for certain pharmaceutical applications, especially drug discovery where there is interest in molecular materials that can only be crystallised as nanocrystals. There is also an interest in engineering to use FELs to study very fast reactions and phase changes in molecules such as in fuel additives, and to study deformations at very short timescales to better understand advanced materials in applications with extremes of temperature and mechanical stress.

FEL performance can greatly exceed that of synchrotrons, but the availability, costs, and experimental set-up time can be a dissuading factor. Many researchers have a strong desire for such performance, while other applications can be fully achieved at a synchrotron facility. Each new XFEL must therefore offer performance characteristics to make it worthwhile, which requires discussion with potential users to identify the desired parameters for the design goals. There must also be a focus on enhancing the technology such that the costs of construction and operation follow a downward trend to move XFEL technology into a more accessible range for researchers and industrial applications. These performance and cost criteria have driven the design choices for the new XFEL project, CompactLight, which is described in the following section.

1.1.3: CompactLight XFEL

CompactLight is an international collaboration funded as a European Commission Horizon 2020 programme. It consists of 26 partner institutes from across Europe,

Asia, and Australia working towards the conceptual design of a next-generation X-ray FEL facility beyond the current state-of-the-art [1]. The primary objective is to develop a compact and affordable XFEL facility design with specifications driven by the demands of potential users and associated science. The project outline describes the following advantages it should have over existing FEL facilities:

- Lower beam energy due to enhanced undulator performance
- A more compact layout, due to lower energy and high gradient of X-band structures
- Lower electrical power demand and footprint

The design is not for any individual application, but rather to develop a facility that can be used by many different users for various fields of research. For CompactLight, discussions were held with potential users, highlighting an interest in using FELs to explore:

- Materials far from equilibrium, such as light-induced superconductivity
- Nonlinear X-ray optics
- Multidimensional attosecond spectroscopy
- Charge migration and ultrafast X-ray biomolecule imaging
- Surface chemistry and pathways for catalysis
- Matter under extreme conditions

There were strong requests for improving the coherence and stability of FEL radiation pulses. In conjunction with the talks, a survey was used to analyse the desired parameters, finding the preferred pulse energy (3-100μJ), a desire for very good stability of pulse energy, pulse durations in the range 10-100fs, over 100Hz pulse repetition rate, and >70% transverse coherence. The questionnaire allowed users to comment on additional features that would benefit their experiments, giving the following preferred criteria: pulse energy >3mJ, shorter pulse duration, higher stability in pulse energy and duration, 1-10kHz rep rate, laser-FEL synchronisation better than 50fs, FEL-pump FEL-probe capabilities with a large photon energy difference, small focused spot size, tunability extended to higher photon energies,

and better reliability of two-colour pulse generation. Based on the consultation and survey data, the main target parameters were summarised as shown in table 1.1 [2].

Table 1.1: Target operating parameters for CompactLight XFEL design

Parameter	Unit	Soft X-ray FEL	Hard X-ray FEL
Photon Energy	keV	0.25 – 2.0	2.0 – 16.0
Wavelength	nm	5.0 – 0.6	0.06 – 0.08
Repetition Rate	Hz	1000	100
Pulse Duration	fs	0.1 – 50	1 – 50
Polarisation	-	Variable, selectable	Variable, selectable
Two-pulse delay	fs	±100	±100
Two-colour separation	%	20	10
Synchronisation	fs	<10	<10

The work in this thesis is partly associated with the CompactLight project, to investigate and develop the high-power microwave sources to drive the lineariser. The parameters required for the particular microwave source, the gyroklystron, are further derived from the parameters listed in table 1.1. The overall design goals dictate the required linac characteristics, which in turn dictate the required lineariser parameters. The gyroklystron presented in this thesis is designed with consideration of the lineariser. The concept of linearisation and the role of the gyroklystron in the system is discussed in the following sections.

1.1.4: Radiofrequency Particle Acceleration

The electron beam in a modern XFEL is usually accelerated by an RF linac. This section presents a short introduction to the basic concepts of RF linacs [41].

Accelerators based on DC accelerating voltages cannot achieve particle energy more than a few tens of MeV. In an RF linac, fields are applied in a series of many individual

RF cavities which allows for a total voltage gain much higher than the maximum applied voltage. Electromagnetic waves in a vacuum have electric fields perpendicular to the propagation and a constantly changing polarity. To solve this, resonant cavities can be used to create longitudinal electric fields of the correct polarity and keep up with the particle motion. Since each cavity can only reach a field strength of a few tens of MVm^{-1}, many cavities (and hence very long machines) are required. Avoiding such length is achieved for proton or ion accelerators using circular structures, allowing for multiple passes through the same accelerating structures. However, this is not practical for electrons, as energy losses due to synchrotron radiation severely limit the maximum kinetic energy. It is therefore preferable to maximise the acceleration gradient (i.e., the energy increase in the beam per metre of the structure). Higher frequencies are generally desired, but depending on the bunch properties needed, a lower frequency may still be more appropriate overall. The frequency is the main design parameter of a linac, and its selection often comes down to a careful trade-off between the relative merits and challenges of different options.

It is an increasing trend in the design of RF linear accelerators to look towards higher operating frequencies, as this can increase the acceleration gradient. More specifically, there has been recent interest in the development of 12GHz (X-band) acceleration structure such as in the design of the proposed RF option for CLIC at CERN [42], and in the driving linacs for CompactLight which are used in conjunction with a 6GHz subharmonic injector. RF linacs use bunched electron beams, and performance depends on the quality of the bunch. A standard single-mode cavity has a non-constant field profile, and the nonlinear effect of this limits the bunch quality. To solve this issue, some form of bunch linearisation must be used, as discussed in the following section.

1.1.5: Electron Bunch Linearisation

Advanced FELs such as CompactLight require the electron bunches to be extremely short, as bunch length is one of the main factors which determine the time resolution that can be achieved with such a light source. The initial compression of an electron bunch is caused by a linearly correlated energy spread. This can be done by ballistic bunching, which causes velocity differences, or in magnetic chicanes, which cause path-length differences. In any method, electrons will fall back from or catch up with each other based on these differences and form bunches. There are a couple of factors which limit the shortest bunch that can be achieved. The space-charge effect is unavoidable. The other factors are due to phase-space correlations which arise from the curvature of accelerating fields and nonlinear shifts of particles in drift regions. These factors can be minimised [43]. Linearisation is the process by which these nonlinearities are corrected for and doing so allows for shorter bunches and higher efficiency to be achieved.

The conventional approach of harmonic linearisation was first presented in 1986 [44, 45]. Harmonic linearisation is a technique in which a harmonic of the accelerating field is included to approximate a regime where there is no time-dependence of the field in the reference frame of the electron bunch. Some studies superimpose the fields in one cavity, such as in the multifrequency cavities which have been studied at Stanford University to improve the beam brightness [46]. In this case the sum of the field components produces a flat-topped field profile as shown in figure 1.4, which offers
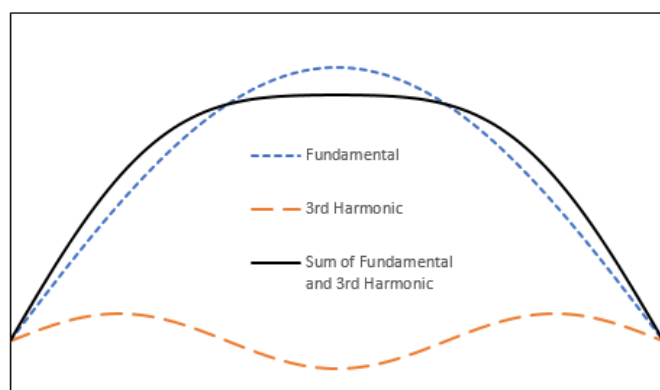
Figure 1.4
Flat-topped field by the sum of fundamental and 3rd harmonic

superior performance to a simple sinusoidal accelerating field profile. In relativistic beam lines such as in a high-energy linac, the fields at the additional frequencies can

be provided by additional separate cavities which is a simpler and more practical solution.

Although ideal point-by-point error compensation is impossible, the harmonic fields can significantly reduce the time dependence of the net field seen by the beam. Additionally, the magnetic field is naturally minimised in the process of flattening the electric field, and the transverse forces are reduced, which helps to reduce the beam emittance. Other linearisation techniques exist [43, 47-49], but none of these methods are under consideration for use with CompactLight, due to their lower reliability and readiness for practical application.
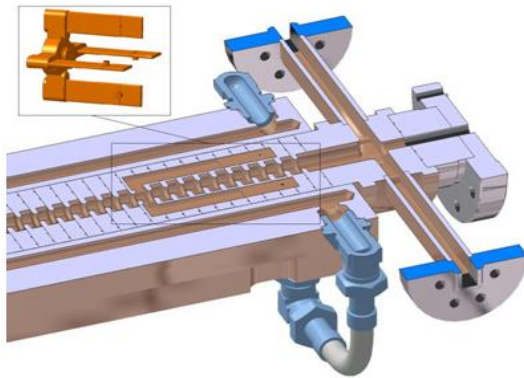
Figure 1.5
The CERN/PSI cavity
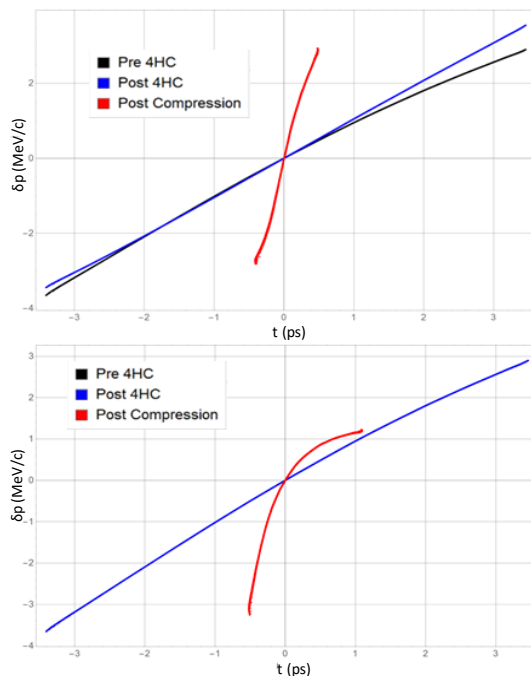
Figure 1.6
Energy deviation along bunch length in CLARA, with linearising cavity (top) and without (bottom) Image from ref. 54

Harmonic linearisation has been used in a design study performed for the TESLA X-FEL and TTF User Facility [50]. It was shown that the peak current could be efficiently enhanced by using a third harmonic accelerating section to correct for nonlinearities in the longitudinal phase space. The technique is also currently in use at the SwissFEL facility [35] and in FERMI@ELETTRA [51, 52]. It will also be used in the CLARA FEL, which is currently under construction in the UK [53, 54]. The design for the CLARA lineariser uses a cavity operating at the fourth harmonic (11.994GHz) of the 3GHz main frequency, chosen to match technological availability, and based on a cavity previously developed by PSI and CERN, shown in figure 1.5 [55, 56]. The

effectiveness of the cavity is illustrated in figure 1.6 [54]. With the cavity, the bunch is compressed to 0.8ps. Without it, the bunch is only compressed to 1.7ps and a clear nonlinearity can be seen. This result emphasises how crucial the lineariser is to achieving good beam performance in a linac.

Similar lineariser design principles to those used for CLARA have been proposed for the CompactLight XFEL. As the frequencies and requirements of CLARA and CompactLight differ, the technology cannot be directly copied over, but the underlying physics is the same. The CompactLight layout will include a 6GHz injector and 12GHz linacs to accelerate the beam. The physics of klystrons severely limits their output power capacity at very high frequencies, therefore alternative high-power microwave sources, such as gyroklystron have been studied to power the linearising cavities. Additionally, the CLIC project proposal for a future linear collider at CERN features two alternatives for the drive system for the first experimental stage [42]. The first is a two-beam acceleration system, and the second is a more conventional RF-based system. In the latter case, a 12GHz main linac frequency would be used, requiring a harmonic linearising system at 36GHz or 48GHz. In the early stages of CompactLight, a 12GHz system with either a 3rd or 4th harmonic lineariser was discussed. The layout was later updated to instead feature a 6GHz injector. 3rd, 4th, 6th, and 8th, harmonic options were considered for the lineariser and ultimately, due to the expected performance and level of existing development, the 6th harmonic (36GHz) option was selected. Collaboration between the University of Strathclyde and the University of Electronic Science and Technology of China (UESTC) led to the design of a compatible 36GHz three-cavity gyroklystron design in 2017 [57]. Operating at the fundamental harmonic in the TE$_{0,2}$ mode, PIC simulations predict a stable power output of over 3MW which comfortably meets requirements. Although the selection has now been made for the CompactLight baseline, the 48GHz option remains of interest for comparison of feasibility, and potential application in similar facilities in the future.

While it is broadly true that higher harmonics are more effective, there are trade-offs to consider. The performance of voltage modulators, amplifiers, pulse compressors,

and mode converters may not meet the same standards at a very high frequency. Existing technology is also an important factor, and currently S-, C-, X-, and Ka-band structures have received the most attention. The development of a strong amplifier candidate at 48GHz marks a significant step toward this frequency becoming a solid choice for a future lineariser. The 48GHz gyroklystron has the most potential as the driver for a 4th harmonic lineariser of a 12GHz accelerating system. In this context, it represents a good middle ground between pushing to a higher frequency and still being able to deliver high output power. Achieving a large enough power output at 72GHz (6th harmonic), for example, would be exceptionally difficult, and the small physical dimensions of such an amplifier would raise the technological demands in manufacturing tolerance and cathode performance. Hypothetically, a coaxial or high-order mode gyroklystron could alleviate some of these size issues, but the additional complexity and general lack of technological development of co-axial gyro-klystrons at such frequencies makes them less desirable. Additionally, linearising structures at the 3rd and 4th harmonics have been more widely developed and used than higher harmonics and hence the technological expertise is more readily available for the design and construction of 3rd or 4th harmonic structures at Ka-band or V-band frequencies.

1.2: High Power Microwave Sources

Vacuum microwave electronics is a diverse field of study with many different types of devices including klystrons, gyro-devices, backward-wave oscillators, crossed-field amplifiers, and many others. For this thesis, only the klystron and the gyro-device family are of major interest, and a brief overview of several such devices is provided in the following sections (1.2.1 to 1.2.3). These devices have a broad range of applications such as in accelerators, radar, plasma heating, communications, and more.

In a high-energy accelerator application, the electron beam needs to match the phase of the EM wave in the acceleration structure, therefore amplifiers are ideal as the driving sources. Oscillators, such as the backward wave oscillator, the gyrotron, and the magnetron have limitations in this application. There are also different types of amplifiers, such as the traveling wave tube, klystron, gyroklystron, and gyro-traveling wave amplifier (gyro-TWA). The traveling wave tube can achieve a maximum power of a few hundred watts in Ka frequency band, which is not enough power to drive the lineariser. Klystrons can achieve 75MW at 12GHz [58, 59], but as the frequency increases, the possible output power drops dramatically. Gyro-devices are fast-wave devices and have large power capability. The gyroklystron has a high gain and narrow bandwidth, which is more suitable to drive a cavity structure than the gyro-TWA which has a lower power and broad bandwidth.

This section provides further detail on the requirements for different applications and an overview of the related microwave sources. The relative merits and applications of each are presented without detailed theory, as the purpose of this section is to provide a simple overview of the available technology.

1.2.1: Gyrotrons

The gyrotron was the first member of the gyro-device family to be invented [60]. It is an oscillator which can deliver hundreds of kW of power at microwave and millimetre-wave frequencies. It is based on a principle called the cyclotron resonance maser (CRM) mechanism, sometimes known in this context as the electron cyclotron maser (ECM) mechanism, which depends on the resonance between a field mode and the electron cyclotron mode [61-64]. The operation of the CRM mechanism in a gyrotron can be summarised as follows, while a more thorough mathematical description is presented in section 2.1:

- A relativistic electron beam with helical trajectories is produced.
- The beam passes through a resonator.
- The cavity field modulates the beam into phase bunches.
- The satisfaction of a resonance condition between a cavity field and the electron bunch enables the transferal of energy between the beam and field.
- Beam energy lost to the field is released as a coherent output microwave power.
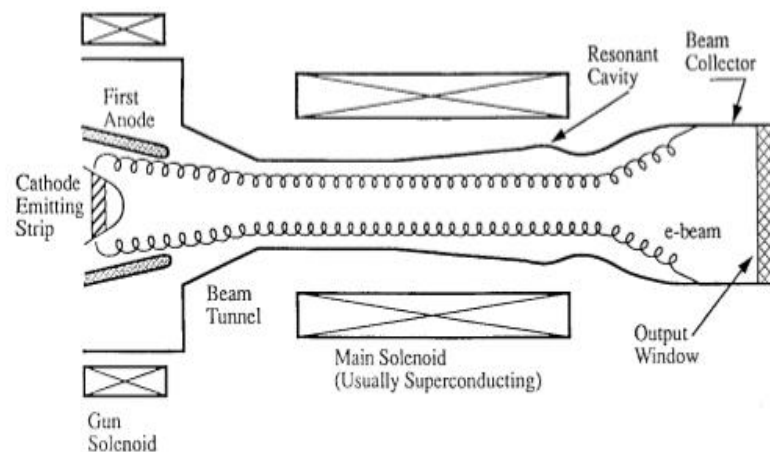
Figure 1.7
Typical Gyrotron Arrangement
(image from ref. 65)

A schematic is shown in figure 1.7 [65], showing the layout of a simple gyrotron. Many modern gyrotrons have more complicated collectors and output mode conversion structures than that shown above, but the main interaction structure does not differ

greatly, featuring the bunching and extraction processes occurring in the same resonant cavity. Gyrotrons can operate with high efficiency and in many different operating modes, including very high order whispering gallery modes. The use of such modes can allow for stable operation at high power, and then mode-converters at the output can change that power to the desired mode with relatively small losses.

The gyrotron is of historical significance as it was the first CRM device, but it is still widely used today. While solid-state physics has dominated many applications, the unique ability of microwave tube devices to produce hundreds of kW of continuous wave (CW) at high frequency has caused them to remain highly relevant, with applications in many fields. Gyrotron class oscillators have been used for many applications such as plasma heating, electron cyclotron drive current in fusion plasma, generation of extreme ultraviolet light, electronic paramagnetic resonance spectroscopy, and industrial material processing, but the main applications are in radar and communications.

As the understanding of the underlying mechanisms of the gyrotron grew, several other gyro-devices were invented, expanding CRM vacuum electronics into a large family of related devices, each suited to different applications. Several such devices are described in the following sections.

1.2.2: Klystrons and Gyroklystrons
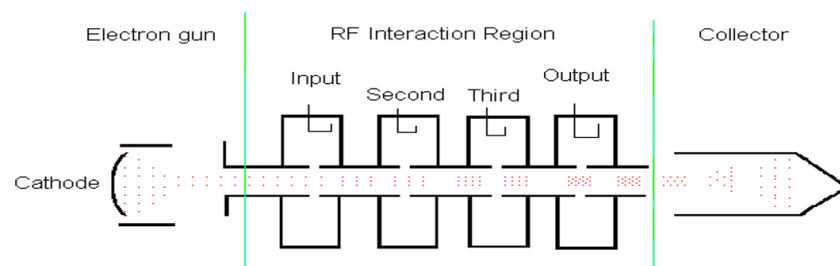
Figure 1.8
Schematic of a 4-cavity klystron

The explanation of the gyroklystron first requires an introduction to the linear (O-type) klystron. Proposed in 1935 by Heil and Arsenjewa-Heil [66], and first tested in 1937 [67, 68], the klystron predates the gyrotron and CRM mechanism and was the first device to utilise the concept of electron bunching. In the klystron's case, this takes the form of velocity modulation to create axial bunches, unlike the CRM mechanism which uses phase modulation to create azimuthal bunches.

In a klystron, an electron beam passes through a cavity called the buncher, as shown in figure 1.8, in which there is a standing wave acting as an AC voltage. As a continuous beam passes through the cavity, the electrons experience different voltages. This means that some electrons pass through during the accelerating phase, and other pass through during the decelerating phase. The electrons then leave the cavity into a drift region where no fields are present, so they continue moving with the velocity they left the cavity with. In the drift region, the accelerated electrons will catch up to the slower electrons ahead, converting the continuous beam into a series of longitudinal bunches. One or more intermediate cavities serve to reinforce the bunching effect. The electrons then reach another cavity called the catcher or output cavity, positioned such that bunches arrive when the field opposes their motion. This causes them to lose kinetic energy, which is transferred to the field and coupled out through a waveguide. Finally, the spent beam is deposited on a collector.

Klystrons are widely used today in a range of applications from communications and radar to particle accelerators. The operating frequency of a klystron depends mainly on cavity size with a smaller cavity having a higher frequency. Power-handling capacity also depends on cavity size, with a larger cavity allowing a greater maximum power within it. As these requirements conflict with each other, there is a significant fall-off in the output power that can be obtained at high frequencies. An approximate trend is the output power is proportional to $\frac{1}{f^2}$ [69]. This is a gradual trade-off rather than an exact limit, but the rough point at which high power multi-MW-level klystrons cease to be viable is around the Ku-band. The use of large coaxial multi-beam

klystrons (MBK) has been explored to work around this limitation. The MBK is compared with the gyroklystron in more depth in section 1.3.4.

In cases where klystrons are unsuitable, the gyroklystron is often a viable solution. The gyroklystron can, in a simplified sense, be thought of as a union of concepts of the gyrotron and the klystron. Like the klystron, a beam passes through a series of cavities, the first of which begins the bunching process, and the last of which allows for energy extraction. The key difference is that the bunching is not axial, but azimuthal, as in the gyrotron. The operating frequency therefore depends on the resonance condition of the electron orbits and the cavity field rather than solely on cavity size, thus enabling the use of a larger cavity with larger power-handling capability. Therefore, for high operating frequencies, a gyroklystron can deliver significantly higher output power than a linear klystron.

Section 1.3 presents a detailed review of the history and applications of the gyroklystron. Here, the devices are discussed only regarding the application in an XFEL. RF accelerators (section 1.1.4) require a high-power microwave source to drive the accelerating structures. Since the frequency range for XFEL linacs is X-band and below, linear klystrons are generally a suitable power source. X-band klystrons delivering power 50MW and more were developed at SLAC and have been available for many years, and are widely favoured in linear accelerator applications [59, 70]. An extensive research program at SLAC investigated the possibility for gyroklystrons as drivers for future linear accelerators [71], but currently no active or proposed linac uses gyroklystrons instead of klystrons as the main drive, due to improved klystron designs and the current lack of desire to use accelerating frequencies higher than X-band. However, the linearising system is another matter, as it requires an operating frequency significantly higher than the main drive. The proposed system for CompactLight features a 6GHz injector and a series of 12GHz RF linacs. Both of these frequencies can comfortably be delivered using klystrons. The lineariser will operate at the 6th harmonic of the 6GHz injector frequency, which is 36GHz. Current commercial klystrons cannot deliver the multi-MW power needed at this frequency or higher. Gyroklystrons therefore become a strong candidate, such as the 36GHz

amplifier designed by Strathclyde and UESTC [57], and the 48GHz design is presented in this thesis.

1.2.3: Gyro-TWAs and Gyrotwystrons

The gyro-travelling-wave tube amplifier (gyro-TWA, sometimes gyro-TWT or gyro-TWTA) is a device capable of wide-band operation, which makes it useful in certain radar and communications applications [72, 73]. The power achievable is generally lower than that of a gyroklystron but the bandwidth can exceed 5% in some cases [74].
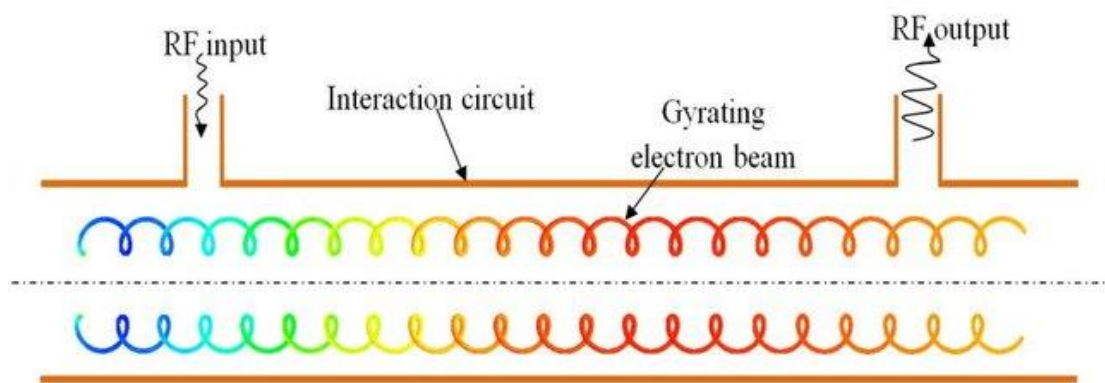
Figure 1.9
Schematic of a gyro-TWA
Image from ref. 69

A schematic is shown in figure 1.9 [75]. The gyro-TWA uses a moderately relativistic electron beam which interacts with a fast waveguide mode. The phase velocities of the fast cyclotron mode and waveguide mode are nearly matched, as well as the axial velocity and the group velocity of the waveguide mode. This allows for high efficiency and gain, and since no resonant structures are used, the bandwidth can be significantly larger than that of a gyroklystron.

A hybrid called a gyrotwystron also exists. It uses the basic structure of a gyroklystron but extends the drift section and replaces the output cavity with a waveguide section like that of a gyro-TWT. The idea is to combine the properties of both devices, taking advantage of the high gain associated with gyroklystron bunching and the large

bandwidth achieved in the gyro-TWA. The bandwidth can be further enhanced by stagger-tuning if multiple pre-bunched cavities are used. Stagger-tuning refers to offset the frequencies of each cavity to improve the overall response. This concept is discussed in chapter 5, where the gyroklystron design process is covered in detail. The gyrotwystron is useful for radar applications which require both high gain and large bandwidth. A related device called the inverted gyrotwystron instead has an input waveguide followed by a drift section and output cavity [76]. It is well suited to serve as a moderate bandwidth frequency-doubling amplifier.

1.3: Historical Development, Recent Advances, and Applications of the Gyroklystron

1.3.1: Early Development

The historical background of the gyroklystron begins with the gyrotron, which was invented in the Russia in the 1960s [60], with the first practical tests being carried out in 1963 [72]. The cyclotron resonance maser (CRM) mechanism which is the main underlying principle of the device was independently discovered at around the same time by a number of groups [61-64], and then first experimentally demonstrated in the early 60s [77-79]. The CRM mechanism extracts power from an electron beam by satisfying a resonance condition between an electron cyclotron mode and an EM field mode. The process was briefly introduced in section 1.2.1 and is described in detail in section 2.1. By the mid-70s, gyrotrons had become an area of major interest around the world [65, 80, 81], but researchers in Russia were still at the forefront of progress in the field, reaching breakthroughs that led to high average power mm-wave gyrotrons with 1.5kW power reported at frequencies above 300GHz [82]. The production of multi-kW power for millimetre wavelengths then drew the attention of plasma physicists. Theoretically, electron cyclotron resonance heating (ECRH) was already known as a possible plasma RF heating technique, but prior to the gyrotron, no source of suitably high-power radiation existed.

Improvements to device performance continued to be achieved, and by the early 1980s, megawatt power gyrotrons operating at high order modes were developed, but initially this was only for devices producing relatively short-pulse radiation (~100μs) [83, 84]. The challenge was then to extend pulse duration and overcome the contradicting requirements of the beam collector and output waveguide – a large collector is needed for deposition of the spent beam, but the radius cannot be increased too quickly, or unwanted mode conversion will occur. An important method to deal with this problem involved the introduction of quasi-optical mode

converters [85-87], which are more complex than the spirally corrugated waveguide sections that had previously been used to transform from one mode to another [88]. They consist of carefully selected geometric arrangements of reflectors and cavity sections and are typically used to convert high-order cylindrical waves into gaussian beams.

In the last two decades, gyrotrons for plasma research have been produced with power outputs of 1MW to 2MW for frequencies in the range of 140-170GHz [89-91]. At lower power outputs, gyrotrons for nuclear magnetic resonance spectroscopy applications have been developed with a frequency reaching slightly over 1THz [92-94]. The references provided for these recent advances are just a small selection from the extensive literature that has been published. More detail can be found in several good review articles [65, 89, 95, 96], as well as reviews more focused on the applications of such devices [97, 98]. Gyrotrons and related devices have been studied and developed without pause since their invention, and progress is set to continue, including applications in modern experiments. One particularly notable example of this is that gyrotrons will be used as one of the external plasma heating systems in the ITER project [99, 100].

Meanwhile, building upon the concepts of existing gyrotron technology, the gyroklystron was first invented in 1967 [101], though the idea behind it can be found in earlier work [102]. Advances in gyrotron technology were often relevant to high-power microwave devices in general, including the gyroklystron. In particular, gyroklystrons tend to make use of the advances made in the design of depressed collectors, CVD diamond output windows, and electron gun designs optimised for low velocity spread [103]. Gyroklystrons tend to operate at low-order, azimuthally symmetric modes, though some exceptions to this are discussed in section 1.3.3. This allows them to use parallel output rather than the complex quasi-optical mode convertor arrangements that are necessary in high-order gyrotrons. Early gyroklystrons suffered from instabilities, resulting in poor performance and less than 10% efficiency, but this was improved to over 30% by the use of 3-cavity designs [104, 105]. Additional improvements were seen due to advances in the carbon-loading

processing techniques used to prepare ceramic microwave absorbers [106]. These developments, alongside improved suppression of the instabilities that limited early devices [107], led to over 33% efficiency even in two-cavity gyroklystrons [108]. The more recent advances in gyroklystron technology have been primarily in two fields of study – radar and accelerators – as covered in the following two subsections.

1.3.2: Gyroklystrons for Radar Applications

The application of gyroklystrons to radar systems is historically one of the most widely studied areas of gyroklystron research, and the most common practical use of them in the present day. The development of gyroklystron-based radar systems largely started in Russia in the 1970s. Meanwhile, the Naval Research Laboratory (NRL) in the USA also took interest in developing their own systems. These two groups were the primary contributors in the early years of this field. Early history can be found in many textbooks and literature reviews, and in this section more recent developments are presented.

Gyroklystron radar devices have been primarily developed for frequencies around 35GHz (Ka-Band) and 94GHz (W-band) due to favourable propagation properties in the atmosphere. Radars for precision tracking of objects, such as missiles, asteroids, and space debris tend to require high-power millimetre waves, which can be generated by gyroklystrons. The first operational radar using gyroklystron technology was the 35GHz radar, RUZA, which was built by Russia in 1989 [109]. In the USA, the NRL, CPI, Litton EDD, and the University of Maryland worked together to develop 94GHz gyroklystrons in the late 90s [110, 111], which were subsequently used in a project called WARLOC staring in 2001 [112, 113]. Capable of 10kW average power output, WARLOC marked a twentyfold improvement compared to existing radars at the same frequency. Further progress has since demonstrated higher peak powers. For example, IAP researchers have presented experiments in which 93.2GHz designs were measured to have a peak output power of 220kW for a two-cavity setup and

340kW for a three-cavity setup [114]. The efficiencies of these two designs were 32% and 27% respectively.

Several recent publications in the field of radar gyroklystrons have come from researchers at the Chinese Academy of Sciences (CAS) in Beijing. A second harmonic two-cavity gyroklystron was developed [115], and soon followed up with a three-cavity gyroklystron, operating in the cylindrical TE_{021} mode [116, 117]. The use of second harmonic reduces the required magnetic field compared with fundamental harmonic devices, and hence typically also reduces the size, weight, and cost of the magnetic structure needed for the beam-wave interaction. However, harmonic operation reduces efficiency, so going beyond the second is rarely feasible. The gyroklystron developed by CAS operated at 35GHz with an efficiency around 16%, and a peak output power of 212kW. The pulse repetition rate was 50Hz. The amplification bandwidth was increased by the use of multi-cavity stagger-tuning to 155MHz. These experimental results matched well with what had been predicted from their PIC simulations, adding confidence to the computational methodology. The Fourier transformed frequency spectrum showed a single spike at 35GHz with no mode competition. The paper concludes with a statement that work was planned to further increase the average output power, but this is not yet reported.

CAS researchers have also looked into W-band gyroklystrons operating at 94GHz [118, 119]. In this area, they have presented a range of simulated results. One example predicts 142kW output power with 33.8% efficiency for a four-cavity gyroklystron operating at the fundamental harmonic in the cylindrical $TE_{0,1,1}$ mode. Another similar design is predicted to produce 145kW with 35% efficiency [120], and another predicts as high as 362kW output [121]. Experimental prototypes are planned based on these various simulation results but are not yet reported.

Work at the Indian Institute of Technology (IIT) has demonstrated the first conceptual design for a kW-level D-band gyroklystron [122]. The design is a second harmonic four-cavity gyroklystron which is predicted to output 1kW of power at 140GHz frequency. The predicted efficiency, however, is only 2.5% so there likely needs to be

further refinement of the design before it progresses to an experimental prototyping stage.

The possibility of gyroklystrons for generating chaotic millimetre-wave radiation, which may be appropriate for certain radar applications [123], has recently been explored with PIC simulations [124]. A delayed feedback system was added to a previously developed 93GHz gyroklystron [114], changing it from an amplifier to an oscillator. It was shown that a gyroklystron with a rapid phase shift leads to unstable eigenmodes. This causes time variations in the eigenfrequencies and a chaotic output which simulation results showed to be on the order of tens of kW, with a spectrum width between 1 and 2GHz.

1.3.3: Gyroklystrons for Accelerator Applications

Researchers at the University of Maryland (UM) and SLAC first proposed the use of gyroklystrons for accelerator applications (in particular for driving electron-positron colliders) in 1985 [125]. As they were looking for amplifiers to operate at higher peak power (P_p) and shorter wavelength (λ) than the high-current klystrons, the quantity $\frac{P_p}{\lambda^2}$ (or $P_p f^2$ in some literature), was used as a comparative value. A fundamental mode four-cavity gyroklystron was designed with a higher value of this parameter than the state-of-the-art klystrons of the time. Early results showed promise, but simultaneous improvements to linear klystrons limited the demand for gyroklystron alternatives for colliders up to 1TeV. However, gyroklystrons were still explored for potential use in future multi-TeV colliders [71]. Theoretical efficiency on the order of 40% was calculated, with a prediction that the use of a multi-electrode depressed collector could increase it to 65% by the highest estimates. Several arrangements were considered over the first decade of this project, starting with a four-cavity system. A sequence of six two-cavity tubes exceeded efficiency goals but fell short of targets for power output. Theoretical models predicted similar peak power at double

the output frequency by operating in the second harmonic, which additionally has advantages in terms of reducing the magnetic field requirement. A series of seven two-cavity second harmonic gyroklystrons was then studied, and it exceeded the design goal power at the cost of a modest reduction in efficiency and gain [71]. This early work consisted of many exploratory studies that led the research program to push forward the state-of-the-art for gyroklystrons up to the 30MW power level, well above previous records.

Looking to push the peak power further toward the goal of 100MW required a higher beam current, and hence a larger beam radius and a larger waveguide to contain it. Cylindrical waveguides are generally unsuitable at this size as suppressing competing modes becomes increasingly difficult for modes beyond TE_{021}. Therefore, coaxial designs were studied as they are capable of supporting a larger beam radius at their low-order harmonics than cylindrical tubes. Simulations of an early two-cavity design showed the capacity to produce a 100MW pulse, but it also had poor mode purity due to overlapping resonances and only 25.4% efficiency [126]. Subsequent work used longer cavities, as this allows for a smaller field amplitude and hence a narrower resonance band. A three-cavity design was simulated and then assembled. Experimental studies showed operation in the $TE_{0,1,1}$ mode at 8.6GHz and achieving peak powers of 75-85MW with 32% efficiency [104, 127]. The theoretical design specification called for 96MW with 40% efficiency, so while the gyroklystron tested fell short of this, it marked significant progress towards that goal, and better performance than previous designs.

Referring back to the previous observations on the advantages of second harmonic operation, a conceptual design for a high-gain frequency-doubling gyroklystron was presented in 2005 [128]. Several arrangements were considered and analysed. The best of these was a six-cavity device featuring three fundamental harmonic cavities followed by three second-harmonic cavities. In 2007 a scaled version of this design was also simulated [129]. The original operated with an output of 17.136GHz, and the new scaled version operated at 22.848GHz. Most dimensions and operating parameters were scaled up or down by the ratio of these two frequencies before

optimising the design. The predicted performance was at least 35MW power output at 20% efficiency, and potentially up to 68MW at 37% efficiency depending on how severely whole-tube modes would reduce the maximum velocity ratio. Despite the promising results, no publication reports the construction and testing of this design. Another design for the same 22.848GHz frequency was suggested in 2013, using a cylindrical four-cavity setup and delivering 20MW of output power with a 120Hz repetition rate of 1μs pulses [130]. Being cylindrical and consisting of only four cavities (rather than six), it would be less complicated to fabricate than the other design at this frequency. References [131] and [132] are the most recent publications on the topic from either UM or SLAC, and it appears that the ambition to use gyroklystrons as the main drive sources has been set aside at present.

In addition to the K-band work described above, UM and SLAC have worked with Calabazas Creek Research, Inc. (CCR), developing a gyroklystron for W-Band linear accelerator applications [133]. They designed and assembled a 91.392GHz second harmonic gyroklystron, predicted to operate at 10MW with a gain of 55dB. This was a six-cavity cylindrical design in which the first buncher cavity operated at the fundamental $TE_{0,1,1}$ mode, and the following ones operated at the $TE_{0,2,1}$. Stagger tuning was used to enhance efficiency and bandwidth. Though it is stated that the device was assembled and ready for full testing in 2003, there is no publication reporting subsequent results, suggesting that the project may have been abandoned in favour of the more common K-band designs.

Communications & Power Industries (CPI) performed a study for CERN to investigate gyroklystrons with consideration of the Compact Linear Collider (CLIC) [134]. A gyroklystron with 50MW peak output power at 30GHz operating frequency was to be designed for testing and conditioning of CLIC. Coaxial and cylindrical variants operating at fundamental and second harmonic were investigated. The design deemed most likely to achieve the specifications was a fundamental mode coaxial TE_{011} four-cavity configuration, which had a predicted output of 68MW at 45% efficiency. Further work between UM and CCR was carried out toward similar design goals. Their simulation results showed 72MW at the fundamental harmonic or 37MW

at the second harmonic [135]. The fundamental harmonic design was a coaxial structure which allows the use of a larger diameter beam, and therefore higher beam current (300A in this instance). The second harmonic design was cylindrical, which is a simpler approach, but it could not meet the 50MW power specification. Though the coaxial design has good predicted power output, this is at the cost of more complex gun design. An inverted MIG was used to deal with the issue of support and cooling of the inner conductor, but further study is required to determine whether the trade-off between that issue and the increased complexity of the gun is beneficial overall. Despite these results, subsequent design reports for CLIC did not include gyroklystrons for the main driving signal.

While the majority of gyroklystron work focused on symmetric cylindrical and coaxial modes, Russian research in Nizhny Novgorod at the Institute of Applied Physics of the Russian Academy of Sciences (IAP), sometimes in collaboration with GYCOM Ltd, has also demonstrated progress in high-order mode gyroklystron design. Notably, in 2013 Zaitsev et al. achieved an experimental design with a result of $P_p f^2 \cong 18000$ [136], which they compared to UM's gyroklystron which had a value of 5900 [104]. The Russian device was tested up to 400keV of electron energy and 200A beam current, while at UM these parameters were 470keV and 480A respectively, and the comparative parameter does not take efficiency, gain, and bandwidth into account. The gyroklystron developed had a two-cavity setup using a triode-type MIG. The most significant difference in design, is that this gyroklystron operated in a $TE_{7,1,1}$ to $TE_{7,3,1}$ sequence, instead of the more common low order symmetric modes. Excitation of spurious oscillations due coupling between the cavities was minimised by the drift tube's absorbing and scattering elements. The measurements were 15MW power at a frequency of 35.4GHz delivered in 0.5µs pulses. The chosen modes allowed the design to utilise the geometry of the injector electrodes from their previous work [137], without the need for modification to accommodate the higher frequency.

Also following on from the previous work, designs based on $TE_{5,2,1}$ to $TE_{5,3,1}$ sequences have been studied [138]. 40% efficiency for 15MW output power was achieved in a two-cavity design producing 0.35µs pulses at a frequency of 30GHz. An input cavity

featuring adjoining rectangular waveguides which provide microwave radiation [139] is used to convert $TE_{0,1,1}$ input to the desired $TE_{5,2,1}$ mode of operation.

The use of asymmetric modes has long been a design feature for gyrotron oscillators as has been discussed in the first report. Applying the use of asymmetric modes to gyroklystrons as described above is an alternative solution to the high-power problem than using coaxial cavities, as stable whispering gallery modes can be achieved in a large cylindrical cavity. This is desirable as the design requirements for coaxial structures are very stringent, thus increasing the cost and difficulty of their production. Researchers at the Indian Institute of Technology (IIT) illustrated the level of precision needed when they performed misalignment analysis using their own design of a four-cavity gyroklystron [140, 141]. Misalignment between RF cavities, drift tubes, and the beam axis was studied, and it was found that RF power output is sensitive to this, while bandwidth remained nearly constant for small misalignments. A 0.1mm misalignment of the RF interaction region axis was shown to cause output power to drop from the initial value of 218kW to 80kW. This was the most impactful misalignment, but a large decrease in output power was also seen for a similar offset of the drift tube axis, and a small decrease for an offset of the cavity axis. Although accurate manufacture is possible and coaxial devices are widely used, this result demonstrates the precision needed. Precise construction is vital in any device, the requirements become even more strict when a coaxial structure is used.

The gyroklystron is developed as an amplifier in almost all cases. An exception to this was a project by the IAP where gyroklystron oscillator was developed [142]. It provides mode selection and the possibility of high frequency mode switching by use of a feedback circuit. The feedback loop contained a variable attenuator to control how much power is delivered back to the input cavity. Increasing the amount of feedback increased the pulse duration and peak output power, up to 1μs and 2MW. Tuning of the magnetic field and beam voltage allows for resonance and self-excitation at different modes. For example, at B = 1.465T and V_0=120kV, the $TE_{4,4,1}$ mode is excited without feedback and the $TE_{7,3,1}$ mode is excited when feedback is

applied. With fine-tuning to the right level of feedback, the issue of mode competition was well-addressed.

Gyroklystrons have received wide-ranging attention with consideration of accelerator systems. Despite many seemingly promising results, no current accelerator or published accelerator design proposal features them as the source of primary driving radiation. A future accelerator proposal might look to an even higher frequency that linear klystrons would struggle to meet, but in the short-term, acceleration structures lower than X-band still dominate the field. However, an X-band accelerating structure requires a Ka-band harmonic lineariser (section 1.1.5). The driving source for the linearising cavity must deliver MW-level power above the frequency range of conventional klystrons. Strathclyde and UESTC have developed a 36GHz gyroklystron appropriate for a lineariser application [57]. However, as discussed in section 1.1.5, there remains significant interest in higher harmonic linearising structures to improve the balance of performance and power demand. 48GHz is a potentially viable frequency for an 8th harmonic lineariser for a 6GHz injector, or a 4th harmonic lineariser for a 12GHz injector. As 48GHz falls well outside the bands commonly used for radar applications, it has previously seen little to no study. As accelerators and XFELs become more widespread, accessible technologies, the interest in better and cheaper lineariser designs will also grow. The demonstration of an efficient driving source for a 48GHz lineariser is a crucial aspect of such designs. The research presented in this thesis presents the design and simulation of a 48GHz gyroklystron. It is the first MW-level gyro-amplifier at this frequency [143]. The analysis of the interaction circuit, electron beam source, input coupler, and pillbox window is presented.

1.3.4: Comparison of the Multibeam Klystron and the Gyroklystron

As stated previously, the conventional single-beam klystron suffers from a steep fall-off in achievable output power at high frequencies. Two options stand out as possible candidates to meet power requirements above Ku-band: the gyroklystron and the Multibeam Klystron (MBK).

The MBK has been studied with success at lower frequencies, such as L-band amplifiers for CLIC [144] and S-band amplifiers at the US Naval Research Laboratory (NRL) [145]. The MBK also shows a lot of promise at X-band [146, 147]. There are only a few publications which discuss MBKs at frequencies beyond this range. For example, MBKs have been developed in Russia with operating frequencies as high as the Ku-band [148], though as radar sources they were designed for kW rather than MW power output. Similarly, kW-level Ku-band MBKs have been studied in India [149, 150]. The body of published work on MBKs at 30GHz and above is very limited. Simulations of a 30GHz MBK have shown 800MW output power with 27% efficiency [151]. The design uses an explosive emission cathode with an extremely high beam current, so is not appropriate to accelerator applications where a lower current and long lifespan thermionic cathode is desired, and no experimental prototype has been developed.

Recent simulation studies have demonstrated good performance of an MBK at 36GHz [152]. Internal presentations and discussions between CompactLight collaborators have shown that the Ka-band gyroklystron and MBK are both suitable based on the design and simulation stage. Hence neither is selected as the one absolute baseline, and both will feature in the conceptual design report and technical overview.

In the Ka-band range, the power of the 20-beam MBK is lower than the gyroklystron but still above the minimum requirement for the application in CompactLight, making it a reasonable alternative. The higher output power of the gyroklystron is a strong advantage but brings with it the disadvantage of a higher voltage, more power invested in cathode heating, and the need for a superconducting solenoid. These

relative advantages and disadvantages make the choice difficult at the Ka-band. However, at the 48GHz frequency of the gyroklystron presented in this thesis, no work has been performed on an MBK alternative. In general, the primary advantage of the gyroklystron over the MBK at high frequencies is that it can deliver higher power, and though they remain competitive at 36GHz it is unlikely that an MBK solution could compete with the gyroklystron in terms of output power at 48GHz.

1.4: Conclusions of the Literature Study and Direction of Research

The physics of gyrotrons, klystrons, and gyroklystrons has been explored for many fields of study and diverse applications. In the case of the gyroklystron, the development of radar technology has been the leading motivator of the field. This has led to many breakthroughs as discussed in section 1.3.2. However, due to propagation properties of microwaves in Earth's atmosphere, only certain frequency bands have seen extensive study. This has left other frequencies, such as V-band, largely ignored despite potential application outside the field of radar technology.

Section 1.3.4 described how the motivation to apply gyroklystron technology to accelerator applications drove many advancements in the theoretical, computational, and experimental background on gyroklystrons, but has not yet led to their use in any completed accelerator facility. However, researchers continue to look toward higher frequency RF linacs. While commercially available klystrons can comfortably deliver very high power at the C-band and X-band main drive frequencies that are used in present design proposals (such as CompactLight and CLIC) and are likely to be used in future facilities, the corresponding lineariser frequencies require new components. As discussed in section 1.1.5, it is desirable to use a high harmonic lineariser in an RF linac as it allows for lower power demand and more compact structures than would be required for a lower harmonic. The challenge raised by this, however, is that it is harder to generate sufficient power at higher frequencies. A linac proposal with a 6GHz injector could hypothetically use 18GHz, 24GHz, 36GHz, or 48GHz lineariser, while a 12GHz injector would likely look to 36GHz or 48GHz. Barring any unforeseen developments, CompactLight will use a 36GHz option (the 6th harmonic of its 6GHz injector), while future projects at C- and X-band are likely to express interest in exploring a 48GHz alternative. There are currently gyroklystron and multibeam linear klystron solutions which are predicted to meet CompactLight's demands at 36GHz. The development of a strong 48GHz lineariser solution may be

no longer essential for CompactLight but remains an important consideration for linac research in general. A proven amplifier solution at 48GHz is required before a lineariser at this frequency is likely to be selected as a design feature of a future linac system.

This thesis therefore aims to meet the following goals:

- To demonstrate a viable design of a MW-level microwave amplifier at 48GHz, a frequency for which no designs have previously been developed.
- To show performance that exceeds the minimum requirements for effective use in a harmonic lineariser, with target performance defined by the CompactLight design goals.
- To provide confident simulation data of a complete design, including the electron gun, interaction circuit, input coupler, and RF windows.

Chapter 2 presents the necessary theory required to understand the gyroklystron and its underlying principles. Chapter 3 then goes into further detail on theoretical and computational methods available to develop the design of the interaction circuit, beginning with a linear model used for initial predictions before moving on to the more advanced methods required for complete analysis. Chapter 4 covers the design of the magnetron injection gun (MIG) from the synthesis equations through to a finished design simulation with detailed performance analysis. Chapter 5 then builds further detail on the gyroklystron background, presenting how to move from the region of abstract theory to practical design choices which can be implemented in simulations. The simulation results are presented in detail in chapter 6. By the end of chapter 6, the viability of the gun and interaction circuit have been proven, but several components are still required for a complete design. These are the input coupler and vacuum windows, which are presented in chapter 7. Finally, the central results and conclusions are summarised in chapter 8.

Chapter 2: The Gyroklystron

A literature review of the gyrotron and gyroklystron was presented in section 1.2. In this chapter, further depth on the operating principle, major components in the device and their mathematical models are presented. Section 2.1 covers the fundamental features such as the CRM mechanism and the waveguide physics required to understand the principle of the device. Section 2.2 covers the magnetron injection gun (MIG) which provides the electron beam for the interaction circuit. The additional structures that complete the device are then discussed in section 2.3, including the input coupler and output components.

2.1: Background Physics

2.1.1: Fundamentals of Microwave Gyro-devices

The main underlying physics that governs gyro-devices is the interaction between electrons and electromagnetic fields; namely Maxwell's equations (2.1 to 2.4), the Lorentz force law (2.5), and the continuity laws for charge and current.

$$\nabla \cdot E = \frac{\rho}{\varepsilon_0} \qquad (2.1)$$

$$\nabla \cdot B = 0 \qquad (2.2)$$

$$\nabla \times E = -\frac{\partial B}{\partial t} \qquad (2.3)$$

$$\nabla \times B = \mu_0 j + \frac{1}{c^2}\frac{\partial E}{\partial t} \qquad (2.4)$$

$$F = q(E + v \times B) \qquad (2.5)$$

As dictated by the Lorentz force law, a magnetic field induces a perpendicular velocity component on electrons passing through it, causing them to follow circular paths. When applying this law to a beam travelling parallel to the field axis, the compound motion of the linear axial motion and circular perpendicular motion results in helical trajectories. As gyro-devices typically use cylindrical or coaxial cavities and waveguides, it is convenient to use cylindrical coordinates (z, r, ϕ), with the device's centreline forming the z-axis. This coordinate system is used for all equations and analysis presented throughout this thesis. The helical trajectory of an electron can be described by its velocity ratio, cyclotron frequency, and Larmor radius, defined respectively as

$$\alpha = \frac{v_\perp}{v_z} \tag{2.6}$$

$$r_L = \frac{v_\perp}{\omega_c} \tag{2.7}$$

$$\omega_c = \frac{eB_0}{m\gamma} \tag{2.8}$$

where B_0 is the applied magnetic field in the interaction region (often referred to as the interaction field), e is the electron charge, m is the electron rest mass, γ is the relativistic factor, and v_z and $v_\perp$ are the electrons' axial and perpendicular velocity components respectively. Equations 2.6 defines the velocity ratio, the choice of which is an important consideration in gyro-device design. The choice for this gyroklystron is discussed in chapter 5 – in most cases a value between 1.1 and 1.5 is used. The Larmor radius (equation 2.7) describes the size of the circular component of the helical motion and is therefore important to the consideration of the cross-sectional profile of the beam. Equation 2.8 shows a dependence on relativistic mass for the cyclotron frequency. This is crucial to the operation of gyro-devices, as it allows for a mechanism known as the Cyclotron Resonance Maser (CRM), or Electron Cyclotron Maser (ECM) depending on the literature [61]. Consider an electron beam with helical trajectories passing through an oscillating electric field. As described by the Lorentz force law and Maxwell's equations, electrons experience different forces depending

on their position and the relative phase of the electric field during their passage through the field region. Some electrons will experience an accelerating phase and others will experience a

Figure 2.1
Progression from uniform distribution to phase bunches

decelerating phase. Any electrons which gain energy have their relativistic factor increased, and hence by equation 2.8 their cyclotron frequency is decreased, which causes them to fall back in phase. Electrons which lose energy instead see their cyclotron frequency increased and advance forwards in phase. The net effect is that the initial uniform phase distribution is modulated into bunches as shown in figure 2.1 [153]. The effectiveness of this bunching process depends on the cavity mode and its coupling coefficient, which is explained in more detail in chapter 3.
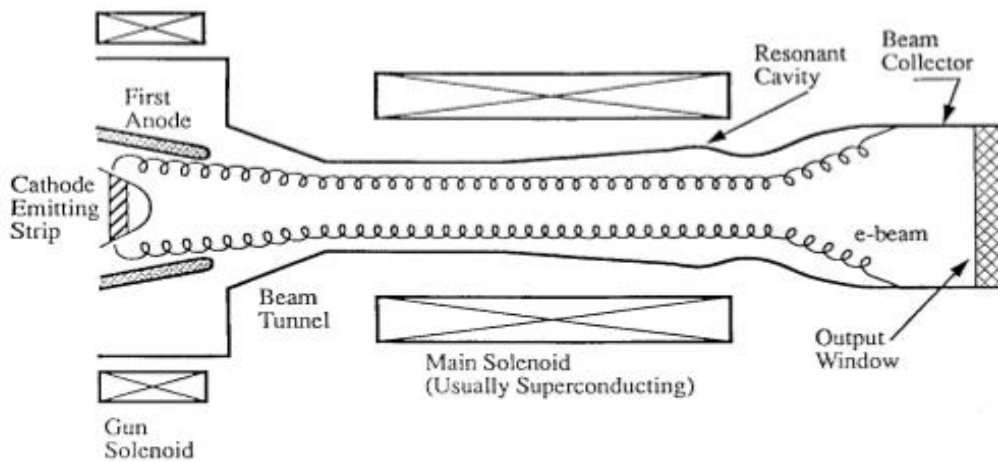
Figure 2.2
Typical gyrotron arrangement
(image from ref. 65)

The process by which power can be extracted through the use of the CRM mechanism is best explained in the context of the gyrotron oscillator, which was the first device based on this principle [60]. In the simplest model of a gyrotron, shown in figure 2.2 [65], a cathode emits electrons into a carefully chosen arrangement of fields which directs them into the interaction region with the desired α and γ. The beam-source in most gyro-devices is generated from a Magnetron Injection Gun (MIG) [154-157], as detailed in section 2.2. For simplicity, in this introductory section, the beam source

51

is not considered, and it is assumed that there is a beam with appropriate characteristics. Electrons in a gyrotron follow helical paths around a line parallel to the device axis. In a gyrotron, a magnetic field is set up to grow along the axis until it plateaus into a maximum constant field throughout the length of the interaction region. Within the interaction cavity, the electrons interact with the RF fields present, causing the bunching described above. Then in the output cavity, the bunched electrons are strongly coupled with the EM wave in the cavity by ensuring the beam radius is appropriately aligned relative to the peak of the relevant mode's coupling curve. Electrons in a decelerating phase of the cavity field lose some of their kinetic energy to the field which can be coupled out as microwave energy output. After the interaction cavity, the magnetic field decreases, and the spent electron beam settles on a collector. The collector also functions as a waveguide, directing the outgoing microwave radiation toward the output window.

The general principle of the CRM mechanism is the transferal of energy from the field to the electrons to form bunches, and then from the tight bunches to the field to create strong coherent output. This transfer depends on the resonance condition between the electron cyclotron motion and the cavity mode. However, the axial velocity v_z of the electrons means a Doppler shift must be accounted for, so the resonance condition is written as

$$\omega - k_z v_z = s\omega_c \qquad (2.9)$$

Where k_z is the axial wavenumber, ω is the operating frequency, ω_c is the cyclotron frequency, and s is the harmonic number. As only fundamental harmonic devices are dealt with in this thesis, s is equal to 1 from this point onward. A change in energy will change not only the cyclotron frequency, but also the axial velocity. These changes have opposite effects – a reduction in the energy increases cyclotron frequency, but also decreases axial velocity causing a corresponding reduction in the size of the Doppler term. In principle, it is possible for these two changes to fully compensate for each other. If this is the case, then if the condition for cyclotron resonance is fulfilled initially, it will still be fulfilled later regardless of the size of

energy changes. This is known as auto-resonance and is the basis of a family of devices called cyclotron auto-resonant masers (CARMs) [158, 159].
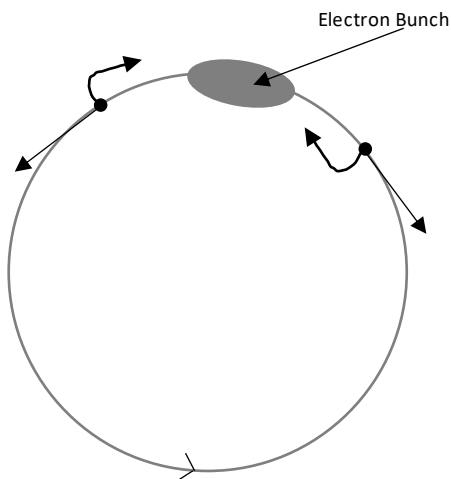
The bunching process is slightly enhanced by the negative mass instability [160], which is a phenomenon caused by the space-charge effect of an electron bunch. Figure 2.3 illustrates the effect of this on two example electrons. The concentration of electrons in the bunch creates a space-charge field which repels other electrons, exerting forces (shown by the straight arrows) on them. The space-charge force on the example electron approaching the bunch will reduce its energy. As described previously, this increases its cyclotron frequency, thus bringing it forward in phase toward the bunch (response shown by curved arrow). The other example electron ahead of the bunch gains energy from the space-charge force, experiences a reduction in frequency and hence falls back in phase toward the bunch. The result is that although the forces are directed away from the bunch, the overall effect is that electrons are brought closer to it, therefore enhancing the bunching strength. It has been shown that this process can slightly improve the gain of a device [161], though it should be noted here that this description is not perfectly accurate, as it does not take into account the formation of many beamlets. The presence of bunches in any given beamlet can influence electrons in nearby beamlets, and this can significantly alter the effect described here. Hence the CRM device works best for a gyrating electron beam which has very low velocity spread.

There are two saturation mechanisms to consider regarding the wave generated by the CRM instability. There is the depletion of the electrons' free energy as some of the transverse kinetic energy of electrons is lost to the wave. The second is the phase trapping of particles by the wave. This occurs when energy has been extracted,

Figure 2.3
The effect of space-charge on an electron bunch
Straight arrows represent space-charge force,
curved arrows represent resulting electron motion.

increasing the cyclotron frequency and transitioning the bunch back into the accelerating phase of their orbit. After consideration of these two saturation processes, the maximum electronic efficiency of a CRM device can be shown to be around 40% (before the addition of energy recovery components such as depressed collectors) [72]. The interaction efficiency can be defined as

$$\eta_{int} = \frac{\langle \gamma_i \rangle - \langle \gamma_f \rangle}{\langle \gamma_i \rangle - 1} \equiv \frac{\gamma_0 + 1}{2\gamma_0} \frac{\alpha_0^2}{a_0^2 + 1} \eta_\perp \qquad (2.10)$$

where γ is the relativistic factor, α is the velocity ratio, the subscripts *i* and *f* refer to the values at the entry and exit of a cavity, and the subscript 0 refers to the value at the interaction region. The angular brackets refer to the average over initial conditions. The interaction process is optimal in a mono-energetic beam, which is not a realistic scenario. Velocity spread is minimised by good electron gun design and field arrangement, but factors such as the thermal distribution of electrons and the finite dimension of the cathode inevitably induce some spread. Additionally, once the electron beam is produced, the coulomb forces between electrons cause an additional spread. Modern electron beam sources can produce beams with velocity spread on the order of a few percent, which helps to reduce its effect to the beam-wave interaction efficiency. Further discussion on the causes of spread and how to minimise it are presented in section 2.2.3.

2.1.2: The Gyroklystron Interaction Circuit
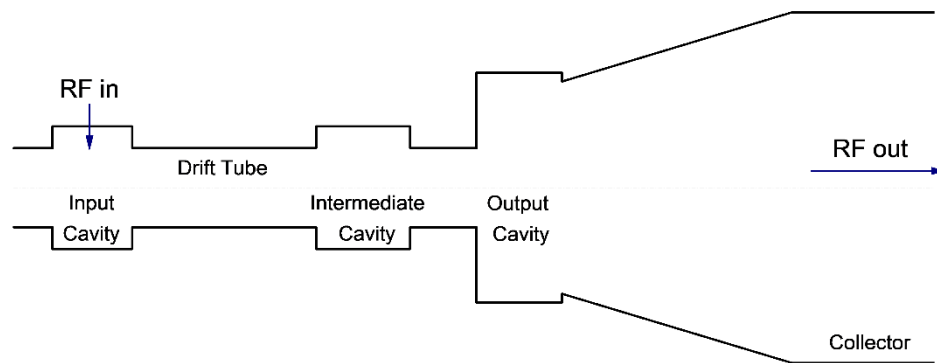
Figure 2.4
Example gyroklystron schematic

Gyroklystrons make use of principles from both the gyrotron and the klystron. Like in a gyrotron, the CRM interaction process is used to create bunches and extract energy, and like in a klystron, there is a multi-cavity set-up which allows it to work as an amplifier rather than an oscillator. Similar to the linear klystron, a gyroklystron uses a bunching cavity, a separate extraction cavity, and usually at least one intermediate cavity to enhance bunching. A schematic of an example gyroklystron is shown in figure 2.4. An annular helical beam passes through a series of cavities. In the input cavity, an electric field generated from a TE cavity mode causes phase-modulation of the electron beam as described by the CRM mechanism (section 2.1.1). This bunching process is the main aspect that differs from the klystron. Where the klystron modulates longitudinal velocity to create axial bunches from a TM cavity mode, the gyroklystron modulates phase to create azimuthal bunches. Hence, there is no significant change in the overall spatial structure of the beam [68]. The modulating field is provided to the input cavity through an input coupler (section 2.3.1) which must excite the correct mode with high purity and stability. After modulation, the beam enters a drift-tunnel to cut off the EM wave, a length of free space where the electrons in the beam drift to form the bunched structure. One or more intermediate cavities then reinforce the bunching effect and improve the gain of the device. When the beam reaches the output cavity, the bunches are tight, and the electrons are in the deacceleration phase. The carefully selected position and properties of the

output cavity cause the electrons to lose energy to the cavity field, which takes the form of coherent electromagnetic radiation. The electrons' arrival must coincide with a decelerating phase of the field to transfer energy in this way. It is therefore extremely important that the bunching process is well optimised for as many electrons as possible to be as close to the ideal phase as possible. Realistic limits on the bunch exist, such as due to space-charge and the time-profile of cavity modes, and in any case, only transverse energy is available for extraction. A high-velocity ratio can improve the efficiency since it means a larger portion of beam energy is available, but if the velocity is too high, the back-streaming electrons can occur and ruin the interaction. The realistic velocity ratio of the electron beam is in the approximate range of $1.1 < \alpha < 1.5$, so a significant portion of the beam's energy will still be in the axial direction. Since only the orbital energy is converted during the interaction, this leaves a significant amount of energy in the spent beam when it is deposited on the collector after the interaction. Designing an appropriate collector for this beam deposition to take away the energy is also not simple (section 2.3.2), and the outgoing wave is often not in the desired form for application, requiring further components after the gyroklystron (section 2.3.3).

There are many variables to consider when developing an arrangement of cavities and fields, which makes gyroklystron design a complex process. In addition, other elements of design add complexity. The beam-source is interconnected and must be designed in conjunction with the interaction region, rather than as two separate entities. The design goals of the overall system dictate some basic beam parameters, while the achievable parameters of the MIG assign certain constraints to the interaction region. A beam with the correct velocity components, relativistic factor, and radius must be produced, and creating a beam source that achieves this while also maintaining low-velocity spread requires a thorough optimisation process. The background and analysis of the MIG hence require more depth, and full detail can be found in section 2.2.

At the other end of the system, the collector, output window, and subsequent wave processing are also important but are not so intertwined with the interaction region

as the MIG. These aspects of the system can generally be freely designed around the final gyroklystron design, but still cannot be thought of as completely separate, since the related reflection parameters could affect the interaction.

2.1.3: Waveguides and Cavities

Understanding and developing a gyroklystron requires a strong foundation in the physics of waves in cavities and waveguides. In this section, the most relevant equations are presented, and further detail can be found in many textbooks. The wave equation in cylindrical coordinates can be expressed as [162]:

$$\nabla_{\perp}^2 E_z = \frac{1}{r}\frac{\partial}{\partial r}\left(r\frac{\partial E_z}{\partial r}\right) + \frac{1}{r^2}\frac{\partial^2 E_z}{\partial \phi^2} = -k_{\perp,TM}^2 E_z \qquad (2.11)$$

$$\nabla_{\perp}^2 B_z = \frac{1}{r}\frac{\partial}{\partial r}\left(r\frac{\partial B_z}{\partial r}\right) + \frac{1}{r^2}\frac{\partial^2 B_z}{\partial \phi^2} = -k_{\perp,TE}^2 B_z \qquad (2.12)$$

To determine the possible modes, the boundary conditions must be considered. For a waveguide of radius r_0, these are:

$$B_r(r = r_0) = E_\phi(r = r_0) = E_z(r = r_0) = 0 \qquad (2.13)$$

The solutions are made up of Bessel functions, which resemble damped sinusoids. The Bessel functions of the second kind are infinite at r=0, and as this position is included in a circular waveguide, they can be ignored, and only the Bessel functions of the first kind need to be considered. The axial solutions are:

$$E_z = DJ_p(k_{\perp}r)\sin(p\phi) \quad \text{for TM modes} \qquad (2.14)$$

$$B_z = AJ_p(k_{\perp}r)\sin(p\phi) \quad \text{for TE modes} \qquad (2.15)$$

The r and φ components of E and B are found through Maxwell's equations and contain derivatives of the above solutions. In the TM case, the roots of the Bessel function ($\mu_{m,n}$) are needed, while for TE the roots of the derivative of the Bessel function ($\mu'_{m,n}$) are needed. The Bessel functions are a well-known piece of mathematics, and tabulated lists of the roots can be found in mathematical reference text books such as [163].

The ones most relevant to this thesis are $\mu'_{0,1} = 3.8317$ and $\mu'_{0,2} = 7.0156$. The perpendicular wavevector depends only on the Bessel root and the radius as $k_\perp = \frac{\mu_{m,n}}{r_0}$ or $\frac{\mu'_{m,n}}{r_0}$, and cut-off frequency is given by:

$$\omega_{co,TM} = c\frac{\mu_{m,n}}{r_0} \tag{2.16}$$

$$\omega_{co,TE} = c\frac{\mu'_{m,n}}{r_0} \tag{2.17}$$

The cut-off frequency therefore depends only on the radius, as c and a given mode's Bessel root are constants. This means that when normalised to $\frac{c}{r_0}$, the relative spacing of cut-off frequencies for different modes is a fixed value. The lowest normalised cut-off frequency is for the $TE_{1,1}$ mode, while the lowest TM mode is the $TM_{0,1}$. The spacing of modes is displayed in figure 2.5.
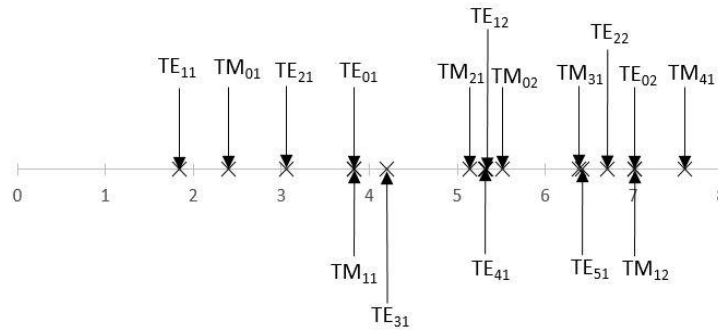
Figure 2.5
Cut-off frequencies in circular waveguides, normalised to the scale r_0/c

The density of modes increases quickly with increasing mode indices. This creates the challenge of mode selection and suppression in the design of high-order gyro-devices. Many gyrotrons operate in very high order modes, but gyroklystrons typically tend to use the low order azimuthally symmetric modes, so while the issue of mode competition must still be considered in their design, it is typically not a large barrier to overcome. The cut-off frequency is discussed here because it is of particular importance in gyroklystron design. There must be no field in the drift-tunnels, so any cavity-mode frequency must be cut-off in them to avoid radiation leaking from the cavities and harming the bunching process. Realistically, a small amount of radiation

leakage will still happen, so for this reason, drift tubes are often lined with a dielectric material that absorbs this power to prevent it from becoming problematic.

The TE$_{0,n}$ cavity modes are well suited to gyro-devices due to their field pattern. Their azimuthally symmetric nature aligns appropriately with the annular beam that a MIG produces. This means no overly complex designs are needed to ensure adequate beam-matching with the EM fields. The symmetry of such modes also allows for 2D analysis to be used without a significant loss of accuracy.

The common idealised model of a cavity assumes perfectly conducting walls, and hence no losses to consider. In a more realistic case, the field in a cavity will decay. The losses are quantified by the quality factor, sometimes referred to as the Q-factor, or most commonly simply as Q. A general definition for Q is given by [162]

$$Q = \omega_0 \frac{\text{average stored energy}}{\text{power loss rate}} \qquad (2.18)$$

where ω_0 is the centre frequency of the resonant line width of the cavity. The total Q is defined as the reciprocal sum of all contributing factors. The contributions one should generally consider are the ohmic Q which describes power lost to the cavity walls, and the diffractive Q which describes power lost upon radiative output. In an open cavity with high-conductivity walls, the diffractive contribution dominates, and in a cavity with small apertures and dielectric wall linings, the ohmic loss contribution dominates. The ohmic Q of a cavity excited in a TE$_{m,p}$ mode is given by [72]

$$Q_{ohm} = \frac{r_c}{\delta}\left(1 - \frac{m^2}{v_{m,p}^2}\right) \qquad (2.19)$$

Where r_c is the cavity radius, m is the mode's azimuthal index, $v_{m,p}$ is its eigenvalue and δ is the skin-depth at frequency f and wall conductivity σ, defined as

$$\delta = \frac{1}{\sqrt{\pi f \mu_0 \sigma}} \qquad (2.20)$$

Some simulation data of the eigenfrequency and Q of sample cavities is presented in chapter 5, displaying how these parameters vary with different cavity aperture radii

and dielectric linings. In this thesis, lossy linings on the walls and the opening for the beam tunnel mean that both ohmic and diffractive Q contributions are relevant. The simulation model can compute a reasonable estimate for the overall Q by examining the decay of an oscillation in the cavity after excitation ends.

2.1.4: Device Materials

For most analysis and simulation work in the design of the gyroklystron, the material choice is not discussed in detail. In many theoretical and computational papers, cavity walls are typically assumed to be perfectly conducting, and dielectric components are assigned numeric values of permittivity, rather than incorporating a named material. This section discusses the materials used in gyroklystron construction and presents the justification for the way materials are defined during the design process.

Copper is the most typical material for RF devices due to its material properties, cost, and availability, though niobium has been used as an alternative in some superconducting systems [164]. In a cavity or waveguide, a higher wall-conductivity results in smaller skin depth (equation 2.20) and smaller power loss. The skin depth for high frequencies is typically on the order of a few micrometres. In the context of the gyroklystron, wall losses to the copper section are a negligible contributor compared with the lossy dielectric linings and diffractive losses at the open ends. Assuming the wall is a perfect conductor is therefore a valid approximation that has a relatively small effect on calculation accuracy.

It is important to consider that depending on the device, different waveguide sections can have different requirements. For example, the drift tubes in a gyroklystron must contain no field or radiation to achieve effective operation. A common technique to solve this issue is to have the drift tubes built containing lossy ceramics which absorb radiation. As an example, the University of Maryland's gyroklystron development program involved testing a range of ceramic materials in various positions in different experiments, including as a lining to the down-taper before the input cavity, as a

coating to drift tube walls, and as a series of absorbing ring-inserts in the drift tube [71]. Dielectric layers such as this become especially important in high-current gyroklystrons as they often have larger beam radii than that which can fit in a fully cut-off drift tunnel.

Dielectrics are also often present in gyroklystron cavities where they are used to suppress the excitation of competing modes. They can also be used to decrease the Q of a cavity when a specific value is desired. The dielectric affects the frequency of the cavity which changes depending on thickness and dielectric constant. This places the requirement that the material cannot be sensitive to temperature, because thermal expansion during operation would alter the frequency, peak-field position, and Q which is particularly important for high duty cycle operation [165]. Additionally, when a high-current beam is used, the risk of parasitic oscillations increase as the beam may resonate with the fundamental $TE_{1,1}$ mode.

A material's dielectric properties can be described in terms of its relative permittivity, ε_r. Generally, this is thought of as a real number, but to account for a lossy medium, it can instead be expressed as a complex number in the form:

$$\varepsilon_r = \varepsilon_r' - \frac{i\sigma}{\omega\varepsilon_0} \qquad (2.21)$$

where σ is the conductivity and ω is the angular frequency. The presence of frequency in this equation means the material can display different responses to different modes, allowing for suppression of the unwanted ones while maintaining the desired Q for the operating mode. In addition to helping absorb radiation, the non-zero conductivity of a lossy dielectric means if any charge is deposited on the ceramic it can be carried away rather than risking build-up on the wall. As the electron beam is well-focused by the applied magnetic field, and the vacuum is in the 10^{-7}mbar range, the amount of deposited charge is extremely low and consideration of it is not required for accurate analysis.

Even a thin dielectric layer in a drift tube can provide high attenuation over a large bandwidth, allowing many modes to simultaneously be suppressed. To further

improve this, some more complex variations can be used. A tapered or saw-toothed lining can reduce reflection and improve near-cut-off loading. A two-layered lining where each material has very different dielectric properties can suppress a larger range of modes than either material would individually. In this thesis a single smooth layer is considered.

There are special requirements on the materials used in a vacuum electron device, such as low out-gas rate, a high evaporation temperature, and it must not poison the thermionic cathode. These limits mean that many materials, such as plastics, cannot be used in vacuum electron devices especially sealed-off tubes where the vacuum is maintained by an ion pump. The dielectric materials commonly used in the vacuum electron devices and their properties are listed in Table 2.1 [165-167].

Table 2.1: Dielectric properties of common materials

Material	Relative Permittivity ε_r	Loss Tangent *tanδ* at 1GHz
Quartz	4.5	1×10^{-4}
Diamond	5.5 to 10	3.5×10^{-4}
Graphite	10 to 15	2×10^{-4}
Alumina (Al_2O_3)	9.3 to 11.5	2×10^{-4}
Silicon	11 to 12	5×10^{-4}
Silicon Carbide	9.7	3×10^{-3}
Beryllia (BeO)	6.1 to 7.5	4×10^{-4}

The most common type of dielectric absorber employed in the vacuum electronics industry is a composite composed of high thermal conductivity, electrically insulating ceramic combined with lossy silicon carbide (SiC). Beryllium Oxide (BeO) has very attractive material properties for the base ceramic due to its high thermal conductivity of $250 Wm^{-1}K^{-1}$. However, there are safety issues that need to be accounted for when using BeO if it is broken and careful disposal is required at end of life use. SiC can accommodate a lot of types of impurities, and certain impure grades of SiC are highly lossy and suitable for use in composite absorbers.

Manufacturing methods allow any composition to be achieved, with the most common BeO:SiC mixes used in vacuum electronics being 60:40 and 80:20. For lower dielectric constants, a microwave absorber consisting of glassy carbon in an aluminium silicate base can be used. These have a low thermal conductivity but are still valid to prevent oscillations in field-free regions such as gyro-device drift tunnels. The average power in these regions should already be low, so there is not much heating effect. The material science is well-developed, and it is reasonable to assign dielectric properties in a simulation as needed and trust that a matching material commonly used in the vacuum tube industry is manufacturable.

The microwave radiation generated in the output cavity is directed along a waveguide section and through an output window. To maintain efficient power output, the reflection of waves at the output window must be kept to a minimum. Placing the window at the Brewster angle is one way to prevent reflection [168]. The window material's absorption and reflection properties are important. Other cases, such as a liquid-nitrogen edge-cooled sapphire window, were used in a gyrotron study [169], but generally CVD diamond is the most typical choice of window material for high average power CW gyrotron oscillators [170, 171]. As the input and output windows have been designed as part of the simulation work in this thesis, further discussion on the choice of window material is presented in chapter 7.

In addition to material choice, the design of walls and inserts can also be used to fine-tune the parameters of devices. Most commonly, these geometric alterations are for mode selection, stability, or conversion, but have also sometimes been used to enhance the physical properties of the device. For example, linear corrugations on coaxial inserts have been shown to reduce ohmic heating in high-order gyrotrons [172] and analysis of a corrugated inner conductor showed that it can reduce the Q-factors for competing modes in a gyrotron cavity whilst keeping the Q-factor of the operational mode equivalent to that of a hollow cavity [173]. Wall corrugations can also be used to aid mode selection, or to provide conversion or coupling between modes. Mode conversion is also sometimes achieved through varying the cross-

sectional profile along the axis [174]. In the case of this thesis, no modal transitions occur within the gyroklystron itself, therefore it is not discussed in further detail.

2.2: The Magnetron Injection Gun (MIG)

2.2.1: Basic Principles and Geometry

A magnetron injection gun (MIG) uses field-enhanced thermionic emission to produce a beam. The desired beam parameters are achieved through the careful arrangement of fields to guide the electrons into the beam tunnel and give them the correct velocity ratio. A simple schematic is shown in figure 2.6, illustrating the two main cylindrical configurations used. The triode-type adds a secondary anode to provide more precise control over the beam properties. The physics of the emission process is described in section 2.2.2 and 2.2.3 presents some background on typical cathode materials, and chapter 4 presents detail on the design process of the MIG.
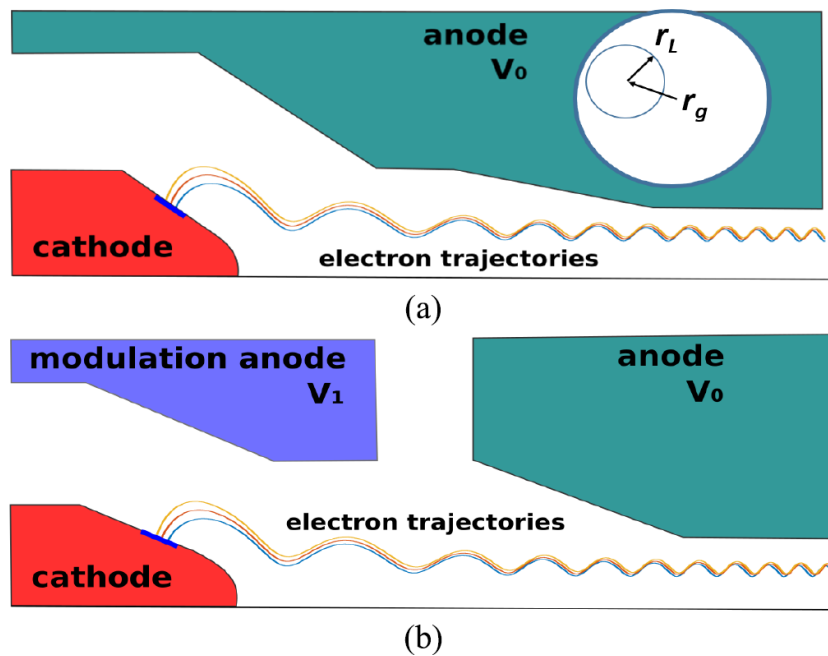
Figure 2.6
Schematic of diode-type (a) and triode-type (b) MIGs

2.2.2: Thermionic Emission and the Schottky Effect

At the surface of a material, energetic electrons can leave the surface. When they leave the surface, they are attracted back by the force due to the image-charge they leave behind. The level of energy required to overcome this force and be emitted is called the work-function. In a metal structure, electron energies are governed by the Maxwell-Boltzmann distribution. When the temperature is increased, the tail of the distribution is stretched such that more electrons have energy over the work-function, allowing them to be emitted from the metal surface. As this emission process is controlled by thermal mechanics, it is known as thermionic emission.

Electrons emitted from a hot wire would form a cloud around it. A current density leaving the wire is created, described by Richardson's Law [175]

$$J = AT^2 e^{\frac{-W}{k_B T}} \qquad (2.22)$$

where T is the temperature, W is the potential energy barrier to be overcome consisting of the work function ϕ multiplied by the electron charge e and k_B is the Boltzmann constant. The parameter A was first thought of as constant, but it was later shown to vary between different emitting materials, though it typically stays within the same order of magnitude [176].

In a typical electron gun for a high-power gyro-device, a thermionic ring cathode emits the electrons, which are then pulled away by applying an electric field from an anode, positioned such that it directs the beam through the waveguide as required. Aside from its crucial role in the guidance and acceleration of the beam, the field is also necessary to maintain the continued emission of electrons. Without it, a cloud of negative charge would build up around the emitter, acting against the further release of charge. With the field, the emission process is not only sustained, but also enhanced as described by the Schottky effect [177, 178]. This is a phenomenon wherein the thermionic emitter is biased negative to its surroundings, creating an electric field of magnitude E_c at its surface. The presence of the field lowers the

surface potential energy barrier by an amount ΔW, hence increasing the emission current. The current density with consideration of this effect can be expressed as a modification of equation 2.22 as

$$J = AT^2 e^{\frac{-(W-\Delta W)}{k_B T}} \qquad (2.23)$$

$$\Delta W = \sqrt{\frac{e^3 E_c}{4\pi\varepsilon_0}} \qquad (2.24)$$

Emission that takes place in regimes where this equation applies is called Schottky emission or field-enhanced thermionic emission, and cannot be thought of as purely temperature limited, but rather as a combined temperature-and-field regime. The equation is reasonably accurate for fields up to around 100MVm⁻¹, above which Fowler-Nordheim tunnelling begins to be a significant contributor to the total emission current [179]. The field used in the MIG presented in this thesis is far below this limit.

2.2.3: Cathode Materials

Thermionic cathodes are frequently made from lanthanum hexaboride (LaB_6) or oxides such as barium oxide (BaO), but other options have seen also some use [162, 180, 181]. Emission characteristics of LaB_6 can be improved through techniques such as doping [182]. Even without advanced doping, a work function around 2.5eV and an emission density above 20A/cm^2 are achievable. Far higher emission densities on the order of several hundred A/cm^2 can be achieved in pulsed regimes [183], but generally this order of magnitude remains unviable for practical application due to various reasons including short lifetimes, non-uniform emission, evaporation of emitter material, or the complexity of production. Emission densities approaching 70A/cm^2 have been shown in experimental studies of scandate cathodes, and a lifespan of at least 5000 hours has been reported at 40A/cm^2 [183, 184]. 30A/cm^2

emission densities have been reported for a range of cathode types and have been experimentally tested in MIG applications [185, 186]. A cathode design using an alloy film coating of osmium, rhenium, and tungsten has been reported as being able to reach an emission density of $60A/cm^2$ with a lifetime of 1800 hours [187].

The choice of cathode material depends not only upon its work function and emission density, but also upon factors such as thermal properties and molecular structure where in general the higher the temperature of operation the shorter the lifetime of the cathode. As thermionic emission is a temperature-controlled process, the material must be one which can maintain its mechanical stability at high temperatures. It must also produce uniform emission. Although it can produce high current densities, the polycrystalline structure of LaB_6 affects emission uniformity due to differences between crystal planes. Further detail on these challenges in physical chemistry and material science that must be overcome for the design of good thermionic emitters is not presented here, as cathodes with appropriate performance characteristics are commercially available.

Table 2.2 presents an overview of the performance that can be expected from several different types of cathode. However, it is important to note that only a very rough comparison can be gained from this, as the lifetime is dependent on the emission density and citated works do not all test at the same temperature where lifetime is very dependent on cathode temperature.

Table 2.2: Performance of various cathodes

Cathode	Emission Density (A/cm^2)	Typical Lifetime (hours)
LaB$_6$ [182]	< 30	> 1000
CeB$_6$ [180]	< 50	> 1500
Scandia-Doped Nanocomposite [183]	> 40	5000
Iridium coated dispenser [188]	7.5	10000
Ternary-Alloy film coated dispenser [187]	60	1800

Of the above, reference [186] is worth further highlighting as the cathode was used as part of a high-current density MIG, thus illustrating the applicability of such a cathode for gyroklystron applications. The cathode used was a Spectra-Mat 612X scandate cathode [189], capable of providing 30A/cm^2 at 1135°C which was among the best commercial cathodes at the time of publication. The results presented in reference [186] strongly support the case that the emission properties discussed in chapter 4 are viable. Additionally, the pulsed operation of the gyroklystron presented in this thesis allows for much slower degradation than a continuous wave cathode at the same emission density. For example, Spectra-Mat provide up to 20A/cm^2 for continuous operation, and up to 120A/cm^2 for pulsed operation. Although these maximum emission limits are advertised without comment on the corresponding lifetime, they nonetheless show that the emission density used in this thesis is well within the reach of commercial cathodes.

It is worth noting briefly that cathodes based on field emission and explosive emission also represent a well-developed field of technology, but they are not as well-suited to the needs of a gyroklystron. Compared with these types of emission, thermionic sources can sustain their current density output for long-pulsed or continuous operation and suffer less surface degradation than explosive processes. The main

disadvantage of a thermionic emitter is that it requires to operate at high-temperature, and the materials used in the thermionic gun need to be carefully chosen to avoid poisoning the cathode due to degradation of the vacuum. However, they remain the most viable electron source for gyroklystron MIGs.

2.3: Related Technology

The bulk of this thesis is on the design and simulation of the interaction cavities and the electron beam source. This section presents an overview of the additional components that are relevant to the gyroklystron, but do not influence the main design work stage.

2.3.1: Input Couplers

In this section, the basic principles of the input coupler are introduced. The design and analysis of these components are presented in chapter 7.

In the earlier discussion of the gyroklystron, it was simply stated that a signal is coupled into the input cavity. This is in fact not a trivial process as it requires conversion of energy from a waveguide mode to a stable cavity mode. A direct connection where the feed-guide leads straight into the cavity would not work for several reasons. The presence of a sufficiently large entrance aperture would affect the shape of the cavity eigenmode and it would be exceptionally difficult to excite the desired mode. In a typical gyroklystron, radiation from a microwave source is carried through a rectangular waveguide to an outer cavity encircling the gyroklystron input cavity. For a cylindrical cavity gyroklystron, this is therefore a coaxial cavity wrapped around the main cylindrical cavity, as shown in Fig 2.7.
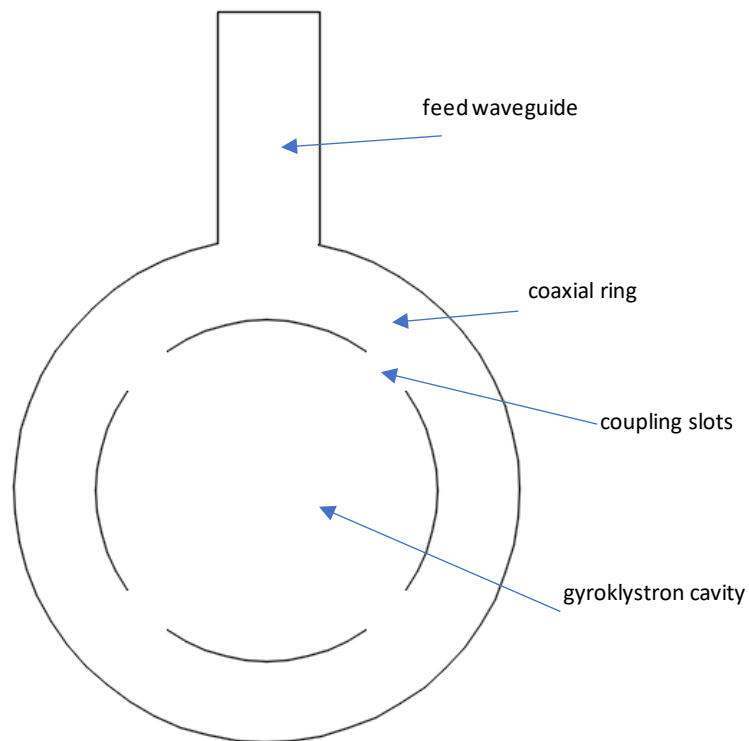
Figure 2.7
Cross-sectional schematic of the input coupler arrangement

An arrangement of slots on the boundary between the two cavities allows radiation to leak through, exciting the desired mode in the main cavity [190]. The operation of an input coupler depends on the outer coaxial cavity diameter, the coupling slot size, and the coupling aperture size. These parameters can be optimised by computer simulation to obtain a geometry that allows the correct mode to stably resonate in the inner cavity. In a well-designed coupler, over 90% of total stored energy can be in the inner cavity with good modal purity [191], and the coupling slots do not significantly alter the mode structure.

2.3.2: Beam Dump Systems

After the interaction, the electron beam is deposited in a region called the collector. Limits on realistic velocity ratio and interaction efficiency mean that the beam still carries a large amount of power when it reaches the deposition region. The energy deposition density profile along the output section can be simulated. Collector simulations are required to ensure surface damage on the collector waveguide is kept to a level which does not harm the performance of the gyroklystron while at the same time making sure the collector has a reasonable lifetime as it would be expensive and impractical to replace. Common waveguide materials such as copper tend to have high electrical and thermal conductivity and are suitable as a collector material in a gyroklystron with high beam power.

Many devices avoid thermal issues by having a low duty cycle, with a pulse repetition rate on the order of a few to tens of Hz. However, in the specific case of CompactLight, the project outline demands a minimum of 100Hz, but strongly emphasises the preferred target of 1000Hz. The pulse duration will be 1.5μs, making the overall duty cycle 0.15% at the maximum repetition rate of 1000Hz.

Reducing the power in the beam is not a good option because with the efficiency limit of the CRM mechanism, there would not be enough output power. Instead, it may be necessary to include cooling systems to reduce the thermal load on the collector.

The power-handling capacity of the material is not the only concern when designing a collector. Rather than have the power wasted as it is deposited on the collector, systems can be added to recover some of the energy remaining in the electron beam. To do this, the cathode potential can be set at -100kV using a high-current power supply, with the collector potential set to be +50kV using a low-current power supply, thus decelerating the beam. This type of system is called a depressed collector, and its use can be seen in the majority of present-day high-power gyrotrons. They have been shown to boost gyrotron efficiency from around 30-35% to over 50% [192]. Further improvements can be seen by using a more complex multi-stage depressed

collector, and computer codes have been developed to aid in calculating optimal collector geometry [193]. Depressed collectors are not specific to the gyrotron, but are applicable to many microwave-beam devices in general, including gyroklystrons [194]. Absorbing some of the excess beam energy and applying back into the system can significantly reduce the energy footprint and running cost of a device.

2.3.3: Output Wave Processing

After the interaction, the microwave output of a gyroklystron is often not simply ready for use in its application. This section provides a brief overview of the components required alongside the gyroklystron for compatibility with the lineariser. The two items that are required are 1) the mode converter, and 2) the pulse compressor. As these components act on the output signal after the device and do not affect the generation of that signal, they can be designed independently.

The mode of the emitted radiation from the output cavity is not necessarily the same as that which is needed for the application in question. The gyroklystron to be developed during this project generates the output radiation in the form of the circular $TE_{0,2}$ mode. A simple down-taper can transform a $TE_{0,2}$ mode to a $TE_{0,1}$ mode. There are many several methods that have been studied for $TE_{0,1}$ to $HE_{1,1}$ conversion such as waveguide bends [195], non-uniform axis and radius [196], or overmoded waveguides [174].

In many applications it is the peak power that is the most important parameter. If a pulse is compressed to a shorter duration, the peak power must also increase because the energy within the pulse is conserved, barring losses during the compression process. The compression method relevant to this thesis is that used in the SLED-II compressor [197, 198]. In the original SLED method, two resonators store energy, and then a phase-reversal triggers the release of this energy. The energy release happens over a shorter interval than the filling time. This process causes the pulse shape to be a sharply decaying exponential, and losses are determined by the

Q's of the resonators. In the SLED-II method, the resonator cavities are replaced by resonant lines. With this change, it is capable of delivering power in a flat output pulse. Losses in this type of compressor are defined instead by the attenuation parameter of the resonant line. A notable advantage of the flat output pulse is that it allows cascading of structures, which is not practical for the exponentially decaying profile from a resonator-based compressor. Internal discussions report that the pulse compressor under development for the 36GHz system is capable of delivering a power gain of 7.7, with similar performance expected for a 48GHz version [199].

The required gyroklystron output power is therefore dependent on the compression factor and all the losses that occur between the end of the interaction region and the linearising cavity. These losses mainly arise during mode conversion, though the small attenuation in the waveguide sections due to the material properties of the waveguide used should also be considered. The output power required for the base-line design has been specified by the CompactLight consortium as 2 MW at 48GHz.

Chapter 3: Theoretical Models for Gyroklystron Design

This chapter describes the theoretical models that were used in the gyroklystron analysis. Firstly, the linear theory is discussed, followed by the nonlinear theory. In each case the applications and limitations of theories are explained. Finally, the principles of the main design tool, particle-in-cell (PIC) simulation, are covered in section 2.3.

3.1 Foundations for Analysis

Both the linear and nonlinear models share some underlying definitions. Firstly, the electric field is defined by the equation [200, 201]

$$E_t(r, \varphi, z, t) = Re\left\{E_0\left[J'_m(k_\perp r)\hat{e}_\varphi + \frac{im}{k_\perp r}J_m(k_\perp r)\hat{e}_r\right]f(z)e^{i(\omega t - m\varphi)}\right\} \qquad (3.1)$$

where J_m is the Bessel function, *f(z)* describes the axial profile of the normalised RF field, and $k_\perp$ is the transverse wavenumber:

$$k_\perp = \frac{v_{mp}}{R_0} \qquad (3.2)$$

where v_{mp} is the pth nonzero root of J'_m and R_0 is the cavity radius.

The electron momentum, phase, and position are respectively expressed as:

$$p = \frac{\gamma\beta_\perp}{\gamma_0\beta_{\perp 0}} \qquad (3.3)$$

$$\theta = n\phi - \omega t_0 + \frac{\pi}{2} \qquad (3.4)$$

$$\zeta = \frac{\pi\beta_{\perp 0}^2}{\beta_{\parallel 0}}\frac{z}{\lambda} \qquad (3.5)$$

where ɸ is the fast time scale phase angle of the electron, *t* is time, *z* is position, *γ* is the relativistic factor, and the β components are the transverse and axial velocity normalised to the speed of light. Symbols with the subscript 0 refer to the value of that parameter upon entry into the interaction region. For all early stages of analysis, an assumption of a mono-energetic beam is used. This idealisation of the beam significantly simplifies the calculations. As efficiency declines with increasing velocity spread, this means early-stage analysis will typically over-estimate the efficiency and power by several percent. This approximation means that it is the ideal beam case under consideration, and the efficiency impact of velocity spread can be considered at a later stage during PIC simulation.

The equations of motion take the form of the pendulum equations, also known as the Yulpatov equations. The formulation of these equations assumes the beam is only weakly relativistic, annular, and only interacts with a single mode. Each of these assumptions is reasonable for basic analysis. The harmonic number *s* is included in the equations for completeness but note that as only a fundamental harmonic device is dealt with in this thesis, s is equal to 1 during all subsequent analysis involving these equations [200].

$$\frac{dp}{d\zeta} = -Ff(\zeta)p^{s-1}\sin\theta \qquad (3.6)$$

$$\frac{d\theta}{d\zeta} = -(\Delta + p^2 - 1) - sFf(\zeta)p^{s-2}\cos\theta \qquad (3.7)$$

In these equations, $f(\zeta)$ is the field profile, which is approximated to a fixed Gaussian profile:

$$f(\zeta) = e^{-\left(\frac{2\zeta}{\mu}\right)^2} \qquad (3.8)$$

The formulation of both the linear and nonlinear models requires the definition of a set of normalised variables, primarily the normalised cavity length, field amplitude in the gyroklystron cavity, and detuning parameter against the electron beam cyclotron frequency which are defined respectively as

$$\mu = \frac{\pi \beta_{\perp 0}^2 L}{\beta_{\parallel 0} \lambda} \qquad (3.9)$$

$$F = \frac{E_0 \beta_{\perp 0}^{s-4}}{B_0 c} \left(\frac{s^{s-1}}{2^{s-1} s!} \right) J_{m \pm s}(k_\perp r_b) \qquad (3.10)$$

$$\Delta = \frac{2}{\beta_{\perp 0}^2} \left(1 - \frac{s \omega_{c0}}{\omega} \right) \qquad (3.11)$$

where L is the actual length, λ is the wavelength, E_0 is the electric field amplitude, B_0 is the magnetic field, s is the harmonic number, ω_c is the cyclotron frequency, and ω is the operating frequency, and r_b is the radius of the beam.

In the linear and non-linear models, the beam is treated as having no thickness. All interaction is considered at r_b. The spread of guiding centre is ignored, as are the radial variations during Larmor orbits of the electrons. This can also lead to a slight overestimation of efficiency, as the thickness of a real beam means that not all electrons are precisely at the position of maximum field.

The beam current is also normalised into the models' unit system as:

$$I = \frac{\sqrt{2}}{\pi^{\frac{5}{2}}} \frac{I_A Q_{tot} e}{c^3 m_e \varepsilon_0} \frac{\beta_{\perp 0}^{-2(3-s)}}{\gamma_0} \frac{\lambda}{L} C_{mp} \qquad (3.12)$$

where I_A is the actual beam current, Q_{tot} is the overall quality factor, and C_{mp} is the coupling coefficient when $r=r_b$. For a given mp mode, the coupling coefficient at position r is given by:

$$C_{mp}(r) = \frac{J_{m \pm 1}^2(k_\perp r)}{(v_{mp}^2 - m^2) J_m^2(v_{mp})} \qquad (3.13)$$

where v_{mp} is the Bessel root corresponding to the mode in question. The full importance of the coupling coefficient in the selection of beam radius is covered in chapter 4 with the necessary extra background and context relating to the cavity design. When selecting beam current, the oscillation start current must be considered. If the beam current exceeds this value, the device may no longer be zero-

drive stable, and may operate in an oscillation regime that prevents it from performing as an amplifier. The normalised start current is defined as:

$$\hat{I}_{st} = \frac{4}{\pi\mu^2}\frac{e^{2x^2}}{\mu x - 1} \tag{3.14}$$

where $x = \mu\Delta / 4$. The actual start current can then be found by rearranging equation 3.12. This provides a hard limit on the beam current that can be used in a device, which is addressed in further detail in the chapters on the MIG and interaction circuit simulation results.

3.2: Linear Theory

One method of studying gyroklystrons is with the small-signal linear theory model [200, 202]. Although it lacks the accuracy and sophistication of particle-in-cell simulations, it is still useful for examining the principle of the gyroklystron and having the initial prediction and requires significantly less computation time to generate results than other methods. While no concrete predictions of real performance can be made due to various limitations of the model, the rough predictions of linear theory can still provide a valid design aid in terms of selecting an appropriate number of cavities, their modes, and the approximate beam parameters. The cavity dimensions refer to an isolated cold-cavity, as linear theory does not consider drift tube radius. The equations used in linear theory are derived using the perturbation theory expansion of momentum p and phase θ, with the limit of a small F parameter. The linearised pendulum equations take the form:

$$p = p^{(0)} + p^{(1)} + \cdots \qquad (3.15)$$

$$\theta = \theta^{(0)} + \theta^{(1)} + \cdots \qquad (3.16)$$

where $p^{(k)}$ and $\theta^{(k)}$ each contain the normalised field amplitude F raised to the kth power. Inserting this expansion into equations 3.6 and 3.7, a linearised set of equations can be obtained.

$$\frac{dp^{(0)}}{d\zeta} = 0 \qquad (3.17)$$

$$\frac{d\theta^{(0)}}{d\zeta} = -\left(\Delta + p^{(0)2} - 1\right) \qquad (3.18)$$

$$\frac{dp^{(1)}}{d\zeta} = -Ff(\zeta)\sin\theta^{(0)} \qquad (3.19)$$

$$\frac{d\theta^{(1)}}{d\zeta} = -2p^{(0)}p^{(1)} - \frac{Ff(\zeta)\cos\theta^{(0)}}{p^{(0)}} \qquad (3.20)$$

The above equations are solved successively for each cavity and drift section. From this, expressions for the normalised momentum at the end of each cavity and the phase angles at the midplane of the following cavity can be obtained [200].

$$p_{out,j} = 1 - \frac{\sqrt{\pi}}{2} \sum_{k=1}^{j} F_k \mu_k e^{-x_k^2} \sin \theta_{c,k} \qquad (3.21)$$

$$\theta_{c,j+1} = \theta_{c,j} + \hat{\mu}_{d,j} \sum_{k=1}^{j} \frac{q_k}{\hat{\mu}_{d,k}} \sin \theta_{c,k} - \hat{\psi}_j, \ \ j = 1, \dots, N-1 \qquad (3.22)$$

where the subscript j refers to the value for the jth cavity and N is the total number of cavities. The new parameters introduced here are:

$$\hat{\mu}_{d,j} = \frac{\sqrt{3}}{2} \mu_j + \mu_{d,j} \qquad (3.23)$$

$$q_j = \sqrt{\pi} F_j \mu_j \hat{\mu}_{d,j} e^{-2x_j^2} \qquad (3.24)$$

$$\hat{\psi}_j = \frac{\sqrt{3}}{2} \mu_j \Delta_j + \mu_{d,j} \Delta_{d,j} + \frac{\sqrt{3}}{2} \mu_{j+1} \Delta_{j+1} + \psi_{j+1} - \psi_j \qquad (3.25)$$

By the process presented in [200] the generalised form for an N-cavity gyroklystron can be derived as:

$$F_j = \frac{\sqrt{\pi}}{2} I \mu_j e^{-x_j^2} q_{j-1} \left(1 + \delta_j^2\right)^{-\frac{1}{2}} \qquad (3.26)$$

$$\frac{q_j}{q_{j-1}} = \frac{\pi}{2} I \mu_j^2 \hat{\mu}_{d,j} e^{-2x_j^2} \left(1 + \delta_j^2\right)^{-\frac{1}{2}} \qquad (3.27)$$

$$for \ j = 2, \dots, N-1$$

where δ_j is the frequency pulling parameter:

$$\delta_j = \frac{2(\omega - \omega_0)Q_0}{\omega} \qquad (3.28)$$

where ω is the working frequency in the loaded cavity and ω_0 and Q_0 describe the unloaded cavity. Generally, it is preferable to minimise δ_j.

F and q are calculated in the first cavity, and then sequentially computed for each subsequent cavity. By the extraction cavity, F is significantly larger than the input, so if too high input values are chosen, non-linear saturation starts to break the model and result in physically impossible particle momenta at the output cavity. This means that the linear model cannot perform computations at the intended MW-level but studying the bunching and efficiency of interaction at low power can still provide useful insight. The values obtained can then be used to calculate rough estimates of the gain and efficiency. Firstly, the perpendicular efficiency is calculated using the momentum data averaged over the initial phase angles θ_0, where the initial arrangement is a uniform distribution from 0 to 2π.

$$\eta_\perp = 1 - \langle p^2(\zeta_{out})\rangle_{\theta_0} \tag{3.29}$$

The total electronic efficiency is then proportional to perpendicular efficiency as

$$\eta_{el} = \left(\frac{\gamma_0 \beta_{\perp 0}^2}{2(\gamma_0 - 1)}\right)\eta_\perp \tag{3.30}$$

There are two equations that can be used to calculate the gain, one using the normalised field amplitude F, and one using the power P.

$$Gain_F(dB) = 20\log_{10}\frac{F_1}{F_N} \tag{3.31}$$

$$Gain_P(dB) = 10\log_{10}\frac{\eta_{el}I_A V}{P_{in}} \tag{3.32}$$

It is assumed that there is perfect mode purity with no harmonic components or risk of mode transitions. Furthermore, the influence of dielectric linings in the cavities is not considered. The impact of these assumptions is smaller than the core linear approximation of the theory, so they do not invalidate any results.

Some further inaccuracy arises from the fact that the actual output cavity is an open-ended structure with an output taper. Its approximation to a closed cavity is therefore less accurate than the other cavities. The error in the output cavity is further emphasised by the small field assumption of the model, as the field is always largest in the output cavity. The small-field requirement of the model means that the

actual beam current and input power cannot produce legitimate results, and much smaller values must be used instead. Since both current and input power influence performance, the results do not translate directly from the linear theory approximation to a realistic device. The gain and efficiency calculated are therefore rough approximations at best. While the numerical value produced by a linear theory code may not accurately resemble the real performance, a high value or lack thereof is still a meaningful result as it suggests whether something of the approximate structure in question is worth developing further. Since the model only requires the calculation of a small number of equations, a computer code can run in a few seconds. Therefore, many results can be gathered very quickly to build up a rough perception of trends and qualities to guide the decision on which preliminary designs to study further with more advance techniques.

Before using the written script for analysis of the 48GHz design, it was tested using data to match that used by Joye in reference [202] which includes detail of a 140GHz gyroklystron designed with the aid of the linear theory model. Figure 3.1 shows that the linear theory MATLAB script created for use in this thesis which is capable of matching the results of similar analytical programs developed elsewhere as demonstrated in figure 3.1 which plots F as defined by equation 3.26 as a function of cavity number.
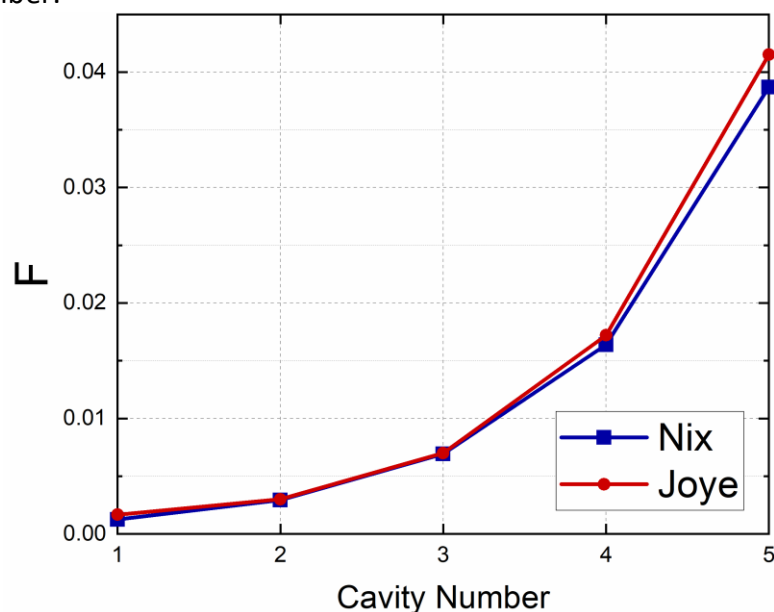
Figure 3.1
Comparison of linear theory results with existing publication

3.3: Nonlinear Theory

The next stage up from linear theory in terms of complexity, runtime, and accuracy, is the nonlinear theory [140, 200]. It is significantly more accurate but requires larger time and computing resources. It is useful mainly for guiding the design and making rough predictions, rather than a comprehensive analysis which requires PIC simulation. Since PIC simulation is very slow, it is clearly preferable to start that stage as close as possible to the final set-up. The nonlinear theory allows for much better estimates of performance and geometry than linear theory alone and can lead to a reasonably close design that should need only minor adjustment in the final PIC simulation stage.

A linear approximation for the bunching process allows it to be characterised by a quantity called the bunching parameter q. Using this, nonlinear equations which describe the energy extraction interaction can be numerically solved to obtain the output efficiency. The use of a normalisation procedure allows for parametric analysis, in which the optimised perpendicular efficiency $\eta_\perp$, bunching parameter q, relative phase ψ, and magnetic detuning parameter Δ each depend only on the normalised cavity length μ and the normalised beam current I. The normalised parameters for nonlinear theory are defined in the same way as in linear theory as introduced in section 3.1.

For a time-independent single mode analysis, the interaction of the electron beam and RF field can be described using the nonlinear pendulum equation, simplified to the form:

$$\frac{dp}{d\varsigma} = i(\Delta - 1 + |p|^2)p + iFf(\varsigma) \tag{3.33}$$

where f(ς) is the axial field profile, which is generally taken as Gaussian in nature, expressed as $f(\varsigma) = e^{-(2\varsigma/\mu)^2}$. Drift tubes are designed to allow no excited modes, so *F* should be zero in those sections. In practice, the field can penetrate slightly into

the drift tube, but reducing the right-hand side of the momentum equation to the first term when applied to the drift tube is a reasonable approximation.

The Electric field amplitude E_0 can be calculated as:

$$E_0 = \sqrt{\frac{QP_{in}}{4\varepsilon_0\pi L}} \cdot \frac{2}{R_w|J_m(v_{mn})|} \tag{3.34}$$

Where J_m is the mth Bessel function, Q is the total quality factor of the individual cavity, v_{mn} is the eigenvalue of the TE$_{m,n}$ mode, P_{in} is the driver power and R_w is the cavity radius.

After the modulating forces are applied in the cavity, the bunching occurs over the drift tube. This can be described in terms of the electron momentum p, and the phase variation θ.

$$p(\varsigma_{in}) = e^{-i(\theta_c + q \sin\theta_c - \psi)} \tag{3.35}$$

Where θ_c is the initial phase (all electrons uniformly distributed over (0,2π)), q is the bunching parameter, and ψ is the RF phase in the cavity.

Even with cut-off drift sections, there is still some requirement on their length to ensure adequate isolation of cavities from each other. The exact minimum isolation limit chosen may vary between groups and projects, but it will always be around 40dB or more, as the isolation of cavities is crucial for the correct operation of a gyroklystron. A 40dB minimum places the requirement on drift tube length L_d that $e^{-2k_zL_d} < 10^{-4}$ which can be rearranged to:

$$L_d > \frac{4.6}{k_z^2} \tag{3.36}$$

Where k_z, the cold cavity dispersion relation, is given by:

$$k_z^2 = \left(\frac{v_{mn}}{R_d}\right)^2 + \left(\frac{\omega}{c}\right)^2 \tag{3.37}$$

To calculate device efficiency, p is calculated at each cavity by the nonlinear pendulum equation, and phase variation θ is calculated at the end of every drift tube.

The average of all the electrons' momenta at the end of the interaction region is taken over the initial phase angle of the electrons, and transverse efficiency is expressed as:

$$\eta_\perp = 1 - \langle p^2(\varsigma_{out}) \rangle_{\theta_c} \tag{3.38}$$

with the triangular brackets denoting the average over initial phase.

The electron efficiency is defined as the net transfer of energy from the beam to the RF wave. It is found by calculating the average loss of electron energy from their initial value.

$$n_{el} = \frac{\beta_{\perp 0}^2}{2(1 - \gamma_0^{-1})} n_\perp \tag{3.39}$$

The maximum wall loss can be defined as heat dissipated per unit area. It is estimated as follows.

$$\left(\frac{dP}{dA}\right)_{max} \approx \sqrt{\frac{8}{\pi}} \sqrt{\frac{1}{\pi Z_0 \sigma}} \frac{PQ}{L\lambda^{1.5}} \frac{1}{v_{mn}^2 - m^2} \tag{3.40}$$

The output power and quality factor must be fixed before calculating the ohmic losses. The presence of v_{mn}, m, and λ in the loss equation means that different modes and frequencies result in different rates of loss. This means that some can be suppressed more than others, which allows for careful geometric choices and selection of dielectric loading materials to aid in mode selection.

The nonlinear theory allows for reasonable estimation of the drift-tube lengths that lead to optimal interaction. While still less accurate than particle-in-cell simulation, the nonlinear theory is very useful in establishing a reasonable starting point for final optimisation in the particle-in-cell model.

3.4: Particle-in-Cell Simulation Technique

This section covers the principles of the simulation software used during this thesis. The simulation model used is a finite-difference time-domain particle-in-cell (FDTD-PIC) code. Finite-difference means that the code analyses geometry, fields, and the distribution of charge and current on a grid and calculates the difference between adjacent grid points to approximate gradients in the fields, charge & current distribution, and material surfaces. If the point-spacing is small enough, this is a suitably accurate approximation. Time-domain means that the code simulates a system as it evolves over time using an iterative process. From an initial condition, Maxwell's equations are solved to obtain the fields and the Lorentz force law is solved to obtain the particle trajectories. Continuity equations are then solved to obtain the current and charge distribution for use in Maxwell's equations during the next timestep. Each step repeats this process, using the results calculated in the previous step as the new initial condition.

This summary of the basic structure is applicable to the FDTD-PIC method in general, and the following sections expand on this description in the specific context of its implementation in MAGIC [203-205], which was the main design and optimisation tool used in this thesis. Several similar packages are commercially available, and some institutes have their in-house codes. The description provided in this section focuses on MAGIC, but the principles covered are the foundation of FDTD-PIC codes in general. The precise implementation and structure of algorithms may differ between codes and software packages, but in any case, the underlying principles as described in 3.4.1 are very similar.

3.4.1: Finite Difference Time-Domain PIC simulation

In this section, the explanation is expanded in more depth for specific implementation of physics that is utilised in MAGIC. The physical basis is the time integration of Faraday's law, Ampere's law, and the particle force equation:

$$\partial_t \vec{B} = -\nabla \times \vec{E} \tag{3.41}$$

$$\partial_t \vec{E} = \frac{-\vec{J}}{\varepsilon} + \frac{1}{\mu\varepsilon}\nabla \times \vec{B} \tag{3.42}$$

$$d_t \vec{p}_i = \frac{\vec{F}_i}{m_i}, \qquad \vec{F}_i = q_i\left[\vec{E}(x_i) + \vec{v}_i \times \vec{B}(x_i)\right] \tag{3.43}$$

$$d_t \vec{x}_i = \vec{v}_i, \qquad \vec{v}_i = \frac{\vec{p}_i}{\gamma_i} \tag{3.44}$$

subject to the constraints imposed by Gauss's law and the divergence of B,

$$\nabla \cdot \vec{E} = \frac{\rho}{\varepsilon} \tag{3.45}$$

$$\nabla \cdot \vec{B} = 0 \tag{3.46}$$

where E and B are the electric and magnetic fields respectively, x_i and p_i are the position and momentum of the ith particle. $J(X)$ and $\rho(x)$ are the current density and charge density resulting from those particles. The integration is performed by using known values of the variables to compute the time derivatives which are used to advance the system in time. The calculations are additionally constrained by the rules of charge continuity which must be satisfied at all times. This integration is referred to as the "time-domain solution".

The time is discretised into steps of the fixed interval δt between variable updates. The finite time difference approximation must be reasonable, i.e., $\frac{E_n - E_{n-1}}{\delta t} \rightarrow \frac{\partial E}{\partial t}$, so that when approximated in this form, the time derivative calculations will provide a new value for the variable at the time δt later than the previous value. Since the

calculations for fields and particles depend on each other's results, a technique called the leapfrog method is applied. This method involves solving some equations on integer time-steps and others on half-integer steps as illustrated in figure 3.2 [206].
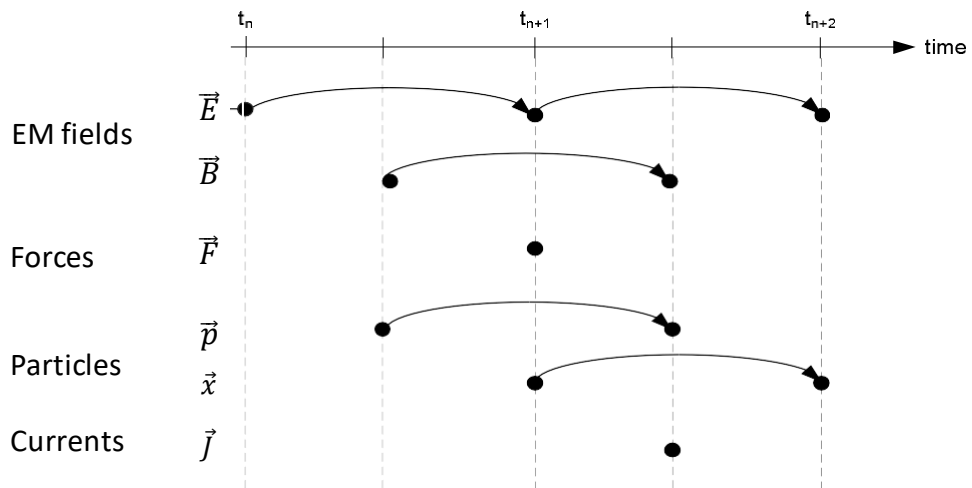
Figure 3.2
Representation of leapfrog method
Image adapted from ref. 206

Space is discretised into orthogonal cells in cartesian, cylindrical, polar, or spherical coordinates. In this case the cylindrical coordinate system is used as it is appropriate for the symmetry of the device. Orthogonality allows the discretisation to be performed as a separate one-dimensional discretisations, each specifying their respective full-grid locations on an axis. Full-grid locations do not need to be spaced uniformly, and it is possible to
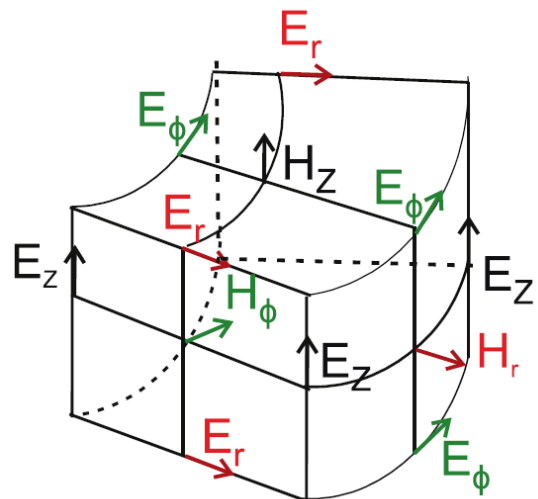
Figure 3.3
Yee cell definition in cylindrical coordinates
Image from ref. 208

have a higher grid density around the areas of peak interest. The algorithm uses spatial staggering of the vector field components wherein electric field vectors are located between a pair of magnetic field vectors and vice versa. This arrangement is

90

known as the Yee cell [207] which can be implemented in cylindrical coordinates as illustrated in figure 3.3 [208]. Each time a field component is updated it depends on the field components around it at the previous time step. The cell-size and time step can each be freely defined in the user input. They should be chosen carefully because if they are too large, the simulation accuracy will suffer, but if they are too small the runtime can become debilitatingly slow. They must be decided such that the finite-difference approximation is valid and numerical instabilities are avoided. The cell-size and time step cannot be decided completely independently of each other. To maintain numerical stability, the distance a macro particle travels in a single time step should be short enough that information is transferred only from a cell to its immediate neighbours. Hence if the spatial grid dimension is reduced, the time step may also need to be reduced to ensure that this condition, known as the Courant-Friedrichs-Lewy (CFL) condition, is satisfied.

The actual number of physical particles in a system is generally far too many for computer memory to manage in a reasonable timeframe. Hence MAGIC uses a model of macro particle representation wherein a single macro particle must represent many physical particles with equal mass and charge and occupy similar regions of phase-space. This representation is reasonable when the number of macro particles is large enough to represent all phase space regions that contribute to the result. The essential particle processes for simulation are creation, destruction, kinematics, and current density allocation. Since macro particles cannot be divided or merged, the statistics are entirely controlled by creation and destruction. Creation models exist for many physical emission processes, and particle data can also be imported from other codes. The emission algorithms available allow for detailed control of the process including uniform, random, or weighted emission profiles. Destruction occurs when particles enter a solid material or penetrate certain types of outer boundary. The kinematic process includes the calculation of forces on each macroparticle and the motion due to those forces. Force calculation takes place in four steps: spatial filtering of the fields, temporal filtering of fields, addition of external fields, and macro particle coordinate weighting. To ensure no problematic mathematical

singularities occur, kinematic calculations are performed with a unique coordinate system for each particle defined by its own location, and then transformed back to the simulation coordinates afterward.

Within MAGIC, there are several algorithms, each suited to various applications. The following two sections describe the eigenmode and Maxwell algorithms, which have each been frequently used throughout this project.

MAGIC offers many data output options, including the ability to save an image for each timestep of the simulation to observe how the fields or particle positions evolve over time. Statistical analysis of the particles can be performed automatically to obtain plots of the average momentum in each direction and the standard deviation of these values.

3.4.2: Eigenmode Solver in MAGIC

For cavity analysis in this thesis, the eigenmode solver has been used extensively. This algorithm produces the eigenvalue solution of the fully time-dependent Maxwell equations. This algorithm can be applied in a 2D or 3D geometry consisting of conductors, dielectrics, symmetries, and polarizers. The geometry must be precise for the results to match analytical data. In MAGIC, this precision is accomplished by the fact that the user can mark objects to create fixed points. Doing so will create localised warping of the grid to fit the geometry, which allows for greater accuracy than the alternative of snapping objects to the nearest grid points. This meshing technique enables reasonably accurate analysis even with relatively low grid-resolution, but the trend that higher resolution leads to higher accuracy still applies. The impact of grid resolution can be considered in relation to a small algorithmic error that arises. There are spatial finite-difference effects inherent in the algorithm, so the reported frequency is slightly downshifted. This offset can be estimated by equation 3.47 [205]

$$f = f_{true}[1 - 0.04(k\delta x)^2]\qquad\qquad(3.47)$$

where k is the wavenumber and *dx* is the grid spacing. If *kdx << 1*, then this effect is very small. Since the error depends on grid spacing, the impact on the results is easily avoided by the use of a fine grid resolution.

The eigenmode solver applies an operator to a given field pattern, and this grows eigenmodes over the frequency range specified. Modes in this range are grown such that the centre frequency grows fastest. When the operator is applied, the centre frequency grows around 3 times as much as the modes outside the window. By default, this happens 30 times, which is typically enough to grow the mode from noise level to near purity. If multiple modes are in the same window, it will prioritise the one nearest the centre. To eliminate this competition, the frequency window can be decreased, but too fine a window can lead to the code taking impractically long to compute or failing to detect any mode at all. For confidence in results, the window should be set no larger than the average mode spacing.

The default options initialise the fields with random patterns, so that there is some field strength for any of the possible modes to grow. In the 2D version, a command can be included to scan only for TM or only for TE modes. To restrict to modes with certain symmetries in the 3D version, a command can be added to define profiles of the initial fields. Using a pre-set field means that the simulation will typically miss any modes that do not match the approximate structure of the pre-set, so one must remember to consider that other modes may exist in any given window. Nonetheless, it remains a useful command when the goal is to locate and analyse specific modes, especially in cases where different modes exist with the same or very similar frequency, such as the $TE_{0,1}$ and $TM_{1,1}$ modes. By default, the algorithm locates the lowest mode, but can be set to search at a specific frequency, over a defined range, or at a list of several frequencies of interest. The detailed definition of where to search for modes and which shapes of mode to search for allows for the efficient location of those of interest.

3.4.3: Maxwell Algorithm in MAGIC

To carry out simulations which involve analysis over time requires a different algorithm. Several time-dependent algorithms exist in MAGIC, of which the ones relevant to this thesis are the "Maxwell" algorithms. There are several slightly different variants of the Maxwell algorithm, the default of which is "Maxwell Centered". It is the simplest time-dependent algorithm available in MAGIC, and therefore very useful for basic applications. It calculates a centred-difference solution to the fully time-dependent Maxwell equations. The algorithm Q is infinite, so there is no damping at any frequency, which makes it excellent for purely electromagnetic simulation. However, it is also very susceptible to the high-frequency noise that is typically produced by relativistic particles, so it is not ideal for the full gyroklystron interaction simulations. It has been used for analysis of cavity eigenfrequency and Q in the absence of the electron beam.

When the beam is present, the "Maxwell High_Q" algorithm has been used instead. This specifies the high-Q solutions of Maxwell's equations. It artificially damps the electromagnetic fields, but damps less at low frequencies. It is suitable for cases involving relativistic particles and cavities. The algorithm Q is a finite frequency-dependent value and contributes to the effective Q as calculated from the reciprocal sum of Qs. This is due to the non-physical damping which occurs at all non-zero frequencies. The degree of damping can be adjusted. A value of zero is equivalent to the centred-difference, and the default and recommended value is 0.85. The High Q algorithm has been used for the main gyroklystron simulations.

3.4.4: Verification of MAGIC Simulation Model

PIC simulation methods have long been used for microwave device design as a solid and accurate method across many different bodies of code and software. Amongst others, MAGIC has been commercially available and widely used for many years, through several updates and additions to its original release. Its effectiveness and accuracy are supported by the

Figure 3.4
An example of comparison between simulated and experimental data for a 2-cavity gyroklystron studied in references 209 and 210.

agreement of results between experimental and simulated data in various publications [209, 210] as shown in figure 3.4.

To further verify the accuracy of MAGIC's algorithms, some basic physical problems were examined. Cylindrical and coaxial cavities were simulated, and the results compared with analytical data. For a range of modes in a simple cylindrical cavity, the largest offset between the simulated eigenfrequency from the expected value was 0.9% while most were within 0.5%. Some larger errors were observed for the coaxial case, particularly at modes of the high azimuthal index. Every mode with an azimuthal index of 0, 1, or 2 was found by magic at a frequency within 2% of that calculated numerically, while indices of 3 or more frequently saw offsets of over 5%. The mode purity and stability issue of high-order modes may play some role in this offset, but a more probable explanation is that the more complex field patterns of these modes may require denser grid resolution to analyse to the same precision. Such an inaccuracy was not seen for the cylindrical case, or any low-order modes. All cavities in the intended design use low order cylindrical modes ($TE_{0,1}$ or $TE_{0,2}$) which are symmetric and typically quite stable. Each had a simulated eigenfrequency within

0.5% of the expected value. Therefore, there is high confidence in the validity of results for the simulations performed with MAGIC.

A 2D model is used in the MAGIC simulations of this thesis. The coordinate system is cylindrical with the centre-line forming the z-axis. The symettry of the system and operating mode means that the accuracy can still meet appropriate standards. However, a limitation of a 2D model is that the $TE_{1.1}$ mode cannot be fully accounted for. Competition from this mode is always a threat, as it cannot be cut-off like high-order modes. Instead the risk of mode competition is minimised with the use of dielectric materials in the cavity and drift tubes which help suppress unwanted oscillations, and the beam geometry which matches the position of electrons to the coupling maximum of the $TE_{0,1}$ mode.

3.5: Summary of the Stages of Design

PIC simulation packages such as MAGIC are the most detailed and accurate simulations available for gyroklystron design work, but this level of detail comes at the price of large computation time. The use of the quicker, less advanced methods of linear and nonlinear theory allows for a much more efficient process. Simulation runtime aside, an approximate design obtained prior to PIC analysis also removes a large amount of work that would be spent on simple trial-and-error if the researchers were to start directly with PIC modelling from scratch. The closer the initial design is to a final function set-up, the faster the optimisation can be. It is therefore important to work with each model, progressively working towards the final state.

Firstly, well-known basic equations were used to estimate cavity sizes for the desired eigenmode and frequency (section 2.1). These estimations were then used as the basis for linear theory studies (section 3.2), which give a rough indication of whether each potential cavity sequence is worth exploring further. The nonlinear theory (section 3.3) can then be used to further verify and adjust the set-up, with a much greater ability to consider drift-tube dimensions and stagger-tuning. This can lead to a reasonable estimation of a device, which can then be tested in PIC simulation (section 3.4). The cavities should first be tested one by one, as MAGIC's eigenmode algorithm can provide better representation of the dielectric linings than the nonlinear theory can. This is likely to result in small adjustments to the cavity dimensions to correct the eigenfrequency. Finally, the cavities can be combined and simulated as a whole device with MAGIC's Maxwell algorithm. The input parameters can be tested over appropriate ranges allowing for the identification of the best performance data achievable.

Chapter 4: Magnetron Injection Gun Design

The fundamental physics of MIG operation was introduced in section 2.2. In this chapter, the design process is presented in more detail, followed by the results of the simulated design and optimisation.

4.1: Design Process of the MIG

4.1.1: MIG Geometry

From the principle of the gyroklystron, there are several requirements on the electron beam properties. This can be summarised as three main criteria for the electrons in the beam [211].

1. They must have the required beam energy.
2. They must have a proper transverse-to-axial velocity ratio.
3. The spread of values in the velocity and velocity ratio must be as small as possible.

In a MIG, thermionic emission from a ring cathode creates an annular beam centred around the gun axis, with no electrons on the axis itself. Figure 4.1 illustrates the beam shape. This beam shape is well suited to the circular azimuthally symmetric $TE_{0,n}$ modes that are typically used in gyroklystrons, as one only has to consider the radius and thickness of the beam (and not the shape) to ensure electrons are only present at points close to the field-coupling maximum.
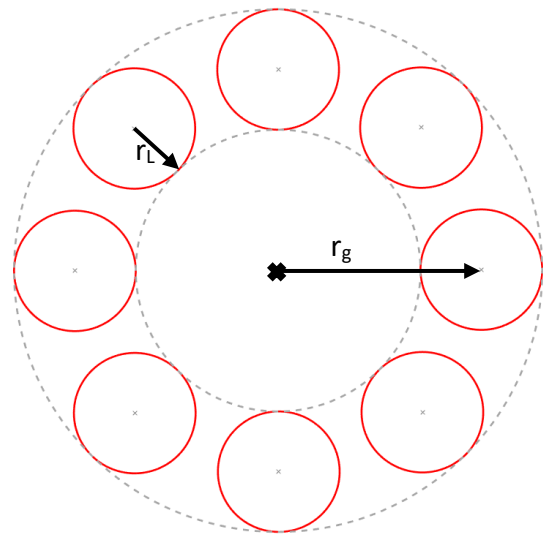
Figure 4.1
Annular beam profile. Electron orbits are shown in red and the beam guiding centre radius r_g and Larmor radius r_L are indicated.

MIGs can be categorised into two main types; the diode-type and the triode-type [89, 212]. The diode-type uses a single anode, while the triode-type has two anodes. Chapter 2 presented a simple schematic of a MIG. In figure 4.2, a similar schematic is presented for the triode-type MIG, with the main parameters labelled. Some devices use another variation called an inverted magnetron injection gun (IMIG) [213-215]. In an IMIG the emitting surface is on the outer wall, allowing for a much larger emitting ring. This type of gun is particularly common in coaxial devices but is over-complicated for cylindrical devices. Therefore, the IMIG is not covered in detail here, and the remainder of the chapter focuses on the design principles of the more widely used and proven diode and triode-type MIGs.
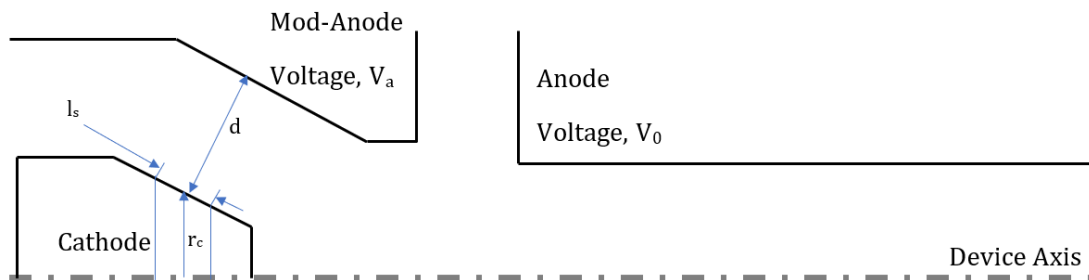
Figure 4.2
Schematic of a triode-type MIG

The first anode in each is called the accelerating anode, or sometimes the control anode. The extra anode in a triode-type gun is called the modulating anode and is used to fine tune the electron beam. Although the modulating anode voltage as an additional tuning parameter can add to the precision of the MIG, it also adds complexity to the system. In the diode-type MIG, tuning is performed by control of the magnetic field at the cathode position. A diode-type MIG has the advantage of being simpler to design and can still offer sufficient tuneability without significant impact on the velocity spread in modest current systems. In a system where a diode-type gun provides adequate beam parameters for the application, the scale of improvement from a triode-type is unlikely to be worth the increased complexity. However, in a high current density device like the gyroklystron of this thesis, the diode-type may not deliver adequate performance. The combination of a high beam current and a small beam radius makes minimising spread a significant challenge, and hence the additional control offered by an extra anode is necessary to achieve suitable performance.

Using one of the very high emission density cathodes mentioned in section 2.2.3, on paper, a very small emitter could meet the current specification. However, operating at such a high density would require more energy dedicated to cathode heating for the cathode to operate at a high enough temperature which would impact the lifespan of the emitter. Alternatively, the same current can be produced by a larger cathode operating in a less extreme temperature region. Unfortunately, too large a cathode also leads to issues as a long slant-length is required which can also result in increased velocity spread or cause the beam's radial thickness to be too large. If the cathode surface area is instead increased by using a larger radius instead of a larger slant-length, a higher compression ratio is needed to achieve the correct beam radius at interaction, but too high a compression ratio also leads to an increase in velocity spread. This is just one example of the complex and delicate trade-offs to consider between parameters in the MIG design. A mathematical model is therefore required to guide the design process, as presented in the following section.

4.1.2: Design Equations

The MIG and interaction circuit must be designed with direct consideration of each other. The MIG must be designed to match the baseline requirements of the interaction circuit, and the interaction circuit must be designed to consider the achievable MIG performance. The interaction magnetic field B_0, the target velocity ratio α, beam voltage V, and the beam radius r_g are fixed, but there are still several parameters to consider. The separation of the cathode and anode determines the peak electric field, and the angle of the surface determines the axial and transverse components of that field. The cathode's centre radius r_c, as well as the cathode angle ϕ_c and slant length l_s can all influence the performance significantly. The magnetic field at the cathode B_c is a very important parameter, usually defined in reference to the interaction field by the magnetic compression ratio:

$$b = \frac{B_0}{B_c} \tag{4.1}$$

The compression ratio relates the electron guiding centre radius and the cathode radius approximately:

$$r_c = \sqrt{b}\, r_g \tag{4.2}$$

Mathematically, there are infinite solutions to equation 4.2, so a more thorough estimation of the compression ratio is needed. Similarly, a well-estimated initial value of each other major design parameter is required to develop an adequate starting point for optimisation. For this reason, a set of trade-off equations for MIG design was developed by Baird and Lawson [157, 216]. While computer optimisation is required for complete design, these equations remain a powerful tool to estimate the starting parameters of the simulation and have seen extensive use in electron gun development [186, 217-219]. The equations are based on the principle of conservation of angular momentum and the assumption of adiabatic electron trajectories and low space-charge effects. The conservation of angular momentum for electrons in cylindrically symmetric DC fields $E(r,z)$ and $B(r,z)$ can be written as:

$$\left(\gamma m r^2 \dot\theta - eB_z \frac{r^2}{2} \right) = constant \ of \ motion \qquad (4.3)$$

where $\dot\theta$ is the angular velocity, e is the electron charge, m is the electron rest mass, B_z is the axial magnetic field, and r is the instantaneous radius of the cycling electrons. The angular momentum can then be considered in the drift region in terms of the Larmor radius r_L and the guiding centre radius r_g

$$\left(\gamma m r^2 \dot\theta - eB_z \frac{r^2}{2} \right) = \frac{eB_z}{2} \left(r_L^2 - r_g^2 \right) \qquad (4.4)$$

The left-hand side of equation 4.4 can be considered in the cathode region, where $\dot\theta = 0$, and the right-hand side is considered in the interaction region, denoted by the suffix 0.

$$B_{zc} r_c^2 = B_0 \left(r_{g0}^2 - r_{L0}^2 \right) \qquad (4.5)$$

The first of the core design equations is then defined by rearranging equation 4.5 and applying the normalisation of distance to r_{L0}. Normalised radii are distinguished in the notation by the use of capital R.

$$b = \frac{R_c^2}{R_g^2 - 1} = \mu^2 R_c^2 \qquad (4.6)$$

where the Tsimring cylindricity parameter μ has been introduced and is defined as [68]:

$$\mu = \frac{1}{\sqrt{R_g^2 - 1}} \qquad (4.7)$$

The MIG cathode must be large enough to generate the beam current I_0 at the selected emission density J_c. The slant length l_s is normalised as above ($L_s = l_s / r_{L0}$), and the second design equation is derived from geometric consideration of the emitter's conical surface. The surface area of the lateral portion of a truncated cone can be calculated as:

$$A_E = \pi (R + r) \sqrt{h^2 + (R - r)^2} \qquad (4.8)$$

where the variables are the dimensions as depicted in figure 4.3. However, as the cathode centre radius r_c is the value considered in the design equations, and is simply the midpoint between the two end radii of the emitter, equation 4.8 is more practical if simplified to the form:
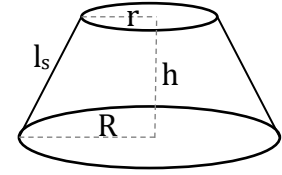
$$A_E = 2\pi r_c l_s \tag{4.9}$$

This geometric equation can then be used to derive the second of the design equations:

$$\frac{L_s}{R_c} = \left(\frac{I_0}{2\pi r_{L0}^2 J_c}\right)\frac{1}{R_c^2} \tag{4.10}$$

The next consideration is the beam's thickness. A useful way to analyse this is in the spread of the guiding centre radii δR_g at the interaction region. A large spread in guiding centre radius leads to a reduction in interaction efficiency. The third design equation is obtained by normalising equation 4.5.

$$R_c^2 = b\left(R_g^2 - 1\right) \tag{4.11}$$

The guiding centre spread and cathode radial difference δR_c are then accounted for.

$$(R_c + \delta R_c)^2 = b\left(\left(R_g + \delta R_g\right)^2 - 1\right) \tag{4.12}$$

which then can be simplified by expanding the brackets, truncating to the first order terms in δR_g and δR_c since these terms are small, and resubstituting equation 4.6 to get:

$$2R_c\delta R_c = b\left(2R_g\delta R_g\right) \tag{4.13}$$

By simple geometry of the conic section, the substitution $\delta R_c = L_s \sin\phi_c$ can be used. Then eliminating b using the definition of μ, and by using equation 4.10, the final form of the design equation can be defined as:

$$\frac{\delta R_g}{R_g} = \left(\frac{\sin\phi_c}{\mu^2 + 1}\right)\left(\frac{I_0}{2\pi r_{L0}^2 J_c}\right)\frac{1}{R_c^2} \tag{4.14}$$

In an idealised model such as linear theory, the beam has zero thickness with its radius perfectly aligned with the coupling maximum. In reality, the beam must have a finite thickness which is related to the cathode thickness in the same form as equation 4.2:

$$\delta r_c = \sqrt{b}\, \delta r_b \qquad (4.15)$$

The fourth design equation relates the normalised distance between the anode and cathode D_{ac} to the Larmor radius at the cathode. The design spacing factor D_F is introduced. If D_F is 2, then the radial change is one full Larmor diameter, and hence the minimum value that avoids the beam meeting the anode. A higher value of D_F increases the clearance between the beam and the modulating anode and increases the required voltage on that anode.

$$\frac{D_{ac}}{R_g} = \frac{D_F \mu}{\cos \phi_c} \qquad (4.16)$$

The mod-anode voltage V_a is normalised as $\Phi_a = \frac{eV_a}{mc^2}$ which sets it to units of 511kV. The equation to estimate the normalised voltage is:

$$\Phi_a = \frac{\ln(1 + D_F \mu)}{\ln(1 + 2\mu)}\left\{\left[1 + \frac{4}{\mu^2}\left(\frac{1+\mu}{1+2\mu}\right)^2\left(\frac{\gamma_0^2 - 1}{R_c^2 \cos^2 \phi_c}\right)\left(\frac{\alpha_0^2}{\alpha_0^2 + 1}\right)\right]^{\frac{1}{2}} - 1\right\} \qquad (4.17)$$

The required electric field at the cathode is given by:

$$\frac{E_c}{E_{max}} = \left(\frac{mc^2}{eE_{max}r_{L0}}\right)\left(\frac{\Phi_a \cos \phi_c}{\ln(1 + D_F \mu)}\right)\left(\frac{1}{R_c}\right) \qquad (4.18)$$

The field should be below the limit of approximately 100kV/cm, as fields higher than this can cause arcing during operation of the MIG.

$$\frac{J_c}{J_L} = \left(\frac{2\pi r_{L0}^2 J_c (1 + D_F \mu)\chi^2}{14.66(10^{-6})\left(\frac{mc^2}{e}\right)^{\frac{3}{2}} \cos^2 \phi_c}\right)\left(\frac{R_c^2}{\Phi_a^{\frac{3}{2}}}\right) \qquad (4.19)$$

where J_L is the Langmuir limiting current density [220] and χ is shorthand for the sum:

$$\chi = e^{\left(\frac{-\zeta}{2}\right)} \left[\zeta + \frac{1}{10}\zeta^2 + \frac{5}{300}\zeta^3 + \frac{24}{9900}\zeta^4 + \cdots \right] \qquad (4.20)$$

where $\zeta = \ln(1 + D_F\mu)$.

It is also useful to consider the velocity of electrons. Using the approximations that the emission velocity is negligible, and that the cathode is perfectly smooth, the initial orbital velocity can be written as

$$v_{\perp c} = \frac{cE_{\perp c}\mu_0}{B_c} \qquad (4.21)$$

where the subscript c refers to the value at the cathode, and the geometric indicators are relative to the magnetic force line. The increase in transverse velocity over the MIG's length is a result of the adiabatic invariance.

$$\frac{p_{\perp}^2}{B} = const. \qquad (4.22)$$

The transverse velocity in the interaction region can then be found:

$$v_{\perp 0} = b^{3/2}\left(\frac{cE_{\perp c}\mu_0}{\gamma_0 B_c}\right) \qquad (4.23)$$

The design equations presented in this section provide a suitable starting point for further study. To design a MIG with reasonable spread requires computer optimisation due to the complexity of the mathematics and a large number of important parameters. However, obtaining a reasonable approximation to begin optimisation from is essential in order to keep computation time within practical limits.

4.1.3: Sources Velocity Spread

Minimising velocity spread is one of the main challenges in the design of MIGs. The velocity spread arises for several reasons [221, 222]:

1. Initial thermal spread of electron velocities
2. Emitter surface roughness
3. Violations of axial symmetry of the fields
4. Nonuniformity of fields on the cathode
5. Nonadiabatic fields between the cathode and anode
6. The space-charge fields of electrons in the beam

Some causes such as radial shift of the cathode and different effects on electrons starting at different points along the emitter width may be reduced by optimal gun design. The surface roughness cannot be reduced to zero and the natural spread of initial thermal velocities is an inevitable consequence of the Boltzmann distribution that can be seen in the energies of electrons in any heated material, so a perfect zero-spread gun cannot exist. Nonetheless, modern MIGs have been designed with velocity spreads under 3% [212, 223], though the achievable spread depends on many device-specific factors, especially beam radius and current requirement. A high-current, small-radius device such as that presented in this thesis will inevitably have a higher velocity spread than a low-current device because the space charge effect scales with current density. Due to the individual requirements on the beam in any given gyroklystron, the MIG and interaction circuit must be designed together and optimised to each other's parameters. The velocity spread is influenced by emitter position and geometry, and by the magnetic field profile. Given the complex shape of the MIG, this leads to many parameters which all must be considered. Optimisation of a MIG design requires consideration of all these elements. The design process is discussed in detail in section 4.2.

4.2: Simulation Results

4.2.1: Simulation of the Magnetron Injection Gun

As discussed in the preceding sections, several parameters are fixed based on considerations of the interaction circuit and specification of a high-power amplifier to drive a pulse compressor which then powers a harmonic lineariser for an X-ray Free Electron Laser (CompactLight). Table 4.1 lists these parameters.

Table 4.1: MIG parameters

Parameter	Value
Operating frequency (GHz)	48
Beam voltage (kV)	140
Beam current I_0 (A)	37
Beam Velocity Ratio α	1.35
Magnetic field in the interaction region B_0 (T)	2.02
Beam guiding centre (mm)	1.77
Pulse duration (μs)	1.5
Maximum pulse repetition rate (Hz)	1000

The repetition rate and pulse duration are determined by the application. 1000Hz is the maximum required, but normal operation will be around 400Hz. With a pulse duration of 1.5µs, the duty cycle is therefore 0.15% and a relatively high current density is feasible, since surface degradation and heating demand is much higher for continuous wave devices than pulsed. Section 2.2.3 provides an overview of cathode properties and shows that the chosen emission density of 20A/cm^2 can be readily achieved with available cathode technology [184, 186, 224].
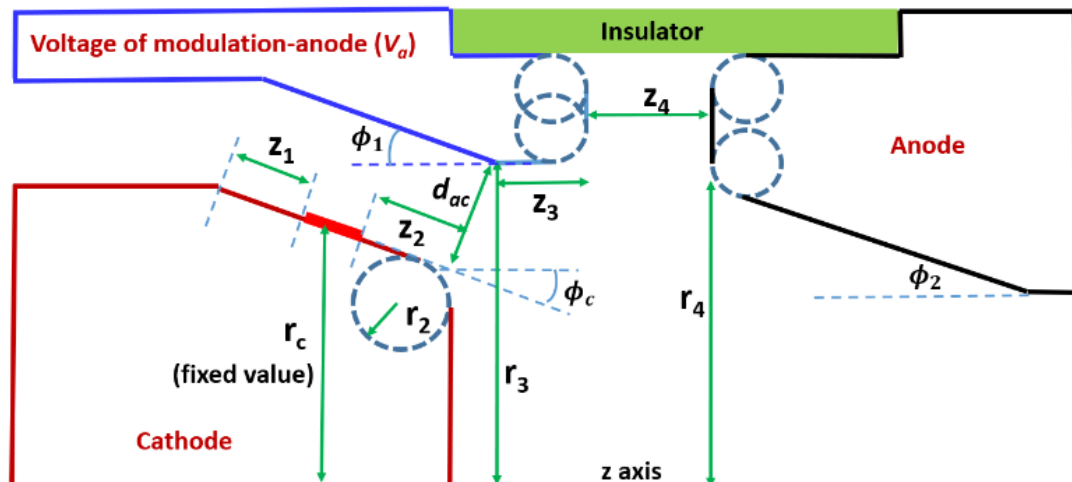
Figure 4.4
Parametrised geometry of the triode-type MIG.

The position, size, and angle of the emitter, along with the position of the two anodes, and the magnetic properties all influence the performance of the MIG. To break this down into a manageable parameter space, the geometry and a range of measurements are illustrated in figure 4.4 showing the geometric parameters identified as dimensions to consider during optimisation. Additionally, the modulating anode voltage V_a and 3 parameters to control the magnetic field profile should also be considered during optimisation. These are the compression ratio b, the magnetic field of the reverse coil B_{rc}, and the relative shift position of the coils to the cathode. This makes a total of 15 parameters for optimisation. Several design goals must simultaneously be fulfilled, particularly the correct values for velocity ratio and guiding centre, while the spread in each of these values is minimised.

The magnetic field profile is controlled by a series of coils illustrated in figure 4.5. The main coil is selected to provide the 2.02T field required over the interaction, while the shim and reverse coils allow for shaping of the field profile through the emission and compression region. For any values of the radial and axial magnetic field components at the cathode, the drive currents through the reverse coils which provide those values can be found.
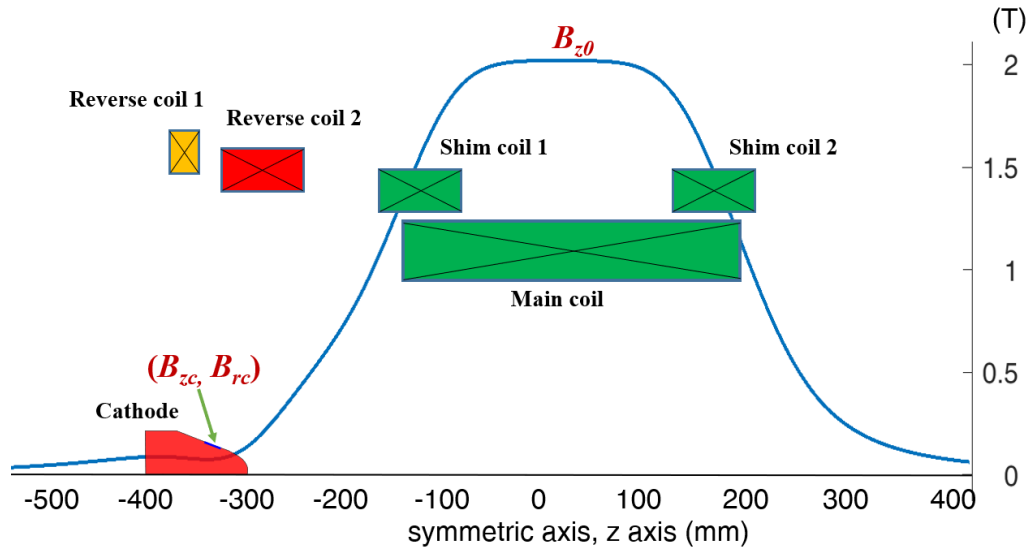
Figure 4.5
Configuration of magnet system in the MIG

The gun design software package TRAK 8.0 was used to design the gun [225]. The software uses finite-element methods [177, 226-228] to calculate trajectories. The cylindrically symmetric structure allows for a reduction of the problem to two dimensions without a large impact on the accuracy. The finite elements are triangular cells, and integral relations over these elements lead to a set of equations for the electrostatic potentials at each vertex. As there are very many particles, calculating the field from each individually by Coulomb's law would be impractical. Instead, a number of nearby charges can be approximated to a continuous cloud with negligible impact on the resulting field around them. This cloud has an enclosed current which can be used to calculate the beam-generated magnetic field which is essential to analysis of the trajectories.

The mesh-dimension used was 0.05mm in the radial direction and 0.1mm in the axial dimension around the emitter, and 0.1mm by 0.2mm in the rest of the device, as the

emission region requires the most precision and a larger mesh in the other sections reduces computation time. A timestep of 2.5×10^{-13}s was used for the iterative particle trajectory interval. The grid and time step parameters were selected such that they are small enough to resolve the smallest geometric features of the system and accurately model the electric field. They were selected to satisfy the CFL condition (see section 3.4.1), and further refinement of the mesh would significantly increase simulation time with no significant impact on the result. The grid in the emission region is shown in figure 4.6. The top image shows the mesh around the cathode and mod-anode. The mesh has an increased density across the emitter itself, shown in the bottom image.
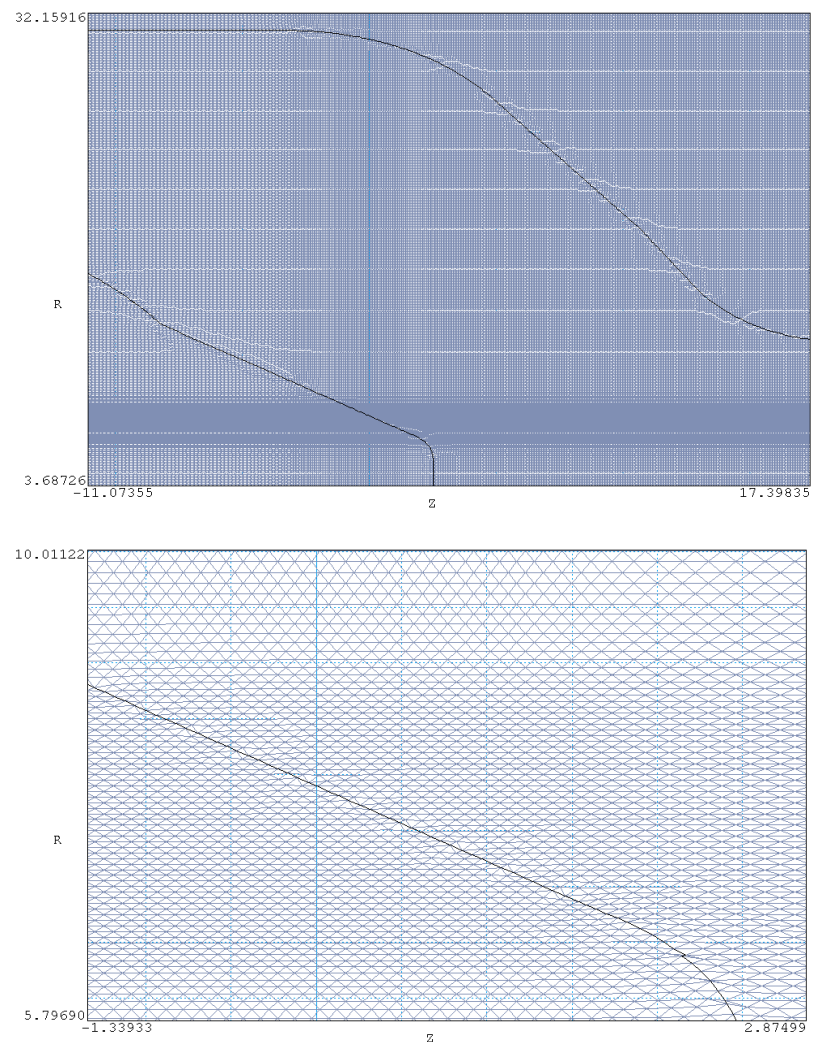

Figure 4.6
Simulation mesh for the MIG optimisation

A multi-objective genetic algorithm (MOGA) was used [229]. In this method, the objectives and design parameters are set. N individuals are randomly generated and the performance of each is calculated. Of the initial N, the best M individuals are selected, and then $N - M$ new individuals are generated by mutation and parametric crossover. The cycle then repeats until the design goals are satisfied or the maximum number of generations is reached. In this work, the final results were obtained after 400 generations, each with a population of 100. Prior to the full optimisation a few trial tests were carried out to define a suitable range of some geometric parameters. The evaluation metrics were that the central α result should be as close as possible to the desired value with as little α-spread as possible. To improve the evaluation metric, penalty factors were applied to any sample where the beam current deviated more than 15% from the desired value. Large penalty factors were also applied based on the percentage of beam current lost in transport to eliminate any samples with beam reflection issues. This evaluation function means that structures with good parameters are accepted and those which deviate from the desired goals or suffer problematic beam transport issues are not.

Table 4.2 shows the initial and optimised parameters. The initial parameters were estimated by the synthesis method as discussed in the preceding section. The initial parameters showed around 25% spread when first simulated, which was reduced to 8.9% by the optimisation routine. The parameters with the largest change in value during optimisation were the modulation anode voltage and the compression ratio.

Parameter	Initial	Optimised
Emitter radius r_c (mm)	7.9	7.9
Emitter current density J_E (A/cm^2)	20	20
Emitter angle ϕ_c	30.0°	33.9°
Voltage on mod-anode V_a (kV, *relative to cathode*)	18.7	32.5
Cathode to mod-anode distance d_{ac} (mm)	15	15.3
Magnetic field compression ratio b	25.0	21.93
Magnetic field angle θ	--	2.1°
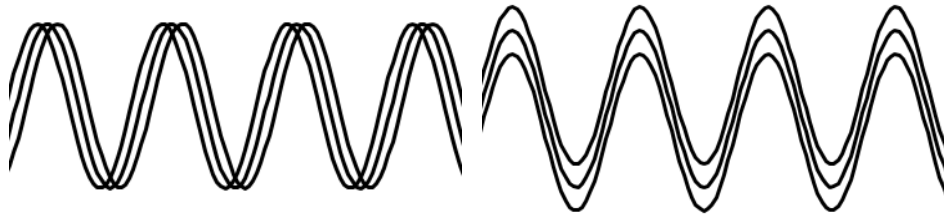
Figure 4.7
Visualisation of electrons with regularly intersecting trajectories (left) and laminar flow (right)

Good beam laminarity is important as spread tends to be exacerbated by non-laminar trajectories. The difference between laminar and intersecting trajectories is illustrated in figure 4.7.

On the left diagram, the initially rightmost trajectory is always to the right, and the initially leftmost trajectory is always to the left, so they will consistently experience accelerating and decelerating space-charge forces respectively, increasing the spread. Laminar flow, as seen in the right-hand diagram, does not have this problem. The space-charge in a laminar beam will still induce some velocity spread, but it is less severe due to the lack of spatial resonance. For this reason, it is generally better to use a laminar beam if the angle needed is compatible with the interaction in question. Increasing the beam current can reduce the angle at which beam topology transitions to laminar flow.
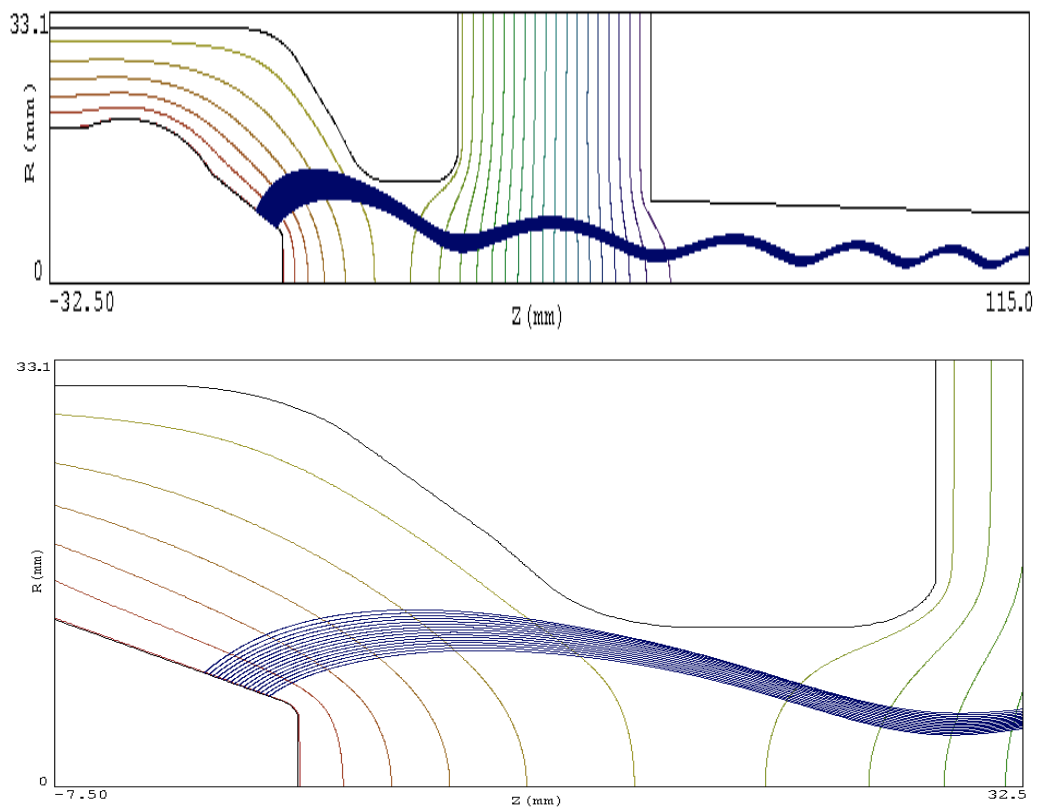
Figure 4.8
Electron beam trajectories in the MIG

Figure 4.8 shows the electron trajectories in the MIG (top) and more detail around the emitter (bottom), illustrating a good laminar profile.

The value of α was observed to be sensitive to the modulation anode voltage V_a. The α-spread was also affected by V_a but only saw a strong trend at higher voltages, while remaining around similar values for low voltages. These trends are illustrated in figure 4.9. Above 34kV, the high α value made reflection of electrons back towards the cathode a significant problem and the beam transportation rate was no longer 100%.
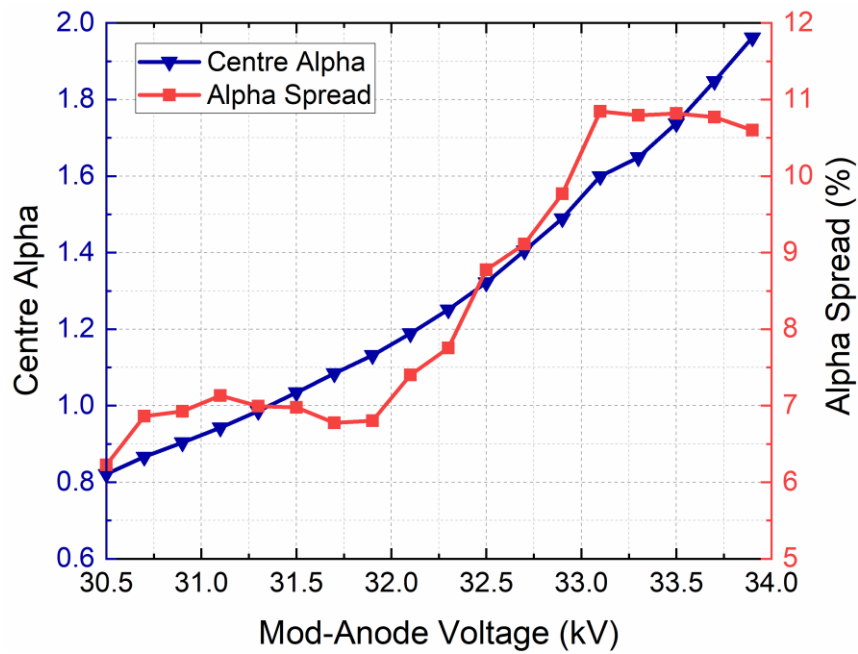
Figure 4.9
Effect of modulation anode voltage on the velocity ratio and its spread

The compression ratio can also be used to change α. However, it also has a moderate effect on the α-spread, as shown in figure 4.10. The compression ratio was controlled in this case by an axial shift of the magnet. The optimal compression ratio of 21.93 was significantly lower than the initial estimate of 25. This is because the radial and axial dimensions of the cathode mean that not all electrons feel the same field. This
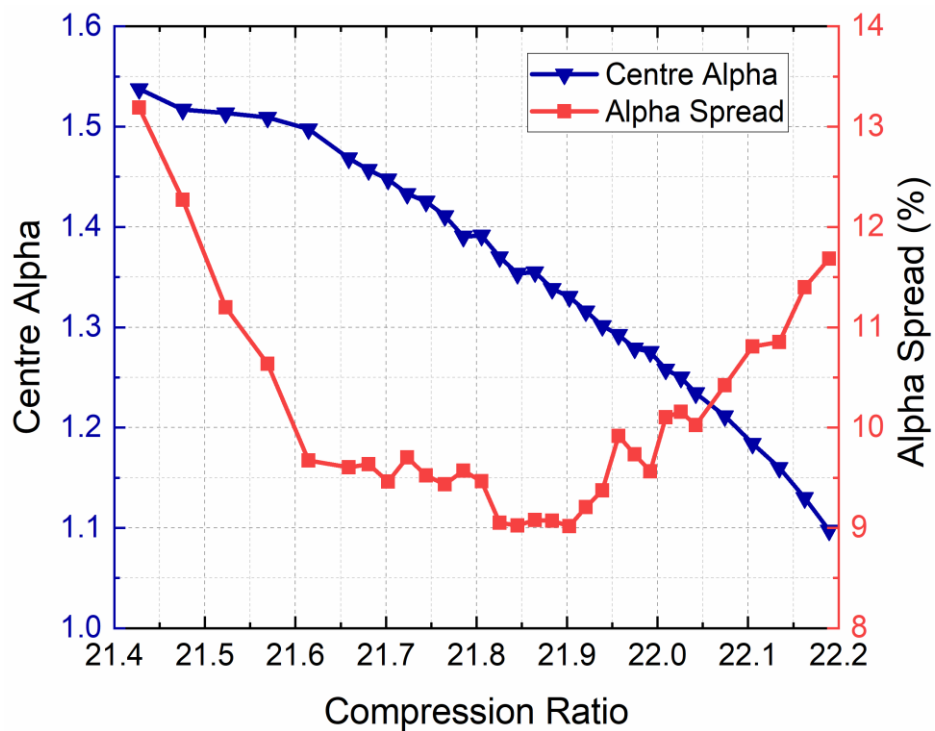
Figure 4.10
Effect of compression ratio on velocity ratio and its spread

can contribute a lot toward the total spread in the beam. The effect is more pronounced for small fields (i.e., large compression ratios). Although the trend became strong for larger offsets, it was observed that the α-spread was almost constant for a magnetic field shift of ±0.25mm which implies a reasonable degree of tolerance in construction. However, the value of α followed a roughly linear trend over the tested range, so too much shift in field position would still be problematic for the design goals.

The above discussion considers an axial field. Introducing a radial component to the field can add further control over the beam parameters. Adjusting B_{rc} while maintaining a constant compression ratio simply means changing the angle of field lines. The magnetic field angle is therefore defined as the angle between the magnetic field line and the device axis. The trends observed when varying the field angle are illustrated in figure 4.11. It was shown that an unsuitable angle can lead to an extremely high α-spread. The optimal angle was found to be 2.1°. With an angle this small, B_{rc} is also small, and there was no significant influence on the beam laminarity.
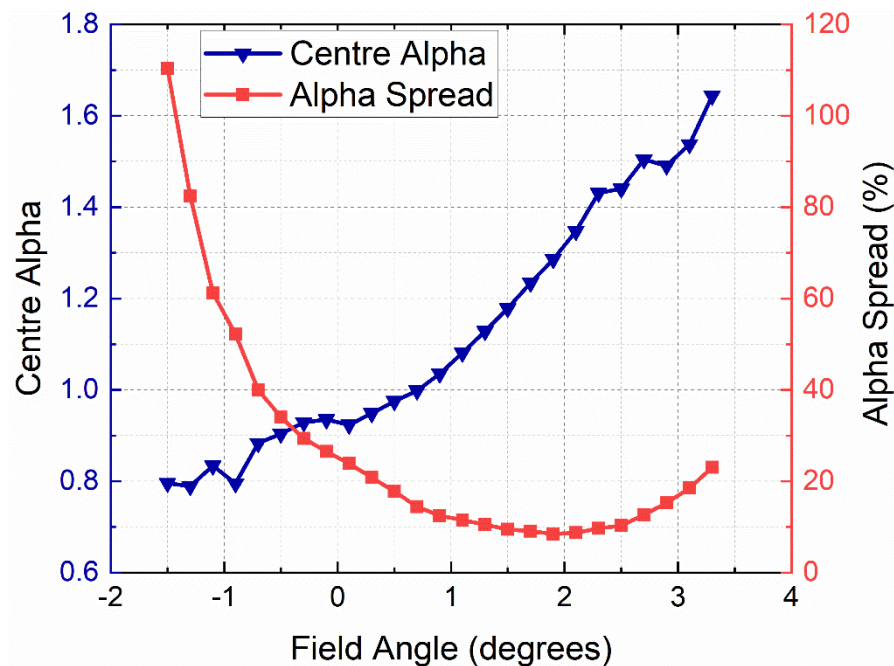
Figure 4.11
Effect of magnetic field angle on velocity ratio and its spread

These parameter sweeps demonstrate the sensitivity of the MIG performance to various design aspects and show that a reasonable spread of 8.9% is feasible. This spread implies that there will be a roughly 13% drop in the output power of the gyroklystron compared with the ideal case of a zero-spread beam. Further discussion of the effect of α-spread is presented in chapter 5, as meaningful analysis of it requires the context of the full simulation of the interaction circuit.

4.2.2: Summary and Conclusions of MIG Simulations

The MIG was designed using the synthesis method followed by computational optimisation in TRAK. A triode-type gun was used for improved control over the beam properties to minimise spread and reflection. After optimisation, an α-spread of 8.9% was achieved, mainly arising from Δv_z, and it was shown that the field angle at the emitter surface was a significant factor in determining beam quality. This level of spread corresponds to around 13% reduction in the output power of the gyroklystron compared with the ideal case, bringing the expected output power to 1.97MW. The analysis of the MIG design provided insightful figures illustrating the impact of various parameters on the spread. Notably, the magnetic field angle was observed to be very impactful if an inappropriate value was chosen, with the required angle being slightly offset from parallel. The optimal compression factor was somewhat lower than the estimated value from the trade-off equations, and it was observed that a slight deviation from the optimal value will not severely impact the α-spread. Considering the combination of high current and small beam-radius required, the achieved spread of 8.9% is low and represents a strong MIG design appropriate to the required application.

Chapter 5: The Gyroklystron Design Process

5.1: Initial Design Choices

This section addresses the broad overarching considerations that influence gyroklystron design. Section 5.1.1 covers how the decisions surrounding the performance targets of the amplifier, and then 5.1.2 expands on how the selected targets influence the most fundamental aspects of design.

The results discussed in this section come from the linear, nonlinear, and PIC models as described in chapter 3.

5.1.1: Performance Targets

Before a gyroklystron can be designed, the required performance characteristics must be determined. Many of these parameters require detailed consideration of the application. In an accelerator, an output power of 50MW or more may be desired of a microwave source for the main accelerating frequency, while a gyroklystron for radar applications might only require output power on the scale of tens to hundreds of kW, though MW-level radar designs do also exist. In the case of the linearising cavity, several MWs is required, but the gyroklystron signal has a lower requirement as it will be used to power a pulse compressor (section 2.2.3) to increase the peak power before being fed into the lineariser. A 1.5µs pulse with a minimum output power of 2MW must be fed into a mode converter and a SLED-II type compressor [198], and then onwards to drive the linearizer. More output power is always desirable to improve the performance of the lineariser. The performance targets required are outlined in table 5.1.

Table 5.1 – Performance targets for the gyroklystron amplifier

Parameter	Target Value	Source
Output Power	At least 2MW	CompactLight; to meet the lineariser power demand after pulse compression
Pulse Repetition Rate	1000Hz	CompactLight; outlined as core goal based on survey of potential users
Pulse duration	1.5μs	CompactLight; based on RF modules and pulse compression
Phase Stability	<0.5°	CompactLight; to meet tight phase stability requirement of lineariser
3dB Bandwidth	At least 200MHz	Compactlight; based on pulse compression method
Gain and Efficiency	*As high as practical*	General aim to minimise running cost and energy footprint

Figure 5.1 shows how the gyroklystron and other components fit together. The mode conversion and pulse compression sections are being designed by other teams within the CompactLight collaboration, and communication with these teams has helped establish the main performance goals of the gyroklystron.

Figure 5.1
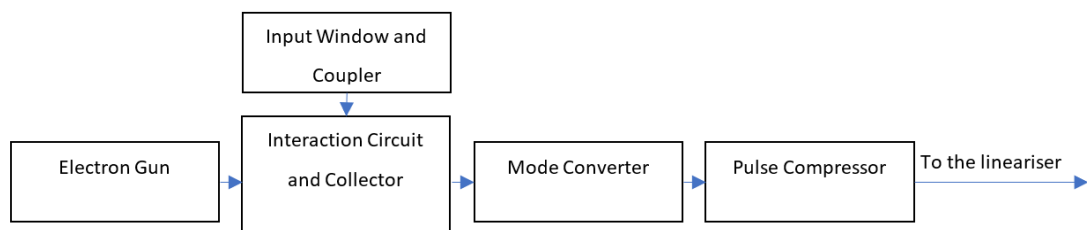*Schematic of gyroklystron and surrounding components*

The bandwidth is the range of frequencies for which the gain does not deviate more than a certain limit from the centre-frequency gain. The limit that is most commonly referred to is 3dB, hence the quantity is sometimes referred to as the 3dB-bandwidth. Figure 5.2 shows the definition of the bandwidth graphically. As accelerators are

118

constructed to work with specific frequencies and energies, they work well with narrow bandwidth components, but even narrow-band applications have a minimum requirement. In general, some level of bandwidth is always important to account for any frequency matching issues that may arise between components in the larger system. In this case, the method of
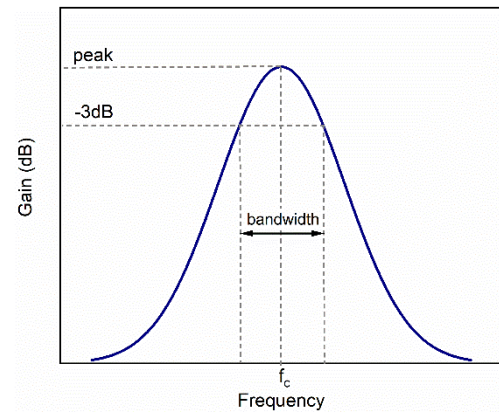
pulse compression sets a minimum value for the bandwidth. Within the pulse compressor the phase of the input signal must be flipped by 180° within a maximum duration of 5ns. This sets a requirement that the bandwidth should be larger than 200MHz to properly amplify the driving signal. This is not a hugely difficult requirement, but it still demands consideration in the design process. Methods of achieving this bandwidth are discussed in section 5.2.1.

Parameters such as gain and efficiency can broadly be summed up simply by the rule that higher is better, though there are often still minimum acceptable values based on the available input microwave power and beam power as well as making sure the gain remains at a level where the amplifier remains zero drive stable. A gyroklystron design is developed around a specific value of γ, achieved by setting the cathode-anode voltage difference. The current is then limited by the cathode properties and space-charge effects in the beam as discussed in chapter 3. Since the beam power is the product of current and voltage, when the maximum safe current is reached, so too is the maximum beam power. This places a minimum constraint on the interaction efficiency. Since the maximum practical efficiency is around 40%, at least 5MW of beam power is necessary to achieve 2MW of output power, $P_{out} = \eta I V$. The selected beam voltage and current were 140kV and 37A respectively, and hence the minimum efficiency to meet 2MW is 38.6%.

The minimum zero drive stable gain is defined by what level of input microwave power is practical. This depends on the power source, cavity capacity, thermal issues,

and the quality of the input coupler. Enhancing the zero-drive stable gain is desirable as achieving the same output power with less input microwave power can lower the requirements on the power source and input coupler, thus simplifying design. Since the running cost associated with the provision of input power is typically extremely small compared to the overall cost of an XFEL facility lowering the input power provides negligible benefit in this regard as long as the input sources are commercially available. Therefore, it is commonly reasonable to decide that maximising efficiency should be considered more important than maximising gain, provided that the input power remains within plausible limits – i.e., it can be delivered without needing an additional expensive amplifier. The following section, 5.1.2, further details how the physical limitations on cavities can lead to compromise on these goals. While it remains true that higher gain is always desirable if the gain is too high then the risk that the amplifier is no longer zero drive stable and begins to oscillate is increased, it shall be seen that in practical terms, the associated challenges and trade-offs can further affect the target performance characteristics.

5.1.2: Determination of the Overall Structure

The first step to designing a gyroklystron for a given performance specification is to decide the approximate shapes and dimensions of the structure. This includes the decision of whether to use cylindrical or coaxial cavities, the number of cavities, and the modes of the cavities.

If operating frequency, target power output, and beam current are all low, it is generally a valid assumption that a simple $TE_{0,1}$ cavity will be adequate, but this is not the case in very high-power or high-frequency devices. The power-handling capacity of a cavity is dependent on its radius, so it can be beneficial to use a large cavity operating in a higher order mode that is equivalent in frequency to a smaller cavity at the $TE_{0,1}$ mode. As the power in each cavity is greater than the previous one, the output cavity will always experience the largest fields. In the earlier cavities, the field

power may be low enough that the $TE_{0,1}$ is still a reasonable choice. It is possible, and not exceptionally complex, to set up a $TE_{0,1}$ input cavity and $TE_{0,2}$ output cavity such that the eigenfrequencies and radii of maximum coupling coefficient are compatible. As the lower order mode has a superior coupling coefficient, it is preferred for the bunching cavities to maximise efficiency, while the higher order mode can be used in the output cavity where the issue of the weaker coupling parameter is outweighed by the increased power-handling capacity. In more extreme cases a device based on the azimuthally symmetric family of circular modes may not be the best option. To achieve very high output power, there must also be high beam power as even in a strong design only around 40% of this power can be converted to microwave output. Since the beam power is dependent only on the voltage and current, one or both of these must be increased to increase the power. Simply increasing the current density within a small beam will also increase the velocity spread which can severely limit the efficiency. Therefore, when a high current is desired, it can instead be preferable to use a larger beam radius. In idealistic terms, one could use a higher $TE_{0,n}$ mode to allow a larger cavity to contain the beam, but realistically the lower modal stability and lower maximum coupling coefficients of such modes make design impractical at best, so higher than $TE_{0,3}$ is rarely attempted. Figure 5.3 shows the relative cavity radii

and peak coupling coefficient for cavities of different sizes as calculated by equation 3.13. Chapter 1 discussed some methods that have been used to get around the high-power issue, with the most widely studied being coaxial geometry, but these techniques are generally only implemented when a simpler setup cannot meet design goals.
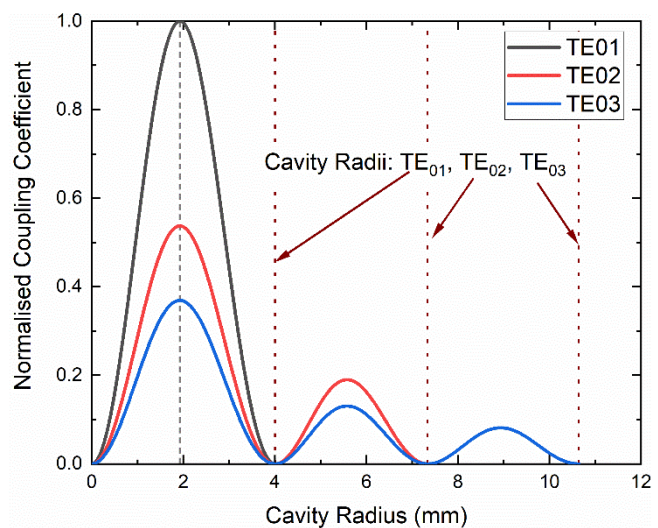

Figure 5.3

Comparison of coupling curves in different sized cavities

The first gyroklystrons were low-efficiency two-cavity designs, but the benefit of additional cavities was demonstrated soon after. With no intermediate cavities, the gain and efficiency are too low for most practical applications. Aside from the early reports on the development of the underlying gyroklystron concept, at least one intermediate cavity is used in almost all published studies and some have used as many as four intermediate cavities. The function of the intermediate cavities is to reinforce the bunching process, thus increasing the gain and efficiency. Further cavities beyond the basic three-cavity form tend to offer only a small improvement in efficiency, with the main benefit being in the gain. Ideally, the smallest number of cavities that can match the performance targets is preferable as additional cavities complicate the optimisation and manufacture. However, there can be situations where the relative merits of an additional cavity outweigh the problem of complexity. Hypothetically, a 3-cavity and 4-cavity design might show similar efficiency and output power, but the latter may display a higher gain and hence less input power demand. The choice between the two is then no longer trivial and must come down to a trade-off between several factors. The gain, efficiency, design complexity, thermal issues, length, and input power availability can all influence this decision. There are two main drawbacks to adding more cavities. The optimisation process becomes increasingly complex and time-consuming, and thermal issues in the cavities become more problematic. Each cavity stores more energy than the previous one, and the 3rd cavity of a 4-cavity gyroklystron can have as much as three times the stored energy of a 2nd cavity in a 3-cavity gyroklystron. Despite these difficulties, it can still be worth using an extra cavity if minimising the required input microwave power is a crucial goal.

The linear theory (chapter 3) can be used to make rough estimations of the performance of different arrangements. Since the linear theory is dependent on a small-field approximation, it cannot be used to study interaction at the MW-level of the final device. For linear theory to produce stable results, the power must be on the order of mW rather than MW. Since performance can vary significantly with parameters such as the input microwave power and beam current, results gathered

with linear theory are not directly transferable to real performance. The predictions are therefore simply a rough ballpark figure that suggests whether further study and optimisation is worthwhile. Three options were considered as shown in table 5.2. To find the maximum performance required sweeps across drift-tube length, cavity Q, input power, and beam current. The full description of linear theory can be found in chapter 3 and additional context on the figure in table 5.2 is presented in the appendix.

Table 5.2: Linear Theory performance estimates

Cavities	Efficiency (%)	Gain (dB)
3-cavity ($TE_{0,1}$-$TE_{0,1}$-$TE_{0,2}$)	33	30
4-cavity ($TE_{0,1}$-$TE_{0,1}$-$TE_{0,1}$-$TE_{0,2}$)	38	37
4-cavity ($TE_{0,1}$-$TE_{0,1}$-$TE_{0,2}$-$TE_{0,2}$)	24	43

Given the low accuracy of these estimates, either of the first two options could be worth considering. The better predicted performance of the 4-cavity variant is not far enough above to rule out the 3-cavity variant. An issue not accounted for in the linear model is that power increases in each subsequent cavity, so the 3rd cavity of the second design might be subject to highly problematic thermal issues at more realistic values of power. Thermal performance is a very important consideration in any microwave amplifier, especially in this case where a repetition rate of 1000Hz is desired. Based on this linear theory analysis and the success of the 3-cavity design at 36GHz [57], a 3-cavity design was initially selected on the condition that a 4-cavity alternative may be revisited should subsequent nonlinear simulations suggest limitations in the 3-cavity version's performance.

5.2: Cavity and Drift-tunnel Design

The broad discussion of the preceding section provides a foundation for the gyroklystron configuration. This section provides a deeper discussion on how to use that foundation to develop a specific design. Firstly, the process of selecting cavity dimensions and eigenfrequencies is presented. Then the beam parameters are discussed by consideration of velocity ratio, guiding field, and beam-wave resonance. Finally, the drift-tube design is discussed.

5.2.1: Determination of Cavity Parameters

When considering a gyroklystron cavity, two of the most important parameters are the eigenfrequency of the relevant mode, and its quality factor. The general physics of these properties has been presented in chapter 2. In this section, detail is provided on how to apply that general background to the design process based on the performance targets and beam parameters.

While some applications may require a high Q to maximise stored energy, this is not necessarily the case for a high-power gyroklystron. A high Q means that a high amount of energy can be stored in the cavity, which leads to increased wall-heating and may cause breakdown. Therefore, the fields in the input and intermediate cavities of a gyroklystron should not be larger than is necessary to apply effective bunching. Secondly, the fill time should be considered. Cavity fill time is defined as:

$$t_{fill} = \frac{Q_L}{\omega} \tag{5.1}$$

where Q_L is the loaded Q of the cavity. Fill time is the time that is required for the fields in a cavity to build up to $\frac{1}{e}$ of their saturation level. It is sometimes desirable to lower Q to limit the fill time [162]. especially in applications that require a fast

response or short pulsed operation. For a loaded 48GHz cavity, fill time is typically on the order of a few nanoseconds.

The selection of Q must also account for the start oscillation criteria. It must be chosen such that operation is stable without the risk of transition into an oscillation regime. If a spurious resonance is excited offset from the drive, it can ruin the interaction and lead to zero gain or violate the requirement that the device must be zero-drive stable. A typical high-power gyroklystron therefore uses relatively low-Q cavities.

The choice of eigenfrequency is not simply a case of designing all cavities to have an eigenfrequency equal to the operating frequency. The bunching quality and bandwidth can both be improved significantly by employing a degree of stagger-tuning. This is a technique based on the idea of offsetting each cavity from the eigenfrequency to enhance the frequency response. Reference [230] provides a general formalism for stagger-tuning, while in reference [231], Calame et. al describe a more specific method of selecting frequencies for input and intermediate cavities in a 3-cavity gyroklystron. To improve high frequency response, an input cavity with slightly higher eigenfrequency is used, and to counteract the effect this has on low frequency response, the second cavity has a slightly lower eigenfrequency. The estimated frequencies were calculated by equations 5.2 and 5.3 which were determined in [231] by consideration of the resonance curve of the output cavity.

$$f_1 = f_0 + \frac{f_0}{3Q_0} \qquad (5.2)$$

$$f_2 = f_0 - \frac{f_0}{Q_0} \qquad (5.3)$$

where f_0 and Q_0 are the cold-cavity frequency and quality factor of the output cavity. In this case, f_0 is also slightly downshifted from the operating frequency. This is because the hot frequency of a cavity is usually on the order of 0.5-1% higher than cold cavity frequency, so a reasonable estimate for f_0 is around 47.7GHz. Initially the estimate of $Q_0 = 100$ was taken which gave expected values for f_1 and f_2 of 47.88GHz

and 47.22GHz respectively. The calculated eigenfrequency values from equations 5.2 and 5.3 are estimates only and may still be adjusted after further optimisation.

Once the cavity frequencies are determined, the radius and length must be chosen. Based on the cylindrical cavity eigenmode equation, there is a wide range of radii and lengths that would display the correct mode at the desired frequency. During the first steps of design, it is practical to use a closed-cavity approximation. With this approximation, one can estimate the desired combination with consideration of the cut-off radius and reasonable beam guide radius. It is then simple to calculate the corresponding length that gives the correct frequency for the choice of radius. Alternatively, an estimate for the optimal output cavity length is that it should be on the order of $(s\beta_\perp^2)^{-1}$ where s is the harmonic number and $\beta_\perp$ is the normalised perpendicular velocity [126]. This is only an estimate, however, and the chosen geometry may differ somewhat following optimisation.

The cut-off radii for the $TE_{0,1}$ and $TE_{0,2}$ modes are 3.81mm and 6.97mm respectively. It is generally good to have a cavity radius slightly above cut-off, as this limits the number of modes available to compete with the operating mode. The ideal pairing of length and radius is that which places the beam in line with the maximum coupling coefficient (section 3.1). Rather than the exact alignment of these radii, there should be a slight offset to account for the distance at which electrons orbit the guiding centre. The optimal guiding radius is estimated by:

$$r_g^2 = r_{Cmax}^2 - r_L^2 \qquad (5.4)$$

where r_{cmax} is the radius of the maximum coupling coefficient and r_L is the Larmor radius. Figure 5.4 displays the relative size and alignment of the coupling maximum and beam guiding centre.
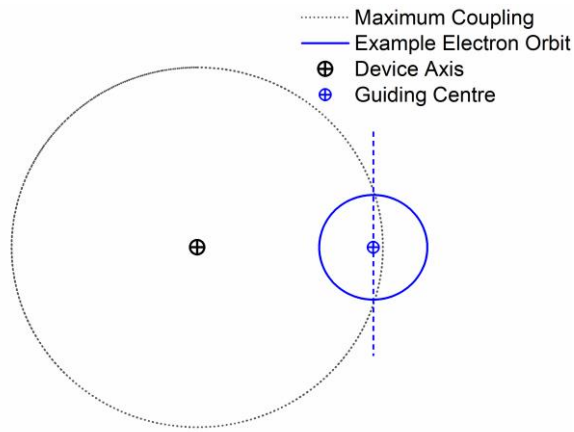
Figure 5.4
Relative radii of peak coupling position and electron orbits

The curves shown in figure 5.5 display the variation of the coupling coefficients (equation 3.13) for $TE_{0,n}$ modes (n=1:4) of an arbitrary 48GHz cavity with fixed dimensions. The coupling coefficient is normalised to its maximum value for a $TE_{0,1}$ mode, As the coupling coefficient depends on the ratio of r/r_c and not on r_c independently, it has the same maximum values (C_{01}=0.1422, C_{02}=0.0764) whichever combination of cavity length and radius is chosen.

Figure 5.5
Variation of coupling coefficients for azimuthally symmetric modes in a cylindrical cavity

127

The maximum value of the coupling coefficient decreases at higher order modes and the first peak of each mode is always its largest. For $TE_{0,n}$ modes the first maximum always occurs at the same normalised radius, marked in figure 5.5 by the dotted vertical lines.

Generally, the highest coupling coefficient is desired, but the lower value at higher modes does not exclude them from consideration, as other design criteri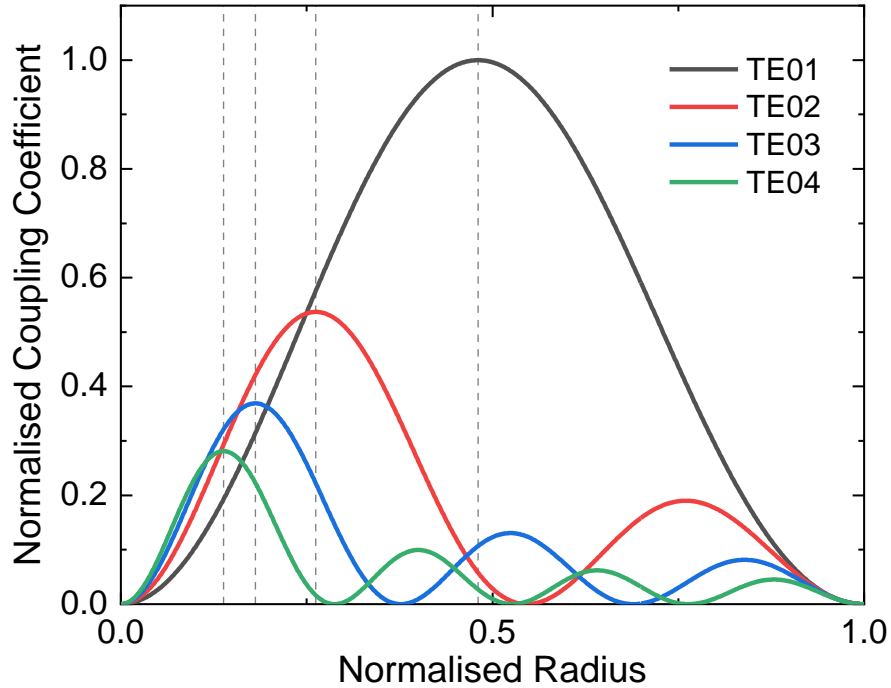a such as the power handling capacity may outweigh the issue of weaker coupling. Consideration of these calculations alone only demonstrates the mathematically ideal beam radius, saying nothing about the practicality of this value. It is of course important to also consider what is technologically achievable with the MIG cathode, as discussed in chapter 3. It is sometimes appropriate to use a higher order coupling maximum if the first has too small a radius to be practical (for example, $TE_{0,3}$ devices often use the second maximum), but this also costs efficiency and may place the beam too close to the drift-tube walls.

Figure 5.5 illustrates the coupling of different modes in the same cavity. If instead the coupling curves for each mode are considered in separate cavities of different sizes, it is clear that it is possible to have a cavity of a certain mode at one radius, and then a cavity of a different mode at a different radius such that the maxima of their respective coupling coefficients occur at the same radius. The frequency can then be made to match by adjustment of the cavity length, allowing for efficient bunching in a $TE_{0,1}$ input and intermediate cavity, and efficient interaction in a $TE_{0,2}$ output cavity in the same device. Since the maximum value of the coupling coefficient for a $TE_{0,1}$ cavity is at $0.481r_c$ and for a $TE_{0,2}$ cavity it is at $0.263r_c$ for any values of r_c, it is simple to calculate the relative radii. Comparing these numbers, the relative radii should be $r_{c1} = 0.547r_{c2}$. Now combining consideration of the stagger tuned frequencies, the slight offset between beam radius and coupling maximum, and the coupling curves,

the cavity sizes can be better estimated. Figure 5.6 shows the coupling coefficient in each cavity, with the radial dimension normalised to the guiding centre radius.
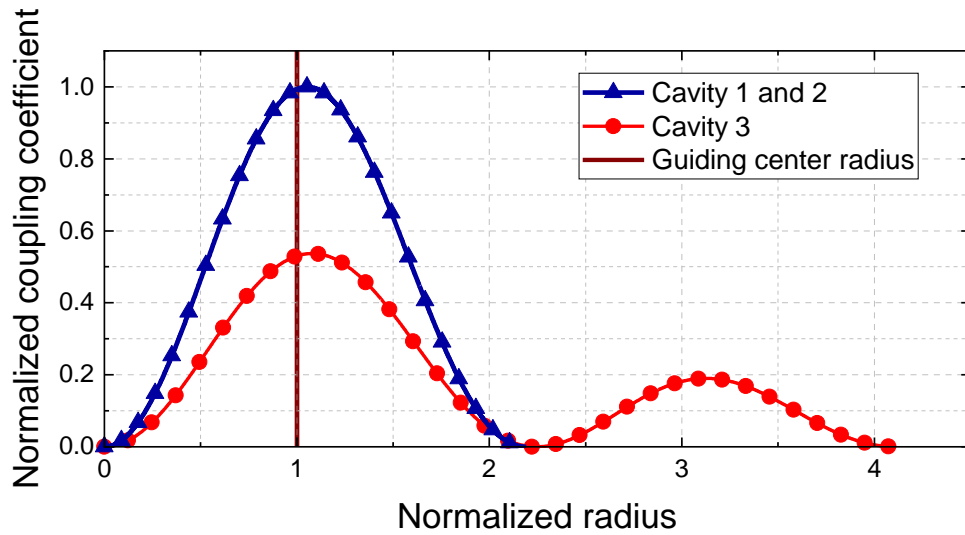
Figure 5.6
Coupling curves of a $TE_{0,1}$ and a $TE_{0,2}$ cavity of compatible radii

All the dimensions that have been discussed here are estimates and are based on the closed-cavity approximation. While some adjustment of geometry is required to account for the drift-tunnels and possible dielectric linings, the approximation is a suitably close estimate for the input and intermediate cavities. After the frequency and initial geometry are decided, these cavities can then be studied using more advanced simulations. In this case, the eigenmode algorithm in MAGIC was used. Based on simulation results, dimensions can then be adjusted to correct for the presence of the drift-tubes and dielectric linings. The output cavity's open-ended shape has a more significant effect on its eigenfrequency, making the closed-cavity comparison less accurate. MAGIC is not as well-suited to this specific case, and it must instead be considered with a non-linear model of the cavity.

Due to its open-ended geometry, the output cavity in particular requires additional analysis as it differs more than the others from the closed-cavity approximation. Figure 5.7 shows an example geometry for an output cavity with relevant dimensions labelled.
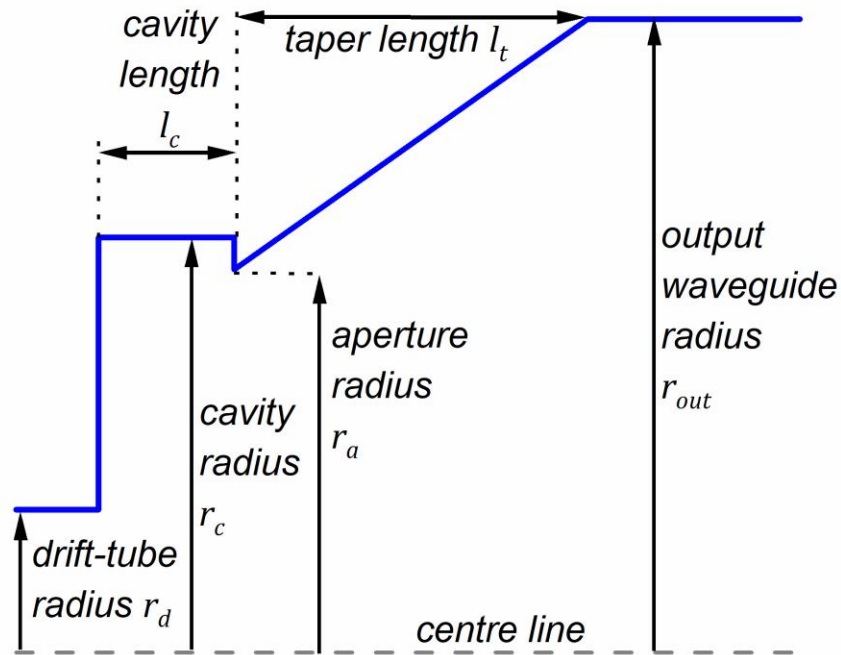
Figure 5.7
Relevant dimensions of an example output cavity

MAGIC is not well-suited to the modal study of cavities of this shape, so nonlinear methods were used in MATLAB. The code used was a subsection of a non-linear code developed by Wang et. al [57] for study for the entire interaction system. In this code, the complex shape of the output cavity is analysed with the mode-matching technique presented in reference [232] and the references therein. In this method, steps in the cavity structure are treated by scattering matrices which are then cascaded to form left and right matrices from which the eigenvalue equation can be obtained. The eigenvalue equation is then solved through a 2-dimensional search in complex frequency. The method can produce accurate results for the Q and resonant

frequency in complex cavities with both steps and smooth tapers and is therefore very well-suited to the consideration of the gyroklystron output cavity.

Keeping the cavity length and radius constant, the variation of Q was examined. Firstly, the output taper was considered. The cavity Q fluctuated by about ±3 as the final output waveguide radius was optimised. Slightly smaller variations in Q were observed as the angled section's length was adjusted. This result is as expected and as is desirable. The lack of sensitivity to the geometry of the taper and output waveguide simplifies matters such that one is able to adjust the output section for better handling of beam collection and output radiation without having any unwanted side-effects on the cavity performance.
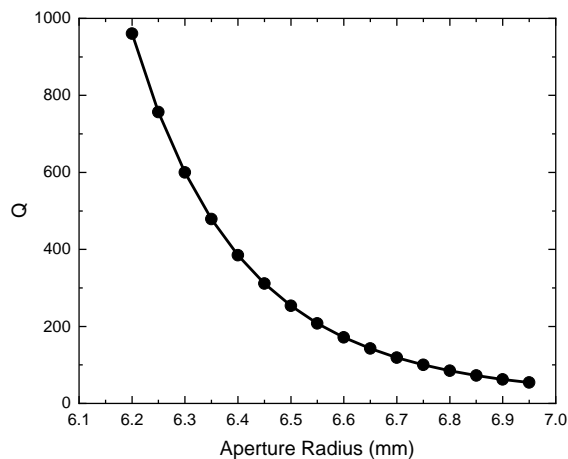
Figure 5.8
Variation of Q with aperture radius

A much larger variation of Q was observed when the aperture radius was altered as shown in figure 5.8. As there were no lossy dielectric linings used in this cavity and the walls are highly conductive, the diffractive component of Q is dominant. Although the ohmic contribution would vary slightly as the total surface area of the walls changed, this effect is negligible when considered alongside the much larger diffractive contribution. Therefore, the assumption of perfectly conducting walls in the simulation is valid. The aperture adjustment also had a minor effect on the resonant frequency, causing a reduction of about 0.8% of the original value over the range of the dataset.

5.2.2: Determination of Velocity Ratio and Magnetic Field

A high-velocity ratio leads to a high efficiency, but also requires a high compression ratio, which is associated with high velocity spread (section 4.1). The increased velocity spread could then counteract any potential improvement to efficiency. Too low a value of velocity ratio will fail to deliver the required interaction efficiency, while above a value of around 1.5, many back-streaming electrons were observed. Therefore 1.35 was selected as compromise between the two extremes. It is high enough to enable good efficiency, but low enough to avoid overwhelming spread issues.

The magnetic field is then chosen with consideration of the resonance condition of the beam-wave interaction. Figure 5.9(a) illustrates the shape of the dispersion diagrams. The hyperbola is the dispersion curve for a cavity mode. The velocity of light lines are the asymptotes of this curve. The solid straight line is the dispersion line of the beam. The cavity mode, beam, and light dispersion lines are respectively described by the following equations:
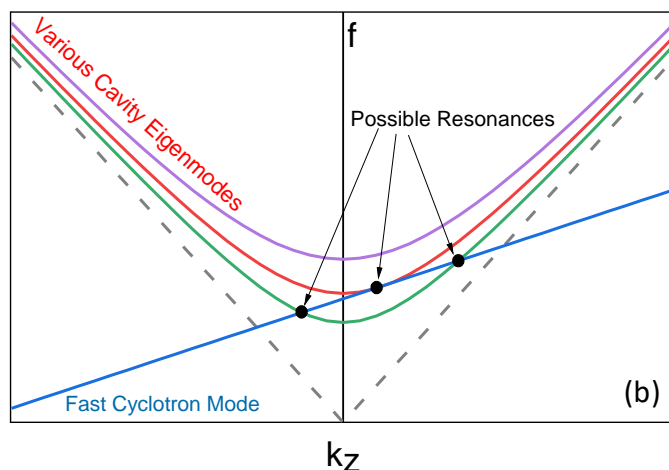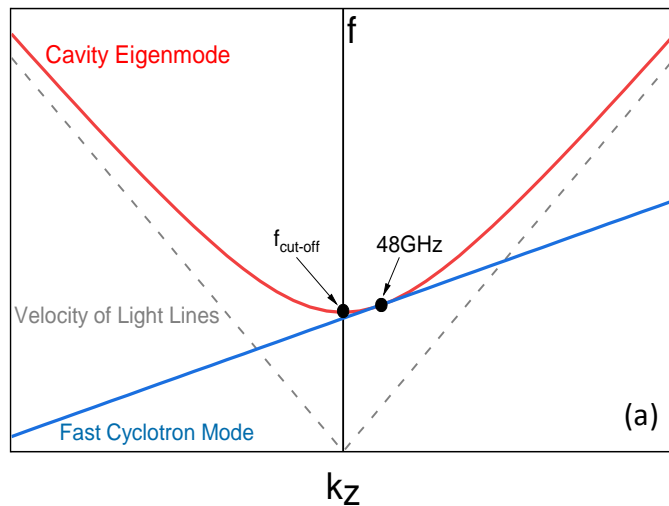

Figure 5.9
Beam-wave interaction resonance.
(a) Tuning to the mode of interest
(b) Consideration of other potential resonances

$$\omega = c\sqrt{k_z^2 + k_\perp^2} \tag{5.5}$$

$$\omega = k_z v_z + s\omega_c \tag{5.6}$$

$$\omega = |k_z|c \tag{5.7}$$

The beam dispersion line can be adjusted by controlling the magnetic field B, and the velocity ratio α. Tuning over B (which means adjusting the cyclotron frequency as per equation 2.7) raises the position of the beam dispersion line, while tuning over α can be used to adjust the gradient. As the velocity ratio of 1.35 was already selected, the magnetic field was the tuning parameter here. Using a simple MATLAB script, a 2.02T field and a velocity ratio of 1.35 were observed to create the desired resonance condition at 48GHz in the output cavity. This corresponds to a cyclotron frequency of roughly 44.3GHz. Figure 5.9(a) is simplified to show only a single mode, as the resonance was tuned to match a single desired mode. Figure 5.9(b) shows a range of modes, illustrating that the cyclotron mode can also meet the resonance condition with other lower order modes. In general terms, figure 5.9(a) describes any arbitrary collection of modes. In the specific case of this gyroklystron, a $TE_{0,1}$ resonance is desired and the relevant lower mode is the $TE_{1,1}$. The leftmost resonance in figure 5.9(b) is the backward-wave interaction, but if any $TE_{1,1}$ was excited it would be cut off in the beam tunnels and would not propagate. The rightmost point is a travelling-wave interaction, which typically has a weaker beam-wave coupling than the main resonant mode, especially with the level of velocity spread observed in this case. The risk of problematic excitations at these points is also reduced by several factors. The resonance points with the $TE_{1,1}$ mode occur far away from the operating frequency, the coupling coefficient for the $TE_{1,1}$ mode is low at the position of the beam radius, and the beam current is lower than the oscillation start-current as defined in equation 3.14.

5.2.3: Drift-tunnels

The drift-tunnels must be designed with the strict requirement that no oscillation occurs within them, and that no microwave energy from the cavities is carried along them. If this requirement is not fulfilled, then at best the performance of the device will greatly suffer and at worst it will completely prevent the interaction from functioning as intended. The simplest measure against this is to set the drift-tube radius below cut-off for the relevant mode, preventing radiation from travelling. In extreme cases where total cut-off is impossible, additional dielectric inserts can be used to absorb leaked radiation. Since the cavity itself is designed to be just above cut-off in this case, keeping the drift-tube radius small as possible. The drift-tube in this gyroklystron is therefore limited only by the obvious requirement that the electron beam must be able to propagate through it. The average guiding centre radius is 1.77mm, and the Larmor radius is 0.53mm. To leave some space, the drift-tunnel radius was set to 2.5mm.

An initial estimate for lengths of the drift-tunnels is that the drift region between cavities 1 and 2 should be around four times that between cavities 2 and 3. The final drift lengths may differ from this estimate after some trial and adjustment using linear and nonlinear theory analysis. Using the nonlinear code, parameter sweeps were performed to compare different combinations of drift-tunnel lengths leading to the choice of 20mm and 7.2mm respectively.

Chapter 6: Gyroklystron Simulation Results

This chapter presents the main design results for the interaction circuit, while the other components (coupler, windows, and collector) are presented in chapter 7. Figure 6.1 presents a schematic overview of the system for illustrative purposes only. It does not represent exact scale and several of the components shown were studied in separate simulations.
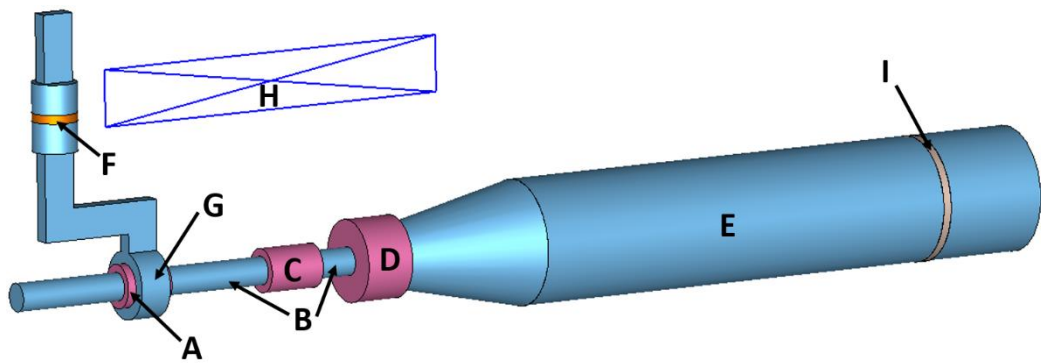

Figure 6.1
Schematic of gyroklystron
Cavities are highlighted in pink.
A – Input Cavity, B – drift tubes, C – intermediate cavity, D – output cavity, E – collector and output waveguide, F – pillbox-type input window, G – coaxial input coupler, H – solenoid, I – single-disc output window

6.1: Analysis of Cavity Designs

6.1.1: Cavities with Drift-Tunnels and Dielectrics

To better inform the gyroklystron design process, several simulation studies were carried out to observe the influence of various features of the cavities. An important part of the cavity design is the dielectric lining on the outer wall, which helps to reduce Q to the target value and suppress unwanted modes. However, it also alters the eigenfrequency away from that of the closed-cavity approximation. Therefore, this study provides an important comparison to assess the validity of the use of that approximation and provides an idea of how much the final dimensions may deviate from the initial approximation. Figure 6.2 shows the variation of the frequency at which MAGIC found a $TE_{0,1}$ mode in a fully closed cylindrical cavity. The cavity dimensions were chosen to match those of the 36GHz gyroklystron design [57] as a convenient reference point, but the result is mainly to illustrate general trends rather than to directly inform design choices and hence the decision of specific cavity dimensions is arbitrary.
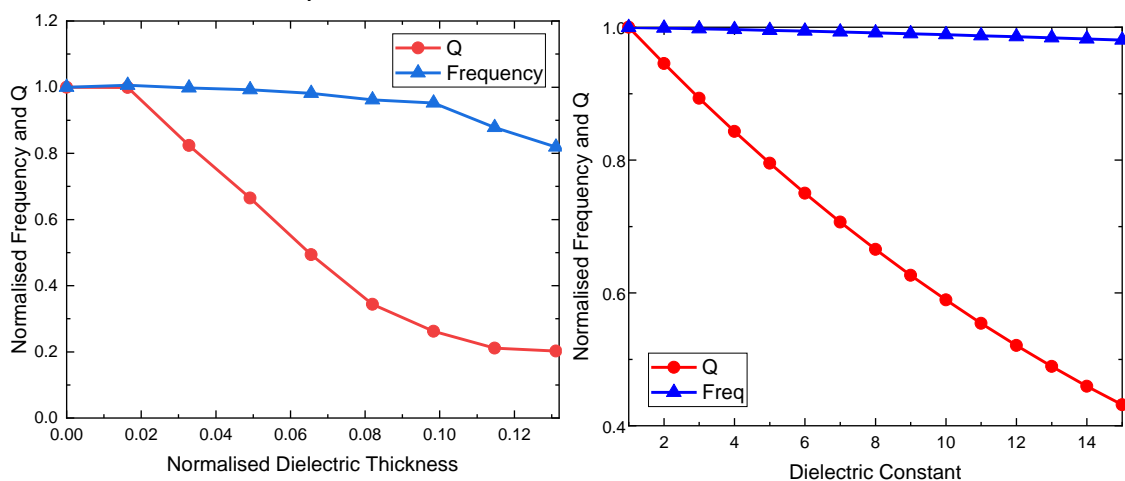

Figure 6.2
The effect of dielectric thickness (left) and dielectric constant (right) on the cavity frequency and Q

The eigenfrequency and Q are normalised to their values in an empty cavity of the same dimensions (15000 and 36.7GHz), and the dielectric thickness is normalised to the cavity radius (5.45mm). When varying dielectric thickness, the dielectric constant

was fixed at 12 and when varying the dielectric constant, the dielectric thickness was fixed at 0.3mm. The Q here is the wall loss Q, which is calculated as part of the Magic Eigenmode algorithm. The walls use the default conductor properties of the MAGIC input, which match those of copper. Local power loss at the wall scales with how far into the material the fields can penetrate [218]:

$$\frac{dP_{loss}}{dA} = \left(\frac{\omega\delta}{4\mu_0}\right)|B_{tan}|^2 \qquad (6.1)$$

where B_{tan} is the tangential magnetic field component and δ is the skin-depth (equation 2.20). Since copper has a very high conductivity and hence a very small skin-depth, wall losses in this study are mainly due to the dielectric. The frequency was observed to fall off very slowly at first, and then more quickly. The Q initially dropped off steeply. The Q curve then approaches a minimum value. Beyond the range shown in figure 6.2, the Q began to rise with a slow linear trend, but in that region the eigenfrequency had also fallen very far from its original value. As Q is also dependent on frequency, the results may not be strictly comparable at such different frequencies. A cavity so far offset from the specified frequency is not useful to the gyroklystron design, so only the displayed region of the graph holds relevant meaning, as this is where the frequency is still within reasonable proximity of the initial value. The initial reduction in Q is much faster than that in frequency, so a thin dielectric can give strong control of Q while having only a small effect on frequency. The results suggest that a dielectric thickness greater than around 10% of the cavity radius would cause a significant drop in cavity frequency. In principle, the dimensions of the cavity could be adjusted to show the correct frequency, but given the importance of keeping radii compatible between different cavities, it is more practical to use thinner linings where possible, as changing radius in one cavity may demand a change in the radii of the other cavities.

Also shown in figure 6.2 are the results for the frequency and Q of a cavity when adjusting the dielectric constant ε_r. For this, the cavity and dielectric dimensions were kept constant. Over the tested range of $\varepsilon_r = 1$ to 15, there is only a drop of around 2% in frequency, while the Q falls off by almost 60%. This means very little adjustment

of cavity dimension needs to be made to maintain the correct eigenfrequency if the dielectric properties are changed, giving good control over Q. Although the material science is advanced and materials with specified properties can be produced, it is generally preferable to use something readily available, rather than create an expensive individual demand for a non-standard composition. Several materials have seen use in cavity design, as described in section 2.1.4.

Next, the effect of the presence of drift-tubes was studied. The variation of the eigenfrequency with increasing drift-tunnel radius was observed. It was recorded that even when drift tube radius exceeded 80% of the cavity radius, only a 4% reduction in eigenfrequency was observed, as shown in figure 6.3. This observation, along with those for

Figure 6.3
Variation of cavity eigenfrequency with drift-tube radius

the dielectric studies, justifies the use of the empty closed-cavity approximation in initial design work.

Although the results discussed in this section confirm that the approximation error to be small, they also show it to be non-negligible. While approximations are very useful for initial design stages, it is shown here that before the subsequent stage of optimisation, each cavity must be considered one by one to correct for the small errors of the approximation. This can be done through individual examination of each cavity in MAGIC.

6.1.2: Analysis of Gyroklystron Cavities

Estimates for the dimensions of the other cavities were found as discussed in section 5.2.1, and then the eigenmode script in MAGIC was then used to correct for the approximation error. The field pattern in the input cavity is shown in figure 6.4, illustrating the desired pattern of a $TE_{0,1}$ mode in the cavity and no excitation in the drift-tunnels. Increasing the mesh density was observed to have minimal effect on the result (~0.2% shift in calculated eigenfrequency at double mesh density) while increasing simulation time to an extent that would be impractical for the subsequent studies of the full interaction circuit.
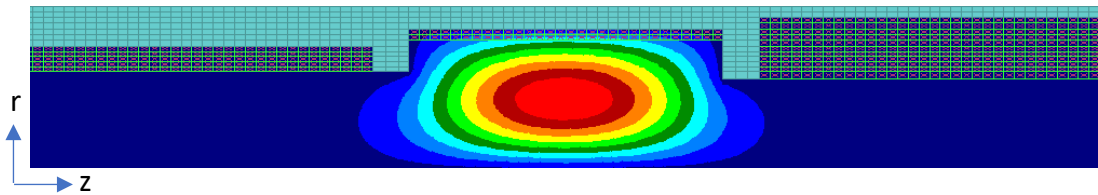
Figure 6.4
Eigenmode in input cavity

The general trends of how the cavity dimensions, dielectric linings, and drift radii affect the eigenfrequency and Q are known, so it was a case of educated trial and error to home in on the desired parameter. To correct the frequency required a small change in radius as the change in length to gain the same effect would have made for an impractically short cavity. To maintain appropriate alignment of the average beam guide radius and the radius of maximum coupling coefficient, the second cavity was restricted to the same radius as the first cavity. This required a moderate lengthening of the cavity to a length of 10.2mm to maintain the correct frequency. After these studies, a set of selected dimensions was obtained, as shown in table 6.1.

Table 6.1: Cavity parameters

Cavity	Length (mm)	Radius (mm)	Eigenfrequency (GHz)	Q
1	8.66	3.88	47.86	180
2	10.2	3.88	47.22	180
3	9.3	7.28	47.7	100

6.2: Gyroklystron Simulation Results and Optimisation

The design of a gyroklystron is a complex task due to the large number of free parameters. As performance depends on the parameters of the beam, the cavities, and the fields, extensive optimisation is needed to create a good quality design. This optimisation, however, requires computationally intensive and time-consuming simulation work. The better the starting point, the more this issue is alleviated. Therefore, it is beneficial to begin with quicker analytical tools such as linear theory which was described in chapter 3. The results of these models, while far from perfect performance predictions, can offer a far superior starting point for the PIC simulation and save a lot of time compared with starting with PIC from scratch. The process of how the gyroklystron geometry was obtained has been described in the preceding chapters. In this section, the results of PIC simulations are presented, including the initial confirmatory simulations, followed by broad parameter sweeps to assess performance.

Figure 6.5 shows an example of the simulation set-up. The beam is generated with the properties specified in an emission command. For the initial simulations, an ideal beam (zero velocity spread) is used, while the effects of spread are discussed later in the chapter. For measurement purposes, a non-physical object (labelled E in figure 6.5) is defined in the simulation to perfectly absorb all incoming radiation. Note that in subsequent figures the drift-tube dielectric linings and the absorber are hidden for sake of clarity and to more accurately represent the physical device. The magnetic field profile is created by the definition of coils representing a solenoid creating a stead 2.02T field over the interaction region, which then falls off over the output waveguide region.
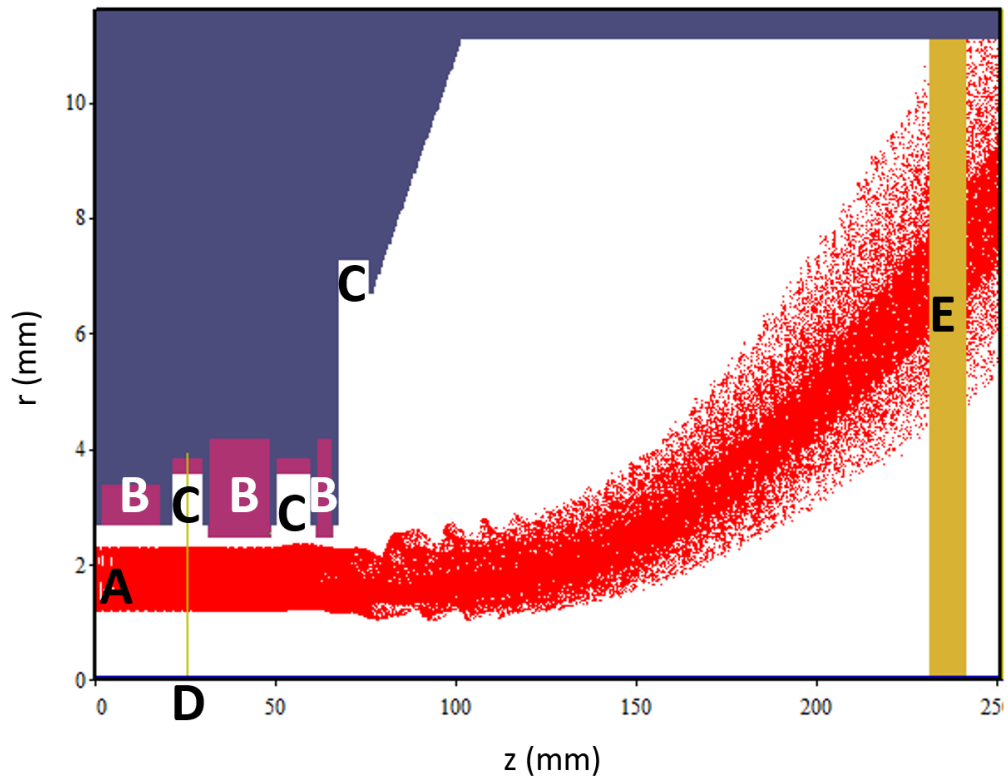
Figure 6.5
Overview of MAGIC simulation model
Blue = copper; purple = dielectric; white = vacuum; red = electrons (macroparticles) ; yellow = non-physical simulation objects for excitation/measurement
A – beam generated with specified properties, B – beam tunnel with dielectric layer, C – cavities; input and intermediate feature dielectric linings, D – drive signal artificially induced on area of vacuum, E – non-physical geometric object for measurement purposes.

6.2.1: Initial Gyroklystron Simulation

Simulations were performed, featuring the cavities together and using a beam with ideal properties. The beam in these simulations is emitted with the desired properties from a flat surface at the simulation boundary, rather than using a realistic cathode. This choice is necessary to maintain a reasonable runtime for broad parameter sweeps. A 140kV, 30A beam with no velocity spread was used with a 2.02T guiding field. The velocity ratio was 1.35. The operating parameters used were selected based on a combination of results from the analytical study, linear theory, nonlinear theory, and comparison to existing similar designs, as discussed in the previous chapter. The

cavities had dimensions with the parameters listed in table 6.1 and the drift tube lengths were 20mm and 7.2mm respectively.

The initial simulation of the gyroklystron in MAGIC was able to achieve 1.5MW of output power, reaching a steady rate of output after 15ns as shown in figure 6.6.
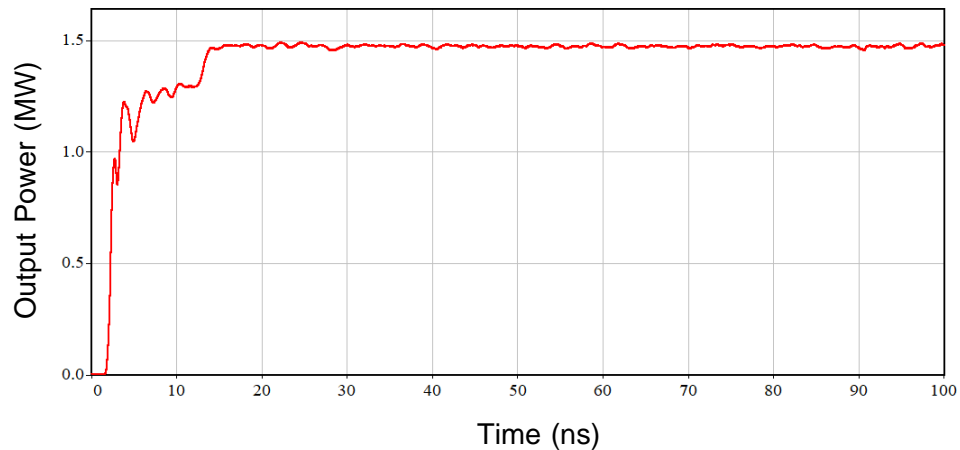
Figure 6.6
Output power of initial gyroklystron test

To illustrate the power transfer between the beam and cavity, a plot of the relativistic factor along the device length is shown in figure 6.7.
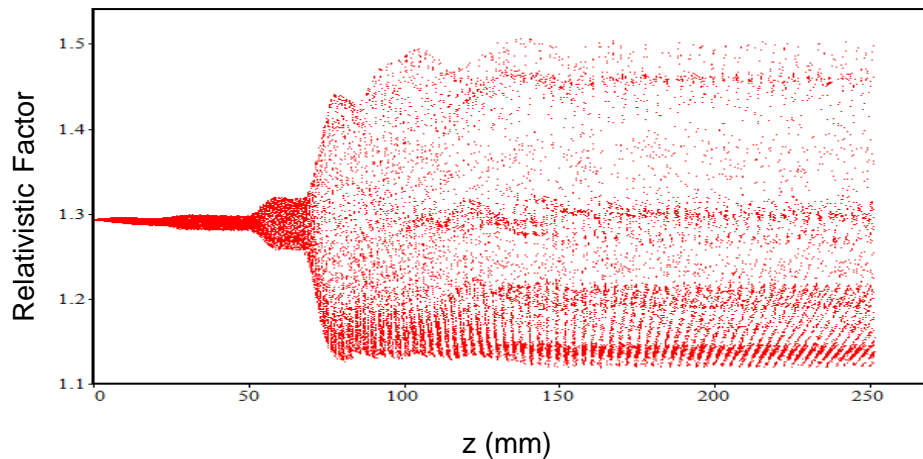
Figure 6.7
Variation of relativistic factor along device length

The position z = 0 is the position of beam-generation in the simulation. Over the course of the interaction circuit, it can be observed that the range of γ values increases. At the position of the output cavity, a large portion of the electrons lose energy as shown by the corresponding drop in γ. Since perfect bunching is impossible,

142

there is some range of final energies. A large proportion of electrons are bunch around the desired phase resulting in the main band in the bottom of figure 6.7. Another band can be seen close to the starting value of γ and another at a higher value. These respectively correspond to electrons that experience low-field phases and decelerating phases opposite the main bunch. Comparing the average value of γ at the start and end of the device is one method of calculating the interaction efficiency (equation 2.10), but since the MAGIC method measures output power directly, it is simpler in this case to calculate the interaction efficiency by comparing the output power with the beam power. The interaction efficiency in the initial test run was slightly above 28%. For this initial proof-of-concept test, a semi-arbitrary input power was used. The output power can be improved by increasing the input power until a saturation level is reached, so the initial result of 1.5MW was expected to be somewhat below the highest achievable output power. To improve the efficiency and power output to the 2MW requirement, the beam voltage, beam current, detuning parameter, drive frequency, beam radius, and input power can all be considered. Multiple parameter sweeps were carried out to test the gyroklystron performance and identify a parameter set that provides strong performance, as described in the following section.

6.2.2: Parameter Sweep Results

The beam current is the most obvious tuning parameter to consider when looking to enhance power output because it would mean there was more available beam power for interaction. However, since the MIG cathode and velocity spread place limitations on current, there is not much room to increase it, but even the modest increase from the initially selected 35A to 37A enhanced the gain and output power. For this new current, the input power was gradually increased over a wide range, resulting in the trend shown in figure 6.8.
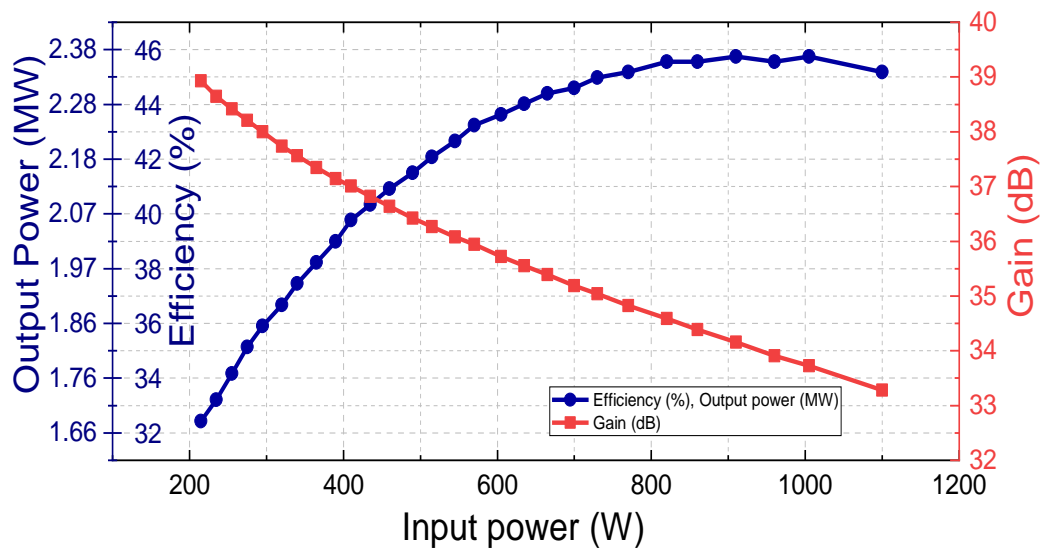
Figure 6.8
Variation of output power and gain when input power is increased

Increasing input microwave power does not linearly increase output power. The relative benefit of each additional portion of input power reduces as it is increased. For example, when the input power was ~300W the output power was 1.9MW. Then for an input power of ~600W, the output power was 2.3MW − in this example, doubling the input power showed only around a 20% increase in output power. The rate of increase in gain continues to shrink, up until the saturation value which occurs at an input power of 910W, resulting in a saturated gain of 34dB and an output power of 2.4MW. The input power of 605W was selected as the value above which further increase offers too little benefit to be considered worthwhile. At this value, the

performance characteristics are an output power of around 2.3MW, a gain of 36dB, and an efficiency of 44%.
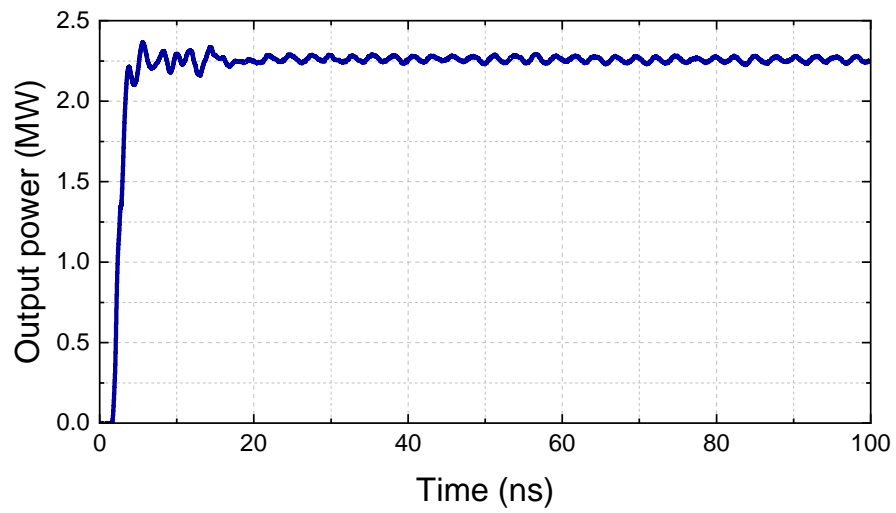
Figure 6.10
Variation of output power over time
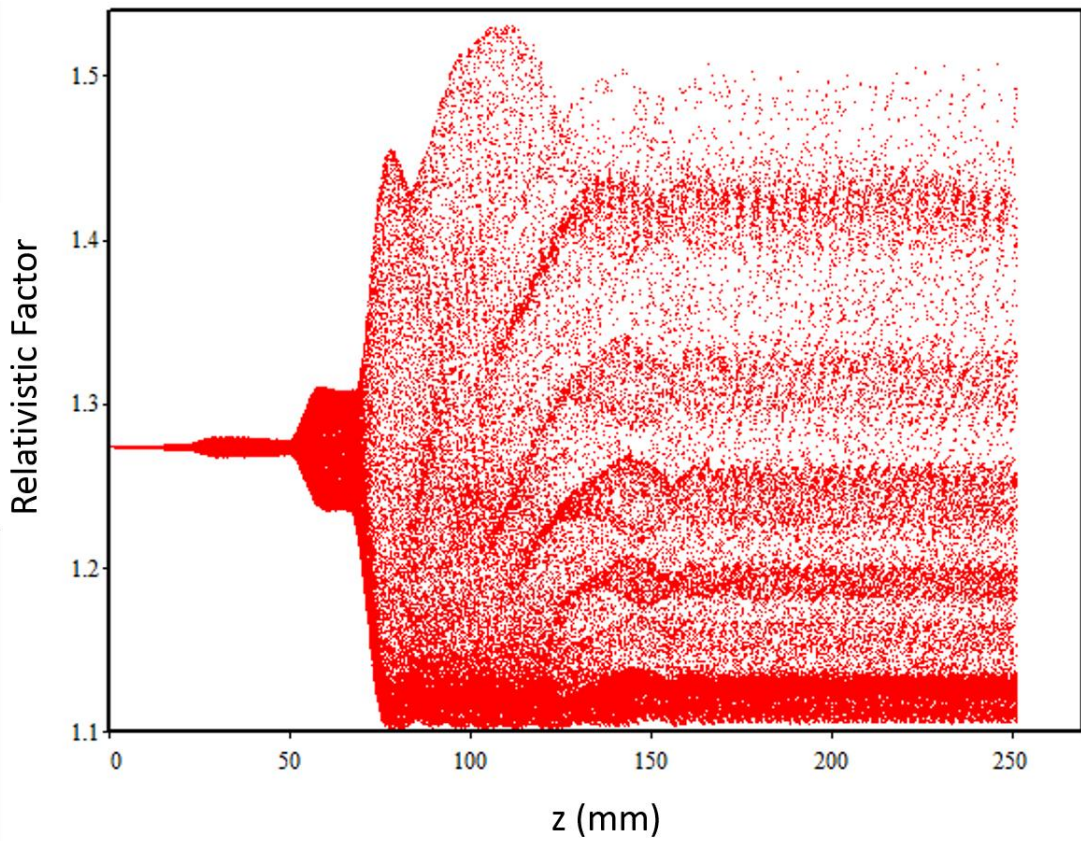
Figure 6.9
Variation of relativistic factor along device length

The plot of the output power over time in figure 6.9 shows that it takes around 5ns to rise to the operating power. After around 15ns, the output power has settled on a reasonable steady value of 2.26MW, with small fluctuations on the order of 2% which are caused by the time-varying beam emission in MAGIC.

Figure 6.10 shows how *y* changes as the electron beam passes through the interaction circuit. The general trend is much like that observed in figure 6.6, but in this case the improved selection of powers shows a larger reduction in *y,* thus showing the higher efficiency of the interaction compared with the earlier lower current version.

The trajectories electrons through the interaction region was also observed to check that there are no unexpected anomalies, such as deposition of charge on the tunnel walls. The trajectories are shown in figure 6.11, where it can be seen the beam passes through at a fixed radius before power extraction in the output cavity and deposition on the collector. This confirms the correct beam trajectory.
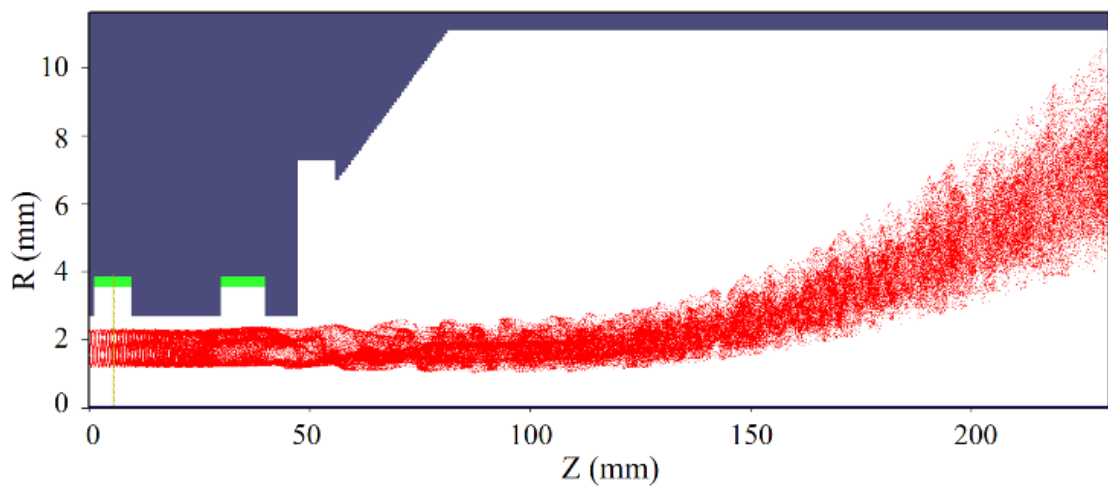
Figure 6.11
Electron trajectories through the interaction circuit

Figure 6.9 showed only the power of the output wave, but it is important to also assess whether the outgoing wave is in the correct form. This is done by observing the Fourier transform, as shown in figure 6.12.
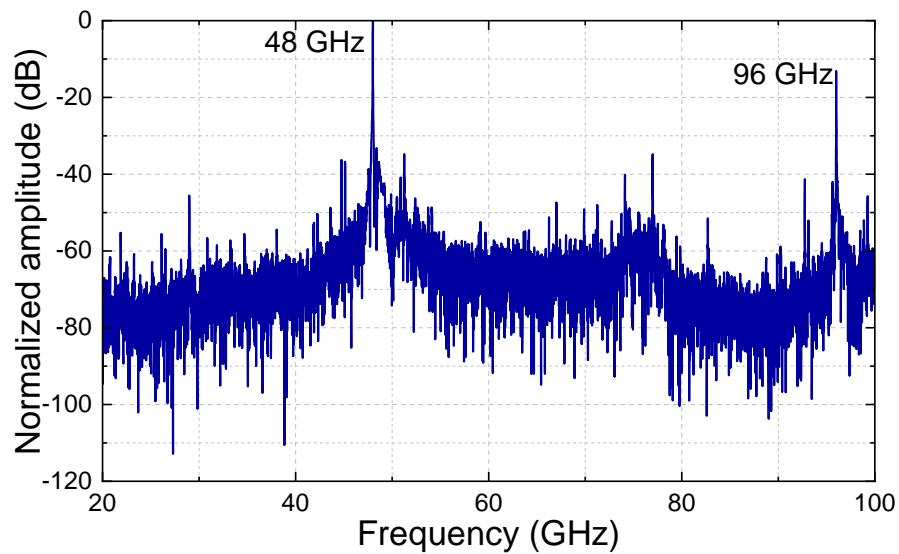
Figure 6.12
Fourier transform of output signal

A secondary peak can be seen at 96GHz, which is the second harmonic of the output frequency. The square ratio of amplitudes for the fundamental to second harmonic components is 21. This value, though not exceptional, is high enough that it will not majorly impact the performance of subsequent mode-conversion and pulse compression devices. Another factor to consider with the output mode is the potential power loss due to the magnetic component of the outgoing wave. A changing magnetic field in a conductor induces loops of electrical current known as eddy currents. The eddy currents cause some heating of the walls. It was found that with 2MW of output power in the $TE_{0,2}$ mode, the maximum H-field at the wall of the output waveguide is around $1.85\mu Am^{-1}$. In this case, the wall is copper with a very high conductivity which means the skin depth will be small thus limiting the formation of eddy currents. The $TE_{0,2}$ mode can propagate with low loss along the output waveguide of the gyroklystron before mode conversion and pulse compression.
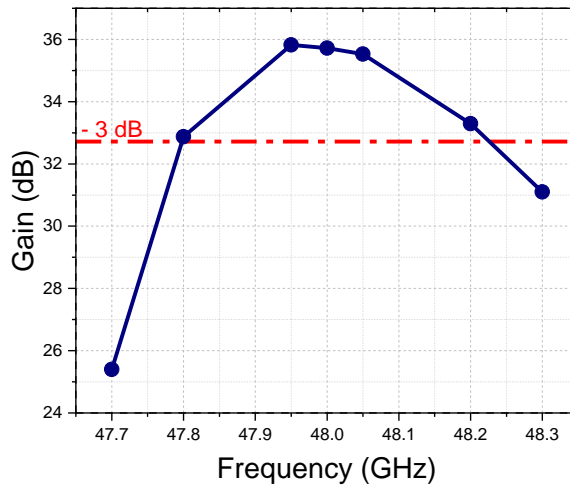
Figure 6.13
Variation of gain with drive frequency

As discussed in section 5.1.1, the bandwidth is another very important parameter. To measure it, the gain of a range of frequencies centred around the actual operating frequency can be considered. This analysis is shown in figure 6.13, where several different frequencies of driving power were simulated, resulting in a bandwidth reading of approximately 400MHz, well above the 200MHz minimum requirement for the pulse compressor.

The parameter set described above meets the performance targets with an ideal beam. Although it is useful to consider the optimal case, the true performance will be slightly reduced from that described above. A realistic electron beam always has some level of velocity spread, which is known to impact performance. While many contributions can be limited as shown in the MIG analysis in chapter 4, it is impossible to have a zero-spread beam. Figure 6.14 displays the predicted output power as a function of the axial velocity spread. It is also useful to consider the spread of the velocity ratio, rather than just the velocity. Figure 6.15 displays this trend. The optimised MIG had an α-spread of 8.9%, and hence the expected gyroklystron output power is 1.97MW as shown in figure 6.15.

148
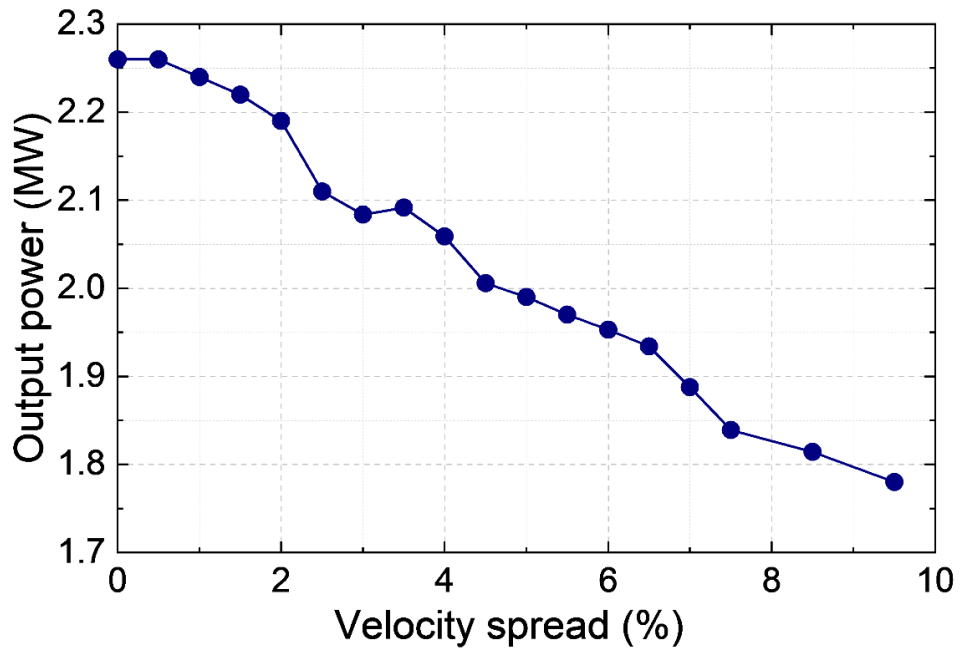
Figure 6.14
Impact of velocity spread on the output power
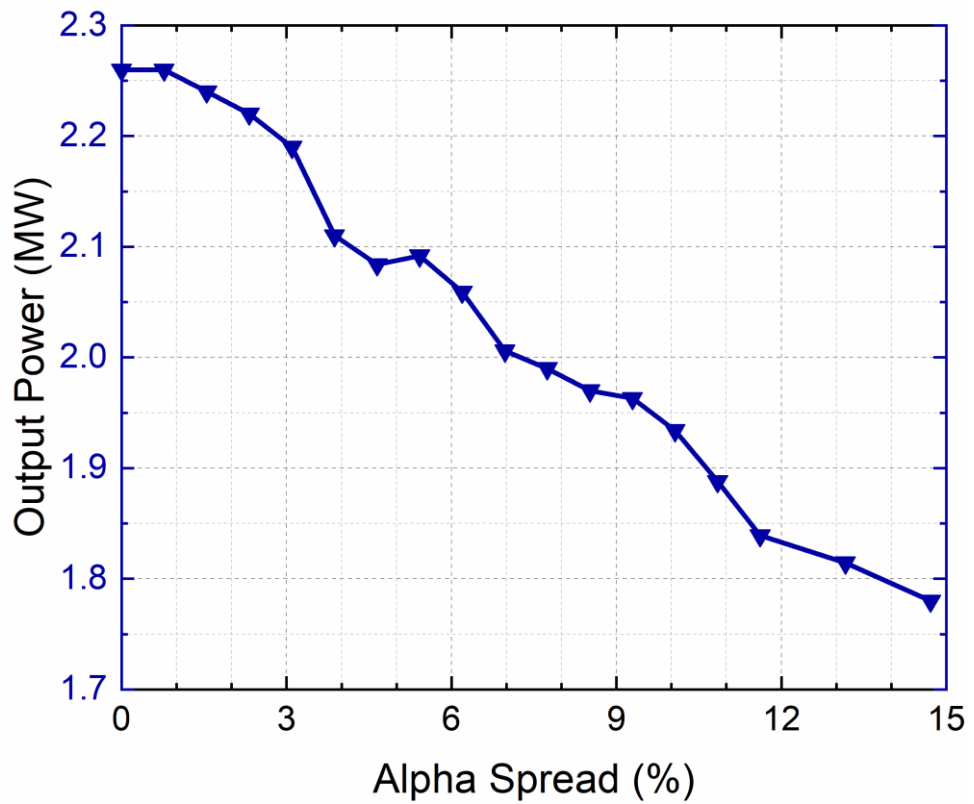
Figure 6.15
Impact of Velocity Ratio Spread on the output power.

6.2.3: Limitations on Beam Current

Figure 6.16 displays the trend that the predicted output power continues to rise roughly linearly as the beam current is increased. This data agrees with the expectation that increasing current is the most direct way to improve power output.
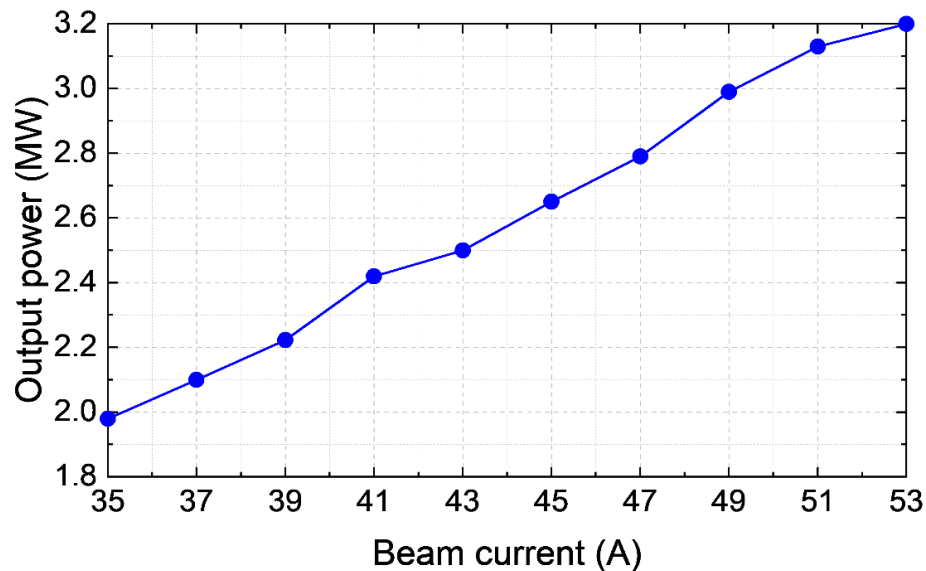
Figure 6.16
Variation of output power with current

However, in practical terms one cannot simply increase the current indefinitely. As discussed in chapter 4, there are limitations based on the cathode and the MIG geometry. There are also some details of the interaction circuit that limit the maximum usable current. The oscillation start-current is a very important parameter as the gyroklystron must operate with no risk of spurious excitations. If the gyroklystron falls into an oscillation regime, it would ruin the interaction process and zero-drive stability requirement. The start currents for modes near the operation parameters are shown in figure 6.17, which shows that the operating value sits safely below these limits. Figure 6.18 shows how the start current varies with the velocity ratio. In each of these figures, the start current was calculated using equation 3.14. Close to the selected value the start current does not deviate much, and thus the operation can be expected to remain stable if there is any deviation from the chosen parameter.
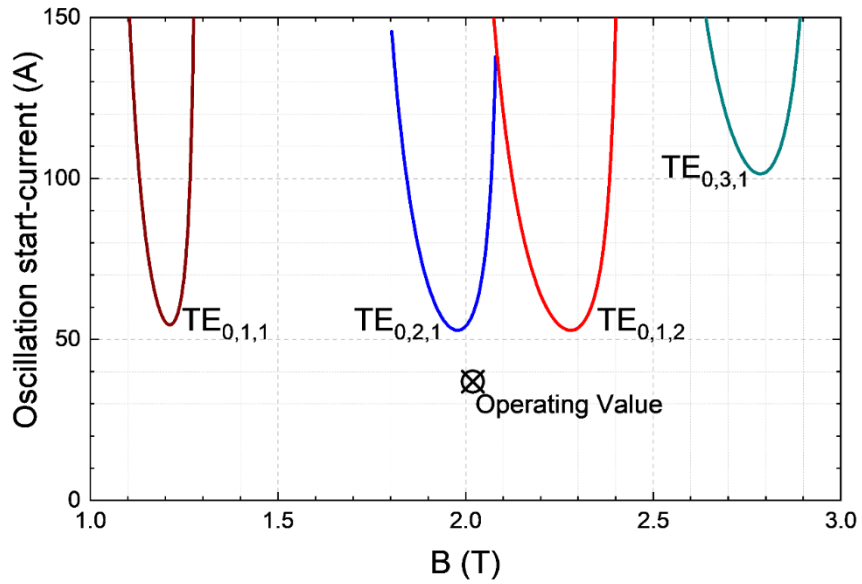
Figure 6.17
Start current as a function of B for various modes in the output cavity

At the operating value, the TE_{02} mode has a start-current of 59A, so there is high confidence in stable performance at 37A. While this result suggests the current could be significantly higher, the MIG analysis in chapter 4 showed that the corresponding increase in velocity spread and the limitations on cathode emission density prevents the design from taking advantage of further current increases.
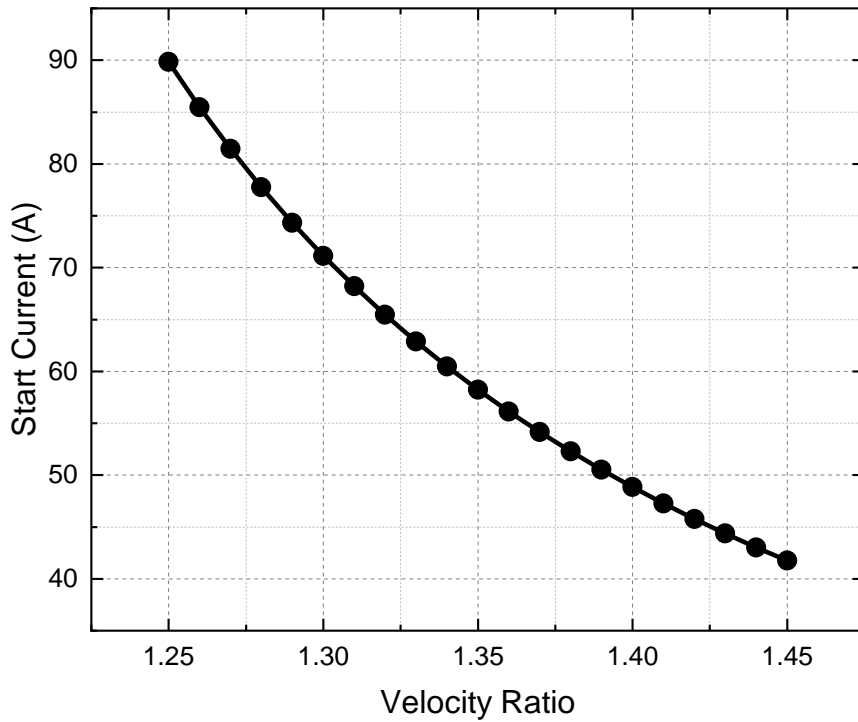
Figure 6.18
Start-current in the output cavity as a function of beam velocity ratio

6.2.4: Phase Stability

In accelerator applications, to ensure correct operation there must be good phase synchronisation across the system, which may consist of hundreds of RF amplifiers. The RF phase drive signals must be controllable to guarantee that RF wave crests and electron bunches can be made to coincide correctly. Therefore, the stability in the phase of the amplifiers output signal is an important parameter to consider. Reference [233] provides analytical and experimental study of the phase stability in the gyroklystron, which can be calculated by

$$d\phi = (1 + \alpha^2)^{\frac{1}{2}} \frac{\omega L_{int}}{c} \frac{(\gamma^2 - 1)^{\frac{1}{2}}}{\gamma + 1} \left(1 + \frac{\Delta}{2} \frac{\alpha^2}{1 + \alpha^2} \frac{\alpha^2 - \gamma}{\gamma}\right) \frac{dV}{V} \tag{6.2}$$

where Δ is the normalised detuning parameter given by

$$\Delta = \frac{\gamma^2}{\gamma^2 - 1} \frac{\alpha^2 + 1}{\alpha^2} \frac{2}{\omega} \left(\omega - \frac{\Omega}{\gamma}\right) \tag{6.3}$$

In this equation, Ω is the non-relativistic cyclotron frequency, L_{int} refers to the distance between from the input cavity to the end of the interaction circuit, and $\frac{dV}{V}$ is the voltage stability. Equation 6.2 gives a result in radians, so the simple conversion to degrees must be carried out to get a result in an easily comparable form. The phase stability was calculated to be 2.6° per 0.1% voltage instability. This is slightly better than in the 36GHz gyroklystron (which has a phase stability of 3.4° per 0.1% voltage instability) mainly due to the shorter length of the interaction circuit of the 48GHz gyroklystron. Since most parameters in equation 6.2 are fixed by the optimised design of the circuit, the main factor that influences the phase stability is the voltage modulator. Scandinova produce modulators that can produce 0.02% stability as a baseline (0.52° phase stability from the gyroklystron), with enhanced options to achieve 1000Hz repetition rate and 0.004% stability [234]. Therefore, the 48GHz gyroklystron can potentially achieve slightly over 0.1° phase stability. The requirement specified to serve the lineariser is a maximum of 0.5°, so the 36GHz and

48GHz gyroklystrons are both safely within specification limits, provided that a sufficiently high-spec modulator is purchased to power them.

6.3: Finalised Gyroklystron Design and Performance Characteristics

6.3.1: Summary of Performance Characteristics

A three-cavity set-up was used, with a modal sequence of $TE_{0,1}$-$TE_{0,1}$-$TE_{0,2}$ in order to balance gain, efficiency, power handling, complexity, and thermal issues. The MIG presented in chapter 4 delivers a 37A electron beam, with a beam voltage of 140kV, and a velocity ratio spread of 8.9%. The predicted performance of the gyroklystron is summarised in table 6.2, which lists the key parameters in both the ideal-beam case, and the realistic case which considers the aforementioned electron beam characteristics achieved by the MIG design. The requirements set by CompactLight (see table 5.1) include the required output power, a minimum bandwidth, a specified pulse duration, and safe operation at 1000Hz (discussed in chapter 7). There is no externally specified requirement for the gain and efficiency aside from the general statement that higher is better. The beam parameters were determined internally as discussed in chapter 5.

Table 6.2: Performance of the Gyroklystron

Parameter	Value		
	CompactLight Requirement	Ideal Beam (no spread)	Realistic Beam (8.9% α-spread)
Output Power	2.0MW	2.3MW	2.0MW
Gain	-	36dB	35dB
Efficiency	-	44%	38%
Bandwidth	200MHz	400MHz	400MHz
Pulse duration	1.5μs	1.5μs	1.5μs
Possible P.R.F	1000Hz	1000Hz	1000Hz

The gyroklystron is predicted to perform well and meet the selected design goals. However, the simulation model cannot perfectly represent reality due to the necessity for discretisation of space and time and the simplification into 2D simulation space. Section 3.4.4 discusses the verification of the MAGIC simulation model, showing that similar, but not necessarily identical, performance in experimental study is expected. There is therefore high confidence in the viability of the design presented and its ability to match the design goals for a 48GHz lineariser system.

The results in this chapter assume certain requirements which must be verified for a complete design – namely the ability to excite an appropriate mode in the input cavity and the ability to handle the beam deposition on the collector. These requirements are further discussed in chapter 7 where appropriate designs have been developed for the coupler, windows, and collector.

Chapter 7: Input and Output Components

The literature review and background presented in chapter 2 introduced the input coupler and output window in general terms. This chapter describes the design process in further detail and presents simulation results for each of these components. 7.1 presents analysis of a four-slot coaxial input coupler. 7.2 presents a pillbox-type input window and a single-disc output window, each of which has been optimised for minimal reflection parameters. 7.3 details thermal analysis of the beam deposited on the collector.

7.1: Design of a Coaxial Input Coupler

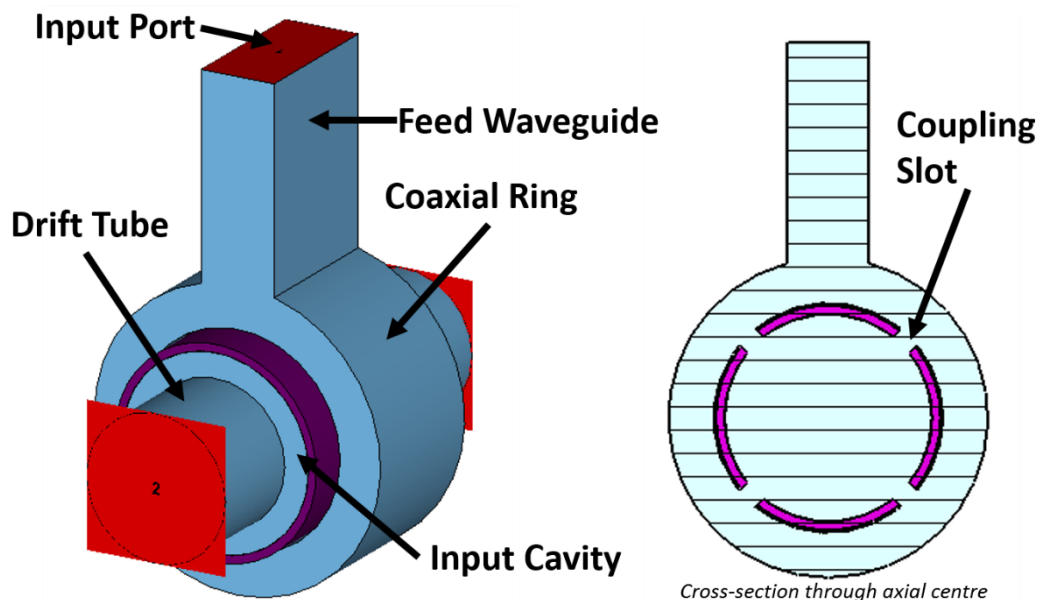### 7.1.1: Field Modes in the Structure

Figure 7.1
Schematic of the input coupler. 3D model (left) and cross section (right).
Ports marked in red, vacuum in blue, and dielectric in purple.

In the input coupler [190, 235], a microwave signal from a microwave source is carried through a rectangular waveguide. This waveguide connects to a coaxial cavity. The coaxial cavity surrounds the cylindrical input cavity of the gyroklystron interaction circuit. A series of slots on the shared wall act as apertures for field energy to pass through to excite a mode in the inner cavity. A schematic is shown in figure 7.1.

The cylindrical section is the first cavity of the interaction circuit and hence the dimensions of it are pre-determined based on the design described in the previous chapters. The challenge therefore is to optimise the other dimensions based on the existing cylindrical cavity such that the desired performance is achieved. The coupler must be able to display at least the same bandwidth as the interaction circuit, the resulting mode purity in the input cavity must be high, and input power should not be wasted due to reflection from the cavity.

Since the inner cavity has already been designed, there are three aspects to consider: the rectangular feed waveguide, the coaxial region, and the size and shape of the apertures. The rectangular waveguide analysis begins with the basic requirement that the correct mode will propagate. The cut-off frequency equation can be used to determine whether a given mode can be supported by the waveguide:

$$ f_{c.o} = \frac{c}{2} \sqrt{\left(\frac{m}{a}\right)^2 + \left(\frac{n}{b}\right)^2} \tag{7.1} $$

where a and b are the long and short dimensions of the cross-section respectively, and m and n and the indices in the usual mode notation $TE_{m,n}$. For the $TE_{1,0}$ mode to have a cut-off frequency below 48GHz, the minimum dimension of the long side is approximately 3.15mm. However, since the difference between the cut-off frequencies of this and the next lowest mode is large, there is no obligation to set the dimension close to the minimum value. A significantly larger dimension can be used, provided that the other low-order modes are still cut-off to avoid the risk of impurity. On paper, this gives a moderate amount of freedom in the basic geometry of the feed guide, but to simplify component matching with other sections and minimise

construction cost, is preferable to use a standard waveguide. The standard rectangular sizes WR19 and WR22 both have a recommended frequency range that includes 48GHz for lowest order ($TE_{1,0}$) mode propagation with the next mode's cut-off frequency higher than 48GHz and were therefore both considered as possible options.

After the rectangular section, the input wave reaches a coaxial section which surrounds the cavity. The eigenfrequency of the $TE_{m,n,p}$ mode in a coaxial cavity is given by [236]

$$f = \frac{c}{2\pi} \sqrt{\left(\frac{x_{m,n}}{r_b}\right)^2 + \left(\frac{p\pi}{L_c}\right)^2} \tag{7.2}$$

where L_c is the cavity length and r_a and r_b are the inner and outer radii respectively, and $x_{m,n}$ is the root of the equation:

$$\frac{J'_{m,n}(x_{m,n})}{Y'_{m,n}(x_{m,n})} - \frac{J'_{m,n}\left(\frac{r_a}{r_b}x_{m,n}\right)}{Y'_{m,n}\left(\frac{r_a}{r_b}x_{m,n}\right)} = 0 \tag{7.3}$$

where J' and Y' are the derivatives of the Bessel functions of the first and second kind respectively. Numerical analysis of equations 7.2 and 7.3 can be performed to determine the dimensions of a coaxial structure with the desired eigenfrequency. The z-dimension of the coaxial section was chosen to match that of the rectangular waveguide, because this is favourable for minimising reflection where they connect to each other.

Another approach is to view the coaxial cavity instead as a ring-shaped waveguide, where propagation of modes is in the θ-direction instead of the conventional z-direction. The meeting point of the feed guide and the coaxial cavity section can then be reasonably modelled as an E-plane tee. In the ring-guide when the wave passes each of the apertures to the inner cavity, it is considered like a scattering event where the phase and amplitude change. Each aperture is treated as a dipole radiator

considering two magnetic moments in the plane of the aperture and one perpendicular electric moment [190, 235].

Consider the junction where the feed guide meets the ring guide. This type of intersection can be described in terms of the scattering parameters. The parameter S_{11} describes the reflection at port 1, the meeting point of the two sections.

$$S_{11} = \frac{b-1}{b+1} \tag{7.4}$$

Where b is the coupling coefficient, defined as:

$$b = \frac{Q_{ohmic}}{Q_{external}} \tag{7.5}$$

Ohmic loss should be low, which makes $b \gg 1$, resulting in a high reflection coefficient. Increasing internal losses would reduce reflective losses, but any benefit would be negated by the increase in ohmic losses. Hence in a practical circuit, there will always be a significant reflective loss. The minimal reflection coefficient S_{11}^0 within the desired operation band $\Delta\omega^0$ and total reflection outside that band has a limitation that can be written as [235]

$$\ln\left(\frac{1}{S_{11}^0}\right) \leq \frac{\pi\Delta\omega_{loss}}{\Delta\omega^0} \tag{7.6}$$

where $\Delta\omega_{loss}$ is the cavity bandwidth in the absence of external loss.

The apertures can be treated using an approximation to equivalent electric and magnetic dipoles [237]. Each aperture can be treated as an electric dipole with strength proportional to the normal component of the electric field and a magnetic dipole with strength proportional to the tangential component of the magnetic field. The proportionality constants depend on the size and shape of the aperture and are called the electric and magnetic polarisabilities (α_e and α_m) of the aperture. They characterise the radiating or coupling properties of the aperture. Each slot is defined by dipole moments given by

$$P_{i_r} = \varepsilon_0 \alpha_e \hat{r} \cdot \left(E_{g1} + E_{r1} - E_{r2}\right) \tag{7.7}$$

$$M_{i_\theta} = \alpha_{m\theta}\hat{\theta} \cdot \left(H_{g1} + H_{r1} - H_{r2}\right) \qquad (7.8)$$

$$M_{i_z} = \alpha_{mz}\hat{z} \cdot \left(H_{g1} + H_{r1} - H_{r2}\right) \qquad (7.9)$$

where *g1* indicates the net field incident on the aperture from the ring-guide side, *r1* indicates the field radiated into the ring guide, and *r2* indicates the field radiated into the cavity.

With proper design, the resulting fields after consideration of the dipole moments will be a TE$_{4,1,1}$ mode in the coaxial section and a TE$_{0,1,1}$ mode in the cylindrical cavity. The full description of the calculations can be found in the literature [190, 235] and is not presented here as it is based on well-known physics of S-parameters that is well-implemented in commercially available codes such as CST Studio Suite [238] which has been used for the simulations described throughout this chapter.

7.1.2: Design and Simulation

The simulation of the input coupler was performed in CST microwave studio. The algorithm uses the finite integration technique (FIT) which reformulates Maxwell's equations in their integral form [239, 240].

$$\oint_{\partial A} \vec{E} \cdot d\vec{s} = -\int_A \frac{\partial \vec{B}}{\partial t} \cdot d\vec{A} \qquad (7.10)$$

$$\oint_{\partial A} \vec{H} \cdot d\vec{s} = \int_A \left(\frac{\partial \vec{D}}{\partial t} + \vec{J}\right) \cdot d\vec{A} \qquad (7.11)$$

$$\oint_{\partial V} \vec{D} \cdot d\vec{A} = \int_V \rho dV \qquad (7.12)$$

$$\oint_{\partial V} \vec{B} \cdot d\vec{A} = 0 \qquad (7.13)$$

To solve these equations, a finite calculation domain must be defined thus enclosing the considered problem. Within the domain, space is then divided into a suitable mesh. Curved surfaces, such as the walls of cylindrical cavities, can be accurately considered by use of the perfect boundary approximation (PBA) wherein the integration path can be formed to follow the material surface rather than the cell edge [241] thus avoiding the need for staircase approximations in geometry.

Due to the differences between different MAGIC and CST, the cavity geometry had to be altered slightly from the version calculated with MAGIC to successfully excite the desired $TE_{0,1}$ mode. The transfer of energy from the input port to the cavity depends mainly on the shape of the coaxial section and the four coupling slots. Therefore, even though the radius was adjusted away from MAGIC's prediction of the cavity size, the coupler design simulation was still insightful.

The treatment of the dielectric is a large factor in the difference between the codes. Since the reflection characteristics depend on the aperture properties more than the cavity Q, it is reasonable not to include a dielectric lining in the initial study, and instead use a slightly adjusted cavity radius. Figure 7.2 shows a contour plot of the
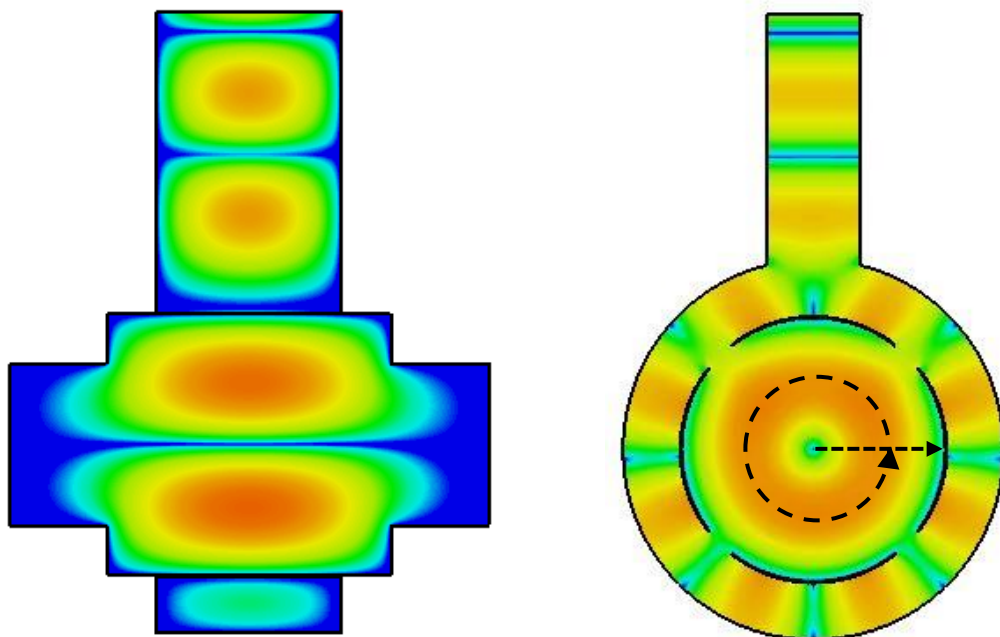
Figure 7.2
Contour plot of cavity field in simplified model

field on a cross section through the axial centre of the cavity. The dotted lines indicate the position of the radial and azimuthal lines used to generate 1D field plots used in subsequent figures. The field profile visually matched that of a $TE_{0,1}$ mode. The $TE_{0,1}$ mode is cut off in the drift tube which has a radius of 2.5mm.

To supplement the visualisation and better assess the modal structure, a 1D plot along a radial line was generated as shown in figure 7.3. A circular line was also added to measure the azimuthal uniformity of the field, as shown in figure 7.4.

Figure 7.2 displays the expected radial profile of a TE_{01} mode of zero electric field at the centre and cavity wall, and a maximum at approximately $0.48r_c$. The largest deviation from the average field in figure 7.4 was around 2%, suggesting a reasonably uniform mode. The four peaks on the azimuthal line correspond to the positions of the four coupling slots, suggesting that the slots warp the field profile slightly with the two slots nearest to the feed waveguide having the largest impact. Based on the contour plot and the two 1D plots, the cavity mode was observed to be excited correctly with a reasonable level of purity.
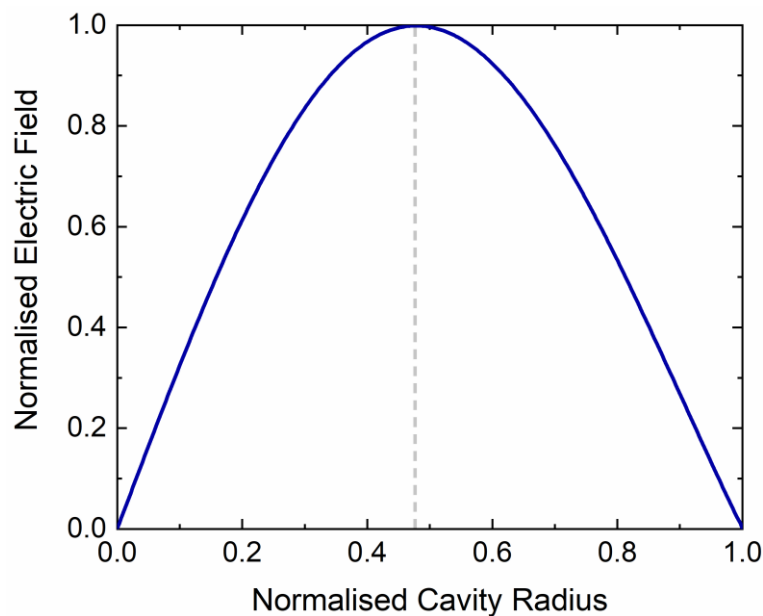
Figure 7.3
Normalised field profile along the cavity radius.
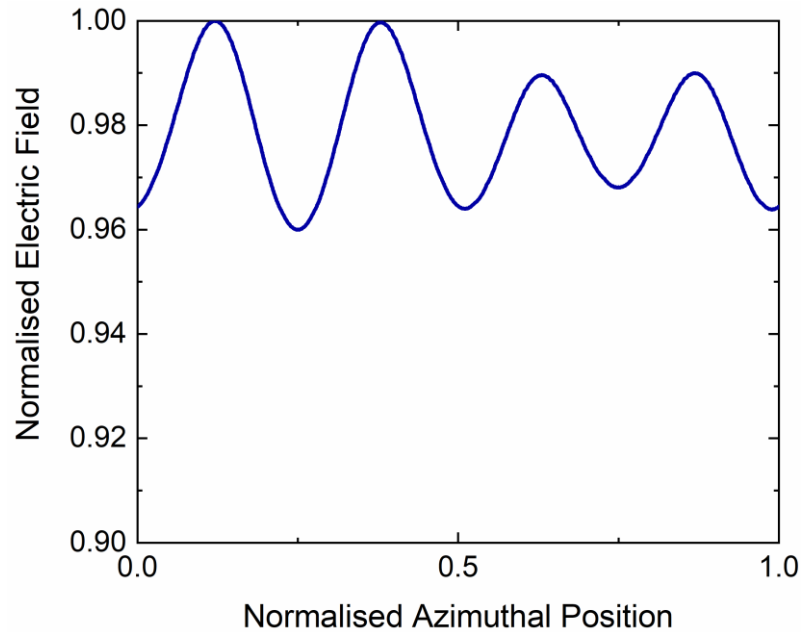
Figure 7.4
Field around a circle aligned with TE₀₁ pattern.

The simulation model was then updated to include the dielectric cavity lining. Sweeps were performed over a range of aperture dimensions and small adjustments were made to the cavity radius and dielectric thickness. The field near the peak phase, shown in the left of figure 7.5 appears to be suitable. The right side of figure 7.5 shows the same coupler at a different arbitrary phase revealing that the mode is not the pure circular $TE_{0,1}$ shape that is desired.

Figure 7.6 show the cavity field along a radial line (left) and an azimuthal line (right). The purple dashed line marks the start of the dielectric lining. The inclusion of the dielectric noticeably shifts the position of the maximum field to a slightly lower radius, occurring at around $0.45r_c$ instead of $0.48r_c$. As in the simplified case, the presence of the coupling slots causes the deviation from the perfect $TE_{0,1}$ profile. The variation in field along the azimuthal coordinate, shown in figure 7.6, features peaks and troughs roughly 11% above or below the average field along the line.
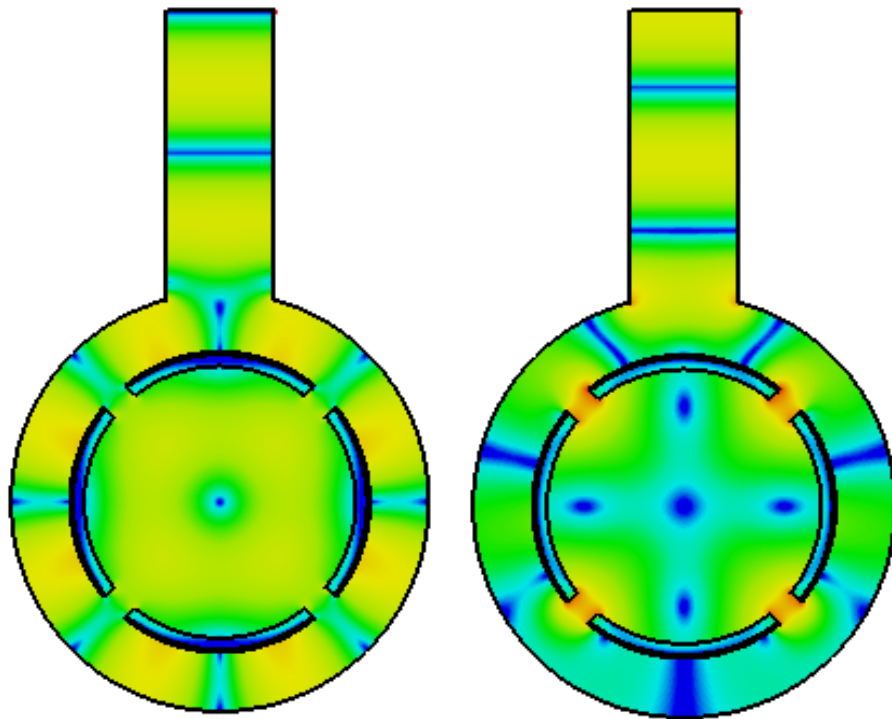
Figure 7.6
Field excited by the input coupler, shown at two different phases of the oscillation.
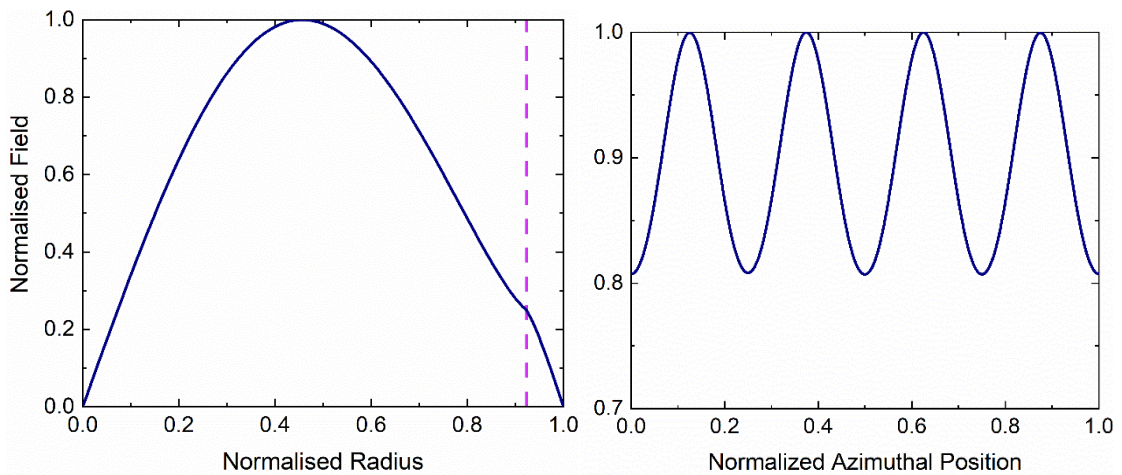
Figure 7.5
Normalised field excited by the coupler along a radial line (left) and around an azimuthal line (right)

Although the slight reduction in peak field radius and the variation in field strength around the azimuthal co-ordinate will reduce the effectiveness of bunching, the impact on performance is not likely to be large. The offset in peak field position is smaller than the Larmor radius of electron orbits, and thus does not majorly impact

the beam-wave coupling coefficient. The azimuthal variation in field profile is also non-ideal, but not debilitating as it would be possible to increase input power such that all points have a strong enough accelerating and decelerating effect to cause adequate bunching.

7.2: Design of Input and Output Windows

7.2.1: Window Material Options

The dielectric characteristics of a material are the one of most important considerations for its application as a window. The real and imaginary parts of the dielectric constant ε were introduced in chapter 2 (equation 2.21). The permittivity determines the radiation wavelength in a material:

$$\lambda_d = \frac{\lambda}{\sqrt{\varepsilon_r'}} \tag{7.14}$$

To avoid reflection, the window thickness d should be equal to an integer number N of half wavelengths:

$$d = N \left(\frac{\sqrt{\lambda_d}}{2} \right) \tag{7.15}$$

This condition is complicated by the thermal properties of the material. While a window may be matched at room temperature, it might cause reflection after the thermal expansion due to the heating it experiences during device operation. The thermal issue is most prominent in CW, long-pulsed or high duty cycle operating regimes. Since the operation of the gyroklystron in this thesis has a relatively low duty cycle (~0.15%), heating effects are not extreme, but still should be considered in the decision of window material.

The input window presented in this chapter was designed based on a re-scaling of similar components developed by the University of Strathclyde for a 36GHz gyroklystron and for a W-band gyro-TWA [242]. The window was set to the properties of 99.4% pure Al_2O_3 with a relative dielectric constant of 9.4, as this material offers a good balance between mechanical, thermal, and optical properties.

The output window must handle larger power and match stricter reflection requirements. Several material options may be considered for an output window,

including diamond, boron nitride, Si$_3$Ni$_4$, sapphire, and doped silicon [72, 73, 165, 170, 243-247]. For very high power (1MW) CW operation, CVD diamond has been a favoured choice for decades in sources such as the gyrotron oscillators for ITER [72, 248, 249] but diamond windows very expensive. Sapphire is also a good material for RF windows due to its mechanical and electric properties and its more affordable cost than diamond [245, 250]. Boron nitride offers good performance while being significantly cheaper than diamond windows [251]. Although its physical strength is relatively low, it benefits from a low thermal dependence of its properties and does not have a high fragility when subject to temperature gradients. The intended pulse repetition frequency (PRF) for CompactLight would be up to 1000Hz with a pulse duration of 1.5μs. This makes the average power low enough that boron nitride is a safe choice for the output window, whereas it is not typically the window of choice for a high-power CW device such as the gyrotron oscillators for fusion plasma heating.

7.2.2: Pillbox-type Window Structure

There are two fundamental requirements on the window:

- It must ensure and maintain perfect sealing of the vacuum from the outside with sufficient mechanical strength.
- It must have low reflection and insertion losses.

Several configurations are used for various microwave devices. In this case, the pillbox window type is most appropriate. Since a rectangular waveguide section is required in the input coupler design, this type of window section is well-suited to the gyroklystron as there will be no need for any additional waveguide steps or tapers to match it to the coupler. The circular geometry is favoured over a rectangular dielectric window because its rotational symmetry and larger cross-sectional area help to reduce the stress from thermal loading from the wave passing through. In general, a pillbox window offers a reasonable balance between reflection and bandwidth. Compared with simple single-disc windows it can have a superior

bandwidth, and compared with multi-disc and Brewster windows, it has simpler geometry. The geometry of a pillbox window is illustrated in figure 7.7. For analytical purposes, the structure can be further broken down into the following sequence [242]:
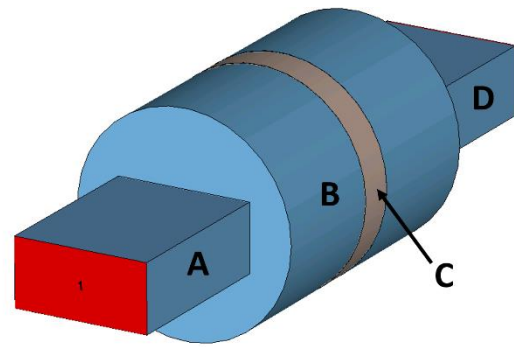
Figure 7.7
Geometry of Pillbox-type Input Window
red = port; blue = vacuum; brown = alumina
A – waveguide from microwave source, B- cylindrical pillbox section, C – alumina disk, D – feed waveguide to input coupler

1. Rectangular waveguide
2. Step from rectangular to circular region
3. Circular waveguide
4. Vacuum-dielectric interface
5. Dielectric disc
6. Dielectric-vacuum interface
7. Circular waveguide
8. Step from circular to rectangular region
9. Rectangular waveguide

The steps and interfaces can each be described using scattering matrices. The full expansion and formulation of the scattering matrices for a pillbox window structure can be studied in several papers [252-255] and the references therein. The scattering matrix for the full structure of the pillbox window can be constructed by cascading each individual section's matrix from left to right. Some simplifying details can benefit the calculations. There is no mode conversion during the straight sections, so the rectangular waveguides, circular waveguides, and dielectric disc all have diagonal scattering matrices. The rectangular waveguides affect only the phase, and since amplitude is the only relevant parameter to the performance, they can be left out of the calculation. The mathematics of S-parameters is well implemented in commercially available codes. All the required calculations can be performed within CST Microwave Studio, which has been used throughout this chapter. The most important result is the value of S_{11}, which is a measure of the reflection by comparing

the amplitude of the input signal to the amplitude of the reflected signal. As the reflection is frequency dependent, in addition to minimising the value of S_{11}, it is also important to ensure that its minimum value aligns with the centre frequency and that it is suitably low over the relevant range of frequencies (i.e. the bandwidth of the amplifier).

7.2.3: Design and Simulation of a Pillbox Input Window

The rectangular dimensions were chosen to match the standard WR22 waveguide as it has suitable dimensions for the propagation of 48GHz radiation and matches the rectangular waveguide that feeds the input coupler. With the rectangular waveguide fixed, the variable parameters were therefore only those of the cylindrical region and the ceramic disc. The initial disc thickness was estimated at one quarter of the wavelength. The length and radius of the cylindrical section were estimated initially, and then optimised in CST microwave studio. The optimiser function computes the S-parameters for different parameter sets until it settles on a set that satisfies a user-defined goal function. The first function defined was to find the minimum while forcing the minimum to occur at the desired value of 48GHz. Using this function, the solver quickly settled on a combination of dimensions which gave the S_{11} minimum value of -58dB at 48GHz. Figure 7.8(a) shows that the reflection was highly sensitive to frequency as expected.

Figure 7.8(b) shows the same data but cut down to only include frequencies close to the operating frequency, with the 400MHz bandwidth of the interaction circuit highlighted. The pillbox window's highest S_{11} parameter within this bandwidth was -16.94dB, which corresponds to around 2% of input power being reflected. The length of the rectangular waveguide section was observed to have negligible effect on the result. The dimensions determined by the optimiser are shown in table 7.1.

Table 7.1: Parameters after first optimisation routine

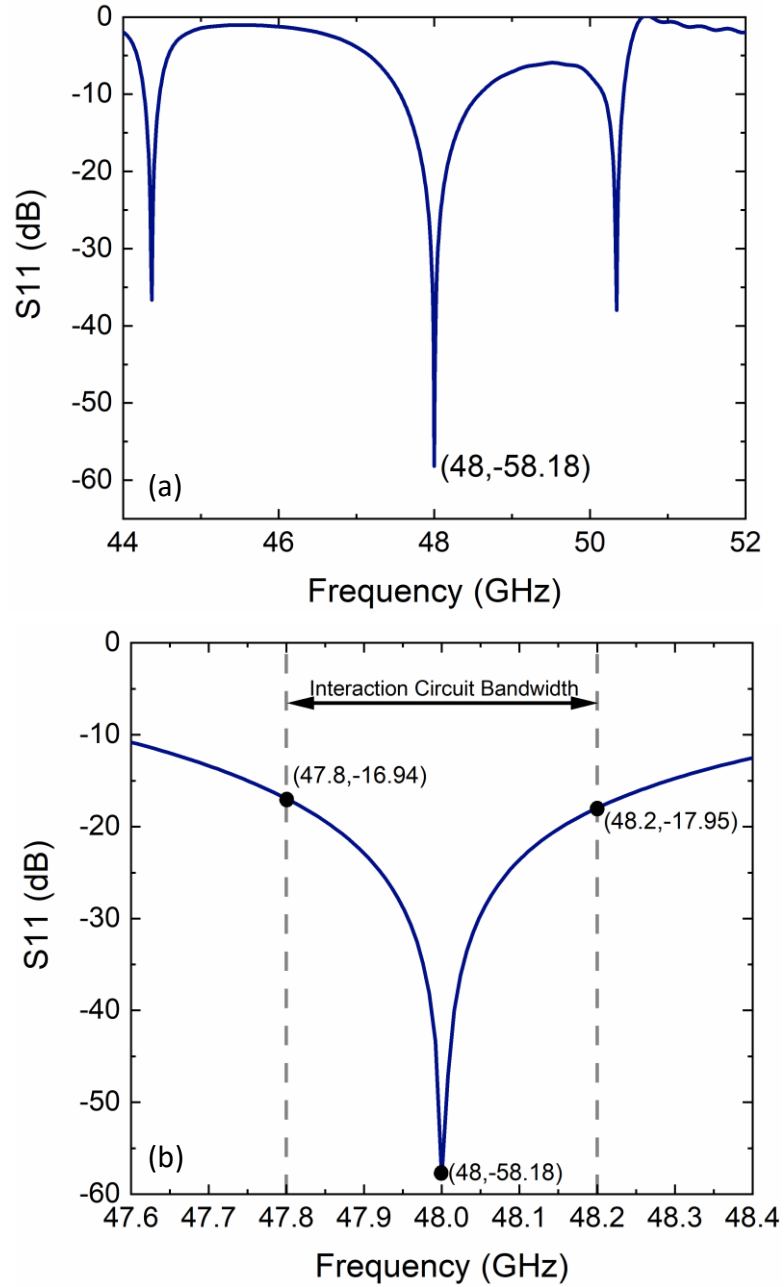| Parameter	Size (mm)
Pillbox Radius	4.031
Pillbox Half Length	5.848
Ceramic Thickness	1.648

Figure 7.8
S_{11} parameter of the pillbox window
(a) over a wide frequency range
(b) over a narrow range with the interaction circuit bandwidth limits highlighted.

S_{11} for the centre frequency was extremely low after this first optimisation sequence. However, the reflection at the edges of the bandwidth was high at around -17dB. The original optimiser specification only examined the position and magnitude of the minimum of reflection. A more thorough optimisation routine was then set-up to also consider the maximum value with the bandwidth. The same optimiser parameters as before were used, with the extra target that S_{11} should be below -20dB in the range of 47.8GHz to 48.2GHz. This failed to achieve a good goal function, but slightly lowered the maximum reflection within the bandwidth from -16.94dB to -17.60dB at the cost of increasing the reflected amplitude at 48GHz to -55.18dB. The optimiser was reconfigured to only meet the -20dB requirement and ignore other goals as a rough test of the feasibility, since too many simultaneous goals increase computation time. The optimiser achieved this goal after 13 iterations. However, the minimum was shifted off-centre in frequency, resulting in a reflection of -32.78dB at 48GHz, which is a significant increase over the previous optimisations. Although this result was far from the desired performance, it showed that a -20dB limit was potentially feasible. It was then considered that the minimum could be allowed to shift away from the centre frequency, provided the value at 48GHz remained below a given threshold. The 4th optimiser run was therefore set with the goals of $S_{11} < -20dB \ when \ 47.8GHz < f < 48.2GHz \ ; S_{11} < -40dB \ when \ f = 48GHz$. These commands allowed CST to successfully identify a parameter set that met targets. The results achieved by each of the four optimisation runs are shown in figure 7.9.
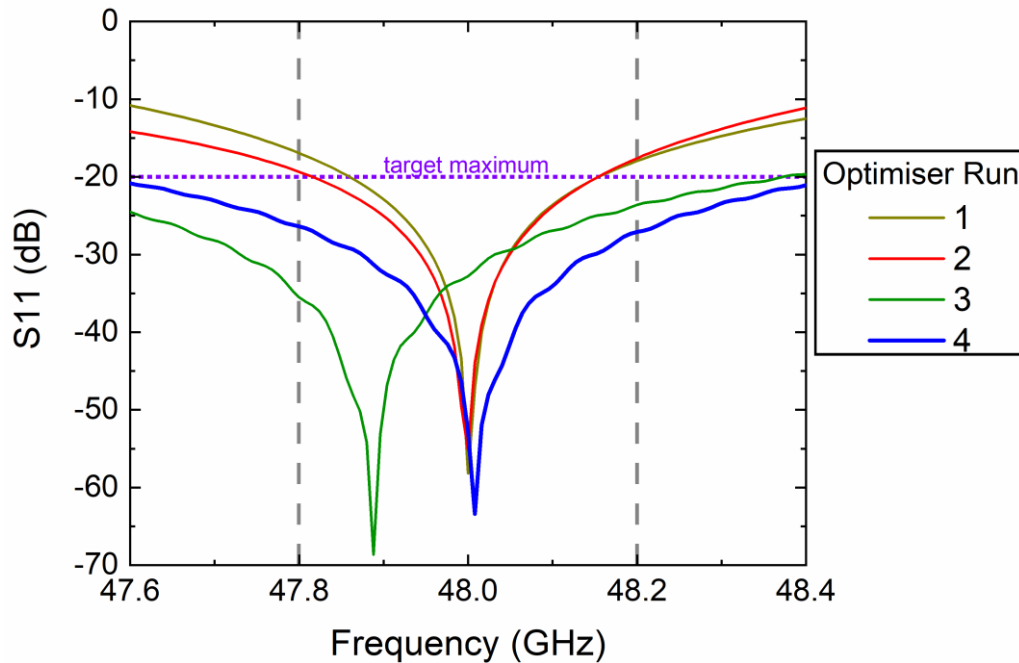
Figure 7.9
S₁₁ parameter result for the four optimisation runs.

Figure 7.9 illustrates the progression of results from the initial over-simplified optimiser goal to the first successful design. The initial optimiser, only concerning the minimum, and forcing that minimum to be at 48GHz showed decent, but far from optimal performance. The second run was similar, but due to too many simultaneous goals, not all could be satisfied, and it failed to mark a noteworthy improvement. The third run was not expected to produce a viable parameter set, but only to demonstrate whether achieving below -20dB over the chosen range was feasible. Finally, the fourth run was able to completely satisfy its goals with results considerably better than the baseline targets, with a reflection of -52.80dB at 48GHz, and no higher than -26.36dB within the frequency range of the interaction circuit bandwidth. However, the curves do not follow the expected smooth shape. It was subsequently found that increasing the mesh density and reducing the frequency range of the simulation improved the quality of the result. The effect of improving mesh density is shown in figure 7.10. A modest increase of the mesh density from 20 cells per wavelength to 30 was observed to be a suitable balance, with further

increase in mesh density showing very little difference in result and a significant increase in simulation time.
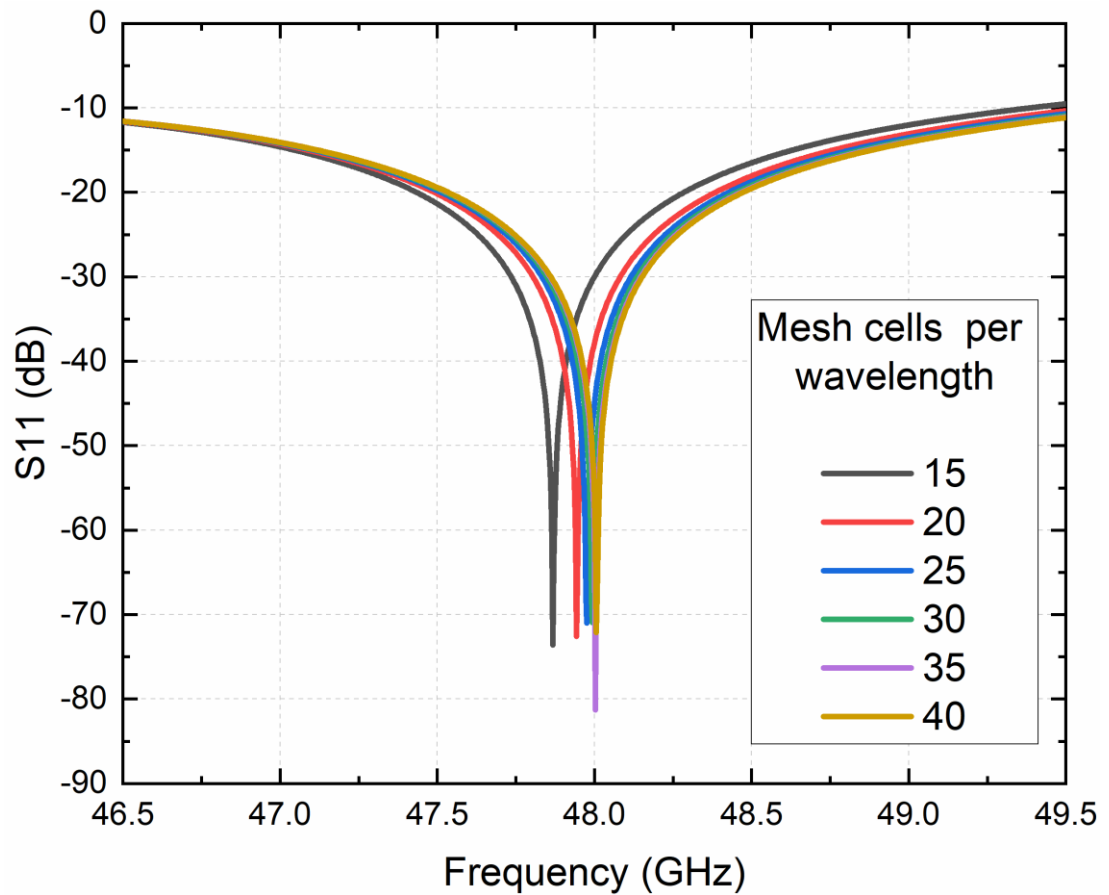
Figure 7.10
Comparison of pillbox window simulation result for increasing mesh density

With the observation that a moderately improved mesh was necessary, the optimiser was repeated with tighter goals resulting in the S_{11} parameter results shown in figure 7.11, with the optimised dimensions shown in table 7.2.
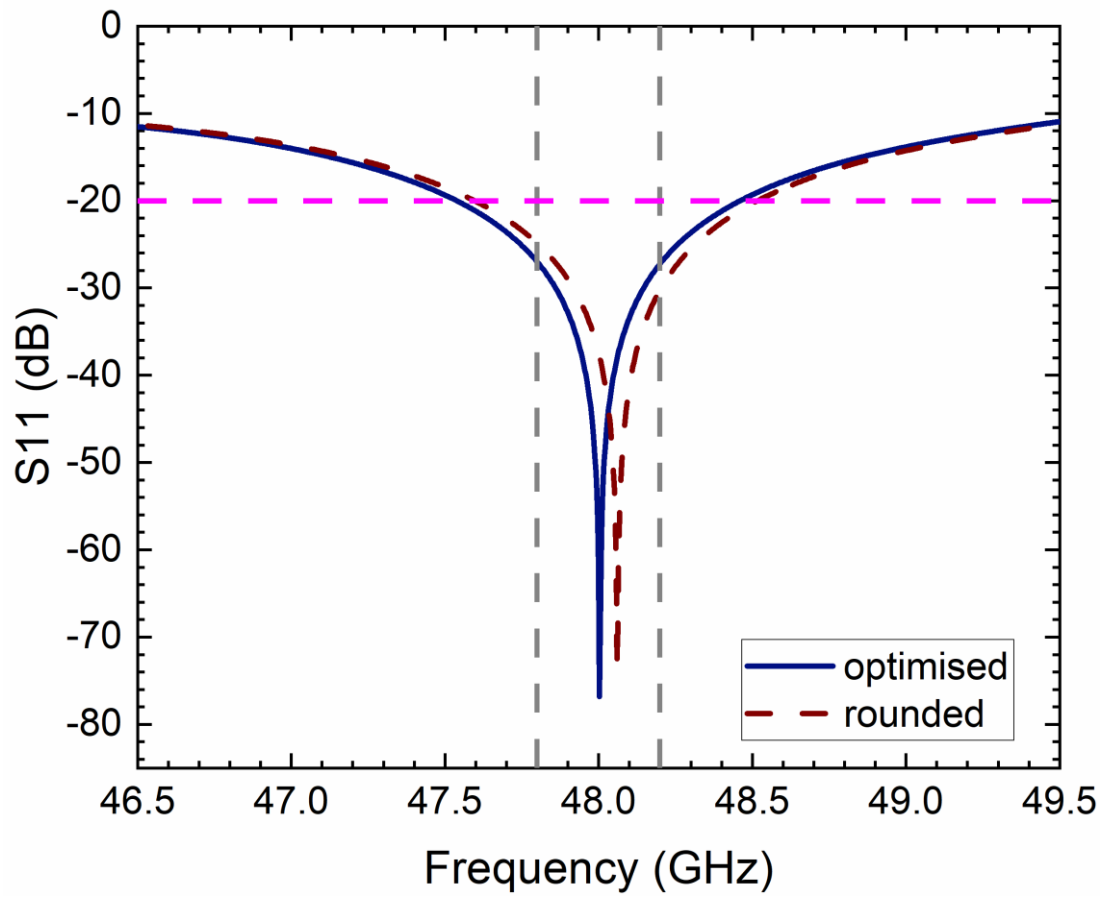
Figure 7.11
S$_{11}$ parameter of the pillbox-type input window

Table 7.2: Optimised Dimensions of the pillbox window

Parameter	Size (mm)
Rectangular Waveguide	5.6896 by 2.8448 (WR22)
Pillbox Radius	4.6422
Pillbox Half-length	5.5321
Ceramic Disc (Al$_2$O$_3$) Thickness	1.5911

The simulation does not consider machining precision or any potential non-uniformity of the thickness, and the optimiser computes the dimensions to more significant figures than can reliably be achieved in practice. Sub-μm accuracy in window thickness may potentially be achieved with precise grinding methods, but as a conservative consideration results were recalculated with the dimensions of the cylinder and window rounded to the nearest 10μm, as shown by the dashed curve in figure 7.11. Additional simulations were then carried out to observe the sensitivity to the dimensions. Figure 7.12 illustrates how sensitive the S_{11} parameter is to the thickness of the window. The minimum value of reflection remained low for each case, but the frequency at which the minimum occurs varied thus changing the values within the band of interest. The maximum value within the bandwidth of the gyroklystron does not change drastically and remains under the -20dB target that was set initially. The value at 48GHz changes by a much larger amount and therefore high machining precision is needed to guarantee the predicted performance.
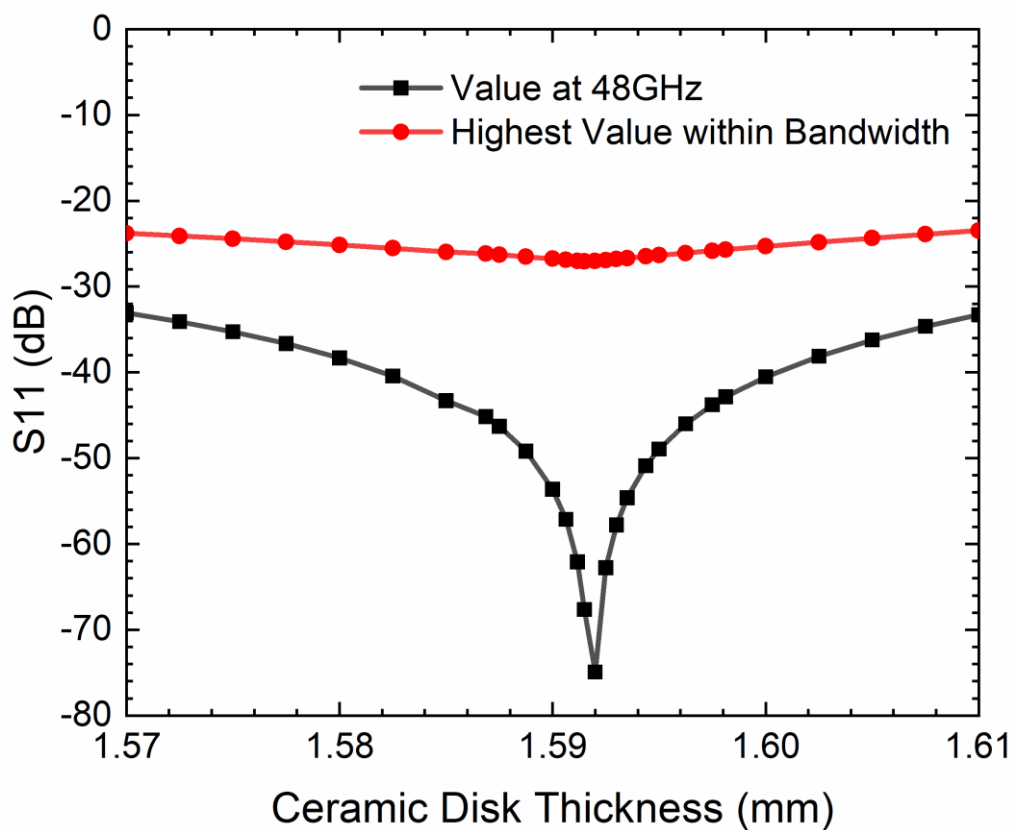
Figure 7.12
S_{11} parameter as a function of window thickness

A similar sensitivity test was carried out for the pillbox radius, as shown in figure 7.13. The level of sensitivity was again very high, but the range of values predicted to meet performance requirements is large enough that even the conservative estimate of machining precision would be easily sufficient.
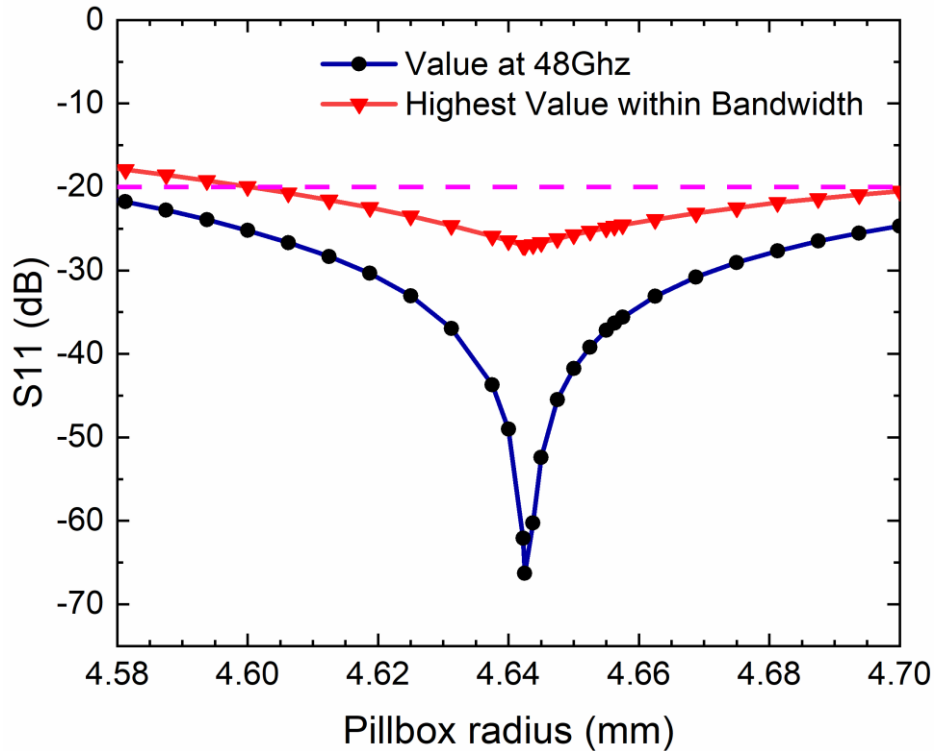
Figure 7.13
S_{11} parameter as a function of pillbox radius

7.2.4: Design and Simulation of a Single-Disc Output Window

Since the output waveguide is cylindrical, a single disc was the most practical window type for the geometry as it meant there was no need for additional steps, tapers, or bends. The design was therefore simpler than the pillbox-type input window, as there were fewer parameters to consider. However, since reflection from the output window would propagate back toward the cavities and the amount of power in the signal is much higher, the targets for maximum reflection had to be considerably

stricter to preserve the interaction. Targets were decided as $S_{11} < -50dB$ at 48GHz, and $S_{11} < -35dB$ over the device bandwidth.

Since the window had to be compatible without additional taper sections, the radius was fixed as the same as that used for the output waveguide of the interaction circuit. An initial estimate of a quarter-wavelength window-thickness was used, and the optimiser function was used to minimise reflection over the bandwidth.

Figure 7.14 shows the reflection parameter of the window for a $TE_{0,2}$ mode after applying the optimiser conditions of under -40dB reflection over the interaction bandwidth and under -75dB reflection at 48GHz with window thickness as the only variable. These optimiser goals are stricter than the actual target value to allow for further improvement rather than concluding the run when the baseline goal is met.
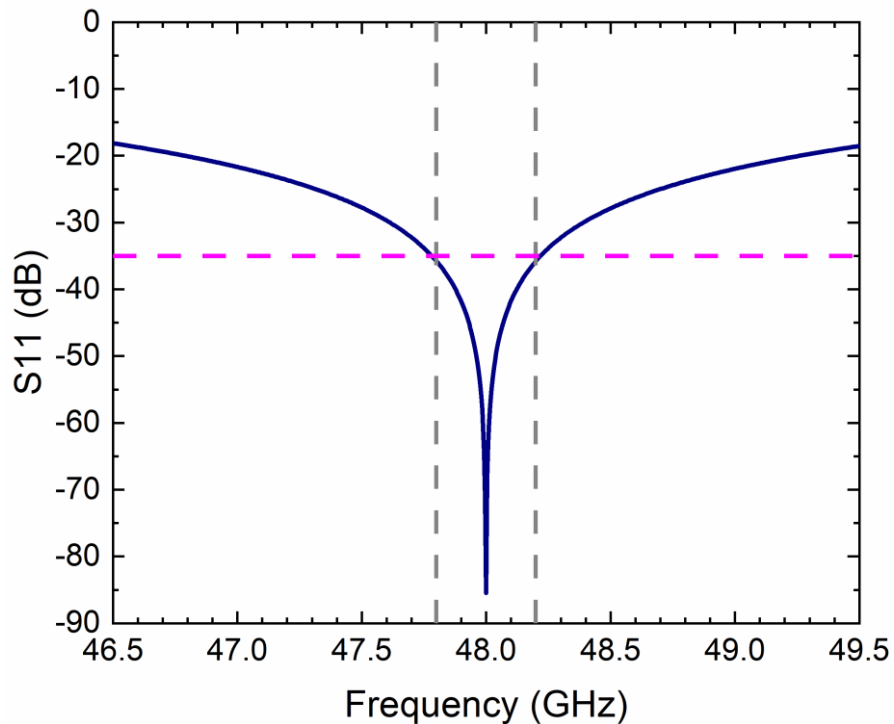
Figure 7.14
S_{11} Parameter of a $TE_{0,2}$ mode passing through the output window.

The target performance was achieved when the window thickness was 1.5112mm, with a minimum S_{11} parameter of -85.49dB at 48GHz and the highest value in the bandwidth was -35.94dB at 47.8GHz. A repeat of the optimiser was computed with stricter limits. The optimiser then settled on a window thickness of 1.5121mm,

resulting in a maximum reflection of -35.78dB within the bandwidth, and a shift of the minimum to occur at 48GHz with a value of -85.36dB.

It was observed that there is a very high sensitivity of the reflection parameter to the window thickness, as shown in figure 7.15. The value of the minimum remained below -75dB for the range of the parameter sweep, but its position changed almost linearly over a range of about 1GHz, thus causing the values at the relevant frequencies to be much higher.
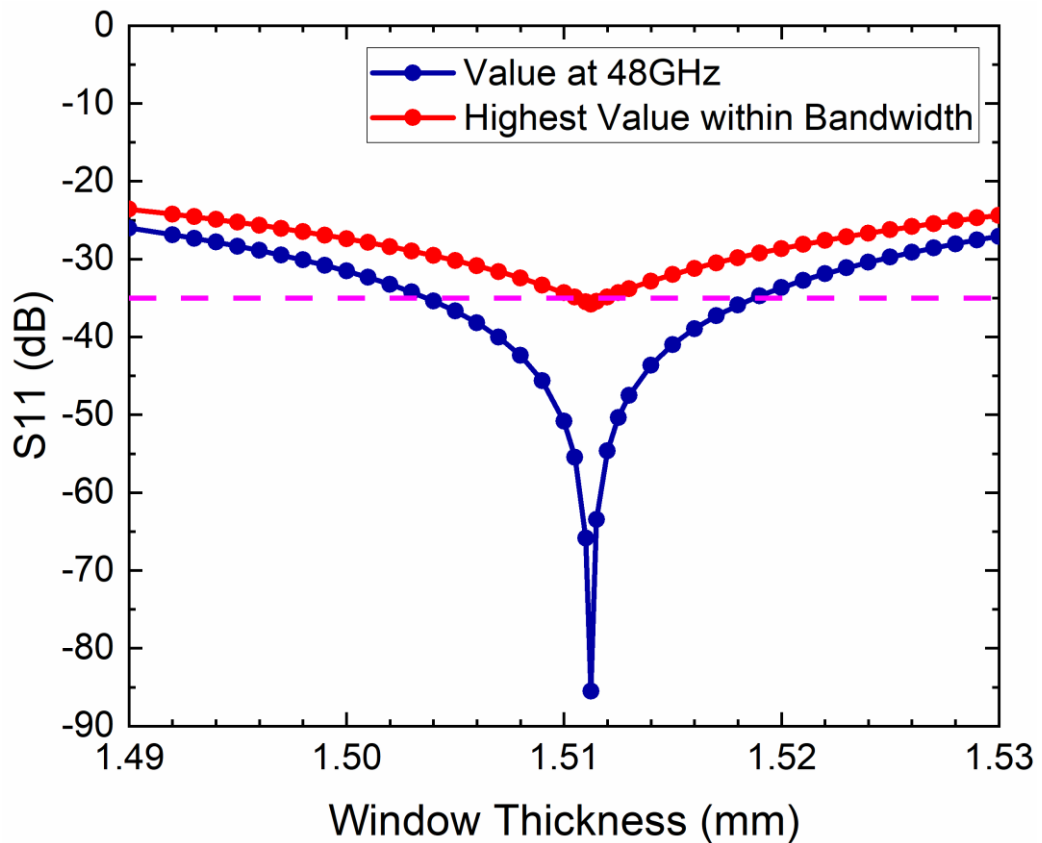
Figure 7.15
Sensitivity of S_{11} parameter to window thickness

From figure 7.15, it can be seen that to ensure the -35dB maximum reflection is met over the bandwidth requires at least μm-level precision in the machining of the output window disc.

Since the output signal from the interaction contains a small second harmonic component, the reflection parameters around 96GHz were also considered. The reflection at 96GHz was calculated to be -14.43dB. The second harmonic component

has a normalised amplitude more than 10dB below the fundamental, so even with the relatively high reflection parameter, the reflected amplitude would be very small.

7.2.5: Summary of Window Designs

Input and output windows appropriate to the gyroklystron have been designed and optimised to display minimal reflection around 48GHz.

The input window was designed in a pillbox configuration as the geometry and expected performance characteristics were compatible with the application. A WR22 rectangular waveguide was used. The window material used was Al_2O_3 with a relative dielectric constant of 9.4. Several sets of optimiser goal functions were used, eventually leading to the geometry that showed reflection below -26dB across the frequency range of the interaction circuit's bandwidth and below -60dB at 48GHz. However, the simulation is purely mathematical and does not account for the precision of manufacture techniques. The optimised result is for a window with zero surface roughness and a perfectly uniform thickness calculated to many significant figures and displayed noticeable sensitivity on a sub-μm scale. Further simulations were carried showing the reflection parameters as window thickness and pillbox radius were varied. The trends were very strong over very small differences, but within a range of around ±10μm in each dimension performance is still expected to meet the outlined goals. While current machining techniques can potentially provide significantly better precision, 10μm precision is taken as a cautious baseline, which would result in at most -26dB reflection over the bandwidth and -44dB at 48GHz.

The output window was designed in a single-disc configuration in order to match the output waveguide of the gyroklystron without additional tapering. The window material used was BN. The only free parameter in this case was the window thickness, so optimisation was quick. In the ideal case, the maximum reflection within the bandwidth was -35.94dB and the reflection at 48GHz was -85.49dB. However, the sensitivity to the window dimension was on a scale very close to that of machining

precision. Within a cautious estimate of machining precision, a reflected amplitude of no more than-30dB is still expected. This is slightly worse than the initially selected targets but are not high enough to significantly harm the expected performance of the amplifier.

The selected window materials are expected to be able to safely handle the pulsed power levels in this system. Nonetheless, it is relevant to discuss potential breakdown scenarios that should be considered during prototyping. The heating effect of the radiation passing through can cause stress on the material. The rotational symmetry of the circular window designs reduces the risk of cracking compared with rectangular structures where different expansion along length and breadth may be a concern. The output window is downstream of the collector, so there should not be any electrons impacting its surface. However, even a very small number can become problematic if a multipacting effect occurs. This is not expected to be a major issue in this instance but is nonetheless important to look out for during the prototyping stage of design.

7.3: Thermal Analysis of the Beam Deposition Region

The optimal interaction efficiency in any gyroklystron is around 40%. Hence 60% or more of the original beam power is still present in the beam when it is deposited on the collector after interaction. It is therefore important to consider the power-handling capacity of the structure. The pulsed operation of the device means that the average power is much lower than the peak power. Although this reduces the challenge somewhat when compared with continuous-wave gyrotrons, the small device radius and high peak power can still lead to significant thermal effects which must be accounted for. An estimate of the average power loading per area Pd_{ave} can be found as follows:

$$Pd_{ave} = \frac{(1-\eta)IV\tau f_{rep}}{2\pi r L} \tag{7.16}$$

where η is the interaction efficiency, I and V are the beam current and voltage respectively, τ is the pulse duration, f_{rep} is the pulse repetition frequency, r is the collector radius, and L is the length of the deposition region. L can be estimated from the PIC results as shown in figure 7.16. Although it is useful for initial consideration, there are some limitations of this estimate. Firstly, L is an imprecise measurement due to the beam thickness. Secondly, this estimation also only reveals the average power over the deposition region, but since the deposition is not uniformly distributed, important detail such as power density distribution may be missed. The average power over the region as a whole is therefore less informative than the average power on a point-by-point basis. To achieve this level of detail with meaningful accuracy requires particle tracking simulation. Here, a two-stage process has been used. Particle data exported from the PIC simulation was imported into CST Particle Studio's trajectory solver. The particle deposition results from the trajectory

Figure 7.16
Deposition region

181

solver were then used as a heat source in CST's thermal analysis program. The following sections further detail the process and results.

7.3.1: Trajectory Analysis

The particle information after interaction (obtained through the PIC simulations described in chapter 6) was exported from MAGIC and converted into a format suitable to import into CST Particle Studio. This export interface was positioned 140mm along the output waveguide measured from the output cavity aperture. The coordinates used throughout this chapter set z = 0 to be located at this interface position. The trajectory solver program in CST was used to compute the path of electrons from the import interface to deposition. The deposition distribution was recorded as a surface plot on the collector wall. As only the deposition surface was relevant to this simulation, the only geometric object required was that which represents the vacuum of the waveguide. The magnetic field was included as a simple 1D definition along the z-axis, with a range of slightly different field profiles considered. The particle data was exported from the PIC simulations in MAGIC at a position far from the cavity aperture where no resonant modes were present. The number of simulation particles was varied between 20000 and 1000000 with only negligible influence on the results and a moderate impact on simulation time. Hence the 20000 macroparticle model was used. A high grid density was used to ensure no important detail was lost around the deposition region. A mesh dimension of 100 maximum cells per model box edge was selected as the appropriate balance point between high resolution and reasonable runtime. The figures produced in the trajectory solver are useful for quick checks, ensuring that the magnetic field profile and electron trajectories look believable, but detailed consideration is more easily made during the second stage using the thermal solver, described in the following section.

Some different magnetic field profiles were tested, as shown in figure 7.17. Since the orbital radius depends on the field, changing the profile can change the length of the region the electrons are deposited over. Since the total beam power is constant, this can slightly reduce the power density. The differences in peak deposition density were small, but a slight reduction was observed using the second field profile, and hence this was selected moving forward.
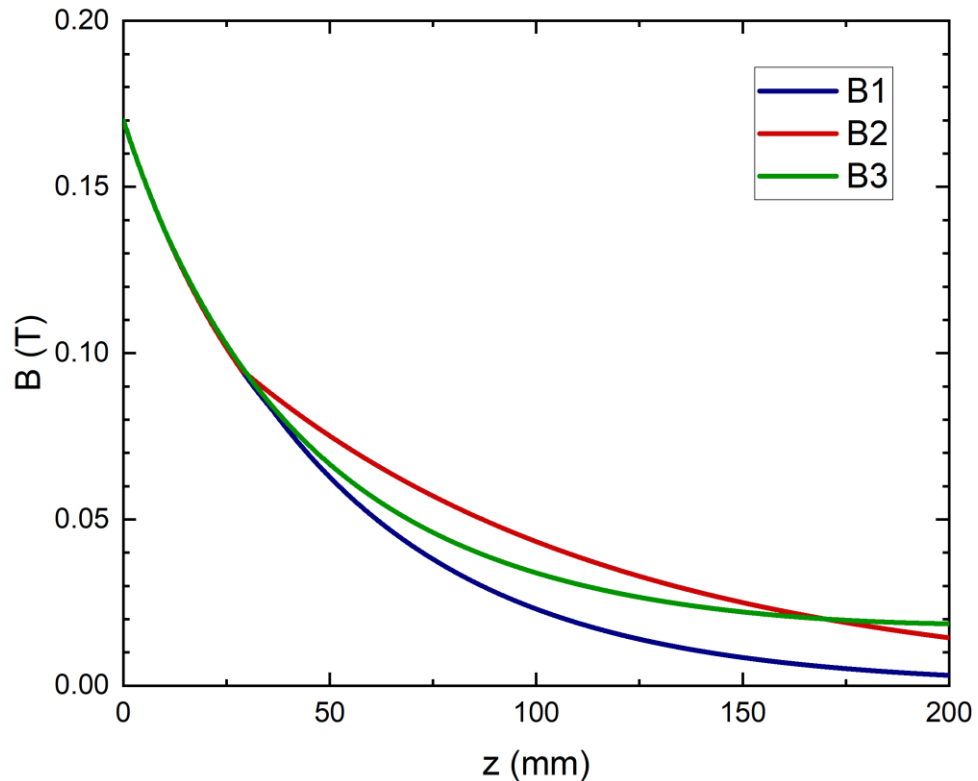
Figure 7.17
Different field profiles considered.

The deposition surface area can also be increased by changing the radius of the collector or adding an additional taper. This was a more effective way of reducing the maximum observed temperatures, but care must be taken as the introduction of taper risks causing mode conversion.

7.3.2: Thermal Solver

The thermal solver used the particle deposition data from the trajectory solver as a heat source. The particle collision loss data is a surface plot, so does not depend on the geometry of anything except the internal surface of the wall. Therefore, a simple cylinder of copper was used to quickly compare collision information.

The interaction circuit simulations do not directly consider the pulsed operation of the gyroklystron. To reflect this, a simple scaling factor can be applied when importing the particle loss data to the simulation file. For 1.5µs pulses at a repetition rate of 1000Hz, the scaling factor is 0.0015. However, this assumes two things: perfect square pulses and optimal interaction. While the device should operate only at the optimal frequency, it is an important precaution to design the collector to safely handle the full beam power rather than only the power remaining after efficient interaction. Since the efficiency was around 40%, the imported beam contains 60% of the full beam power, so the scaling factor should be divided by 0.6. The exact rise time depends on the modulator parameters. A linear rise (and fall) over 2µs is assumed as a conservative estimate but a sub-µs rise is likely plausible. To translate the linear rise to a contribution to the scaling factor, the average power during the rise and fall is considered. Since the rise is linear, the average is half of the full power, so this simulation can treat it as a 3.5µs square pulse. The necessary scaling factor was 0.00583, which was rounded up to 0.006.
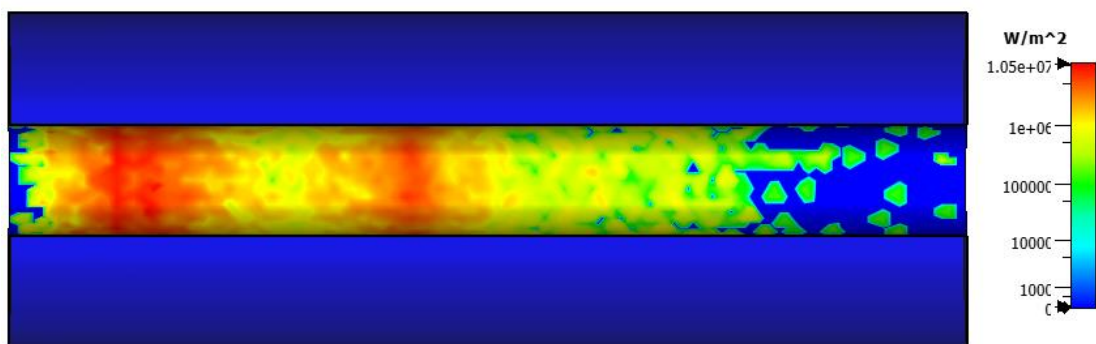
Figure 7.18
Imported particle collision losses on an example structure (11.6mm non-tapered collector)

Figure 7.18 shows the imported particle collision data as a contour plot on the waveguide's internal surface. The maximum value was 1.05kW/cm^2, which is very high. The contour plot shows that only some localised regions display such extreme loading, while most remain significantly lower. Figure 7.19 shows the field along an arbitrary line, illustrating again that the extreme loading is localised.
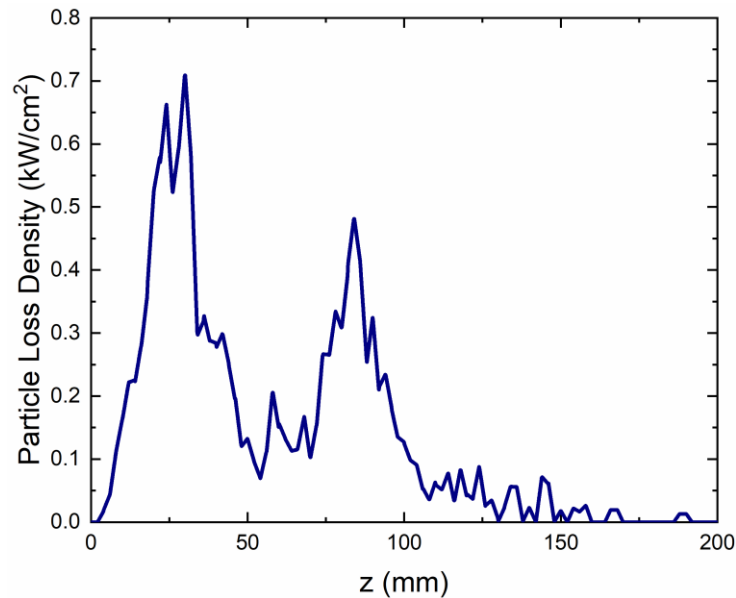
Figure 7.19
Imported particle collision losses on an arbitrary line along the collector wall

The two peaks occur to due to the distribution of electrons in the beam. As the magnetic field falls off, the beam radius expands, depositing electrons on the wall. Since electrons pass through this expansion region with different positions and perpendicular momenta, they follow different trajectories with the peaks in deposition density corresponding to higher concentrations of electrons in the relevant parameter space.

As well as surface loading, the resulting temperature increase of the structure is important to consider. Collectors often use cooling channels to allow heat to transfer from the metal to pressurised cold water which is pumped through the system to reduce the thermal load on the material. Including a representation of the cooling structure was the next step toward building a more realistic simulation than the copper block. The heat transfer rate (in Watts) between a surface and a liquid can be calculated by

$$\dot{Q} = F \times A \times (T_2 - T_1) \qquad\qquad (7.17)$$

where *F* is the film coefficient, *A* is the surface area of the transfer surface, T_2 is the temperature of the surrounding fluid, and T_1 is the temperature of the solid surface. However, this equation in isolation provides limited scope for analysis as the temperature distribution is non-uniform and the film coefficient of water can be anywhere in a large range of values depending on properties.

The most typical cooling-channel geometry uses grooves parallel to the device axis, though radial grooves and crossed grooves have also seen some study [256], as have helical grooves [257]. In this instance, only longitudinal grooves have been considered. The number of grooves and their dimensions allow for many different variations of the geometry. Complete design of the pumping and piping system was not considered as it is beyond the scope of a typical CST simulation. Instead, the cooling effect was approximated by setting thermal surface properties to the outer boundary of the structure, a method which has also been applied in [258]. A heat transfer rate of 30kWm^{-2} was applied, and parameter sweeps were performed varying the thickness, depth, and number of grooves in the structure. Differences in the maximum temperature were observed to change only on the order of a few percent over several different versions of cooling channel geometry and a large range of heat transfer coefficients. The geometry selected is illustrated in figure 7.20, but this should be considered an example only as a complete design of the channel geometry would require an advanced simulation to include fluid dynamics programs, which is beyond the

Figure 7.20
Cooling channel geometry

scope of the CST model used here. The model used is suitable to estimate maximum temperatures in the structure and optimise the profile of the deposition surface. The crucial results that must be considered are:

186

- The electron deposition density is imported as a heat source.

- The maximum temperature in the structure. A reasonable upper bound to set as a limit is 400°C (673K).

- The limit for the temperature at the boundary. A reasonable upper limit is around 70°C (343K).

Figure 7.21 displays the temperature distribution in the 11.6mm collector. With the assigned thickness of the wall, the temperature meets the requirement at water-boundary surface. Although the maximum temperature is lower than the selected limit, it was still desirable to lower it to improve lifespan, and the high values of particle deposition were above limitations.
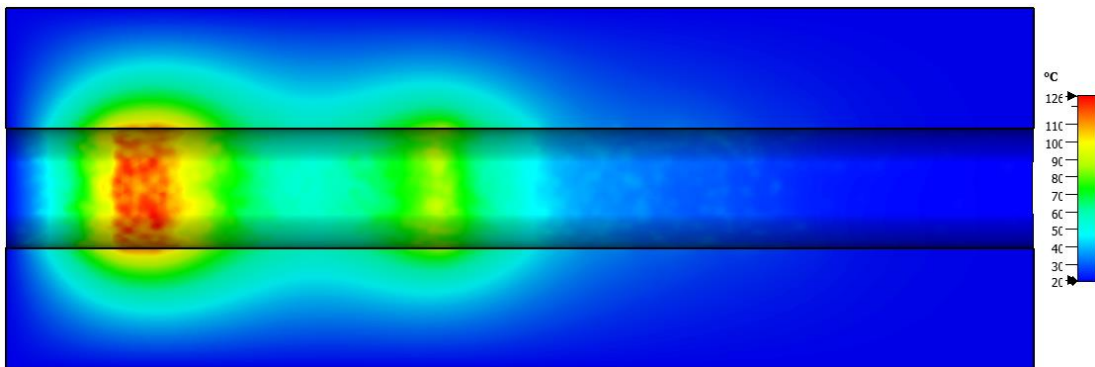
Figure 7.21
Contour plot of temperature in the deposition region for an 11.6mm collector

To reduce the loading, the collector surface geometry was considered. A tapered surface or larger radius would increase the surface area over which particles are deposited, thus lowering the peak loading. The maximum surface area without considering complex corrugations is a cylinder of large radius. The particle export interface is far from the cavity aperture, meaning there is room to include the required tapering before the deposition surface.

An example structure 16mm radius collecting surface showed a slightly lower peak temperature, as shown in figure 7.22, and also a lower maximum particle collision loss of 0.71kW/cm^2, however this was again at a small, localised point, while the
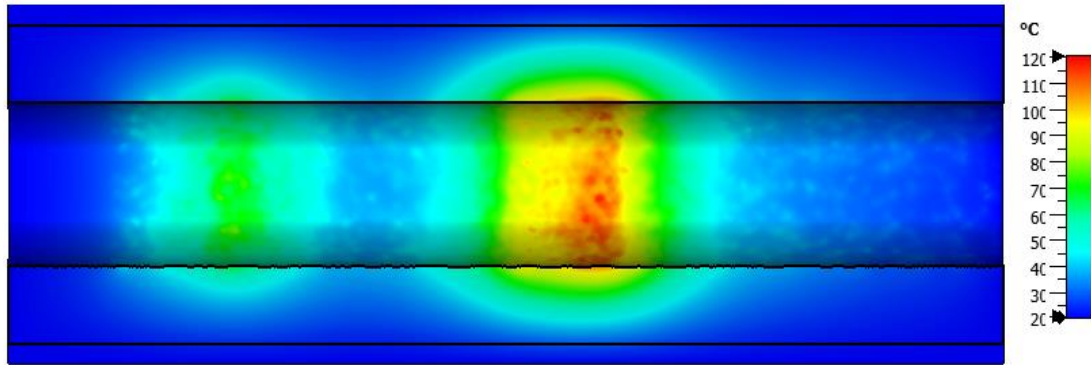
Figure 7.22
Contour plot of temperature in the deposition region for a 16mm collector

maximum along a typical line along the surface was below 0.5kW/cm^2, such as that shown in figure 7.23.
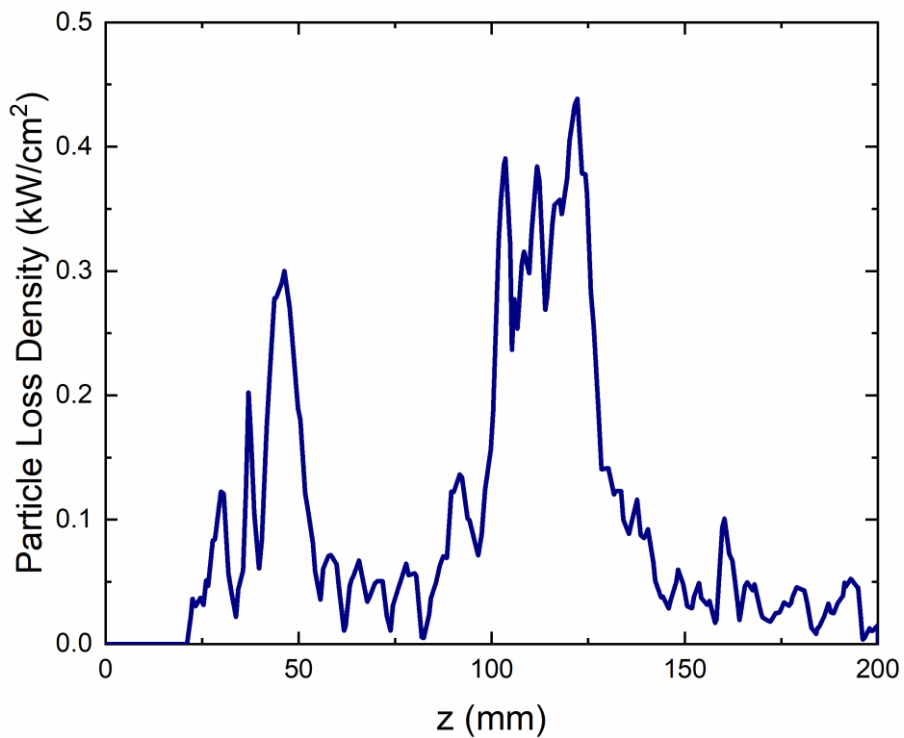
Figure 7.23
Imported particle collision data along a surface line for the 16mm radius collector

The particle collision data depends only on the deposition surface and can therefore be analysed without concern for the geometry of anything beyond that surface. The temperature figures shown give some further insight into the feasibility, showing that overheating is unlikely. However, the above temperature plots considered only an arbitrary thickness of the wall and further simulation shows that the wall thickness

has a large effect on maximum temperature. If the distance between the deposition surface and the water interface is too large, cooling is inefficient. Figure 7.24 shows the difference in maximum simulated temperature for a range of wall thicknesses.
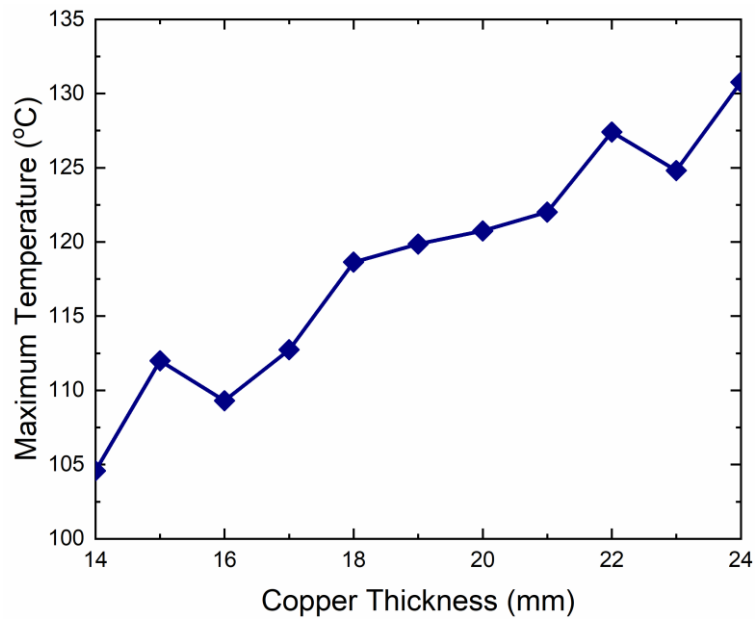
Figure 7.24
Variation of maximum simulated temperature with wall thickness

The results presented in this section demonstrate the feasibility of the collector. The maximum temperature result should be taken as a rough estimate, since the full design of the cooling mechanisms would require further study with a more advanced simulation model which can give a complete representation of the fluid dynamics in the water channels. The particle collision density is determined by the geometry of the internal wall and the magnetic field profile and is hence accurate regardless of the external wall geometry. It has been shown that the particle deposition loading remains within safe limits.

Chapter 8: Conclusions and Future Work

This chapter summarises the main conclusions of the thesis in section 8.1, and then section 8.2 discusses the steps that could follow from this foundation.

8.1: Main Results and Conclusions

A gyroklystron amplifier operating at 48GHz has been designed with consideration of powering a microwave pulse compressor for driving a harmonic lineariser system of an RF linac. This frequency has previously received little attention and hence no suitable amplifiers were available to support the lineariser concept. The work presented in this thesis details the first published design for a multi-MW RF amplifier at 48GHz. The targets for operating parameters were established by consideration of the CompactLight XFEL, informed through discussions with other members of the project.

The design process began with the consideration of fundamental equations, such as those for eigenfrequencies and waveguide cut-off frequencies. This was used to guide work through a linear theoretical model (section 3.1), which established some rough estimates to aid in the choice of cavity size and number. While valuable for some initial estimations, the linear theory can offer no deep analysis, and more accurate methods are required. The rough estimate from linear theory was improved using a nonlinear model (section 3.2). By this method, a basic structure was established, which was finalised and optimised by particle-in-cell simulation (section 3.3).

Alongside the interaction circuit design, the electron beam source was developed. The beam source is a magnetron injection gun, which uses field-enhanced thermionic emission operating in the temperature-limited regime to produce a high-current beam which is then given the desired properties and guided through the interaction circuit by an optimised arrangement of fields. Initial studies suggested that a simple

diode-type gun would not satisfy requirements, and hence a triode-type gun was designed and optimised using the particle tracking software TRAK. The analysis of the interaction circuit and gun was intertwined, as the required parameters for interaction dictate the MIG goals, while the achievable MIG performance dictates the maximum current and efficiency of the interaction.

2.3MW of output was predicted for the ideal beam case, but as no beam source can fully eliminate the spread in the velocity and velocity ratio, the realistic output is limited by the MIG design. The MIG presented in this thesis achieved a velocity ratio spread of 8.9%. With consideration of this value, the expected output power of the gyroklystron is 2.0MW, with an efficiency of 38% and gain of 35dB. The output signal of the gyroklystron would travel via a mode converter and pulse-compressor before reaching the lineariser. These components set a bandwidth requirement, which the presented design achieves with a 3dB-bandwitdh of 400MHz. These parameters show strong performance and demonstrate the gyroklystron to be a good candidate for a 48GHz lineariser system.

To complete the gyroklystron design, the vacuum windows and input coupler were also designed. The windows were developed using optimisation routines in CST Microwave Studio to minimise the reflection over the gyroklystron bandwidth. The windows were able to meet the target reflection parameters required provided high machining precision is applied in their construction. The input coupler has also been designed to successfully excite a useable mode in the input cavity. The purity of the coupled mode is slightly below target but remains suitable for bunching the electron beam. Finally, the collector was considered, and reasonable particle deposition density was demonstrated, though the complete design of the cooling channels will require further study in the experimental stage of the project.

As the first published work on a 48GHz amplifier at the multi-MW power level, this thesis marks a step toward 48GHz systems becoming more attractive for use in linac design. A high drive frequency enables a high acceleration gradient, and hence there

is incentive to develop 12GHz accelerators, which would be well-served by a 48GHz (4th harmonic) linearisation system.

8.2: Related Future Work

8.2.1: Cooling System Design

In this thesis, the collector has been considered using particle tracking and thermal analysis. Reasonable performance has been demonstrated, and there is good confidence in the result. The results for particle collision losses are reliable as that parameter primarily depends on the internal surface geometry of the collector wall. However, the heat transfer was modelled as a simple surface property without the full design of the cooling channels. The calculated thermal properties of the collector structure demonstrate feasible performance, but the complete design of the cooling system is an engineering challenge rather than a physics problem. Simulation with a more detailed model that can fully account for fluid dynamics and flow rate in the cooling channels could provide a solid point to begin consultation with manufacturers to finalise a functional hydraulic system to be used to cool the collector.

8.2.2: Options to Increase Gain and Output Power

There are several options for future work that involve new designs that could be developed from the ground up, with the direction influenced by this work. Although the design target has been met, an alternate design with higher gain could still be of interest, depending on the trade-off between reducing input power demand and the initial cost and complexity of design and manufacture. The 2MW output power predicted by the simulations in this thesis meets the target that was set, but higher output power would still be beneficial to the lineariser application and the progress of gyroklystron design work in general. Several options could be considered to improve the power or gain:

1. A three cavity gyroklystron operating with a larger accelerating potential (<500kV) and current (200A to 300A) driving a Magnetron Injection Gun for larger output power at PRFs up to 100Hz.

2. A four (or more) cavity gyroklystron.

3. A gyroklystron operating at the second harmonic of the cyclotron frequency.

4. A gyroklystron operating at higher-order mode to allow for a larger output cavity.

5. An Inverted Magnetron Injection Gun with a larger area thermionic cathode emitter compatible with cylindrical or co-axial cavities.

6. A coaxial beam-wave interaction circuit to allow a larger radius beam guiding center. It will help to increase the emitter radius and reduce the current density of the cathode.

For a four-cavity gyroklystron, the optimisation process would be more complicated, but would still follow the same general design process. While the final design would be more costly to manufacture due to the larger size and more critical alignment requirement, it could potentially produce the same output power with less input power thus reducing the capital procurement cost of the driver. Part of the limitation on output power comes from the cavity size and maximum beam current, so with a similar dimension to the output cavity, one would still expect the saturated output to be similar. Although the maximum output power might not be increased, a four-cavity design would potentially allow for higher gain and a significant reduction in the required input power to achieve the same output. Initial linear theory examination of the 4-cavity option did not suggest major benefits over the 3-cavity version, but linear theory only offers rough predictions, and it would require a more detailed study with nonlinear theory and PIC simulation to confirm or deny that prediction. If improvements to the cost-effectiveness of the amplifier due to the reduced output power of the driver were to be achieved with a 4-cavity design, the financial benefit would likely be negligible when considered in the context of the overall construction and running cost of an XFEL facility.

If aiming for a higher output power value, the $TE_{0,2}$ cylindrical cavity may prove to be too small. $TE_{0,3}$ devices do exist but have not been demonstrated at comparable power and frequency values to the multi-MW 48GHz range. It would remain to be

seen from a design study whether the larger power-handling capacity could effectively offset the issue of the lower coupling coefficient observed in such a cavity. The possibility of a $TE_{0,3}$ mode in the output may be worth studying at least to the stage of linear and nonlinear simulations, and then only continuing into full PIC optimisation if the prior results are promising. However, due to the lower coupling coefficient of the third-order mode, it is unlikely that this would prove to be an effective solution. Alternatively, one could consider larger cavities using the higher-order modes that were briefly mentioned in section 1.3.3. These could allow for higher power, but the need for additional mode conversion structures may increase the cost and space requirements, and the challenge of correctly exciting such a mode may prove too debilitating.

A higher-order or 4-cavity solution combined with the use of either a MIG or IMIG should not be immediately ruled out as an option to achieve higher power at 48GHz. The development of a 48GHz gyroklystron operating at the second harmonic of the cyclotron frequency with either a cylindrical or coaxial cavity is also worth further consideration. Coaxial designs require extremely precise manufacturing to ensure proper alignment, but this challenge is to be balanced with issues of mode control and conversion in high-order cylindrical cavities. Additionally, coaxial gyroklystrons have been widely studied and hence there is a larger depth of existing theoretical and experimental work available to aid design considerations. Therefore, a follow-up study into new designs with higher output power would likely consider both a 4-cavity cylindrical design and a 3- or 4-cavity coaxial design that allows for a larger beam voltage and current. No option should be categorically ruled out before some analysis to assess the feasibility and relative merits of each has been carried out.

8.2.3: 3D Simulations and Fabrication of the Presented Design

The results presented demonstrate a promising device. The level of confidence in the simulation models used in this thesis is high, and agreement between the simulation

model and experimental work has been presented in previous gyroklystron studies [210]. Nonetheless, further confirmation through other simulation packages and 3D models would further enhance the credibility of the results. The 2D model by definition cannot analyse the effect of azimuthal variations and hence cannot quantify potential competition from the $TE_{1,1}$ mode which can only exist in a 3D model. The effect of the azimuthal dimension is expected to be negligible with 3D analysis producing very similar results, just as was the case for the 36GHz model developed by Strathclyde and UESTC [57].

Following this rigorous verification of results, a device prototype should then be manufactured for experimental tests. A prototype gyroklystron would require all components, including the vacuum windows, coupler, and collector. In this thesis, the interaction circuit, MIG, input coupler, input window, output window, and collector have all been considered. Most of these components have been presented in detail, while the collector has been considered in a more simplified simulation. Complete design of the cooling channels and water pump would be required before a prototype could be constructed.

8.3: Closing Remarks

The predicted performance of the design presented in this thesis meets the requirements outlined for CompactLight. Compatible values for output power (2MW), frequency (48GHz), efficiency (38%), gain (35dB), and mode of operation ($TE_{0,1}$-$TE_{0,1}$-$TE_{0,2}$) have been achieved. The required voltage (140kV), current (37A), pulse duration (1.5µs), and phase stability (<0.5%) are compatible with commercially available modulators such as Scandinova K100 which can operate at the required pulse repetition frequency of 1000Hz and voltage stability of 0.004%. Although the CompactLight plan has since settled on a 6th harmonic lineariser, the demonstration of a viable power supply for an 8th harmonic alternative provided value to the project and beyond. The design presented here could represent a viable driver for a harmonic lineariser in future acceleration applications. In particular, it may be relevant in the 4th harmonic lineariser system of a 12GHz main frequency. 12GHz is a likely candidate for future accelerators as it is within the limitations of current commercial amplifiers. An accelerator driven by 12GHz SLAC klystrons would require a lineariser beyond that for which conventional klystrons can deliver sufficient power. While both gyroklystron and MBK solutions have been demonstrated at 36GHz, the 48GHz option was an open question. This thesis presented a 48GHz gyroklystron that would be appropriate to drive a 48GHz lineariser.

The significance of this work is further enhanced by its place among the first studies at the frequency band around 48GHz, which has previously been largely under-explored within the high-power microwave community. Prior work has often focused around 36GHz and 94GHz due to their favourable atmospheric transmission properties for Radar applications. The growing interest in C-band and X-band accelerating systems over recent years has introduced a new interest in V-band frequencies, and in turn re-introduced the idea of gyroklystrons as components of accelerator systems.

The work presented in this thesis demonstrates that the gyroklystron is a suitable device to deliver high-efficiency, MW-level performance at 48GHz while also meeting tight specifications for parameters such as phase stability and bandwidth dictated by the requirements of the harmonic lineariser.

Appendix: Linear Theory Data

This appendix provides more detail on the results of chapter 5, namely table 5.1 as repeated below.

Cavities	Efficiency (%)	Gain (dB)
3-cavity ($TE_{0,1}$-$TE_{0,1}$-$TE_{0,2}$)	33	30
4-cavity ($TE_{0,1}$-$TE_{0,1}$-$TE_{0,1}$-$TE_{0,2}$)	38	37
4-cavity ($TE_{0,1}$-$TE_{0,1}$-$TE_{0,2}$-$TE_{0,2}$)	24	43

The above data was gathered using a linear theory model constructed in MATLAB from the equations in section 3.1 and section 3.2 with the efficiency and gain being the results of equations 3.30 and 3.32 respectively. Note that linear theory cannot offer complete performance predictions and these numbers should be treated as no more than rough ballpark figures to aid in the set-up of the subsequent non-linear analysis. The linear model is not detailed enough to consider factors such as stagger-tuning or the effect of dielectric linings and drift tunnels, hence cavity dimensions used here differ from the final design. In each example above, each $TE_{0,1}$ cavity had a radius of 4mm and length of 9.9mm and each $TE_{0,2}$ cavity had a radius of 7.3mm and length of 10.5mm. Since the linear theory depends on a small-field approximation, the MW-level power of the final device cannot be accurately implemented. Instead beam current and input power were set several orders of magnitude below their actual values (while keeping V_b high for the correct y). As illustrated in Chapter 6, altering these parameters can have a significant effect on the result. Despite these limitations, the output of the linear theory can provide some useful insight into which options to consider moving forward. In this case the linear theory implied that either of the first two could potentially be appropriate. The first option proved suitable following nonlinear simulation so it was not deemed necessary to explore the 4-cavity alternative at this stage, though it may remain of interest for the future development of a higher gain alternative.

Bibliography

[1]   "CompactLight Homepage." http://www.compactlight.eu/Main/HomePage (accessed 2020).

[2]   A. Mak, P. Salén, V. Goryashko, and J. Clarke, "XLS Deliverable D2.1, WP2: FEL Science Requirements and Facility Design," *CompactLight Design Reports,* 2018.

[3]   H. P. Freund and T. M. Antonsen, Jr., *Principles of Free Electron Lasers*. Cham: Cham: Springer, 2018.

[4]   J. M. J. Madey, H. A. Schwettman, and W. M. Fairbank, "A Free Electron Laser," *IEEE Transactions on Nuclear Science,* vol. 20, no. 3, pp. 980-983, 1973, doi: 10.1109/TNS.1973.4327304.

[5]   H. Motz, "Applications of the Radiation from Fast Electron Beams," *Journal of Applied Physics,* vol. 22, no. 5, pp. 527-535, 1951, doi: 10.1063/1.1700002.

[6]   R. M. Phillips, "The Ubitron, a high-power traveling-wave tube based on a periodic beam interaction in unloaded waveguide," *IRE Transactions on Electron Devices,* vol. 7, no. 4, pp. 231-241, 1960, doi: 10.1109/T-ED.1960.14687.

[7]   J. M. J. Madey, "Stimulated Emission of Bremsstrahlung in a Periodic Magnetic Field," *Journal of Applied Physics,* vol. 42, no. 5, pp. 1906-1913, 1971, doi: 10.1063/1.1660466.

[8]   L. R. Elias, W. M. Fairbank, J. M. J. Madey, H. A. Schwettman, and T. I. Smith, "Observation of stimulated emission of radiation by relativistic electrons in a spatially periodic transverse magnetic field," *Physical Review Letters,* vol. 36, no. 13, pp. 717-720, 1976, doi: 10.1103/PhysRevLett.36.717.

[9]   D. A. G. Deacon, L. R. Elias, J. M. J. Madey, G. J. Ramian, H. A. Schwettman, and T. I. Smith, "First operation of a free-electron laser," *Physical Review Letters,* vol. 38, no. 16, pp. 892-894, 1977, doi: 10.1103/PhysRevLett.38.892.

[10]   M. Billardon *et al.*, "First operation of a storage-ring free-electron laser," *Physical Review Letters,* vol. 51, no. 18, pp. 1652-1655, 1983, doi: 10.1103/PhysRevLett.51.1652.

[11]   M. Billardon *et al.*, "Free electron laser experiment at Orsay: A review," *IEEE Journal of Quantum Electronics,* vol. 21, no. 7, pp. 805-823, 1985, doi: 10.1109/JQE.1985.1072733.

[12]   G. N. Kulipanov *et al.*, "The VEPP-3 storage-ring optical klystron: Lasing in the visible and ultraviolet regions," *Nuclear Inst. and Methods in Physics Research, A,* vol. 296, no. 1-3, pp. 1-3, 1990, doi: 10.1016/0168-9002(90)91179-F.

[13]   T. I. Smith, H. A. Schwettman, R. Rohatgi, Y. Lapierre, and J. Edighoffer, "Development of the SCA/FEL for use in biomedical and materials science experiments," *Nuclear Inst. and Methods in Physics Research, A,* vol. 259, no. 1, pp. 1-7, 1987, doi: 10.1016/0168-9002(87)90421-9.

[14]   K. E. Robinson *et al.*, "Panorama of the visible wavelength FEL oscillator," *Nuclear instruments & methods in physics research.,* vol. 259, no. 1-2, pp. 49-55, 1987, doi: 10.1016/0168-9002(87)90428-1.

[15]   R. Warren, B. Newnam, J. Winston, W. Stein, L. Young, and C. Brau, "Results of the Los Alamos free-electron laser experiment," *IEEE Journal of Quantum Electronics,* vol. 19, no. 3, pp. 391-401, 1983, doi: 10.1109/JQE.1983.1071854.

[16]   W. B. Colson and A. M. Sessler, "Free Electron Lasers," *Annual Review of Nuclear and Particle Science,* vol. 35, pp. 25-54, 1985.

[17]   E. A. Seddon *et al.*, "Short-wavelength free-electron laser sources and science: a review," *Reports on Progress in Physics,* vol. 80, p. 115901, 2017, doi: 10.1088/1361-6633/aa7cca.

[18]   P. Schmuser, M. Dohlus, and J. Rossbach, *Ultraviolet and Soft X-Ray Free-Electron Lasers: Introduction to Physical Principles, Experimental Results, Technological Challenges*. Berlin, Heidelberg: Berlin, Heidelberg: Springer Berlin Heidelberg, 2009.

[19]   V. Ayvazyan *et al.*, "Generation of GW radiation pulses from a VUV free-electron laser operating in the femtosecond regime," *Physical review letters,* vol. 88, no. 10, pp. 104802-104802, 2002, doi: 10.1103/PhysRevLett.88.104802.

[20] W. Ackermann *et al.*, "Operation of a free-electron laser from the extreme ultraviolet to the water window," *Nature Photonics,* vol. 1, no. 6, pp. 336-342, 2007, doi: 10.1038/nphoton.2007.76.

[21] S. Schreiber, B. Faatz, and K. Honkavaara, "Operation of FLASH at 6.5nm wavelength," *Proceedings of EPAC08,* pp. 133-135, 2008.

[22] J. Rossbach, Schneider, Jr., and W. Wurth, "10 years of pioneering X-ray science at the Free-Electron Laser FLASH at DESY," *Physics Reports,* vol. 808, pp. 1-74, 2019, doi: 10.1016/j.physrep.2019.02.002.

[23] P. Emma *et al.*, "First lasing and operation of an ångström-wavelength free-electron laser," *Nature Photonics,* vol. 4, no. 9, pp. 641-647, 2010, doi: 10.1038/nphoton.2010.176.

[24] T. Ishikawa *et al.*, "A compact X-ray free-electron laser emitting in the sub-ångström region," *Nature Photonics,* vol. 6, no. 8, pp. 540-544, 2012, doi: 10.1038/nphoton.2012.141.

[25] I. Tetsuya, "SACLA Laser Sets New Record," *Synchrotron Radiation News,* vol. 24, no. 4, pp. 20-20, 2011, doi: 10.1080/08940886.2011.602004.

[26] E. Allaria *et al.*, "The FERMI free‐electron lasers," *Journal of Synchrotron Radiation,* vol. 22, no. 3, pp. 485-491, 2015, doi: 10.1107/S1600577515005366.

[27] C. J. Bocchetta *et al.*, "FERMI@Elettra Conceptual Design Report," *Sincrotrone Trieste,* 2007.

[28] T. Y. Lee *et al.*, "Design status of PAL-XFEL," *28th International Free Electron Laser Conference,* pp. 210-213, 2006.

[29] "Pohang Accelerator Laboratory - 2017 Science Highlights," *Pohang Accelerator Laboratory,* 2018.

[30] M. Altarelli, "The European X-ray free-electron laser facility in Hamburg," *Nuclear Inst. and Methods in Physics Research, B,* vol. 269, no. 24, pp. 2845-2849, 2011, doi: 10.1016/j.nimb.2011.04.034.

[31] R. Abela *et al.*, "XFEL: The European X-Ray Free-Electron Laser - Technical Design Report," *DESY Hamburg,* 2006.

[32] Z. Zhao *et al.*, "Shanghai Soft X-Ray Free-Electron Laser Facility," *Zhongguo Jiguang = Chinese Journal of Lasers,* vol. 46, no. 1, p. 0100004, 2019, doi: 10.3788/CJL201946.0100004.

[33] Z. Zhentang *et al.*, "Status of the SXFEL Facility," *Applied Sciences,* vol. 7, no. 6, p. 607, 2017, doi: 10.3390/app7060607.

[34] J. M. Christopher *et al.*, "SwissFEL: The Swiss X-ray Free Electron Laser," *Applied Sciences,* vol. 7, no. 7, p. 720, 2017, doi: 10.3390/app7070720.

[35] T. Schietinger *et al.*, "Commissioning experience and beam physics measurements at the SwissFEL Injector Test Facility," *Physical Review Accelerators and Beams,* vol. 19, no. 10, p. 100702, 2016, doi: 10.1103/PhysRevAccelBeams.19.100702.

[36] C. Erny and C. P. Hauri, "The SwissFEL Experimental Laser facility," *Journal of Synchrotron Radiation,* vol. 23, no. 5, pp. 1143-1150, 2016, doi: 10.1107/S1600577516012595.

[37] P. Abbamonte *et al.*, "New Science Opportunities Enabled by LCLS-II X-ray Lasers," *SLAC National Accelerator Laboratory,* 2015.

[38] "LCLS Strategic Facility Development Plan," *SLAC National Accelerator Laboratory,* 2019.

[39] "Free-Electron Laser (FEL) Strategic Review." https://stfc.ukri.org/files/fel-report-2016/ (accessed September 2021.

[40] S. Boutet, *X-ray Free Electron Lasers: A Revolution in Structural Biology*. Cham: Cham: Springer International Publishing, 2019.

[41] S. Bernal, *A practical introduction to beam physics and particle accelerators*. San Rafael, CA, USA: Morgan & Claypool Publishers, 2016.

[42] M. Aicheler *et al.*, "A Multi-TeV linear collider based on CLIC technology: CLIC Conceptual Design Report," *CERN: CLIC Design Reports,* 2012.

[43] B. Zeitler, K. Floettmann, and F. Grüner, "Linearization of the longitudinal phase space without higher harmonic field," *Physical Review Special Topics. Accelerators and Beams,* vol. 18, no. 12, p. 120102, 2015, doi: 10.1103/PhysRevSTAB.18.120102.

[44] T. I. Smith, "Intense Low Emittance Linac Beams for Free Electron Lasers," *SLAC International Linear Accelerator Conference,* 1986.

[45]   T. I. Smith, "Production of intense low emittance beams for free electron lasers using electron linear accelerators," *Nuclear Instruments and Methods in Physics Research, A,* vol. 250, no. 1, pp. 64-70, 1986, doi: 10.1016/0168-9002(86)90861-2.

[46]   C. E. Hess, H. A. Schwettman, and T. I. Smith, "Harmonically Resonant Cavities for High Brightness Beams," *IEEE Transactions on Nuclear Science,* vol. 32, no. 5, pp. 2924-2926, 1985, doi: 10.1109/TNS.1985.4334228.

[47]   G. Penco *et al.*, "Passive Linearization of the Magnetic Bunch Compression Using Self-Induced Fields," *Physical Review Letters,* vol. 119, no. 18, p. 184802, 2017, doi: 10.1103/PhysRevLett.119.184802.

[48]   N. Y. Huang *et al.*, "Bunch compression in the driver linac for the proposed NSRRC VUV FEL," *6th International Particle Accelerator Conference,* pp. 1738-1740, 2015.

[49]   T. K. Charles *et al.*, "Comparison of bunch compression schemes for the AXXS FEL," *6th International Particle Accelerator Conference,* pp. 1399-1402, 2015.

[50]   K. Flöttman, T. Limberg, and P. Piot, "Generation of ultrashort electron bunches by cancellation of nonlinear distortions in the longitudinal phase space," *FLASH reports,* 2001.

[51]   G. D'Auria *et al.*, "The X-band system for the FERMI@Elettra FEL project," *Proceedings of IPAC'10,* pp. 2173-2175, 2010.

[52]   G. D'auria, S. Di Mitri, G. Penco, and C. Serpico, "RF activation and preliminary beam tests of the x-band linearizer at the FERMI@ElettraFEL project," *Proceedings of IPAC'12,* pp. 1721-1723, 2012.

[53]   J. A. Clarke *et al.*, "The conceptual design of CLARA, a novel fel test facility for ultra-short pulse generation," *FEL 2013: Proceedings of the 35th International Free-Electron Laser Conference,* pp. 496-501, 2013.

[54]   L. S. Cowie *et al.*, "An X-Band Lineariser for the CLARA FEL," *Unpublished internal report,* 2018.

[55]   M. Dehler *et al.*, "X-band RF structure with integrated alignment monitors," *Physical Review Special Topics. Accelerators and Beams,* vol. 12, no. 6, p. 062001, 2009, doi: 10.1103/PhysRevSTAB.12.062001.

[56]   M. Dehler *et al.*, "Fabrication of the CERN/PSI/ST X-band Accelerating Structure," *Proceedings of IPAC2011, San Sebastián, Spain,* pp. 86-88, 2011.

[57]   L. Wang *et al.*, "Design of a Ka-band MW-level high efficiency gyroklystron for accelerators," *IET Microwaves, Antennas & Propagation,* vol. 12, no. 11, pp. 1752-1757, 2018.

[58]   B. Weatherford *et al.*, "Exploratory study of X-band Klystron designs for maximum efficiency," *2018 IEEE International Vacuum Electronics Conference (IVEC),* pp. 23-24, 2018, doi: 10.1109/IVEC.2018.8391533.

[59]   G. Caryotakis, "The X-band Klystron Program at SLAC," *3rd International Workshop on RF Pulsed Power Sources for Linear Colliders (RF 96),* vol. SLAC-PUB-7146, pp. 72-80, 1996.

[60]   A. V. Gaponov, M. I. Petelin, and V. K. Yulpatov, "The Induced Radiation of Excited Classical Oscillators and its Use in High-Frequency Electronics," *Izvestiya Vuz. Radiofizika,* vol. 10, no. 9-10, pp. 1414-1453, 1967.

[61]   J. L. Hirshfield and J. M. Wachtel, "Electron Cyclotron Maser," *Physical Review Letters,* vol. 12, no. 19, pp. 533-536, 1964, doi: 10.1103/PhysRevLett.12.533.

[62]   R. Q. Twiss and J. A. Roberts, "Electromagnetic Radiation from Electrons Rotating in an Ionized Medium Under the Action of a Uniform Magnetic Field," *Australian Journal of Physics,* vol. 11, no. 3, pp. 424-446, 1958.

[63]   J. Schneider, "Stimulated Emission of Radiation by Relativstic Electrons in a Magnetic Field," *Physical Review Letters,* vol. 2, no. 12, pp. 504-505, 1959.

[64]   A. V. Gaponov, "Interaction between electron fluxes and electromagnetic waves in waveguides," *Izvestiya Vuz. Radiofizika,* vol. 2, p. 837, 1959.

[65]   B. Levush, B. G. Danly, and R. K. Parker, "A quarter century of gyrotron research and development," *IEEE Transactions on Plasma Science,* vol. 25, no. 6, pp. 1322-1335, 1997.

[66]   A. Arsenjewa-Heil and O. Heil, "Eine neue Methode zur Erzeugung kurzer, ungedämpfter, elektromagnetischer Wellen großer Intensität [A new method for the generation of short, undamped electromagnetic waves of high intensity]," *Zeitschrift für Physik,* vol. 95, no. 11-12, pp. 752-762, 1935, doi: 10.1007/BF01331341.

[67]   R. H. Varian and S. F. Varian, "A High Frequency Oscillator and Amplifier," *Journal of Applied Physics,* vol. 10, no. 5, pp. 321-327, 1939, doi: 10.1063/1.1707311.

[68]   S. E. Tsimring, *Electron Beams and Microwave Vacuum Electronics* (Wiley Series in Microwave and Optical Engineering). Hoboken, New Jersey, USA: John Wiley & Sons, 2007.

[69]   G. Burt *et al.*, "A millimeter-wave klystron upconverter with a higher order mode output cavity," *IEEE Transactions on Electron Devices,* vol. 64, no. 9, pp. 3857 - 3862, 2017, doi: 10.1109/TED.2017.2724581.

[70]   D. Sprehn *et al.*, "Latest Results in SLAC 75 MW PPM Klystrons," *AIP Conference Proceedings,* vol. 807, no. 1, 2006.

[71]   V. L. Granatstein and W. Lawson, "Gyro-amplifiers as candidate RF drivers for TeV linear colliders," *IEEE Transactions on Plasma Science,* vol. 24, no. 3, pp. 648-665, 1996, doi: 10.1109/27.532948.

[72]   G. S. Nusinovich, *Introduction to the Physics of Gyrotrons*. Baltimore, Maryland, USA: The John Hopkins University Press, 2004.

[73]   M. Thumm, "State-of-the-Art of High-Power Gyro-Devices and Free Electron Masers," *Journal of Infrared, Millimeter, and Terahertz Waves,* vol. 41, no. 1, 2020, doi: 10.1007/s10762-019-00631-y.

[74]   W. He, L. Zhang, C. R. Donaldson, A. W. Cross, and A. D. R. Phelps, "Demonstration of a high power broadband mm-wave gyro-TWA," *10th UK-Europe-China Workshop on Millimeter Waves and Terahertz Technologies (UCMTT),* 2017.

[75]   M. Thottappan, S. P. Singh, and P. K. Jain, "Analysis and PIC simulation of a Gyrotron travelling wave tube amplifier," *Journal of Microwaves, Optoelectronics and Electromagnetic Applications,* vol. 12, no. 2, pp. 307-324, 2013, doi: 10.1590/S2179-10742013000200006.

[76]   H. Guo, J. Rodgers, S. Chen, M. Walter, and V. L. Granatstein, "Experimental investigation of a phase-locked harmonic multiplying inverted gyrotwystron," *1996 IEEE International Conference on Plasma Science,* p. 304, 1996, doi: 10.1109/PLASMA.1996.551682.

[77]   K. Chow and R. Pantell, "The Cyclotron Resonance Backward-Wave Oscillator," *Proceedings of the IRE,* vol. 48, no. 11, pp. 1865-1870, 1960, doi: 10.1109/JRPROC.1960.287421.

[78]   I. B. Bott, "Tuneable Source of Millimetre and Submillimetre Radiation," *Proceedings of the IEEE,* vol. 52, 1964.

[79]   I. B. Bott, "A Powerful Source of Millimetre Wavelength Electromagnetic Radiation," *Physics Letters,* vol. 14, no. 4, p. 293, 1965, doi: 10.1016/0031-9163(65)90206-4.

[80]   V. A. Flyagin, A. V. Gaponov, M. I. Petelin, and V. K. Yulpatov, "The Gyrotron," (in English), *IEEE Transactions on Microwave Theory and Techniques,* Article vol. 25, no. 6, pp. 514-521, 1977, doi: 10.1109/tmtt.1977.1129149.

[81]   M. J. Smith, "The Gyrotron," *Electronics and Power,* vol. 27, no. 5, pp. 389-392, 1981, doi: 10.1049/ep.1981.0193.

[82]   N. I. Zaytsev, T. B. Pankratova, M. I. Petelin, and V. A. Flyagin, "Millimeter and Submillimeter Waveband Gyrotrons," *Radiotekh Elektron,* vol. 5, pp. 1056-1060, 1974.

[83]   A. A. Andronov *et al.*, "The gyrotron: High-power source of millimetre and submillimetre waves," *Infrared Physics,* vol. 18, no. 5, pp. 385-393, 1978, doi: 10.1016/0020-0891(78)90045-3.

[84]   A. V. Gaponov *et al.*, "Powerful Millimetre-wave Gyrotrons," *International Journal of Electronics,* vol. 51, no. 4, pp. 277-302, 1981.

[85]   L. I. Pangonis and M. V. Persikov, "Analysis of wave models based on radiation from waveguides with an inclined aperture," *Radiotekh Electron.,* vol. 16, pp. 2300-2302, 1971.

[86]   S. Vlasov, I. Orlova, and M. Petelin, "Quasioptical transformation of natural waves of waveguides having a circular cross section by means of axially symmetrical reflectors," *Radiophysics and Quantum Electrons,* vol. 15, no. 12, pp. 1466-1470, 1972, doi: 10.1007/BF01033270.

[87]   S. Vlasov and I. Orlova, "Quasioptical transformer which transforms the waves in a waveguide having a circular cross section into a highly directional wave beam," *Radiophysics and Quantum Electronics,* vol. 17, no. 1, pp. 115-119, 1974, doi: 10.1007/BF01037072.

[88]   N. Kovalev, I. Orlova, and M. Petelin, "Wave transformation in a multimode waveguide with corrugated walls," *Radiophysics and Quantum Electronics,* vol. 11, no. 5, pp. 449-450, 1968, doi: 10.1007/BF01034380.

[89]   U. Singh, N. Kumar, and A. K. Sinha, "Gyrotron and its Electron Beam Source: A Review," *Journal of Fusion Energy,* vol. 31, no. 5, pp. 489-505, 2012, doi: 10.1007/s10894-011-9495-z.

[90]   G. Dammertz, E. Borie, C. T. Iatrou, M. Kuntze, B. Piosczyk, and M. K. Thumm, "140-GHz gyrotron with multimegawatt output power," *IEEE Transactions on Plasma Science,* vol. 28, no. 3, pp. 561-566, 2000, doi: 10.1109/27.887673.

[91]   A. Kasugai, R. Minami, K. Takahashi, N. Kobayashi, and K. Sakamoto, "Long pulse operation of 170 GHz ITER gyrotron by beam current control," *Fusion Engineering and Design,* vol. 81, no. 23, pp. 2791-2796, 2006, doi: 10.1016/j.fusengdes.2006.07.077.

[92]   M. Glyavin and A. Luchinin, "A terahertz gyrotron with pulsed magnetic field," *Radiophysics and Quantum Electronics,* vol. 50, no. 10, pp. 755-761, 2007, doi: 10.1007/s11141-007-0066-0.

[93]   T. Idehara *et al.*, "Development of Terahertz FU CW Gyrotron Series for DNP," *Applied Magnetic Resonance,* vol. 34, no. 3, pp. 265-275, 2008, doi: 10.1007/s00723-008-0132-6.

[94]   M. Y. Glyavin, A. G. Luchinin, and G. Y. Golubiatnikov, "Generation of 1.5-kW, 1-THz coherent radiation from a gyrotron with a pulsed magnetic field," *Physical Review Letters,* vol. 100, no. 1, p. 015101, 2008, doi: 10.1103/PHYSREVLETT.100.015101.

[95]   M. Glyavin *et al.*, "Terahertz gyrotrons: State of the art and prospects," *Journal of Communications Technology & Electronics,* vol. 59, no. 8, pp. 792-797, 2014, doi: 10.1134/S1064226914080075.

[96]   G. Nusinovich, M. Thumm, and M. Petelin, "The Gyrotron at 50: Historical Overview," *Journal of Infrared Millimeter & Terahertz Waves,* vol. 35, no. 4, pp. 325-381, 2014, doi: 10.1007/s10762-014-0050-7.

[97]   N. Kumar, U. Singh, T. Singh, and A. Sinha, "A Review on the Applications of High Power, High Frequency Microwave Source: Gyrotron," *Journal of Fusion Energy,* vol. 30, no. 4, pp. 257-276, 2011, doi: 10.1007/s10894-010-9373-0.

[98]   N. Kumar, U. Singh, A. Bera, and A. K. Sinha, "A review on the sub-THz/THz gyrotrons," *Infrared Physics and Technology,* vol. 76, pp. 38-51, 2016, doi: 10.1016/j.infrared.2016.01.015.

[99]   J. Jacquinot *et al.*, "Progress on the heating and current drive systems for ITER," *Fusion Engineering and Design,* vol. 84, no. 2, pp. 125-130, 2009, doi: 10.1016/j.fusengdes.2009.01.100.

[100]   T. Omori *et al.*, "Progress in the ITER electron cyclotron heating and current drive system design," *Fusion Engineering and Design,* vol. 96-97, pp. 547-552, 2015, doi: 10.1016/j.fusengdes.2014.12.023.

[101]   I. I. Antakov, A. V. Gaponov, V. A. Gintsburg, M. I. Petelin, and V. K. Yulpatov, "An amplifier of electromagnetic oscillations in centimeter, millimeter, and sub-millimeter wavelength regions: International Patent Number 302050," 1967.

[102]   J. M. Wachtel and J. L. Hirshfield, "Interference beats in pulse-stimulated cyclotron radiation," *Physical Review Letters,* vol. 17, no. 7, pp. 348-351, 1966, doi: 10.1103/PhysRevLett.17.348.

[103]   W. Lawson, J. Calame, V. L. Granatstein, G. S. Park, C. D. Striffler, and J. Neilson, "The design of a high peak power relativistic magnetron injection gun," *International Journal of Electronics,* vol. 61, no. 6, pp. 969-984, 1986, doi: 10.1080/00207218608920933.

[104]   W. Lawson *et al.*, "High-power operation of a three-cavity X-band coaxial gyroklystron," *Physical Review Letters,* vol. 81, no. 14, pp. 3030-3033, 1998, doi: 10.1103/PhysRevLett.81.3030.

[105]   W. M. Bollen, A. H. McCurdy, B. Arfin, R. K. Parker, and A. K. Ganguly, "Design and Performnance of a Three-Cavity Gyroklystron Amplifier," *IEEE Transactions on Plasma Science,* vol. 13, no. 6, pp. 417-423, 1985, doi: 10.1109/TPS.1985.4316455.

[106]   J. P. Calame and W. G. Lawson, "A modified method for producing carbon-loaded vacuum-compatible microwave absorbers from a porous ceramic," *IEEE Transactions on Electron Devices,* vol. 38, no. 6, pp. 1538-1543, 1991, doi: 10.1109/16.81651.

[107]   W. Lawson *et al.*, "Efficient operation of a high-power X-band gyroklystron," *Physical Review Letters,* vol. 67, no. 4, pp. 520-523, 1991, doi: 10.1103/PhysRevLett.67.520.

[108]   W. Lawson, J. P. Calame, B. P. Hogan, M. Skopec, C. D. Striffler, and V. L. Granatstein, "Performance characteristics of a high- power X- band two-cavity gyroklystron," *IEEE Transactions on Plasma Science,* vol. 20, no. 3, pp. 216-223, 1992, doi: 10.1109/27.142822.

[109]   A. A. Tolkachev, B. A. Levitan, G. K. Solovjev, V. V. Veytsel, and V. E. Farber, "A megawatt power millimeter-wave phased-array radar," *IEEE Aerospace and Electronic Systems Magazine,* vol. 15, no. 7, pp. 25-31, 2000, doi: 10.1109/62.854021.

[110]   B. G. Danly *et al.*, "Development and testing of a high- average power, 94-GHz gyroklystron," *IEEE Transactions on Plasma Science,* vol. 28, no. 3, pp. 713-726, 2000, doi: 10.1109/27.887710.

[111]   M. Blank *et al.*, "Demonstration of a 10 kW average power 94 GHz gyroklystron amplifier," *Physics of Plasmas,* vol. 6, no. 12, pp. 4405-4409, 1999, doi: 10.1063/1.873726.

[112]   M. T. Ngo, B. G. Danly, R. Myers, D. E. Pershing, V. Gregers-Hansen, and G. Linde, "High-power millimeter-wave transmitter for the NRL WARLOC radar," *Third IEEE International Vacuum Electronics Conference,* pp. 363-364, 2002, doi: 10.1109/IVELEC.2002.999424.

[113]   G. J. Linde, M. T. Ngo, B. G. Danly, W. J. Cheung, and V. Gregers-Hansen, "WARLOC: A high-power coherent 94 GHz radar," *IEEE Transactions on Aerospace and Electronic Systems,* vol. 44, no. 3, pp. 1102-1117, 2008, doi: 10.1109/TAES.2008.4655367.

[114]   E. V. Zasypkin, I. G. Gachev, and I. I. Antakov, "Experimental study of a W- band gyroklystron amplifier operated in the high-order TE021 cavity mode," *Radiophysics and Quantum Electronics,* vol. 55, no. 5, p. 309, 2012.

[115]   Z.-H. Geng and P.-K. Liu, "Design of a ka-band second harmonic gyroklystron amplifier by using a self-consistent nonlinear simulation," *IEEE Transactions on Plasma Science,* vol. 34, no. 3, pp. 534-540, 2006, doi: 10.1109/TPS.2006.875761.

[116]   P.-K. Liu *et al.*, "Recent Results in the Development of a Ka- Band Second Harmonic Gyroklystron Amplifier," *2007 IEEE International Vacuum Electronics Conference,* pp. 1-2, 2007, doi: 10.1109/IVELEC.2007.4283304.

[117]   S.-X. Xu *et al.*, "A Ka-Band Second Harmonic Gyroklystron Amplifier," *IEEE Transactions on Plasma Science,* vol. 40, no. 8, pp. 2099-2104, 2012, doi: 10.1109/TPS.2012.2199522.

[118]   S.-X. Xu, P.-K. Liu, and Z.-H. Geng, "Numerical simulation of a W- band four- cavity gyroklystron amplifier," *Physics of Plasmas,* vol. 19, no. 3, 2012, doi: 10.1063/1.3685728.

[119]   S.-X. Xu *et al.*, "A W-band four-cavity gyroklystron amplifier," *Journal of Infrared & Millimeter Waves,* vol. 32, no. 3, pp. 205-209, 2013, doi: 10.3724/SP.J.1010.2013.00205.

[120]   Q.-Z. Xue *et al.*, "Design of a W-Band Four-Cavity Gyroklystron Amplifier," *39th International Conference on Infrared Millimetre and Terahertz Waves,* 2014.

[121]   C. Ou, Y. Liu, and X. Niu, "Optimization design and simulation of W-band gyro-klystron amplifier," *Journal of Vacuum Science and Technology,* vol. 35, no. 2, pp. 207-213, 2015, doi: 10.13922/j.cnki.cjovst.2015.02.15.

[122]   M. V. Swati, M. S. Chauhan, and P. K. Jain, "Design Methodology and Beam-Wave Interaction Study of a Second-Harmonic D-Band Gyroklystron Amplifier," *IEEE Transactions on Plasma Science,* vol. 44, no. 11, pp. 2844-2851, 2016, doi: 10.1109/TPS.2016.2611140.

[123]   D. C. Bell and R. M. Narayanan, "Theoretical aspects of radar imaging using stochastic waveforms," *IEEE Transactions on Signal Processing,* vol. 49, no. 2, p. 394, 2001, doi: 10.1109/78.902122.

[124]   R. M. Rozental, I. V. Zotova, N. S. Ginzburg, A. S. Sergeev, and V. P. Tarankov, "Chaotic Generation in a W-Band Gyroklystron With Delayed Feedback," *IEEE Transactions on Plasma Science,* 2018, doi: 10.1109/TPS.2018.2797601.

[125]   K. R. Chu, V. L. Granatstein, P. E. Latham, W. Lawson, and C. D. Striffler, "A 30-MW Gyroklystron Amplifier Design for High-Energy Linear Accelerators," *IEEE Transactions on Plasma Science,* vol. 13, no. 6, pp. 424-434, 1985, doi: 10.1109/TPS.1985.4316456.

[126]   P. E. Latham, W. Lawson, and V. Irwin, "The design of a 100 MW, Ku band second harmonic gyroklystron experiment," *IEEE Transactions on Plasma Science,* vol. 22, no. 5, pp. 804-817, 1994, doi: 10.1109/27.338296.

[127]   J. Cheng *et al.*, "Experimental studies of a high power, X-band, coaxial gyroklystron," *IEEE Transactions on Plasma Science,* vol. 27, no. 4, pp. 1175-1187, 1999, doi: 10.1109/27.782298.

[128] W. Lawson, "The design of a high-power, high-gain, frequency-doubling gyroklystron," *IEEE Transactions on Plasma Science,* vol. 33, no. 2, pp. 858-865, 2005, doi: 10.1109/TPS.2005.845087.

[129] S. Tiwari and W. Lawson, "Design of a High- Gain K-Band Coaxial Gyroklystron," *IEEE Transactions on Plasma Science,* vol. 35, no. 1, pp. 23-26, 2007, doi: 10.1109/TPS.2006.889289.

[130] P. Purohit and W. Lawson, "Design of a high-power, high-gain, 2nd harmonic, 22.848 GHz gyroklystron," *AIP Advances,* vol. 3, no. 8, p. 082134, 2013, doi: 10.1063/1.4820387.

[131] M. Veale, P. Purohit, and W. Lawson, "Design of a high-power, high-gain, 2nd harmonic, 22.848 GHz gyroklystron," *AIP Advances,* vol. 3, no. 8, p. 082134, 2013, doi: 10.1063/1.4820387.

[132] W. Lawson, J. P. Calame, G. S. Nusinovich, and B. Hogan, "Reflections on the University of Maryland's Program Investigating Gyro-amplifiers as Potential Sources for Linear Colliders," *Terahertz Science and Technology,* vol. 10, no. 1, pp. 1-43, 2017.

[133] R. L. Ives, "10 MW, 91 GHZ gyroklystron for high frequency accelerator research," *Proceedings of the IEEE Particle Accelerator Conference,* vol. 2, pp. 1119-1121, 2003.

[134] M. Blank, P. Borchard, S. Cauffman, K. Felch, Y. M. Mizuhara, and W. Lawson, "Design of a 50 MW 30 GHz gyroklystron amplifier for accelerator applications," *Third IEEE International Vacuum Electronics Conference,* pp. 85-86, 2002, doi: 10.1109/IVELEC.2002.999273.

[135] M. Read, L. Ives, J. Neilson, and W. Lawson, "Development of a 50 MW 30 GHz Gyroklystron," *2007 IEEE International Vacuum Electronics Conference,* pp. 1-2, 2007, doi: 10.1109/IVELEC.2007.4283313.

[136] N. I. Zaitsev, Y. M. Guznov, S. V. Kuzikov, M. E. Plotkin, and E. M. Tai, "Experimental Investigation of the Relativistic Millimeter-Wave Gyroklystron," *Radiophysics and quantum electronics,* vol. 56, no. 8-9, pp. 492-496, 2014, doi: 10.1007/s11141-014-9453-5.

[137] N. I. Zaitsev *et al.*, "Pulsed high- order volume mode gyroklystron," *Radiophysics and Quantum Electronics,* vol. 48, no. 10-11, pp. 737-740, 2005, doi: 10.1007/s11141-006-0002-8.

[138] N. I. Zaitsev, A. K. Gvozdev, S. A. Zapevalov, S. V. Kuzikov, and V. N. Manuilov, "Experimental study of a multimegawatt pulsed gyroklystron," *Journal of Communications Technology and Electronics,* vol. 59, no. 2, pp. 164-168, 2014, doi: 10.1134/S1064226913120188.

[139] N. I. Zaitsev, I. S. Kulagin, S. V. Kuzikov, M. E. Plotkin, and I. Syratchev, "Microwave components for 30 GHz high-power gyroklystron," *Conference Digest of the Joint 32nd International Conference on Infrared and Millimetre Waves, and 15th International Conference on Terahertz Electronics,* pp. 369-370, 2007.

[140] M. S. Chauhan, M. V. Swati, and P. K. Jain, "Design and Simulation of a Gyroklystron Amplifier," *Physics of Plasmas,* vol. 22, p. 033111, 2015.

[141] M. S. Chauhan, M. V. Swati, and P. K. Jain, "Nonlinear Analysis of a Gyroklystron Amplifier with Misaligned Electron Beam," *Journal of Fusion Energy,* vol. 35, no. 2, pp. 289-298, 2016, doi: 10.1007/s10894-015-0021-6.

[142] Y. M. Guznov *et al.*, "Megawatt-power Ka- band gyroklystron oscillator with external feedback," *Applied Physics Letters,* vol. 103, no. 17, p. 173505, 2013, doi: 10.1063/1.4826453.

[143] L. J. R. Nix *et al.*, "Demonstration of efficient beam-wave interaction for a MW-level 48 GHz gyroklystron amplifier," *Physics of Plasmas,* vol. 27, p. 053101, 2020, doi: https://doi.org/10.1063/1.5144590.

[144] J. Cai and I. Syratchev, "Modeling and Technical Design Study of Two-Stage Multibeam Klystron for CLIC," *IEEE Transactions on Electron Devices,* vol. 67, no. 8, pp. 3362-3368, 2020, doi: 10.1109/TED.2020.3000191.

[145] D. K. Abe *et al.*, "Multiple-beam klystron development at the Naval Research Laboratory," *2009 IEEE Radar Conference,* pp. 1-5, 2009, doi: 10.1109/RADAR.2009.4976975.

[146] Z. Liu, H. Huang, X. Jin, S. Li, T. Wang, and X. Fang, "Investigation of an X-Band Long Pulse High-Power High-Gain Coaxial Multibeam Relativistic Klystron Amplifier," *IEEE Transactions on Electron Devices,* vol. 66, no. 1, pp. 722-728, 2019, doi: 10.1109/ted.2018.2879193.

[147] D. Yaogen *et al.*, "Research Progress on X-Band Multibeam Klystron," *IEEE Transactions on Electron Devices,* vol. 56, no. 5, pp. 870-876, 2009, doi: 10.1109/TED.2009.2015630.

[148]   A. N. Korolyov, E. A. Gelvich, Y. V. Zhary, A. D. Zakurdayev, and V. I. Poognin, "Multiple-beam klystron amplifiers: performance parameters and development trends," *IEEE Transactions on Plasma Science,* vol. 32, no. 3, pp. 1109-1118, 2004, doi: 10.1109/TPS.2004.828807.

[149]   A. K. Bandyopadhyay, D. Pal, A. Saini, D. Kant, S. Saha, and L. M. Joshi, "Design of a Ku band miniature multiple beam klystron," *AIP Conference Proceedings,* vol. 1715, p. 020052, 2016, doi: 10.1063/1.4942734.

[150]   M. Kumar *et al.*, "Design of a high frequency miniature multi beam klystron (MBK)," *2011 IEEE International Vacuum Electronics Conference (IVEC),* pp. 321-322, 2011, doi: 10.1109/IVEC.2011.5747005.

[151]   T. Wang *et al.*, "Output microwave characteristics of a Ka-band relativistic klystron amplifier with spatially nonuniform multibeam electron emission," *Physics of plasmas,* vol. 27, no. 8, p. 83106, 2020, doi: 10.1063/5.0013000.

[152]   J. C. Cai, I. Syratchev, and G. Burt, "Design Study of a High-Power Ka-Band High-Order-Mode Multibeam Klystron," *IEEE Transactions on Electron Devices,* vol. 67, no. 12, pp. 5736-5742, 2020, doi: 10.1109/TED.2020.3028348.

[153]   A. D. R. Phelps, "Experiments on beam plasma interactions and EM waves in magnetized plasmas," *AIP Conference Proceedings,* vol. 1445, no. 1, pp. 74-82, 2012, doi: 10.1063/1.3701888.

[154]   G. S. Kino and N. J. Taylor, "The design and performance of a magnetron-injection gun," *IRE Transactions on Electron Devices,* vol. 9, no. 1, pp. 1-11, 1962, doi: 10.1109/T-ED.1962.14882.

[155]   A. Midford, G. S. Kino, and W. W. Hansen, "New types of crossed field electron guns," *IRE Transactions of Electron Devices,* vol. 8, no. 2, pp. 175-175, 1961, doi: 10.1109/IEDM.1960.187163.

[156]   W. E. Waters, "A theory of magnetron injection guns," *IEEE Transactions on Electron Devices,* vol. 10, no. 4, pp. 226-234, 1963, doi: 10.1109/T-ED.1963.15183.

[157]   J. Mark Baird and W. Lawson, "Magnetron injection gun (MIG) design for gyrotron applications," *International Journal of Electronics,* vol. 61, no. 6, pp. 953-967, 1986, doi: 10.1080/00207218608920932.

[158]   V. L. Bratman, N. S. Ginzburg, G. S. Nusinovich, M. I. Petelin, and P. S. Strklkov, "Relativistic gyrotrons and cyclotron autoresonance masers," *International Journal of Electronics,* vol. 51, no. 4, pp. 541-567, 1981, doi: 10.1080/00207218108901356.

[159]   A. W. Fliflet, "Linear and non-linear theory of the Doppler-shifted cyclotron resonance maser based on TE and TM waveguide modes," *International Journal of Electronics,* vol. 61, no. 6, pp. 1049-1080, 1986, doi: 10.1080/00207218608920939.

[160]   Y. Y. Lau, "A unified theory of the diocotron, cyclotron maser, and negative-mass instabilities," *IEEE Transactions on Electron Devices,* vol. 31, no. 3, pp. 329-337, 1984, doi: 10.1109/T-ED.1984.21524.

[161]   Y. Y. Lau, M. J. Baird, L. R. Barnett, K. R. Chu, and V. L. Granatstein, "Invited paper. Cyclotron maser instability as a resonant limit of space charge wave," *International Journal of Electronics,* vol. 51, no. 4, pp. 331-340, 1981, doi: 10.1080/00207218108901340.

[162]   J. Benford, J. A. Swegle, and E. Schamiloglu, *High Power Microwaves*, Second Edition ed. (Series in Plasma Physics). Boca Raton, Florida, USA: Taylor & Francis Group, 2007.

[163]   M. Abramowitz, *Handbook of mathematical functions, with formulas, graphs, and mathematical tables*, [9th Dover printing with corrections]. ed. New York: New York, Dover Publications, 1970.

[164]   R. J. Barker and E. Schamiloglu, *High-Power Microwave Sources and Technologies* (IEEE Press Series on RF and Microwave Technology). New York, USA: IEEE Press, 2001.

[165]   J. P. Calame and D. K. Abe, "Applications of advanced materials technologies to vacuum electronic devices," *Proceedings of the IEEE,* vol. 87, no. 5, pp. 840-864, 1999, doi: 10.1109/5.757257.

[166]   J. F. Shackelford and R. H. Doremus, *Ceramic and glass materials: structure, properties and processing*, 1st ed. 2008.. ed. New York: Springer, 2008.

[167]   T. Kimoto and J. A. Cooper, *Fundamentals of silicon carbide technology: growth, characterization, devices and applications* (Fundamentals of SiC technology). Singapore: John Wiley & Sons Singapore Pte. Ltd., 2014.

[168] G. Dammertz *et al.*, "Recent results of the 1- MW, 140-GHz, TE22,6-mode gyrotron," *IEEE Transactions on Plasma Science,* vol. 27, no. 2, pp. 330-339, 1999, doi: 10.1109/27.772259.

[169] E. Giguet, P. Thouvenin, and C. Tran, "Status of the 118Ghz -0.5MW quasi-CW gyrotron for Tore Supra and TCV Tokamaks," *22nd International Conference on IR & MM Waves,* pp. 104-105, 1997.

[170] M. Thumm, "Development of Output Windows for High-Power Long-Pulse Gyrotrons and EC Wave Applications," *International Journal of Infrared and Millimeter Waves,* vol. 19, no. 1, pp. 3-14, 1998, doi: 10.1023/A:1022514528711.

[171] R. Heidinger, R. Schwab, R. Sporl, and M. Thumm, "Dielectric loss measurements in CVD diamond windows for gyrotrons," in *22nd International Conference on IR & MM Waves*, Wintergreen, VA, 1997, pp. 142-143.

[172] O. S. Kononenko and Y. V. Gandel, "Theoretical and Numerical Investigations of TE and TM Modes in a Coaxial Cavity Gyrotron," *2006 European Microwave Conference,* pp. 1515-1518, 2006, doi: 10.1109/EUMC.2006.281366.

[173] C. T. Iatrou, S. Kern, and A. B. Pavelyev, "Coaxial cavities with corrugated inner conductor for gyrotrons," *IEEE Transactions on Microwave Theory and Techniques,* vol. 44, no. 1, pp. 56-64, 1996, doi: 10.1109/22.481385.

[174] A. Patel *et al.,* "Millimeter-wave TE01-TE11-HE11 mode converter using overmoded circular waveguide," *Journal of electromagnetic waves and applications,* vol. 32, no. 14, pp. 1768-1778, 2018, doi: 10.1080/09205071.2018.1468286.

[175] O. W. Richardson, "On the Negative Radiation from Hot Platinum," *Proceedings of the Cambridge Philosophical Society,* vol. 11, pp. 286-295, 1901.

[176] C. R. Crowell, "The Richardson constant for thermionic emission in Schottky barrier diodes," *Solid State Electronics,* vol. 8, no. 4, pp. 395-399, 1965, doi: 10.1016/0038-1101(65)90116-4.

[177] S. Humphries, *Charged Particle Beams*. Albuquerque, New Mexico: John Wiley and Sons, 1990.

[178] J. Orloff, *Handbook of Charged Particle Optics*, Second Edition ed. New York, USA: CRC Press, 2008.

[179] E. L. Murphy and R. H. Good, "Thermionic Emission, Field Emission, and the Transition Region," *Physical Review,* vol. 102, no. 6, pp. 1464-1473, 1956, doi: 10.1103/PhysRev.102.1464.

[180] M. Bakr, M. Kawai, T. Kii, and H. Ohgaki, "CeB6: Emission Performance and Uniformity Compared With LaB6 for Thermionic RF Guns," *IEEE Transactions on Electron Devices,* vol. 63, no. 3, pp. 1326-1332, 2016, doi: 10.1109/TED.2016.2520951.

[181] M. Bakr *et al.,* "Comparison Between Hexaboride Materials for Thermionic RF Gun," *Proceedings of IPAC'10,* vol. 02 Synchrotron Light Sources and FELs, pp. 1782-1784, 2010.

[182] S.-Y. Ning *et al.,* "Enhanced thermionic emission performance of LaB6 by Ce doping," *Journal of Alloys and Compounds,* vol. 760, pp. 1-5, 2018, doi: 10.1016/j.jallcom.2018.05.154.

[183] D. M. Kirkwood *et al.,* "Frontiers in Thermionic Cathode Research," *IEEE Transactions on Electron Devices,* vol. 65, no. 6, pp. 2061-2071, 2018, doi: 10.1109/ted.2018.2804484.

[184] W. Liang, Y. Wang, J. Wang, W. Liu, and F. Yang, "DC Emission Characteristic of Nanosized-Scandia-Doped Impregnated Dispenser Cathodes," *IEEE Transactions on Electron Devices,* vol. 61, no. 6, pp. 1749-1753, 2014, doi: 10.1109/ted.2014.2319298.

[185] L. R. Barnett, N. C. Luhmann, C. C. Chiu, Y. C. Yan, and K. R. Chu, "An Improved magnetron injection gun using advanced high current density cathodes for a W-band TE01 Gyro-TWT," *2008 IEEE International Vacuum Electronics Conference,* pp. 400-401, 2008, doi: 10.1109/IVELEC.2008.4556368.

[186] L. R. Barnett, N. C. Luhmann, C. C. Chiu, and K. R. Chu, "Relativistic performance analysis of a high current density magnetron injection gun," *Physics of Plasmas,* vol. 16, no. 9, 2009, doi: 10.1063/1.3227649.

[187] R. K. Barik *et al.,* "Development of alloy-film coated dispenser cathode for terahertz vacuum electron devices application," *Applied surface science,* vol. 276, pp. 817-822, 2013, doi: 10.1016/j.apsusc.2013.04.004.

[188] S. Kimura *et al.,* "Ir-coated dispenser cathode for CRT," *IEEE Transactions on Electron Devices,* vol. 37, no. 12, pp. 2564-2567, 1990, doi: 10.1109/16.64533.

[189] I. Spectra-Mat. "Dispenser Cathodes." https://www.spectramat.com/product/dispenser-cathodes/ (accessed 28/09/2020, 2020).

[190]   W. M. Manheimer, M. Blank, and M. Garven, "Simple theory of input couplers for gyroklystron amplifiers," *IEEE Transactions on Plasma Science,* vol. 26, no. 3, pp. 433-443, 1998, doi: 10.1109/27.700775.

[191]   S.-X. Xu, P.-K. Liu, S.-C. Zhang, and Y.-N. Su, "Design of an input coupler for a Ka-band second harmonic gyroklystron amplifier," *IEEE International Symposium on Microwave, Antenna, Propagation and EMC Technologies for Wireless Communications,* vol. 2, pp. 1108-1110, 2005, doi: 10.1109/MAPE.2005.1618114.

[192]   K. Sakamoto *et al.*, "Major improvement of gyrotron efficiency with beam energy recovery," *Physical Review Letters,* vol. 73, no. 26, pp. 3532-3535, 1994, doi: 10.1103/PhysRevLett.73.3532.

[193]   A. Singh, D. S. Weile, S. Rajapatirana, and V. L. Granatstein, "Integrated design of depressed collectors for gyrotrons," *IEEE Transactions on Plasma Science,* vol. 25, no. 3, pp. 480-491, 1997, doi: 10.1109/27.597263.

[194]   G. P. Saraph, V. L. Granatstein, and W. Lawson, "Design of a single-stage depressed collector for high-power, pulsed gyroklystron amplifiers," *IEEE Transactions on Electron Devices,* vol. 45, no. 4, pp. 986-990, 1998, doi: 10.1109/16.662816.

[195]   L. Gu, Y. Liu, and S. Chen, "Design of TE01-to-HE11 mode converters for high-power millimeter wave applications at 35 GHz," *Review of scientific instruments,* vol. 91, no. 3, pp. 34706-034706, 2020, doi: 10.1063/1.5131781.

[196]   X. Niu *et al.*, "High-power TE01 - TE11 mode converter for gyroklystron," *Journal of Fusion Energy,* vol. 32, no. 4, pp. 426-430, 2013, doi: 10.1007/s10894-012-9589-2.

[197]   Z. D. Farkas, H. A. Hogg, G. A. Loew, and P. B. Wilson, "SLED: A Method of Doubling SLAC's Energy," *Proceedings of 9th International Conference on High Energy Accelerators,* p. 576, 1976.

[198]   P. B. Wilson, Z. D. Farkas, and R. D. Ruth, "SLED II: A new method of RF pulse compression," *Proceedings of the Linear Accelerator Conference,* pp. 204-206, 1990.

[199]   A. Castilla *et al.*, "Development of 36GHz RF Systems for RF Linearisers," *Proceedings of the 12th International Particle Acceleration Conference (IPAC'21),* 2021.

[200]   T. M. Tran, B. G. Danly, K. E. Kreischer, J. B. Schutkeker, and R. J. Temkin, "Optimization of gyroklystron efficiency," *Physics of Fluids,* vol. 29, no. 4, pp. 1274-1281, 1986, doi: 10.1063/1.865876.

[201]   A. W. Fliflet, M. E. Read, K. R. Chu, and R. Seeley, "A self-consistent field theory for gyrotron oscillators: application to a low Q gyromonotron," *International journal of electronics,* vol. 53, no. 6, pp. 505-521, 1982, doi: 10.1080/00207218208901545.

[202]   C. D. Joye, "Design of a Wideband 100W, 140GHz Gyroklystron Amplifier," Master of Science in Electric Engineering, Department of Electrical Engineering and Computer Science, Massachusetts Institute of Technology, USA, 2004.

[203]   B. Goplen, L. Ludeking, D. Smithe, and G. Warren, "User-Configurable MAGIC for Electromagnetic PIC Calculations," *Computer Physics Communications,* vol. 87, no. 1-2, pp. 54-86, 1995, doi: 10.1016/0010-4655(95)00010-D.

[204]   G. Warren, L. Ludeking, K. Nguyen, D. Smithe, and B. Goplen, "Advances/Applications of MAGIC and SOS," *AIP Conference Proceedings,* vol. 297, pp. 313-322, 1993, doi: doi.org/10.1063/1.45327.

[205]   L. Ludeking, *MAGIC User Manual*. Mission Research Corporation, 2002.

[206]   D. A. Constable, "The numerical and experimental investigation of gyro-multiplier configurations," PhD, Department of Physics, University of Strathclyde, Glasgow, UK, 2013.

[207]   K. S. Yee, "Numerical solution of initial boundary value problems involving maxwell's equations in isotropic media," *IEEE Transactions on Antennas and Propagation,* vol. 14, no. 3, pp. 302-307, 1966, doi: 10.1109/TAP.1966.1138693.

[208]   Z. kebci, A. Belkhir, A. Mezeghrane, O. Lamrous, and F. I. Baida, "Implementation of the FDTD method in cylindrical coordinates for dispersive materials: Modal study of C-shaped nano-waveguides," *Physica B: Condensed matter,* vol. 533, pp. 33-39, 2018, doi: 10.1016/j.physb.2017.12.054.

[209]   J. J. Choi *et al.*, "Experimental investigation of a high power, two-cavity, 35 GHz gyroklystron amplifier," *IEEE Transactions on Plasma Science,* vol. 26, no. 3, pp. 416-425, 1998, doi: 10.1109/27.700773.

[210]   M. S. Chauhan, M. V. Swati, and P. K. Jain, "PIC simulation study of a 35 GHz, 200 kW gyroklystron," *Journal of Microwaves, Optoelectronics and Electromagnetic Applications,* vol. 12, no. 2, pp. 353-362, 2013, doi: 10.1590/S2179-10742013000200009.

[211]   A. Goldenberg and M. Petelin, "The formation of helical electron beams in an adiabatic gun," *Radiophysics and Quantum Electronics,* vol. 16, no. 1, pp. 106-111, 1973, doi: 10.1007/BF01080801.

[212]   U. Singh, N. Kumar, L. Purohit, and A. Sinha, "Design of Electron Gun for 1.5 MW, 140 GHz Gyrotron," *Journal of Fusion Energy,* vol. 30, no. 1, pp. 53-57, 2011, doi: 10.1007/s10894-010-9343-6.

[213]   V. K. Lygin, V. N. Manullov, A. N. Kuftin, A. B. Pavelyev, and B. Piosczyk, "Inverse magnetron injection gun for a coaxial 1-5MW, 140 GHz gyrotron," *International Journal of Electronics,* vol. 79, no. 2, pp. 227-235, 1995, doi: 10.1080/00207219508926264.

[214]   S. Ruess *et al.*, "Proposal of an inverse magnetron injection gun for future hollow cylindrical-cavity high power gyrotrons," *41st International Conference on Infrared, Millimeter, and Terahertz waves (IRMMW-THz),* vol. Vol.2016, pp. 1-2, 2016, doi: 10.1109/IRMMW-THz.2016.7758916.

[215]   M. E. Read, R. L. Ives, G. Miram, G. Nusinovich, W. Lawson, and V. L. Granatstein, "A magnetron injection gun with inverted geometry for an 80 MW gyroklystron," *Proceedings of the 2003 Particle Accelerator Conference,* vol. 2, pp. 1140-1141, 2003, doi: 10.1109/PAC.2003.1289631.

[216]   W. Lawson, "Magnetron injection gun scaling," *IEEE Transactions on Plasma Science,* vol. 16, no. 2, pp. 290-295, 1988, doi: 10.1109/27.3827.

[217]   U. Singh, A. Bera, R. R. Rao, and A. K. Sinha, "Synthesized Parameters of MIG for 200 kW, 42 GHz Gyrotron," *Journal of Infrared, Millimeter, & Terahertz Waves,* vol. 31, no. 4, pp. 533-541, 2010, doi: 10.1007/s10762-009-9608-1.

[218]   M. V. Kartikeyan, E. Borie, and M. Thumm, *Gyrotrons: High-Power Microwave and Millimeter Wave Technology*. Germany: Springer, 2004.

[219]   J. C. Mudiganti, M. V. Kartikeyan, and M. Thumm, "Design of Magnetron Injection Guns - A 3D Simulation Approach," *2009 34th International Conference on Infrared, Millimeter, and Terahertz Waves,* pp. 1-2, 2009, doi: doi: 10.1109/ICIMW.2009.5325645.

[220]   I. Langmuir and K. B. Blodgett, "Currents Limited by Space Charge between Coaxial Cylinders," *Physical review,* vol. 22, no. 4, pp. 347-356, 1923, doi: 10.1103/PhysRev.22.347.

[221]   S. E. Tsimring, "On the spread of velocities in helical electron beams," *Radiophysics and quantum electronics.,* vol. 15, no. 8, pp. 952-961, 1972, doi: 10.1007/BF01030951.

[222]   P. Krivosheev, V. Lygin, V. Manuilov, and S. Tsimring, "Numerical Simulation Models of Forming Systems of Intense Gyrotron Helical Electron Beams," *International Journal of Infrared and Millimeter Waves,* vol. 22, no. 8, pp. 1119-1145, 2001, doi: 10.1023/A:1015006230396.

[223]   N. Kumar, U. Singh, A. Bera, and A. K. Sinha, "A gyrating electron beam source for frequency tunable, 200 GHz gyrotron," *Journal of Electromagnetic Waves and Applications,* vol. 31, no. 17, pp. 1947-1958, 2017, doi: 10.1080/09205071.2017.1349001.

[224]   D. M. Kirkwood *et al.*, "Frontiers in Thermionic Cathode Research," *TED,* vol. 65, no. 6, pp. 2061-2071, 2018, doi: 10.1109/ted.2018.2804484.

[225]   *Trak 8.0: Electron/ion Gun Design and Charged Particle Dynamics (User Manual)*. Albuquerque, New Mexico, USA: Field Precision LLC.

[226]   S. Humphries, *Electric and Magnetic Field Calculations with Finite-Element Methods.* Albuquerque, New Mexico, USA: Field Precision LLC, 2018.

[227]   S. Humphries, *Finite-Element Methods for Electromagnetics*. Albuquerque, New Mexico, USA: Field Precision LLC, 1997.

[228]   S. Humphries, *Principles of Charged Particle Acceleration*. Alberquerque, New Mexico: John Wiley & Sons, 1999.

[229]   W. Jiang, Y. Luo, R. Yan, and S. Wang, "Genetic Algorithm-Based Shape Optimization of Modulating Anode for Magnetron Injection Gun With Low Velocity Spread," *IEEE Transaction on Electron Devices,* vol. 62, no. 8, pp. 2657-2662, 2015, doi: 10.1109/TED.2015.2443068.

[230]   G. S. Nusinovich, B. G. Danly, and B. Levush, "Gain and bandwidth in stagger‑tuned gyroklystrons," *Physics of Plasmas,* vol. 4, no. 2, pp. 469-478, 1997, doi: 10.1063/1.872115.

[231]   J. P. Calame *et al.*, "Experimental studies of bandwidth and power production in a three‑cavity, 35 GHz gyroklystron amplifier," *Physics of Plasmas,* vol. 6, no. 1, pp. 285-297, 1999, doi: 10.1063/1.873283.

[232]   J. M. Neilson, P. E. Latham, M. Caplan, and W. G. Lawson, "Determination of the resonant frequencies in a complex cavity using the scattering matrix formulation," *IEEE Transactions on Microwave Theory and Techniques,* vol. 37, no. 8, pp. 1165-1170, 1989, doi: 10.1109/22.31074.

[233]   G. S. Park, V. L. Granatstein, P. E. Latham, C. M. Armstrong, A. K. Ganguly, and S. Y. Park, "Phase stability of gyroklystron amplifier," *IEEE Transactions on Plasma Science,* vol. 19, no. 4, pp. 632-640, 1991, doi: 10.1109/27.90329.

[234]   "Scandinova Product Sheet: K-series K100." https://scandinovasystems.com/products/k-series/k100/ (accessed September 2021.

[235]   A. H. McCurdy and J. J. Choi, "Design and analysis of a coaxial coupler for a 35‑GHz gyroklystron amplifier," *IEEE Transactions on Microwave Theory and Techniques,* vol. 47, no. 2, pp. 164-175, 1999, doi: 10.1109/22.744291.

[236]   W. L. Barrow and W. W. Mieher, "Natural Oscillations of Electrical Cavity Resonators," *Proceedings of the IRE,* vol. 28, no. 4, pp. 184-191, 1940, doi: 10.1109/JRPROC.1940.228082.

[237]   R. E. Collin, *Foundations for Microwave Engineering*, 2 ed. John Wiley & Sons, 2001.

[238]   *CST Studio Suite, Release Version 2020.04.* (2020). Dassault Systemes, Germany.

[239]   T. Weiland, "A discretization method for the solution of Maxwell's equations for six‑component fields," *Electronics and Communication (AEÜ),* vol. 31, pp. 116-120, 1977.

[240]   M. Clemens and T. Weiland, "Discrete electromagnetism with the finite integration technique," *Progress In Electromagnetics Research,* vol. 32, pp. 65-87, 2001, doi: 10.2528/PIER00080103.

[241]   B. Krietenstein, R. Schuhmann, P. Thoma, and T. Weiland, "The Perfect Boundary Approximation Technique Facing the Big Challenge of High Precision Field Computation," *Proceedings of the XIX International Linear Accelerator Conference (LINAC'98),* pp. 860-862, 1998.

[242]   L. Zhang, C. R. Donaldson, A. W. Cross, and W. He, "A pillbox window with impedance matching sections for a W-band gyro-TWA," *IEEE Electron Device Letters,* vol. 39, no. 7, pp. 1081-1084, 2018, doi: 10.1109/LED.2018.2834859.

[243]   M. Neubauer, "Rugged Ceramic Windows for RF Applications," *United States Department of Energy Technical Report,* 2012, doi: doi:10.2172/1053988.

[244]   V. V. Parshin, "Dielectric materials for gyrotron output windows," *International Journal of Infrared and Millimeter Waves,* vol. 15, no. 2, pp. 339-348, 1994, doi: 10.1007/BF02096245.

[245]   V. Kesari, A. K. Singh, R. Seshadri, and S. Kamath, "Boron Nitride and Sapphire Windows for 95‑GHz Gaussian RF Beam," *IEEE Transactions on Electron Devices,* vol. 63, no. 8, pp. 3257-3261, 2016, doi: 10.1109/TED.2016.2576462.

[246]   T. Shimozuma *et al.*, "A forced gas-cooled single-disk window using silicon nitride composite for high power CW millimeter waves," *International Journal of Infrared and Millimeter Waves,* vol. 18, no. 8, pp. 1479-1493, 1997, doi: 10.1007/BF02678306.

[247]   G. Yu, J. M. Dutta, and J. R. Jones, "Potentials of SiC as a gyrotron window material," *Conference Digest of the 2004 Joint 29th International Conference on Infrared and Millimeter Waves and 12th International Conference on Terahertz Electronics,* pp. 299-300, 2004, doi: 10.1109/ICIMW.2004.1422075.

[248]   M. Thumm, A. Arnold, R. Heidinger, M. Rohde, R. Schwab, and R. Spoerl, "Status report on CVD-diamond window development for high power ECRH," *Fusion Engineering and Design,* vol. 53, no. 1, pp. 517-524, 2001, doi: 10.1016/S0920-3796(00)00531-7.

[249]   V. E. Myasnikov *et al.*, "Development of 170 GHz gyrotron for ITER," *Third IEEE International Vacuum Electronics Conference,* pp. 334-335, 2002, doi: 10.1109/IVELEC.2002.999407.

[250]   N. Nayek, A. Naik, and S. Das, "Development of Face-Cooled Tunable Double-Disk Sapphire Window for 42-GHz 200-kW Gyrotron," *IEEE Transactions on Plasma Science,* vol. 43, no. 4, pp. 1024-1028, 2015, doi: 10.1109/TPS.2015.2403391.

[251]   B. V. Prokofiev, "Pyrolytical boron nitride as a window material for high power microwave electron devices," *8th International Vacuum Electron Sources Conference and Nanocarbon,* pp. 205-206, 2010, doi: 10.1109/IVESC.2010.5644458.

[252]   E. K. Duerr, "Millimeter-wave Integrated Horn Antenna," Master of Science in Electrical Engineering and Computer Science, Department of Electrical Engineering and Computer Science, Massachusetts Institute of Technology, 1998.

[253]   R. Keller and F. Arndt, "Rigorous modal analysis of the asymmetric rectangular iris in circular waveguides," *IEEE Microwave and Guided Wave Letters,* vol. 3, no. 6, pp. 185-187, 1993, doi: 10.1109/75.219809.

[254]   R. H. Macphie and K.-L. Wu, "Scattering at the junction of a rectangular waveguide and a larger circular waveguide," *IEEE Transactions on Microwave Theory and Techniques,* vol. 43, no. 9, pp. 2041-2045, 1995, doi: 10.1109/22.414538.

[255]   M.-C. Lin, "A Multilayer Waveguide Window for Wide-Bandwidth Millimeter Wave Tubes," *International Journal of Infrared and Millimeter Waves,* vol. 28, no. 5, p. 355, 2007, doi: 10.1007/s10762-007-9207-y.

[256]   A. Raj, D. Kant, A. K. Bandyopadhyay, and L. M. Joshi, "Optimization of grooved klystron collector design for efficient heat transfer," *International journal of RF and microwave computer-aided engineering,* vol. 29, no. 12, p. n/a, 2019, doi: 10.1002/mmce.21950.

[257]   Y. Shen, W. Jiang, H. Fu, and Y. Luo, "Thermal-hydraulic Design of Collector Cooling for High Power Gyro-TWT," *2018 International Conference on Microwave and Millimeter Wave Technology (ICMMT),* 2018.

[258]   K. Dong, R. Yan, and Y. Luo, "Optimal Design and Thermal Analysis of Undepressed Collectors for 35-GHz Gyro-TWTs," *IEEE Transactions of Electron Devices,* vol. 62, no. 8, pp. 2652-2656, 2015.

Demonstration of efficient beam-wave interaction for a MW-level 48 GHz gyroklystron amplifier

L. J. R. Nix (iD), L. Zhang (iD), W. He, C. R. Donaldson (iD), K. Ronald, A. W. Cross, and C. G. Whyte

View Online   Export Citation   CrossMark

Demonstration of efficient beam-wave interaction for a MW-level 48 GHz gyroklystron amplifier

View Online   Export Citation   CrossMark

L. J. R. Nix,[1,2,a)] (iD) L. Zhang,[1,2] (iD) W. He,[3] C. R. Donaldson,[1] (iD) K. Ronald,[1,2] A. W. Cross,[1,2] and C. G. Whyte[1]

AFFILIATIONS

[1]Department of Physics, SUPA, University of Strathclyde, Glasgow G4 0NG, Scotland, United Kingdom
[2]The Cockcroft Institute, Sci-tech Daresbury, Warrington WA4 4AD, United Kingdom
[3]College of Electronic Science and Technology, Shenzhen University, Shenzhen 518060, China

[a)]Author to whom correspondence should be addressed: laurence.nix@strath.ac.uk

ABSTRACT

The development of high-frequency RF linear accelerators (linacs) requires the consideration of several technological challenges, such as electron bunch linearization. Presented in this paper is the design of the interaction circuit for a 48 GHz MW-level three-cavity gyroklystron amplifier, appropriate for application as a millimeter wave power source in a fourth harmonic linearizing system for an X-band linac. The output cavity is operated at the cylindrical $TE_{0,2,1}$ mode, while the input and buncher cavities are operated at the $TE_{0,1,1}$ mode. The interaction circuit has been designed using a combination of analytical calculations and particle-in-cell simulations. The optimized gyroklystron is shown, through simulation, to deliver an output power of up to 2.3 MW with a gain of 36 dB and an efficiency of 44% at 48 GHz, when driven by a 140 kV, 37 A electron beam.

Published under license by AIP Publishing. https://doi.org/10.1063/1.5144590

I. INTRODUCTION

A gyroklystron is a vacuum electronic device based on the cyclotron resonance maser (CRM) mechanism.[1] Gyroklystrons are generally capable of high power output at narrow bandwidth, as compared with gyrotron traveling wave amplifiers (gyro-TWAs) which are moderate power broadband amplifiers.[2]

Gyroklystrons were first developed in 1967 at the Institute of Applied Physics (IAP) in Russia.[3,4] Since then, they have attracted significant interest, especially in the field of radar systems. Notably, high-power gyroklystron-based radar systems have been developed both in Russia (RUZA, 35 GHz)[5] and the USA (WARLOC, 94 GHz).[6] To reduce the magnetic field strength requirements, some gyroklystron designs have been studied using second harmonic operation.[7–9] Most radar gyroklystrons have been developed at Ka-band ($\sim$36 GHz) and W-band ($\sim$94 GHz) frequencies, though D-band ($\sim$140 GHz) frequencies have also been considered.[10] The efficiency achievable by the gyroklystron has improved greatly since its conception with an overall efficiency close to 40%.[11–13]

Gyroklystrons have also attracted interest in the field of accelerator physics. When designing an RF accelerator, a higher drive frequency generally allows for a higher operating gradient. For linacs with a few GeV electron beams, this will significantly reduce the size of the footprint and the construction costs of the accelerator. However,

achieving the required power at very high frequencies is a major challenge when using linear beam O-type klystrons. It is an increasing trend to employ acceleration structures operating at the X-band instead of the C- and S-bands in linacs. The X-band acceleration structures can be driven by O-type klystrons which are able to deliver 75 MW of output power.[14] However, the output power capability of the klystron drops dramatically with increasing operating frequency due to its small dimensions and the maximum beam current and voltage it can handle. At higher frequency, significant work has been published by several groups, most notably at SLAC and the University of Maryland, describing the study of gyroklystrons as candidates for future TeV linear colliders.[15] This work led to many advancements in the technical and theoretical understanding of gyroklystrons as illustrated, for example, by several high-power coaxial designs at different frequencies from $\sim$8 GHz to $\sim$22 GHz, each capable of delivering tens of MW of output power.[16–19] To achieve high-power handling capacity without the use of coaxial designs, the IAP has carried out studies of high-order mode gyroklystrons, such as a 35.4 GHz gyroklystron predicted to be capable of delivering 15 MW of output power using $TE_{7,1,1}$ and $TE_{7,3,1}$ modes.[20] A $TE_{5,2,1}$ to $TE_{5,3,1}$ mode sequence at 30 GHz was also studied, again predicting 15 MW of output power.[13]

An advanced X-ray free-electron laser (XFEL) is being developed by the CompactLight collaboration across Europe and Asia.[21] The

acceleration structure was developed by the CLIC experimental team at CERN (Geneva, Switzerland)[22] and operates at 12 GHz. The XFEL was proposed to operate with a high repetition rate of 100 Hz for hard X-rays and 1000 Hz for soft X-rays. For an X-band acceleration structure, during the acceleration process, unavoidable nonlinearities in an electron bunch's energy profile are introduced by the accelerating fields. Additional correction systems, called linearizers, are required to achieve performance targets. The most well-developed and reliable technique is the harmonic linearization, wherein an additional cavity at a harmonic of the main drive frequency is added.[23–27] The conventional klystron is challenging to produce sufficient output power to drive the harmonic linearizers for an X-band structure. The gyroklystron is not subject to the same limitations and therefore becomes an attractive solution.

A third harmonic linearizer that would be driven by a 36 GHz gyroklystron has been designed for the 12 GHz acceleration structures of CompactLight. UESTC (Chengdu, China) and the University of Strathclyde (Glasgow, UK) have carried out studies into Ka-band MW gyroklystrons for accelerator applications such as this.[12] Although the third harmonic option and its associated amplifier display good performance, there remains significant interest in the option of a linearizer operating at a higher harmonic, as it could theoretically achieve similar results with lower power demand and a shorter overall length of the linearizer. Therefore, a linearizer operating at the fourth harmonic (48 GHz) of the accelerating frequency has also been proposed.

The output power of the gyroklystron will be fed into an SLED-II type compressor and then to drive the linearizer.[28] The pulse length required from the gyroklystron is 2 μs with a minimum output power of 2 MW at 48 GHz. The compressor also requires the flipping of the phase of the input signal by 180° in a maximum of 5 ns and as quickly as possible, which means the gyroklystron also requires a bandwidth larger than 200 MHz to properly amplify the driving signal while being compatible with the SLED-II type pulse compressor. In this paper, the beam-wave interaction circuit of a gyroklystron as a suitable amplifier at this frequency is presented.

II. PRINCIPLES OF THE GYROKLYSTRON

In a gyroklystron, a gyrating electron beam in a strong axial magnetic field interacts with the TE resonance modes of a series cavities. Figure 1 shows a schematic of a gyroklystron with a three-cavity configuration. The seed microwave signal is coupled into the input cavity and will modulate the electron beam. The electron beam will gradually be bunched in the drift tube, and the bunching is further enhanced by the intermediate cavity. At the output cavity, the electron beam will strongly couple with the cavity mode. If the electrons arrive with the correct phase to lose their kinetic energy, the cavity electromagnetic field will gain energy to result in amplified microwave radiation and then can be coupled out through a microwave window.

It is of essential importance for the gyroklystron to have good phase-bunches to achieve high gain and high efficiency. Usually, having more intermediate cavities will help to reinforce the bunching process and achieve a higher gain. However, every additional cavity increases the complexity of the manufacturing process and assembly, as well as increasing the tolerance requirements. For the MW-level gyroklystron, low-quality factor cavities were used to avoid the oscillation, which results in large Ohmic loss. The thermal issue would become increasingly challenging for a gyroklystron with more intermediate cavities because the energy stored in the later cavities is higher. For example, the energy stored in the third cavity of a four-cavity configuration can be more than three times compared with the second cavity in a three-cavity configuration. Therefore, there is a trade-off between gain improvements, thermal issues, design complexity, and bunching quality that makes the decision of how many cavities to use nontrivial.

III. DESIGN OF THE GYROKLYSTRON

A good design of the gyroklystron requires the consideration of a lot of parameters, including those of the electron beam, the cavities, and the magnetic field. Since the gyroklystron was invented, a few models have been developed to describe the beam-wave interaction process, including the small-signal linear theory with point-gap approximation[29] and the nonlinear theory.[11,30] The linear theory provides a good starting point for the initial parameters such as the beam voltage, the current, the transverse-to-axial velocity ratio α, and the magnetic field strength at the interaction region. The initial beam parameters chosen for the MW gyroklystron operating at 48 GHz are shown in Table I.

The electron beam is generated from a magnetron injection gun (MIG).[31] For a selected beam voltage, the resonance condition between the cyclotron frequency and the cavity eigenmode can be
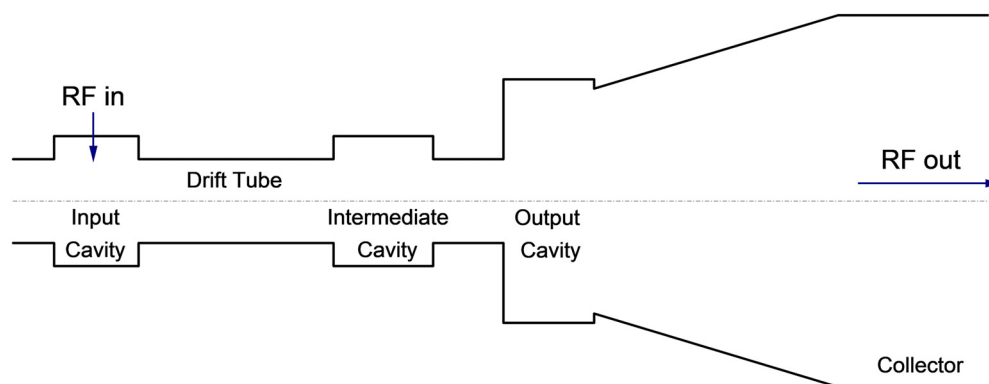

FIG. 1. Schematic diagram of a three-cavity gyroklystron amplifier.

TABLE I. Initial parameters for the 48 GHz gyroklystron.

Beam voltage (V_b)	140 kV
Beam current (I_b)	35 A
Transverse-to-axial velocity ratio (α)	1.35
Magnetic field strength (B_0)	2.02 T

satisfied by adjusting α and B_0 such that the dispersion relations meet tangentially at 48 GHz. A high velocity ratio can help improve interaction efficiency; however, the simulation on the MIG gun shows a higher velocity spread. The experience of electron guns for gyrodevices indicates a larger spread in the experiments compared with the simulations, due to the intrinsic spread from the thermionic emission, especially operating at a higher current density.[32] When α is larger than 1.5, back streaming electrons were also diagnosed in the measurement. Therefore, for the safe operation of the gyroklystron, as well as a balance of the interaction efficiency, the α value of 1.35 was chosen.

The operating modes selected for the gyroklystron are TE modes. Normally, low-order axially symmetric modes ($TE_{0,1,1}$ or $TE_{0,2,1}$) are used due to the electric field at the walls being low. For the MW-level gyroklystron, a relatively large beam current is used. If the cavity was larger in diameter with more modes available, there would be a greater risk of parasitic oscillations being excited due to the high current. However, a larger cavity than the $TE_{0,1,1}$ cavity is still desirable as the power-handling of a cavity is limited by its size. Therefore, the selected design consists of input and intermediate cavities operating at the $TE_{0,1,1}$ mode. The output cavity operates at the $TE_{0,2,1}$ mode as this allows it to be larger in diameter, thus enabling higher power handling capability while still maintaining strong stability and a reasonable coupling coefficient. The use of two compatible modes in this way is an effective technique, as the superior coupling coefficient and stability of the $TE_{0,1,1}$ mode are better for the input cavity compared with using the $TE_{0,2,1}$ for all cavities.[33]

A three-cavity design was considered first. The initial linear theory analysis predicted that such a design was likely to meet requirements. A four-cavity option was also considered. Both of the designs achieved similar efficiencies. The main benefit of additional cavities is to increase the gain, but the three-cavity device achieved the required performance with less energy stored in the intermediate cavity, which is more important for stable operation. Therefore, assessing the relative challenges and merits in thermal stress, design complexity, and performance, the three-cavity option was chosen as a suitable balance between these aspects. It also has the additional benefit of being a suitable length to match the superconducting magnet currently available in the laboratory at Strathclyde.

After selecting the core beam parameters and the general structure, the next step is to choose proper eigenfrequencies and Q factors for the cavities. Stagger-tuning is a technique in which cavity eigenfrequencies are slightly offset from the operating frequency, which is often utilized to increase the bandwidth of a gyroklystron to satisfy the requirement from the microwave compressor.[29] Appropriate stagger-tuned eigenfrequencies of the input and intermediate cavities can be estimated from the equations $f_0 + f_0/(3Q_0)$ and $f_0 - f_0/(3Q_0)$, respectively,[34] where f_0 and Q_0 are the eigenfrequency and the Q factor of the output cavity. Low-quality factor cavities are normally used in the high-power gyroklystron to avoid oscillation. The Q factors shown in

Table II were chosen as the initial parameters for the three-cavity gyroklystron.

The initial dimensions of the cavities were then estimated from the eigenfrequency and cavity eigenmode equations. If it is assumed that there is no leakage of microwaves into the drift tubes, the eigenfrequency f of the operating mode $TE_{m,p,n}$ can be written as the following equation:

$$f = \frac{c}{\lambda_0} = \frac{c}{2\pi} \sqrt{\left(\frac{\nu_{mp}}{R}\right)^2 + \left(\frac{n\pi}{L}\right)^2}, \quad (1)$$

where R and L are the radius and length of the cavity, respectively. At the same time, the guiding radius of the electron beam should be close to the position of the peak electric field strength of the operating mode to maximize the coupling coefficient, which is defined in Eq. (2) for a cavity mode $TE_{m,p,1}$ and a beam radius of r

$$C_{mp}(r) = \frac{J_{m\pm 1}^2(k_\perp r)}{(\nu_{mp}^2 - m^2)J_m^2(\nu_{mp})}, \quad (2)$$

where J is the Bessel function of the first kind, and ν_{mp} is the Bessel root corresponding to the mode in question. The ideal beam radius is slightly offset from the maximum coupling to account for the Larmor radius of the electron orbit, as shown in Fig. 2. When the eigenfrequencies of the cavities are given, their radii and lengths can be calculated from Eqs. (1) and (2). The selected beam radius was 1.77 mm.

The output cavity is an open-ended structure with a discrete step in the structure. The eigenfrequency and the Q factor were calculated by the mode-matching method.[35] By varying the taper angle and the depth of the iris, an output cavity structure meets the design requirements, as detailed in Table II. The output aperture radius had a large effect on the Q factor and a small effect on eigenfrequency. The smooth output waveguide after the taper only had little effect on the eigenfrequency and Q factor. The field profile at the radius of the electron beam is shown in Fig. 3.

The linear theory is not suitable for the accurate design because the beam-wave interaction is strongly nonlinear in high-power gyroklystrons. Also, the output cavity is open-ended and has significant differences to that of a closed cavity, which is not considered in the point-gap linear theory. The nonlinear theory, which can include the accurate field profiles of the cavities in the calculation and solve the beam-wave coupling equation [Eq. (3)], is able to provide more accurate results for the gain and interaction efficiency[8]

$$\frac{dP}{dz} + i\frac{\gamma}{u_z}\left(\frac{\omega}{s} - \frac{\Omega_0}{\gamma}\right)P = -\frac{i\eta_0\gamma}{2u_z}C_{mn}k_{mn}J_{m-s}(k_{mn}R_e)$$
$$\cdot \frac{F(z)}{(s-1)!}\left(\frac{k_{mn}P^*}{2\Omega_0}\right)^{s-1}i^{s-1}, \quad (3)$$

TABLE II. Q factors of the cavities for the 48 GHz gyroklystron.

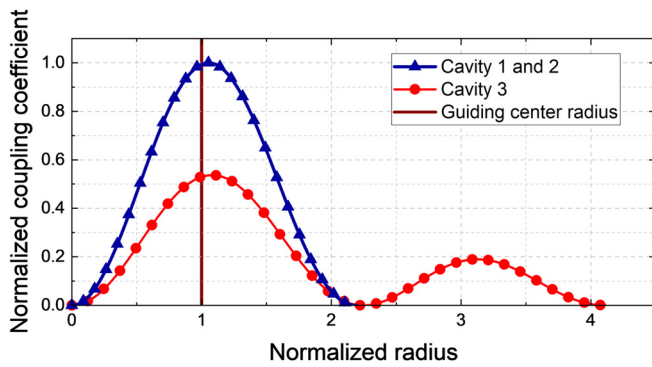| Cavity	Q factor	Frequency (GHz)
Input	180	47.86
Intermediate	180	47.22
Output	100	47.70

FIG. 2. Alignment between the coupling coefficient and the beam guide radius.

$$\left(\frac{d^2}{dz^2} + \frac{\omega^2}{c^2} - k_{mn}^2\right)F(z) = -\mu_0\omega I_0 C_{mn} k_{mn} J_{m-s}(k_{mn}R_e)$$

$$\cdot \frac{1}{2^s u_z}\frac{s}{(s-1)!}\left(\frac{-ik_{mn}}{\Omega_0}\right)^{s-1}\frac{1}{2\pi}\int_0^{2\pi}P^s d\Lambda_0,$$

$$(4)$$

where $P = iu_t \exp\{-i[\Lambda + (1 - m/s)\phi_e]\}$ describes the transverse component of the electron momentum, u_t and u_z are the transverse and the axial components of the normalized momentum u, respectively, $\Lambda = (\omega/s - \Omega)\tau + \omega/s t_0 - \phi$ is the slowly varying component of the phase, Λ_0 is the initial gyrophase, I_0 is the beam current, s is the harmonic number, Ω is the cyclotron frequency for the electron, ϕ describes the angular modulation, ϕ_e is the polar angle of the guiding center, τ is the time since the particle entered the current stage, k_{mn} is the transverse wavenumber, and R_e is the guiding center radius. $F(z)$ is the electric field profile along the z axis.

The nonlinear theory provides a balance between accuracy and simulation time. It is able to provide useful information on the bunching process and the trends that occur when changing the parameters. The initial dimensions of cavities, as well as the length of the drift tubes from the linear theory, were then further optimized using the nonlinear theory calculations to achieve an optimal efficiency. The maximum interaction efficiency was about 40%. Figure 4 shows the interaction efficiencies at the intermediate and output cavities as a
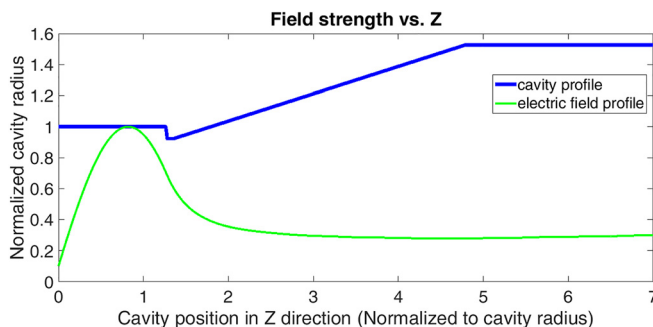
FIG. 3. Geometry of the output cavity and the electric field profile of the operating mode $TE_{0,2,1}$.
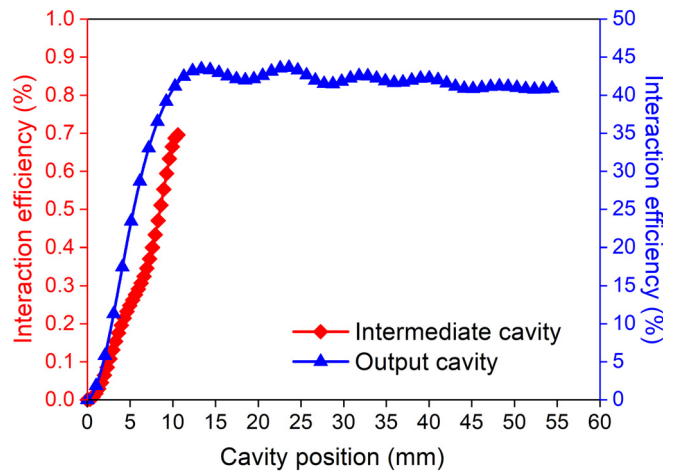
FIG. 4. Interaction efficiency at the intermediate and output cavities.

function of the cavity positions, where position 0 denotes the starting point of the cavity.

IV. PARTICLE-IN-CELL (PIC) SIMULATION OF THE GYROKLYSTRON

The particle-in-cell code simulation method provides increased accuracy at the cost of a much larger computation time. This makes it suited to the final optimization and validation, sweeping across a range of parameters. Here, the finite-difference time-domain PIC code MAGIC[36] was used to validate the design from the nonlinear theory prediction and further improve the gyroklystron performance.

In MAGIC simulations, the cavities were first simulated individually to ensure the correct eigenfrequencies and field patterns when the dielectric material was applied. Figure 5 shows an example of the azimuthal electric field pattern of the intermediate cavity. The gyroklystron cavity dimensions as finalized after MAGIC analysis are shown in Table III.

Dielectric linings are included in the cavities to introduce additional loss and reduce the Q factor. The dielectric material used is SiC due to its high loss tangent.[37] The thicknesses in the input and intermediate cavities are 0.7 mm and 0.3 mm, respectively. The cavities were then assembled with the drift tubes to simulate the performance of the whole gyroklystron. The initial parameter set from the nonlinear theory achieved a steady output power of around 1.7 MW, with 34 dB gain. Further PIC simulations were performed to sweep across various input parameters, such as beam voltage, beam current, detuning parameter, and drive frequency. Figure 6 shows the start-oscillation current for modes in the output cavity using the linear gain theory. The start-oscillation current of the operating mode was 59 A. The output power can therefore be further increased using a higher beam current. With a slight increase in the beam current from 35 A to 37 A, the output power achieved was 2 MW. For this new current value, the performance characteristics were analyzed over a range of input power values, as shown in Fig. 7.

Figure 7 shows the variation of efficiency, gain, and output power as a function of input power. Increasing the drive power in the input
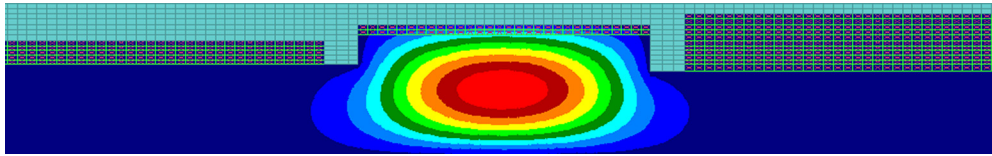
FIG. 5. Field pattern of the azimuthal E-field component of a $TE_{0,1,1}$ mode in the input cavity.

TABLE III. Dimensions of the cavities and drift tubes.

Section	Radius (mm)	Length (mm)
Cavity 1	3.88	8.66
Drift tube 1	2.50	20.00
Cavity 2	3.88	10.20
Drift tube 2	2.50	7.20
Cavity 3	7.28	9.60
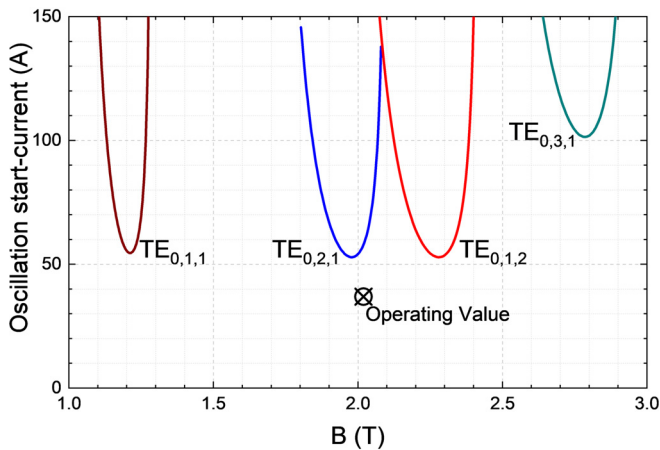
FIG. 6. Oscillation start-current for various modes in the output cavity.
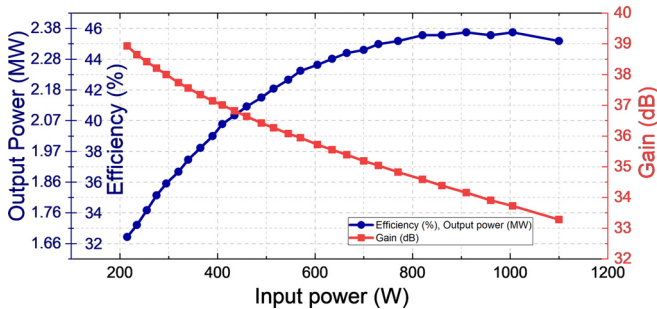
FIG. 7. Variation of the efficiency, gain, and output power as a function of the input power.

cavity improves the efficiency, but with diminishing returns in the output power. For example, at an input power of 295 W, the gyroklystron still operated in the linear gain region. The gain was as high as 38 dB, which enabled 1.9 MW of output power. Increasing the input power enables a higher output power, but the gain drops. For example, when doubling the input power to 605 W, the output power increased to 2.3 MW, i.e., by a modest amount ($\sim$20%). At an input power of over 910 W, the output began to saturate, and the saturated gain was 34 dB. As the results already demonstrated an output power above the 2 MW minimum target, a further increase in the input power was deemed un-necessary and 605 W was chosen as the input power value above which further investment in the input power offers too little reward to be worthwhile. With the selected values of 605 W of drive power and a 140 kV, 37 A beam, the predicted output power is 2.3 MW with a 36 dB gain and a 44% efficiency. The velocity spread of the electron beam was also introduced in the simulation to study its impact on the output power, as shown in Fig. 8. The larger the velocity spread is, the larger the impact on the output power becomes. The highest velocity spread for which the 2 MW requirement is met is slightly above 4%, by which point a 10% drop in the output power was observed. Higher spread continued to reduce the performance up to a spread of 9.5%, above which the oscillation at the output power was observed, and the gyroklystron ceases to maintain a stable operation.

Figure 9 shows the phase space plot of the electrons in the gyroklystron, demonstrating the interaction and subsequent deposition of the beam. The output power as a function of time is displayed in Fig. 10(a). After around 20 ns, the output power settles to 2.3 MW. The output power is reasonably steady, with fluctuations of less than 2%,
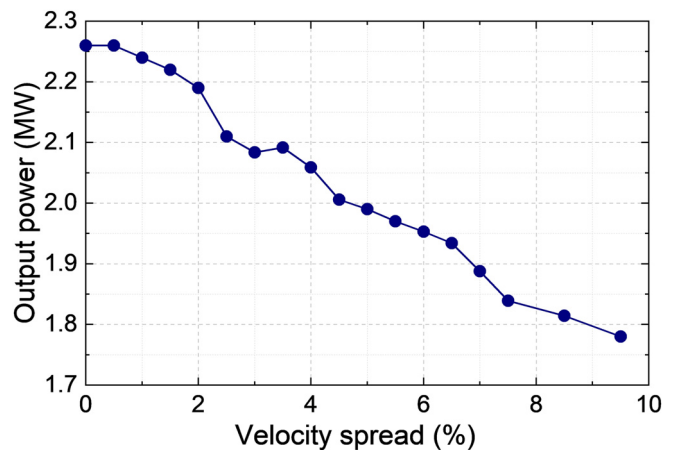
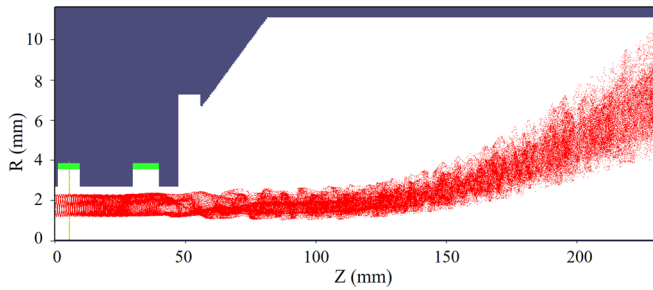**FIG. 8.** Variation of the output power with velocity spread.

FIG. 9. Phase space plot of the electrons in the gyroklystron.

which is mainly caused by the time-varying beam emission model used in the MAGIC simulations. The mode-purity of the outgoing radiation is also important to consider, as it can affect the performance of subsequent mode converters. The Fourier analysis of the output power is displayed in Fig. 10(b), which shows a clear peak at 48 GHz. A secondary peak is visible at 96 GHz, which is the second harmonic. The ratio of squared amplitudes for the fundamental to the second harmonic components is 21.
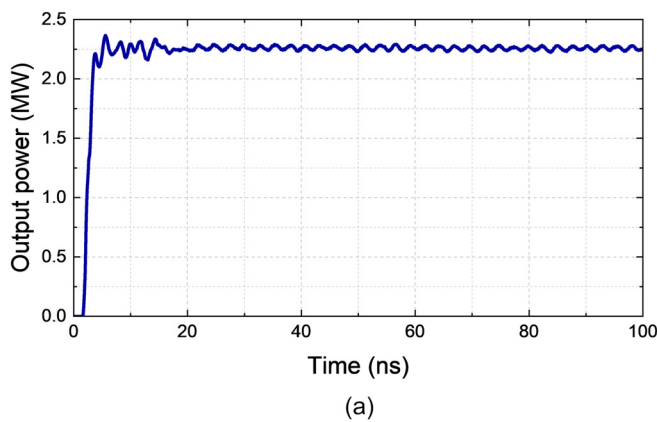
(a)
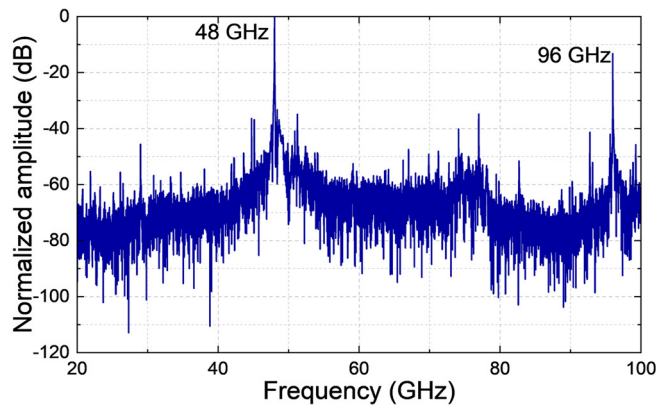
(b)

FIG. 10. Output power (a) and the spectrum of the output signal (b).
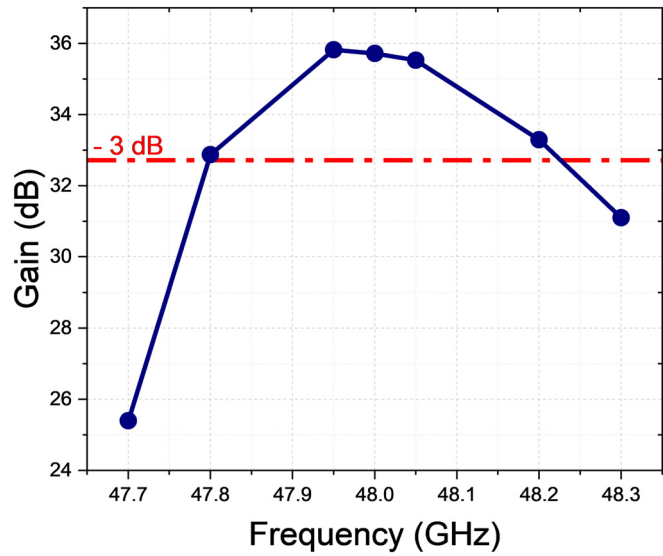
FIG. 11. Variation of gain with operating frequency.

The bandwidth of the gyroklystron was also simulated, and the results are shown in Fig. 11. The 3 dB bandwidth is about 400 MHz, which satisfies the minimum bandwidth requirement from the microwave compressor.

A higher output power is possible with the use of a higher beam current. As displayed in Fig. 12, the simulations showed a linear increment of the output power when the electron beam increased up to 53 A, beyond which oscillation occurred. However, several limiting factors exist with regard to increasing the current. A higher beam current pushes the thermionic MIG gun to operate at a higher current density, which is already at its limit and will significantly reduce its lifetime. Also increasing the beam current will result in larger space-charge effects. It is challenging to maintain the velocity spread of the electron beam under the design criteria of 4% at a higher current. The 37 A beam current was chosen as a main operation parameter to ensure a safe zero-drive stable amplifier operation.
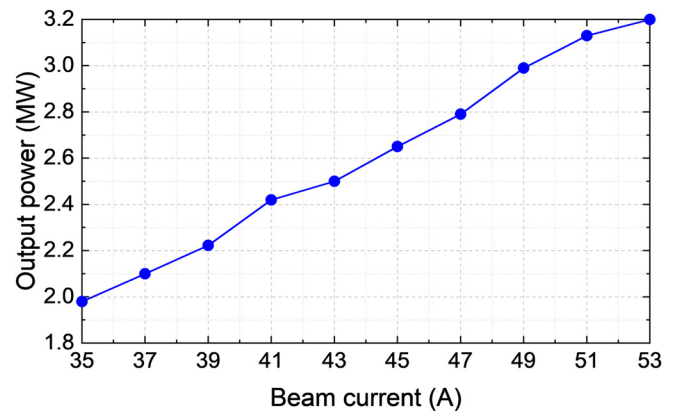
FIG. 12. Variation of the output power with beam current.

V. CONCLUSION

In this paper, the design of a three-cavity $TE_{0,1,1}$–$TE_{0,1,1}$–$TE_{0,2,1}$ 48 GHz gyroklystron amplifier has been presented. The requirements of a harmonic linearizer operating at the fourth harmonic of the 12 GHz linac drive frequency used in CompactLight were designed with consideration. The choice of using the fourth harmonic rather than the third allows for a shorter linearizer and a lower power demand. Vacuum electronic devices of around 48 GHz have previously received little attention, so the new development of an appropriate amplifier was required. The gyroklystron designed here using a combination of linear calculations, nonlinear analysis, and PIC simulations represents a viable microwave source for the application within the linearizer system. Following optimization using PIC simulations, an output power of 2.3 MW with a gain of 36 dB and an efficiency of 44% has been predicted when using a 140 kV, 37 A electron beam. The effect of the velocity spread was also studied. A 4% velocity spread will result in a 10% drop in the output power, but still above 2 MW. The 3 dB-bandwidth is 400 MHz.

ACKNOWLEDGMENTS

REFERENCES

[1] J. L. Hirshfield and J. M. Wachtel, Phys. Rev. Lett. 12(19), 533–536 (1964).
[2] L. R. Barnett, IEEE Trans. Electron Devices 28(7), 872–875 (1981).
[3] I. I. Antakov, A. V. Gaponov, V. A. Gintsburg, M. I. Petelin, and V. K. Yulpatov, International Patent Number 302050 (1967).
[4] A. V. Gaponov, M. I. Petelin, and V. K. Yulpatov, "The induced radiation of excited classical oscillators and its use in high-frequency electronics," Radiophys. Quantum Electron. (Engl. Transl.) 10, 794–813 (1967).
[5] A. A. Tolkachev, B. A. Levitan, G. K. Solovjev, V. V. Veytsel, and V. E. Farber, IEEE Aerosp. Electron. Syst. Mag. 15(7), 25–31 (2000).
[6] G. J. Linde, M. T. Ngo, B. G. Danly, W. J. Cheung, and V. Gregers-Hansen, IEEE Trans. Aerosp. Electron. Syst. 44(3), 1102–1117 (2008).
[7] E. V. Zasypkin, M. A. Moiseev, I. G. Gachev, and I. I. Antakov, IEEE Trans. Plasma Sci. 24(3), 666–670 (1996).
[8] Z.-H. Geng and P.-K. Liu, IEEE Trans. Plasma Sci. 34(3), 534–540 (2006).
[9] S.-X. Xu, P.-K. Liu, S.-C. Zhang, Y.-N. Su, Z.-H. Geng, W. Gu, Q.-Z. Xue, and B. Han, IEEE Trans. Plasma Sci. 40(8), 2099–2104 (2012).
[10] M. V. Swati, M. S. Chauhan, and P. K. Jain, IEEE Trans. Plasma Sci. 44(11), 2844–2851 (2016).
[11] M. S. Chauhan, M. V. Swati, and P. K. Jain, Phys. Plasmas 22, 033111 (2015).
[12] L. Wang, K. Dong, J. Wang, Y. Luo, W. He, A. W. Cross, K. Ronald, and A. D. R. Phelps, IET Microwaves, Antennas Propag. 12, 1752 (2018).
[13] N. I. Zaitsev, A. K. Gvozdev, S. A. Zapevalov, S. V. Kuzikov, and V. N. Manuilov, J. Commun. Technol. Electron. 59(2), 164–168 (2014).
[14] D. Sprehn, G. Caryotakis, A. Haase, E. Jongewaard, L. Laurent, C. Pearson, and R. Phillips, AIP Conf. Proc. 807(1), 137 (2006).
[15] V. L. Granatstein and W. Lawson, IEEE Trans. Plasma Sci. 24(3), 648–665 (1996).
[16] W. Lawson, J. Cheng, J. P. Calame, M. Castle, B. Hogan, V. L. Granatstein, M. Reiser, and G. P. Saraph, Phys. Rev. Lett. 81(14), 3030–3033 (1998).
[17] W. Lawson, IEEE Trans. Plasma Sci. 33(2), 858–865 (2005).
[18] M. Veale, P. Purohit, and W. Lawson, AIP Adv. 3(8), 082134 (2013).
[19] K. R. Chu, V. L. Granatstein, P. E. Latham, W. Lawson, and C. D. Striffler, IEEE Trans. Plasma Sci. 13(6), 424–434 (1985).
[20] N. I. Zaitsev, E. V. Ilyakov, S. V. Kuzikov, I. S. Kulagin, V. K. Lygin, M. A. Moiseev, M. I. Petelin, and A. S. Shevchenko, Radiophys. Quantum Electron. 48(10-11), 737–740 (2005).
[21] A. Mak, P. Salén, V. Goryashko, and J. Clarke, XLS Deliverable Report D2.1.
[22] "A Multi-TeV Linear Collider Based on CLIC Technology," CLIC Conceptual Design Report, edited by M. Aicheler, P. Burrows, M. Draper, T. Garvey, P. Lebrun, K. Peach, N. Phinney, H. Schmickler, D. Schulte, and N. Toge, CERN-2012-007 (CERN, 2012).
[23] T. I. Smith, Nucl. Instrum. Methods Phys. Res., Sect. A 250(1), 64–70 (1986).
[24] M. Dehler, J. Y. Raguin, A. Citterio, A. Falone, W. Wuensch, G. Riddone, A. Grudiev, and R. Zennaro, Phys. Rev. Spec. Top.-Accel. Beams 12(6), 062001 (2009).
[25] T. Schietinger, M. Pedrozzi, M. Aiba, V. Arsov, S. Bettoni, B. Beutner, M. Calvi, P. Craievich, M. Dehler, F. Frei et al., Phys. Rev. Accel. Beams 19(10), 100702 (2016).
[26] G. D'Auria, M. E. Ashmawy, A. Rohlev, M. Scafaru, C. Serpico, A. Turchet, and D. Wang, in Proceedings of IPAC'10 (2010), pp. 2173–2175.
[27] G. D'auria, S. D. Mitri, G. Penco, and C. Serpico, in Proceedings of IPAC'12 (2012), pp. 1721–1723.
[28] P. B. Wilson, Z. D. Farkas, and R. D. Ruth, in Proceedings of the Linear Accelerator Conference (1990), pp. 204–206.
[29] G. S. Nusinovich, B. G. Danly, and B. Levush, Phys. Plasmas 4(2), 469–478 (1997).
[30] T. M. Tran, B. G. Danly, K. E. Kreischer, J. B. Schutkeker, and R. J. Temkin, Phys. Fluids 29(4), 1274–1281 (1986).
[31] G. S. Kino and N. J. Taylor, IRE Trans. Electron Devices 9(1), 1–11 (1962).
[32] S. E. Tsimring, Radiophys. Quantum Electron. 15(8), 952–961 (1972).
[33] C.-H. Du and P.-K. Liu, Millimeter-Wave Gyrotron Traveling-Wave Tube Amplifiers, 2014 ed. (Springer, Berlin, Heidelberg, 2014).
[34] J. P. Calame, M. Garven, J. J. Choi, K. Nguyen, F. Wood, M. Blank, B. G. Danly, and B. Levush, Phys. Plasmas 6(1), 285–297 (1999).
[35] L. Zhang, W. He, C. R. Donaldson, and A. W. Cross, J. Infrared, Millimeter, Terahertz Waves 37(9), 846–856 (2016).
[36] B. Goplen, L. Ludeking, D. Smithe, and G. Warren, Comput. Phys. Commun. 87(1-2), 54–86 (1995).
[37] Y. Takeuchi, T. Abe, T. Kageyama, and H. Sakai, in Proceedings of the 2005 Particle Accelerator Conference (2005), Vol. 2005, pp. 1195–1197.

Magnetron Injection Gun for High-Power Gyroklystron

Liang Zhang, *Senior Member, IEEE*, Laurence J. R. Nix, and Adrian W. Cross, *Member, IEEE*

Abstract— **A magnetron injection gun (MIG) can generate an annular electron beam with a high transverse-to-axial velocity ratio for gyrotron devices. This article compares the different configurations of the MIGs and their suitable applications were analyzed from the theoretical study. Following that, an MIG for a 48-GHz, 2-MW output power gyroklystron was designed and optimized by parameterizing the MIG's geometry and the magnetic field. By using the standard triode-type configuration, a low alpha spread of 8.9% was achieved. The simulation results showed that the magnetic field profile also plays an important role in the MIG design. The angle of the magnetic field on the emitter surface affects the alpha value and the alpha spread, which was not able to be predicted by the synthesis method. It provides an extra degree of freedom for tuning the MIG's performance in the experiment where the geometry of the gun is fixed.**

Index Terms— **Gyroklystron, magnetron injection gun, small orbit beam, velocity spread.**

I. INTRODUCTION

GYROTRON devices based on cyclotron resonance maser (CRM) instability are capable to generate high-power radiation at high frequency [1], [2]. The dominant beam–wave energy exchange is in the azimuthal direction with the TE mode in the interaction circuit. An annular electron beam with a fraction of the electron's momentum in the transverse direction while propagating in a uniform guiding magnetic field is required for effective interaction. Such a beam can be generated by a magnetron injection type of electron gun (MIG) [3], where the electrons travel through an adiabatic magnetic field compression region. The guiding center of the electrons from an MIG is normally off-center. A special case is the axis-encircling beam, which is also called a large-orbit beam, which can be generated by an electron gun with a cusp magnetic field [4], [5].
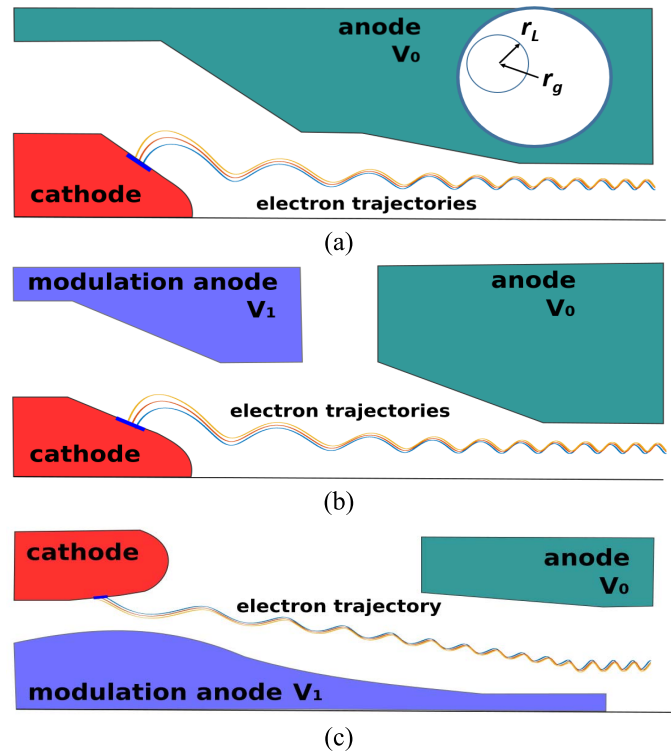
Fig. 1. Different types of MIGs. (a) Diode type. (b) Standard triode type. (c) IMIG.

There are different configurations of MIGs [6]–[8], including the diode-type, standard, and inverse-cathode triode-type guns which have an additional modulation anode, as shown in Fig. 1. Although they are all able to generate a small orbit electron beam, they have their unique properties and are suitable for different applications. The diode MIG has the simplest geometry and a compact structure. It is easy to achieve a robust design and smaller assembly tolerance. The triode structure has an additional electrode with a potential difference from the cathode and the anode, which requires an extra power supply and electric insulation which makes it more complicated to construct and assemble. However, it provides an additional degree of freedom (the potential on the modulation anode) to further adjust the electron beam quality in operation. In an inverse-cathode MIG (IMIG), the modulation anode has a smaller radius than the emitter. Due to the constrain of electric breakdown between the electrodes, the IMIG is suitable for gyrotron devices which have a larger

emitter radius, therefore, allowing sufficient insulation gap distance. The IMIG is also a coaxial structure, therefore, more suitable for gyrotron devices that use a coaxial interaction circuit [9]. It has the advantage of a larger cathode radius (consequently large beam current) but is more challenging to align and assemble, and therefore, it is not commonly used. The other two types of MIGs are more common and widely used in gyrotron devices with cylindrical interaction circuits.

The gyroklystron is a member of the gyrotron device family [10]. It is able to achieve high amplification gain at a narrow bandwidth. The gyroklystrons have been used in applications such as radar and particle accelerators. A gyroklystron operating at 48 GHz with 2-MW output power was designed as a potential high-power microwave source to drive a linearizer for H2020 project CompactLight X-ray free-electron laser [11], [12]. The beam–wave interaction circuit employed a three-cavity configuration. The input and intermediate cavities operated at the TE_{01} mode and the output cavity operates at the TE_{02} mode in a circular waveguide.

In this article, an MIG was designed to generate the required electron beam to achieve a high-efficiency beam–wave interaction. The choice of MIG configuration and the solenoid system is introduced. The simulation and optimization results are presented.

II. OPERATION OF THE MIG

The trajectories of the electrons in an MIG are determined by both the electric and magnetic fields. The electron beam quality depends on not only the electrode structures which decide the electric field distribution but also the coil configuration of the solenoids which determine the magnetic field. The triode-type MIG has the advantage of further tuning the beam parameter such as the beam alpha (transverse-to-axial velocity ratio, $\alpha = v_\perp/v_z$) through the voltage at the modulation anode. For the diode-type MIG, its lack of flexibility can also be compensated by using a dedicated designed magnet system with a more complicated configuration [13], [14]. For example, additional coils at the cathode region can be used to adjust the magnetic field strength and its vector angle at the emitter surface, while keeping the field in the interaction region unchanged. In principle, the two methods do not make fundamental differences in the design stage since both are possible to achieve an optimal design if the electric and magnetic fields are well matched with each other.

The synthesis method has been developed to design the standard triode-type MIG [15]–[18]. Based on the conservation of angular momentum in the electron gun region, it has

$$B_{zc}r_c^2 = B_0\left(r_{g0}^2 - r_{L0}^2\right) \tag{1}$$

where B_{zc} and B_0 are the magnetic fields at the cathode and the interaction region. r_c is the radius of the emitter and r_{g0} and r_{L0} are the guiding center and the Larmor radius at the interaction region, respectively. The equation can be written as $r_c^2 = F_m(r_{g0}^2 - r_{L0}^2)$ by introducing a magnetic field compression ratio $F_m = B_0/B_{zc}$.

Further derivation provides the spread in the guiding center

$$\frac{\Delta r_{g0}}{r_{g0}} = \frac{\sin\phi_c}{\mu^2 + 1}\frac{I_0}{2\pi J_c r_c^2} \tag{2}$$

where ϕ_c is the emitter angle relative to the beam axis, and I_0 and J_c are the beam current and the current density of the emitter, respectively. $\mu = [(r_{g0}/r_{L0})^2 - 1]^{-1/2}$ is the cylindricity parameter. At a small μ where $r_{g0} \gg r_{L0}$, the transverse velocity at the interaction region can be approximated as

$$v_{\perp 0} \approx \frac{F_m^{3/2}E_c\cos\phi_c}{B_0\gamma_0}. \tag{3}$$

The velocity spread mainly comes from the nonuniform electric field at the emitter (E_c) and the magnetic field (B_0/F_m) due to the thickness of the emitter. The velocity spread can possibly be reduced if the electric and magnetic fields are well matched. The space charge depression voltage [19] introduces additional energy spread to the electron beam and can be another source of velocity spread. It contains depression voltage across the beam itself and the depression voltage due to the wall. The impact of depression voltage for a high-energy beam is not a major issue as it can be compensated for by operating at a slightly higher beam voltage. The relation between the alpha spread and the velocity can be obtained if the space charge depression voltage of the beam is ignored. In this case, all the electrons will have the same energy in the interaction region, where $v_{\perp 0}^2 + v_{z0}^2$ is a constant value. The alpha spread is

$$\frac{\Delta\alpha_0}{\alpha_0} = -\frac{\alpha_0^2 + 1}{\alpha_0^2}\frac{\Delta v_{z0}}{v_{z0}} = \left(\alpha_0^2 + 1\right)\frac{\Delta v_\perp}{v_{\perp 0}}. \tag{4}$$

The MIG is normally designed for a specific gyrodevice where the beam parameters at the interaction region are determined by the interaction circuit. In this case, μ and I_0 are known values. From (2), a small guiding center spread can be achieved by choosing large current density and emitter radius, or a small emitter angle. However, r_c is determined by F_m which is normally in a range of 15–25. Its choice is usually made by experience of previous successfully operated MIGs and then validated using the numerical simulation. A high F_m will result in large Larmor radius at the cathode and leads to a larger gap distance d_{ac} between the cathode and the modulation anode, otherwise, the electrons may directly strike on the modulation anode. Also, the improvement by increasing F_m is not significant after a certain value because $r_c \propto \sqrt{F_m}$. J_c also has constraints imposed by the property of the material. A small emitter angle is preferred when designing the electron gun geometry.

The potential on the modulation anode can be calculated from the coaxial field theory and it is

$$V_a = \frac{mc^2}{e}\frac{\ln(1+D_F\mu)}{\ln(1+2\mu)}$$
$$\times\left(\left(1 + \frac{4}{\mu^2}\left(\frac{1+\mu}{1+2\mu}\right)^2\frac{\gamma_0^2-1}{\cos^2\phi_c r_c^2/r_{L0}^2}\frac{\alpha_0^2}{\alpha_0^2+1}\right)^{0.5} - 1\right) \tag{5}$$

TABLE I
KEY PARAMETERS OF THE DESIGNED GYROKLYSTRON

Operating frequency (GHz)	48
Beam voltage (kV)	140
Beam current I_0 (A)	37
Beam alpha	1.35
Magnetic field in the interaction region B_0 (T)	2.02
Output power (MW)	2.3
Output mode in circular waveguide	TE_{02}
Gain (dB)	36
Electronic efficiency	44%
Beam guiding center (mm)	1.77
Pulse duration	1.5 us
Maximum pulse repetition rate	1 kHz

TABLE II
INITIAL PARAMETERS FROM THE SYNTHESIS AND
THE OPTIMIZED PARAMETERS

Parameters	Initial	Optimized
Emitter radius r_c	7.9 mm	7.9 mm
Emitter current density	20 A/cm^2	20 A/cm^2
Emitter angle ϕ_c	30.0º	33.9º
Voltage on modulation anode V_a	18.7 kV	32.5 kV
Cathode to modulation anode distance d_{ac}	15 mm	15.3 mm
Magnetic field compression ratio F_m	25.0	21.93
Magnetic field angle θ	---	2.1º

where γ_0 is the relativistic factor in the interaction region. $D_F = d_{ac}\cos\phi_c/(\mu r_c)$ is a normalized distance factor associated with the distance between the cathode to the modulation anode. Its reasonable range is between 2.5 and 4. A larger value will conflict with the assumption of the derivation of the synthesis method and will be difficult to achieve an optimal design, which will result in a large alpha spread.

The diode-type MIG is a special case of the standard triode-type MIG where the modulation anode is at the same voltage as the main anode. In this case in (5), a large D_F has to be used which is not desirable for the gun design. Equation (5) also shows that α_0 increases as the increment of V_a. The electrons may be reflected back to cathode if the alpha values are too high. To avoid this, the geometry of the cathode has to change accordingly, for example, to increase ϕ_c in order to maintain a small α_0. As a result, the diode-type MIG will need a significantly larger emitter angle than a triode-type one, which will result in a larger spread of the guiding center.

When a gyrodevice operates with a high-order mode, for example, the ITER gyrotrons [20], [21], the peak electric field locates at a large radius, which also means a large guiding center. At the same F_m, a much larger emitter radius can be used as compared with an MIG designed for a lower order mode gyrotron device. The emitter thickness can, therefore, be minimized to reduce the alpha spread. The emitter angle is not a limitation and the diode-type MIG is a better option due to its simple structure. For the gyrodevice operating with a low-order mode and when a high beam current is required, the triode-type MIG can achieve a better beam quality and it is a better option.

III. MIG FOR 48-GHz GYROKLYSTRON

A high-power gyroklystron was designed as the source to drive a linearizer for the CompactLight X-ray free-electron laser. The beam–wave interaction circuit employed low-order operating modes, the TE_{01} mode for both the input and intermediate cavities and a TE_{02} mode for the output cavity while minimizing the mode competition. The key parameters of the gyroklystron are shown in Table I. The parameter of the electron beam generated by the MIG should satisfy the

requirement of the beam–wave interaction with an alpha and guiding center spread as small as possible.

From the analysis in Section II, the triode-type MIG is a better choice as the gyroklystron operated with a low-order mode and the beam current is large. The low-order operating mode results in a small emitter radius. The small emitter angle in a triode-type MIG helps to reduce the spread in the beam. The MIG operates at high voltage. To keep the maximum electric field below the breakdown threshold, the distance between the cathode and anode has to be large and leads to a large D_F in a diode-type MIG. The triode-type MIG that has a lower voltage between the cathode and the modulation anode can achieve a suitable D_F value to achieve a better beam quality.

The initial design of the triode-type MIG was achieved using the synthesis method. The input parameters such as the beam voltage, beam current, and guiding center at the interaction region are shown in Table I. The choice of the current density is a tradeoff between the alpha spread due to the thickness of the emitter and the emission capability of the cathode. A low current density will result in a large emitter thickness and a large alpha spread. However, a high current density will push the limit of the cathode emission capability and reduce the lifetime of the cathode. Gyroklystrons for the accelerator application require a pulse duration of 1.5 μs and the maximum pulse repetition rate of 1 kHz (it normally operates at 400 Hz). The duty circle is less than 0.2%. Therefore, a relatively high current density of 20 A/cm^2 is feasible and it was chosen to estimate the initial parameters. Nanosized-scandia-doped dispenser cathodes with such high current density have been reported with more than 5000-h lifetime [22]. An MIG with a current density of 30 A/cm^2 using a SpectraMat 612X scandate cathode has been designed and tested [23]. Other parameters, such as the magnetic field compression ratio, and the maximum electric field were chosen as 22.5 and 7 kV/mm. The parameters derived from the synthesis are shown in Table II.

The gyroklystron operates under an ultrahigh vacuum which is normally in 10^{-9} mbar level. However, there are still gas molecules inside, and they can be ionized during the operation. It is a complicated process and the neutralization level is not yet well understood [24], [25]. The neutralization effect
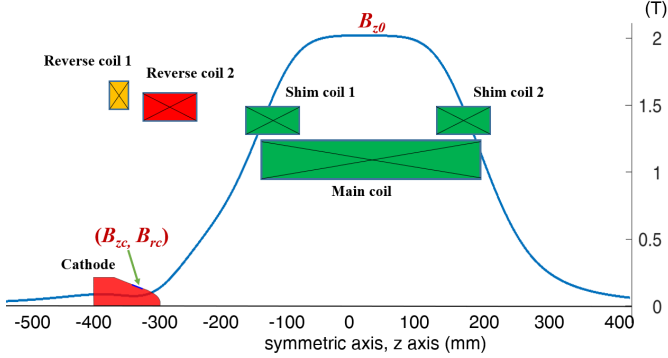
Fig. 2. Configuration of the magnet system and the magnetic field profile.

Fig. 3. Parametrized geometry of the triode-type MIG.

due to the ions in the high-power gyrodevices will affect the beam alpha. Therefore, it is important to have the flexibility to tune the beam parameters during the experiment. Besides the potential on the modulation anode, the magnetic field at the emitter surface provides an additional means of adjustment. The magnetic field of the gyroklystron was generated by a superconducting magnet with a closed-loop cryogenic system because the peak field 2.02 T requires too much drive power and cooling if normal conducting coils are used. The coil system is shown in Fig. 2.

Two sets of shim coils with the same drive current as the main coil were used to compensate for the field drop at the edge of the main coil to maintain the required flat length at the interaction region. To find an optimal magnetic field which matches with the electric field, additional magnet coils, the reverse coils 1 and 2, were used to shape to field profile at the emitter surface. Once the locations of the coils were decided, the overall magnetic field will be determined by the drive currents of the coils. Given the magnetic field strength B_{zc}, B_{rc} at the emitter surface and the field at the interaction region B_0, the unique set of drive currents for the main coil and reverse coils 1 and 2 can be solved. In practice, it is more convenient to use the magnetic field angle instead of B_{rc} and F_m instead of B_{zc}. With the first-order approximation of the off-axis magnetic field, $B_z(r) = Bz(r = 0)$ and $B_r(r) = -r B_z'/2$. The field angle is defined as $\theta = \text{atan}(B_r(r)/B_z(r))$.

Although the synthesis method assumes the adiabatic change of the magnetic field, and it does not consider the effect of the space charge, it provides a good starting point for parameter range scanning. The initial MIG parameters were simulated by charged-particle optics simulation software. Different tools, including MAGIC, CST Particle Studio, OPERA, and TRAK [26], were simulated on an existing cusp gun and compared with the experimental results [27], [28]. TRAK and MAGIC 2-D showed close agreement in alpha spread with values comparing well with the measurement. TRAK was chosen as the simulation tool due to the less computing time needed.

In the simulation, the fine meshes of 0.05 mm in the radial coordinate and 0.10 mm in the axial coordinate were used at the emitter region and meshes with 0.10 mm $(R) \times$ 0.20 mm (Z) were used for the rest simulation region.
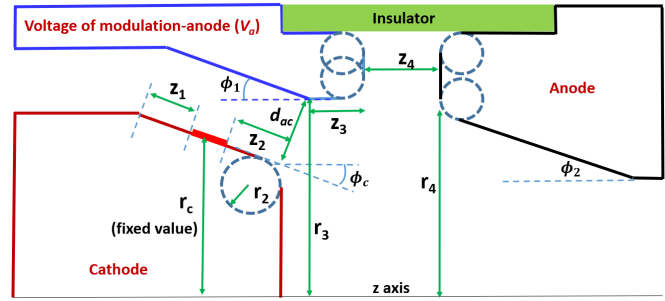
The time step to advance the particle trajectories was 2.5×10^{-13} s. In the simulation, the space charge effect was calculated by iterating the electron charge deposited as the electron trajectories progressed. The simulated results showed a large alpha spread of 25%. One of the reasons was the large emitter thickness due to the large emitted current needed. The nonuniform electric and magnetic fields at the emitter region cause the emitted electrons at different radii to experience different Lorentz forces, which increase the alpha spread. The alpha spread can be reduced by optimizing the electron gun geometry and the coil configuration to find well-matched electric and magnetic fields.

Further optimizations were carried out by parameterizing the geometry, as shown in Fig. 3, and a multiple-objective genetic algorithm [29]. The same method has been used for cusp electron gun design and benchmarked with the experimental measurement [28], [30]. The geometry of the MIG was parameterized and determined by 11 parameters, together with V_a and three parameters to control the magnetic field profile (B_{rc}, F_m, and relative shift position of the coils to the cathode), there are totally 15 parameters.

The particle trajectories of each parameter set were postprocessed using two evaluation functions, which was a combination of factors including the center value of the beam alpha, the guiding center, their spreads, and the beam laminarity. The final results were chosen from the Pareto front of the values of the evaluation functions after 400 generations (each generation contains 100 populations). The final optimized values of the key parameters are also shown in Table II. The optimal magnetic field compression ratio was 21.93, which is less than the initial value of 25. The major reason is the large emitter thickness due to the large emitted current needed. The nonuniform electric and magnetic fields at the emitter region cause the emitted electrons at different radii to experience different Lorentz forces and increase the alpha spread. The effect is more significant when the magnetic field strength is smaller (equivalently large compression ratio).

IV. SIMULATION RESULTS

The beam trajectories are shown in Fig. 4. A detailed plot of the trajectories of the fractional number of the simulated electrons is shown in Fig. 4(b). A good laminar beam was achieved. The normalized beam current as the function of the
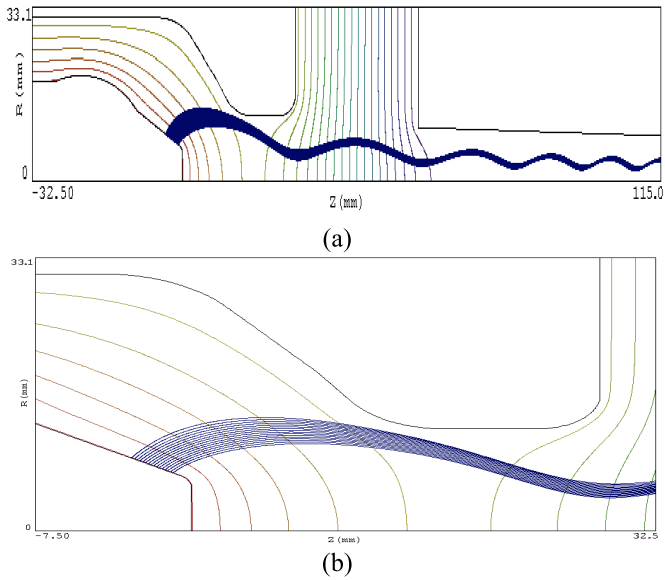
Fig. 4. (a) Electron beam trajectories in the MIG. (b) Detail plot at the cathode region.
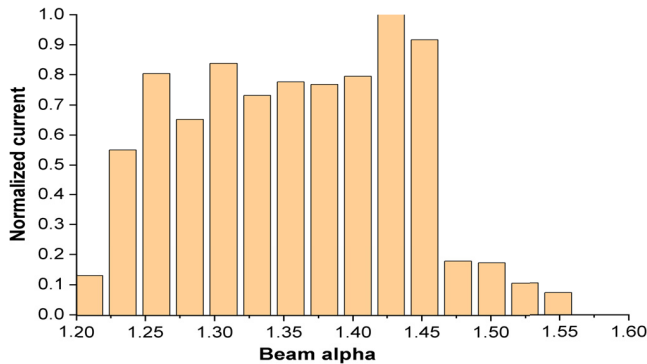

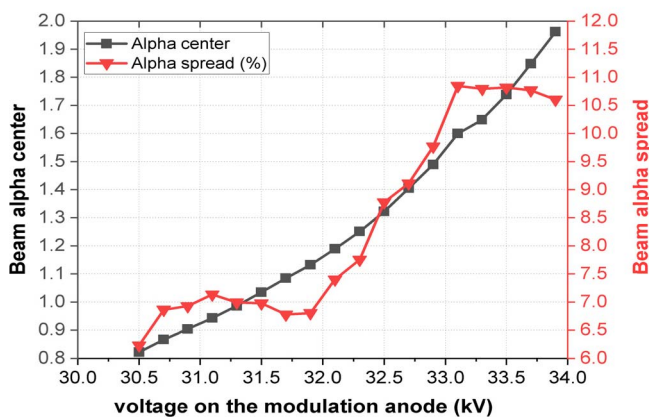Fig. 5. Normalized beam current as the function of beam alpha.

Fig. 6. Electron beam alpha as the function of voltage on the modulation anode.

beam alpha distribution is shown in Fig. 5. The half-width at half maximum (HWFH) alpha spread is about 8.9%.

The beam alpha value can be adjusted by changing the applied voltage on the modulation anode and the results are shown in Fig. 6. As the voltage increases, the alpha value increases, which agrees with the analysis in Section II.
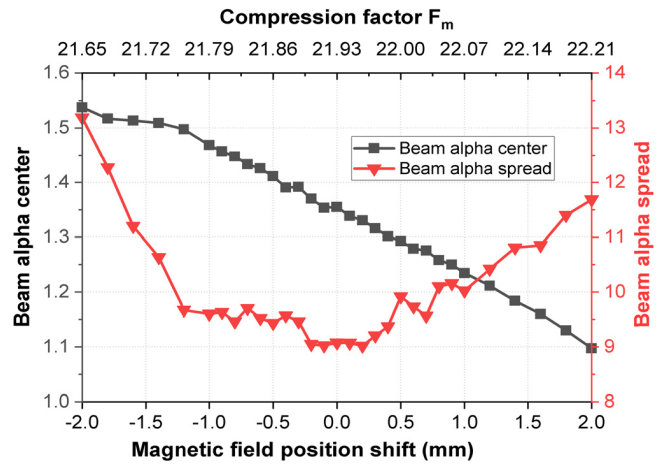
Fig. 7. Electron beam alpha as the function of magnetic field compression factor and the shift of magnetic field profile.

The beam alpha is relatively sensitive to the voltage at the modulation anode. With an approximately 280-V variation of the voltage, the shift of the center alpha value is 0.1. The alpha spreads have similar values at lower voltages but they increase when the voltages become larger. When the voltage is higher than 33.3 kV, although the alpha spread does not increase, the simulations show a long tail at a high alpha value range, which means a small number of electrons have high alpha values. At even higher voltages, larger than 34 kV, part of the electrons is reflected due to the alpha value being too high with the beam transportation rate no longer 100%.

The beam alpha can also be changed by varying the compression ratio F_m, which can be implemented by shifting the position of the superconducting magnet or adjusting the drive currents of the solenoids. The simulation results are shown in Fig. 7. By shifting the position of the magnet by -2 to 2 mm, the magnetic field compression ratio changed accordingly from 21.7 to 22.2, and the beam alpha center value changed linearly from 1.53 to 1.10. However, there is a relatively large difference in the alpha spread when the shift distance is large. A nearly constant alpha spread at ± 0.25 mm was found from the simulation, which indicates the tolerance allowed during assembly.

Not only the B_{zc} affects the beam alpha value and its spread, the simulations showed that the B_{rc} (which is equivalent to the field angle θ) also has a significant impact on the beam quality. From the results shown in Fig. 8, the beam alpha varies when keeping the F_m the same and changing only the θ value. As it increases, the alpha value increases. The optimal θ is 2.1°, where a minimum alpha spread is achieved. The effect on the alpha spread is roughly symmetric at the optimal value. When an inadequate θ is used, the alpha spread can be huge. However, since θ is small, B_{rc} is also small. It did not see a significant influence on the beam laminarity.

The impact of the alpha value and its spread to the beam–wave interaction efficiency of the 48-GHz gyroklystron was also investigated from the PIC simulations. The output power drops as the alpha spread increased. The trend showed that a 1% increment in the alpha spread would result in a 1.55% drop in the output power. With a 9% alpha spread
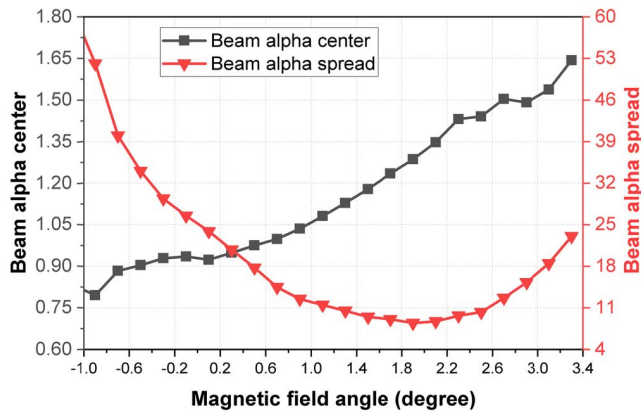
Fig. 8. Electron beam alpha as the function of the magnetic field angle at the emitter surface.
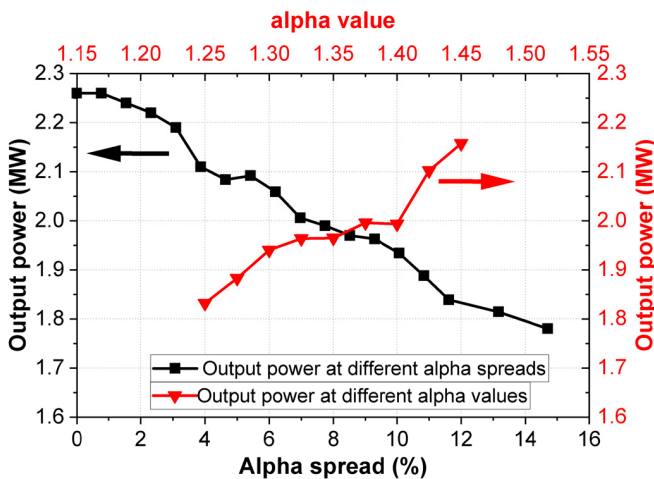

Fig. 9. Output power of the gyroklystron as the function of the alpha value and its spread.

from the MIG, the output power of the gyroklystron was 1.97 MW, slightly less than the required 2 MW. Fixing at a 9% alpha spread, the output powers of the gyroklystron at different alpha values were also shown in Fig. 9. When the beam alpha increases, the output power increases as well due to the transverse beam energy becoming larger. However, when the alpha value was larger than 1.42, the ripple at the output power rapidly increased and the interaction became unstable.

V. DISCUSSION AND CONCLUSION

In this article, the different configurations of MIGs are analyzed and a standard triode-type MIG was designed for a 48-GHz gyroklystron, which is proposed to drive the linearizer for the CompactLight X-ray free electron laser (XFEL). The synthesis method was used to determine the initial parameter values and suitable ranges. The MIG was further optimized and a low alpha spread of 8.9% was achieved. The simulation results showed that the field angle at the emitter surface also played an important role in the beam quality. It changes the alpha value and has a significant effect on the alpha spread, which is beyond the theoretical prediction. Its impact on the

beam laminarity is small because the magnetic field angle is small. An optimal triode-type MIG requires a good match between the electric field and magnetic field at the emitter area. The magnetic field at the emitter surface can be finely adjusted by introducing extra coils at the cathode region to control the magnetic field angle. The experimental study of the MIG and the 48-GHz gyroklystron will depend upon the outcome of the XFEL project, which is currently on the research and development design stage.

REFERENCES

[1] K. R. Chu, "The electron cyclotron maser," Rev. Mod. Phys., vol. 76, no. 2, pp. 489–540, May 2004, doi: 10.1103/RevModPhys.76.489.
[2] G. S. Nusinovich, M. K. A. Thumm, and M. I. Petelin, "The gyrotron at 50: Historical overview," J. Infr., Millim., Terahertz Waves, vol. 35, no. 4, pp. 325–381, Apr. 2014, doi: 10.1007/s10762-014-0050-7.
[3] J. L. Seftor, A. T. Drobot, and K. R. Chu, "An investigation of a magnetron injection gun suitable for use in cyclotron resonance masers," IEEE Trans. Electron Devices, vol. 26, no. 10, pp. 1609–1616, Oct. 1979, doi: 10.1109/TED.1979.19660.
[4] C. R. Donaldson et al., "A cusp electron gun for millimeter wave gyrodevices," Appl. Phys. Lett., vol. 96, no. 14, Apr. 2010, Art. no. 141501, doi: 10.1063/1.3374888.
[5] W. Lawson, "Design of low velocity-spread cusp guns for axis encircling beams," Appl. Phys. Lett., vol. 50, no. 21, pp. 1477–1479, 1987, doi: 10.1063/1.97805.
[6] I. G. Pagonakis et al., "Status of the development of the EU 170 GHz/1 MW/CW gyrotron," Fusion Eng. Des., vols. 96–97, pp. 149–154, Oct. 2015, doi: 10.1016/j.fusengdes.2015.02.050.
[7] S. Ruess et al., "An inverse magnetron injection gun for the KIT 2-MW coaxial-cavity gyrotron," IEEE Trans. Electron Devices, vol. 63, no. 5, pp. 2104–2109, May 2016, doi: 10.1109/TED.2016.2540298.
[8] K. Dong, Y. Luo, W. Jiang, H. Fu, and S. Wang, "Magnetron injection gun design for multifrequency band operations," IEEE Trans. Electron Devices, vol. 63, no. 9, pp. 3719–3724, Sep. 2016, doi: 10.1109/TED.2016.2586522.
[9] V. K. LYGlN, V. N. MANUILOV, A. N. Kuftin, A. B. Pavelyev, and B. Piosczyk, "Inverse magnetron injection gun for a coaxial 1-5MW, 140 GHz gyrotron," Int. J. Electron., vol. 79, no. 2, pp. 227–235, Aug. 1995, doi: 10.1080/00207219508926264.
[10] A. V. Gaponov, M. I. Petelin, and V. K. Yulpatov, "The induced radiation of excited classical oscillators and its use in high-frequency electronics," Radiophys. Quantum Electron., vol. 10, nos. 9–10, pp. 794–813, 1971, doi: 10.1007/BF01031607.
[11] L. J. R. Nix et al., "Demonstration of efficient beam-wave interaction for a MW-level 48 GHz gyroklystron amplifier," Phys. Plasmas, vol. 27, no. 5, May 2020, Art. no. 053101, doi: 10.1063/1.5144590.
[12] L. Wang et al., "Design of a Ka-band MW-level high efficiency gyroklystron for accelerators," IET Microw., Antennas Propag., vol. 12, no. 11, pp. 1752–1757, Sep. 2018. [Online]. Available: https://digital-library.theiet.org/content/journals/10.1049/iet-map.2018.0103
[13] I. G. Pagonakis, K. A. Avramidis, G. Gantenbein, T. Rzesnicki, A. Samartsev, and J. Jelonnek, "Magnetic field profile analysis for gyrotron experimental investigation," Phys. Plasmas, vol. 24, no. 3, Mar. 2017, Art. no. 033102, doi: 10.1063/1.4977460.
[14] C. P. Yuan, T. H. Chang, N. C. Chen, and Y. S. Yeh, "Magnetron injection gun for a broadband gyrotron backward-wave oscillator," Phys. Plasmas, vol. 16, no. 7, Jul. 200, Art. no. 0731099, doi: 10.1063/1.3187903.
[15] J. Mark Baird and W. Lawson, "Magnetron injection gun (MIG) design for gyrotron applications," Int. J. Electron., vol. 61, no. 6, pp. 953–967, Dec. 1986, doi: 10.1080/00207218608920932.
[16] W. Lawson, "Magnetron injection gun scaling," IEEE Trans. Plasma Sci., vol. 16, no. 2, pp. 290–295, Apr. 1988, doi: 10.1109/27.3827.

[17] W. Lawson and V. Specht, "Design comparison of single-anode and double-anode 300-MW magnetron injection gun," *IEEE Trans. Electron Devices*, vol. 40, no. 7, pp. 1322–1328, Jul. 1993, doi: 10.1109/16.216439.

[18] U. Singh, A. Bera, R. R. Rao, and A. K. Sinha, "Synthesized parameters of MIG for 200 kW, 42 GHz gyrotron," *J. Infr., Millim., Terahertz Waves*, vol. 31, no. 4, pp. 533–541, Apr. 2010, doi: 10.1007/s10762-009-9608-1.

[19] A. T. Drobot and K. Kim, "Space charge effects on the equilibrium of guided electron flow with gyromotion," *Int. J. Electron.*, vol. 51, no. 4, pp. 351–367, Oct. 1981, doi: 10.1080/00207218108901342.

[20] J. Jelonnek *et al.*, "From series production of gyrotrons for W7-X toward EU-1 MW gyrotrons for ITER," *IEEE Trans. Plasma Sci.*, vol. 42, no. 5, pp. 1135–1144, May 2014, doi: 10.1109/TPS.2014.2301839.

[21] M. Thumm, "MW gyrotron development for fusion plasma applications," *Plasma Phys. Controlled Fusion*, vol. 45, no. 12A, pp. A143–A161, Dec. 2003, doi: 10.1088/0741-3335/45/12a/011.

[22] F. Yang, J. Wang, Y. Wang, W. Liu, and X. Zhu, "Investigation of nanosized-scandia-doped dispenser cathodes with machined surfaces," *IEEE Trans. Electron Devices*, vol. 63, no. 4, pp. 1728–1733, Apr. 2016, doi: 10.1109/TED.2016.2528580.

[23] L. R. Barnett, N. C. Luhmann, C. C. Chiu, and K. R. Chu, "Relativistic performance analysis of a high current density magnetron injection gun," *Phys. Plasmas*, vol. 16, no. 9, Sep. 2009, Art. no. 093111, doi: 10.1063/1.3227649.

[24] I. G. Pagonakis *et al.*, "Electron trapping mechanisms in magnetron injection guns," *Phys. Plasmas*, vol. 23, no. 2, Feb. 2016, Art. no. 023105, doi: 10.1063/1.4941705.

[25] A. Schlaich *et al.*, "Frequency-based investigation of charge neutralization processes and thermal cavity expansion in gyrotrons," *J. Infr., Millim., Terahertz Waves*, vol. 36, no. 9, pp. 797–818, Sep. 2015, doi: 10.1007/s10762-015-0177-1.

[26] S. Humphries Jr., "Numerical modeling of Space-Charge-Limited charged-particle emission on a conformal triangular mesh," *J. Comput. Phys.*, vol. 125, no. 2, pp. 488–497, May 1996, doi: 10.1006/jcph.1996.0110.

[27] W. He, C. R. Donaldson, L. Zhang, K. Ronald, A. D. R. Phelps, and A. W. Cross, "Broadband amplification of low-terahertz signals using axis-encircling electrons in a helically corrugated interaction region," *Phys. Rev. Lett.*, vol. 119, no. 18, Oct. 2017, Art. no. 184801, doi: 10.1103/PhysRevLett.119.184801.

[28] L. Zhang, W. He, C. R. Donaldson, and A. W. Cross, "Investigation on the optimal magnetic field of a cusp electron gun for a W-band gyro-TWA," *Phys. Plasmas*, vol. 25, no. 5, May 2018, Art. no. 053104.

[29] W. Jiang, Y. Luo, R. Yan, and S. Wang, "Genetic algorithm-based shape optimization of modulating anode for magnetron injection gun with low velocity spread," *IEEE Trans. Electron Devices*, vol. 62, no. 8, pp. 2657–2662, Aug. 2015, doi: 10.1109/TED.2015.2443068.

[30] L. Zhang, C. R. Donaldson, and W. He, "Optimization of a triode-type cusp electron gun for a W-band gyro-TWA," *Phys. Plasmas*, vol. 25, no. 4, Apr. 2018, Art. no. 043120, doi: 10.1063/1.5028262.

Design and Simulation of a High-Power 48GHz Gyroklystron Amplifier for Accelerator Applications

Laurence. J. R. Nix
Department of Physics
University of Strathclyde
Glasgow G4 0NG, UK
laurence.nix@strath.ac.uk

Liang Zhang
Department of Physics
University of Strathclyde
Glasgow G4 0NG, UK
liang.zhang@strath.ac.uk

Adrian W. Cross
Department of Physics
University of Strathclyde
Glasgow G4 0NG, UK
a.w.cross@strath.ac.uk

Abstract—A 48GHz gyroklystron amplifier has been designed using particle-in-cell (PIC) simulation techniques. The beam is provided by a magnetron injection gun (MIG). The gyroklystron is predicted to deliver 2MW of output power at 48GHz with a gain of 35dB and an efficiency of 38%. The design was developed with consideration of the harmonic linearizer of a linear accelerator (linac) that is being designed as part of the H2020 CompactLight X-ray free electron laser (XFEL) project.

Keywords—Gyroklystron; Magnetron Injection Gun; Microwave Amplifier; Vacuum Electronic Devices

I. INTRODUCTION

The gyroklystron is an amplifier based on the principle of the cyclotron resonance maser (CRM) mechanism [1], wherein power is extracted through interaction of an electron beam with the fields in a series of cavities. The application of gyroklystrons has mainly been in radar applications [2, 3]. Although the prospect of gyroklystron-driven accelerators has been explored [4], klystrons are still favored in practice. However, the output power that can be achieved with a klystron falls off at very high frequencies. C-band and X-band drive frequencies are currently of interest to improve acceleration gradients in linacs. While the drive power can be delivered at these frequencies by commercial klystrons, to achieve high-quality bunching requires a linearization system. The most well-developed technique is harmonic linearization [5] which utilizes an additional cavity driven at a harmonic of the drive frequency. The harmonic frequency may be K-band or higher, at which point the gyroklystron is a strong candidate to overcome the difficulty of delivering high power. MW-level, K-band multi-beam klystrons are also being designed but as yet no commercial amplifiers are available [6]. The gyroklystron presented in this work operates at 48GHz and is appropriate to drive an 8th harmonic linearizer for a 6GHz injector or a 4th harmonic linearizer for a 12GHz injector.

II. DESIGN MEHTODOLOGY

A. Magnetron Injection Gun (MIG)

A triode-type magnetron injection gun has been developed as part of this work [6]. The initial parameters were estimated

using the Baird trade-off equations for MIG design [8]. These parameters were then optimized in TRAK [9]. A multi-objective genetic algorithm considering 11 geometric parameters and 4 field parameters was used to develop an optimized design.

B. Interaction Circuit

The interaction circuit was developed through a combination of theoretical models in conjunction with particle-in-cell simulation techniques [10]. Reference [10] details the process and main results. The analysis of the interaction circuit has been presently expanded upon with consideration of phase stability and further analysis on the effect of the spread in velocity ratio α.

C. Vacuum Windows

Vacuum windows have been designed using CST microwave studio to analyse the S-parameters in detail. The input window uses a pillbox-type window, with rectangular sections equivalent to a WR22 standard waveguide which was selected to match the input waveguide structure without introducing the need for additional tapers or steps. For the same reason, a single-disc simple output window was selected for the output.

III. RESULTS AND ANALYSIS

A. MIG and Interaction Circuit

The gyroklystron was predicted to achieve 2.3MW of output in the ideal beam case as presented in [10], as shown in Fig. 1. In practice, an ideal beam cannot exist and as there is always some level of spread in the values for velocity v and velocity ratio α, arising from cathode geometry and space-charge effects. The trajectories of the electrons in the MIG are shown in Fig. 2.

The spread was minimized by the design of the MIG, with a resulting α-spread of 8.9%. The expected power output accounting for this spread is 2.0MW. More detailed discussions of the interaction circuit and MIG are presented in [10] and [7] respectively. The linearizer requires a high level of phase-stability. The phase stability can be calculated by the method presented in [11].
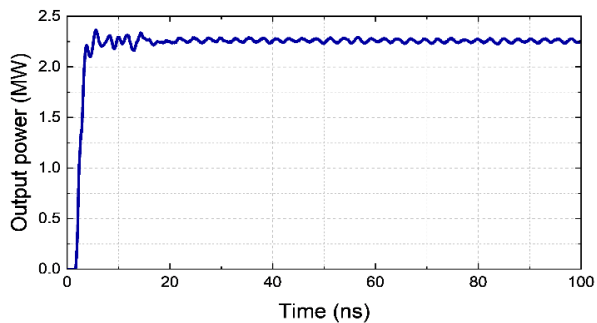
Fig. 1.   Output power of the gyroklystron with an ideal beam.
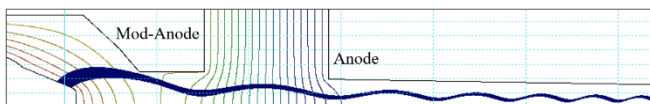

Fig. 2.   Geometry, field lines, and electron beam trajectories in the triode-type magnetron injection gun.
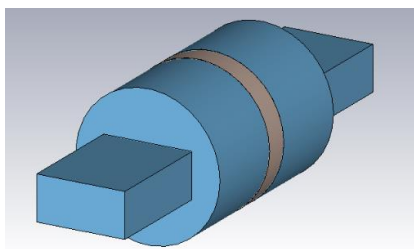

Fig. 3.   Geometry of the pillbox-type input window

The phase stability was calculated to be 0.26° per 0.01% of the modulator's voltage stability. Therefore, with the current standard of modulator commercially available [12], the gyroklystron is theoretically able to meet the high stability requirement of a typical linearizer system.

B. Vacuum Windows

The input window was designed with a pillbox-type structure, as shown in Fig. 3. The ceramic disc was assigned a relative dielectric constant of 9.4 matching that of 99.4% Al_2O_3, which was selected for its balance of mechanical, thermal, and optical properties. The initial estimates of pillbox radius and ceramic thickness were optimized to minimize reflection. The maximum allowable reflection signal amplitude was chosen as -35dB at the centre frequency (48GHz) and -20dB within the gyroklystron's 3-dB bandwidth (47.8 to 48.2GHz). Based on a conservative estimate of 10μm precision in machining, the reflected amplitude was at most -44dB at 48GHz and -26dB within the bandwidth as shown in Fig. 4. With higher machining precision, these reflection characteristics may be improved by a modest amount. The output window design was a single disc matched to the cylindrical output section of the gyroklystron. Boron nitride was selected as the window material as it is a relatively low-cost material that can still offer appropriate thermal properties for the high pulse repetition frequency of 1kHz and 1.5μs pulsed operation regime required by the harmonic lineariser for the X-ray FEL. Power reflected from the output window is more harmful than the input window as it would travel back toward the interaction circuit. Therefore, a stricter limit of -35dB reflection was set as the target maximum over the device bandwidth. This was achieved in simulation, but sub-μm precision would be required to meet this threshold in practice.
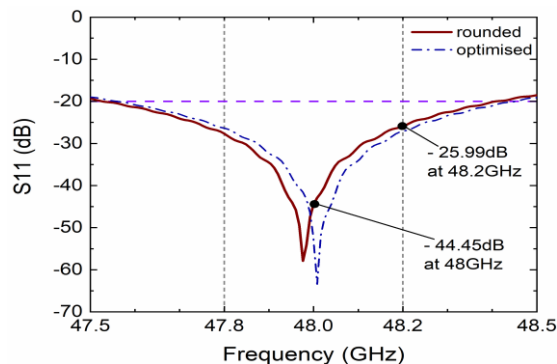

Fig. 4.   Reflection Parameters of the input window with optimal dimensions and with dimensions rounded to the nearest 10μm.

IV. CONCLUSIONS

The design of a high-power 48GHz gyroklystron has been presented. The MIG is predicted to achieve an α-spread of 8.9%. Further simulations of the interaction circuit conclude that this level of spread makes the expected output power 2.0MW, compared with the ideal beam case of 2.3MW. Phase stability calculations show that the gyroklystron is able to deliver good stability, but this is primarily dependent on the modulator properties. Input and output windows have also been designed. The input window displays excellent reflection properties. The output window can also meet the chosen reflection requirement if machining tolerance is high enough.

REFERENCES

[1]   J. L. Hirshfield and J. M. Wachtel, "Electron Cyclotron Maser," *Physical Review Letters,* vol. 12, no. 19, pp. 533-536, 1964.

[2]   A. A. Tolkachev, B. A. Levitan, G. K. Solovjev, V. V. Veytsel, and V. E. Farber, "A megawatt power millimeter-wave phased-array radar," *IEEE Aerospace and Electronic Systems Magazine,* vol. 15, no. 7, pp. 25-31, 2000.

[3]   G. J. Linde, M. T. Ngo, B. G. Danly, W. J. Cheung, and V. Gregers-Hansen, "WARLOC: A high- power coherent 94 GHz radar," *IEEE Transactions on Aerospace and Electronic Systems,* vol. 44, no. 3, pp. 1102-1117, 2008.

[4]   W. Lawson, J. P. Calame, G. S. Nusinovich, and B. Hogan, "Reflections on the university of Maryland's program for investigating gyro-amplifiers as potential sources for linear colliders," *Terahertz Science and Technology,* vol. 10, no. 1, pp. 1-43, 2017.

[5]   T. I. Smith, "Production of intense low emittance beams for free electron lasers using electron linear accelerators," *Nuclear Instruments and Methods in Physics Research, A,* vol. 250, no. 1, pp. 64-70, 1986.

[6]   I. Syratchev, J Cai et al, G. Burt et al, "Design and simulation of a 36GHz, 2.5MW Multi Beam (20) Klystron for accelerator applications", accepted for IEEE Transactions on Electron Devices, 2020.

[7]   L. Zhang, L. J. R. Nix, and A. W. Cross, "Magnetron Injection Gun for High-Power Gyroklystron," *TED,* vol. 67, no. 11, pp. 5151-5157, 2020.

[8]   J. Mark Baird and W. Lawson, "Magnetron injection gun (MIG) design for gyrotron applications," *International Journal of Electronics,* vol. 61, no. 6, pp. 953-967, 1986.

[9]   *Trak 8.0: Electron/ion Gun Design and Charged Particle Dynamics (User Manual).* Albuquerque, New Mexico, USA: Field Precision LLC.

[10] L. J. R. Nix *et al.,* "Demonstration of efficient beam-wave interaction for a MW-level 48 GHz gyroklystron amplifier," *Physics of Plasmas,* vol. 27, p. 053101, 2020.

[11] G. S. Park, V. L. Granatstein, P. E. Latham, C. M. Armstrong, A. K. Ganguly, and S. Y. Park, "Phase stability of gyroklystron amplifier," *IEEE Transactions on Plasma Science,* vol. 19, no. 4, pp. 632-640, 1991.

[12] Scandinova,   "Product   Sheet: K-series   K100," *https://scandinovasystems.com/products/k-series/k100*

Design of a 48 GHz Gyroklystron Amplifier

Laurence J. R. Nix [ID], Liang Zhang [ID], and Adrian W. Cross, *Member, IEEE*

Abstract—**The continued development of linear accelerators at higher frequencies poses several technological challenges. One such challenge is the requirement for high-frequency amplifiers to drive linearization systems. Presented in this article is the design of a 48 GHz gyroklystron amplifier appropriate for application in a harmonic linearizer for a 6 GHz or 12 GHz drive frequency. The beam used in the gyroklystron is provided by a magnetron injection gun (MIG), which has been designed using genetic optimization. The gyroklystron interaction circuit was designed with the aid of a Particle-in-Cell (PIC) simulation study which predicted 2 MW of output power at 48 GHz with a gain of 35 dB and an efficiency of 38%. This article summarizes the preceding work on the interaction circuit and MIG with additional phase stability analysis as well as presenting the design and analysis of vacuum windows, an input coupler, and the collector.**

Index Terms—**Gyroklystron, magnetron injection gun (MIG), microwave amplifier, particle-in-cell (PIC) simulation, vacuum electronic devices.**

I. INTRODUCTION

THE gyroklystron amplifier is a member of cyclotron resonance maser (CRM) mechanism family [1], which also includes gyrotron oscillators and gyro-traveling wave amplifiers. Each of these devices is based on the interaction of a gyrating electron beam with the transverse electric (TE) mode in the interaction circuits.

Historically, most gyroklystron research has related to radar applications [2], [3] and the idea of gyroklystron-driven linear accelerators has also been explored [4]. Although many promising results are summarized in [4] and [5], this line of study did not lead to the use of gyroklystrons as drivers for accelerating cavities and klystrons are still the industry standard. Commercially available klystrons can comfortably deliver the required power at the C-band and X-band drive frequencies which are currently favored in accelerator design [6].

In high-energy linear accelerators, in order to generate the femtosecond bunches required while maintaining a high bunch charge, a magnetic chicane is typically included for bunch compression. An energy chirp is applied to the bunch before compression. As the path length through the chicane is energy-dependent, the bunch is compressed in time. However, as voltage varies sinusoidally, the chirp is nonlinear in time, and an additional section must be included to linearize the chirp. The most well-developed linearization method is harmonic linearization [7], wherein an additional cavity at a harmonic of the drive frequency is used to flatten the field-profile experienced by the electrons. The frequencies required of the linearizer are high, and conventional klystrons cannot deliver sufficient power. For example, the CompactLight X-ray free-electron laser (XFEL) design study features a 36 GHz (*Ka*-band) linearizer, with a power demand beyond currently available commercial amplifiers at that frequency [8]. Two solutions have been proposed; a multibeam (20 beam) klystron (MBK) [9] and a gyroklystron [10] which show comparable performance with each other and both remain viable options moving forward.

There was also a strong incentive to explore the possibility of a 48 GHz (fourth harmonic) linearizer as the voltage required from the linearizer scales with the inverse square of harmonic number relative to injector frequency. The voltage required for a 48 GHz linearizer was 3.5 MV, compared with 6.2 MV at 36 GHz [11], [12]. Therefore, a higher harmonic option can lower the energy cost of the system.

Respectively, Nix *et al.* [13] and Zhang *et al.* [14] describe the work performed on the interaction circuit and magnetron injection gun (MIG) for this project. This article presents the detailed design of the other components in the gyroklystron, including the input coupler, vacuum windows, and the thermal analysis of the collector region. These components together with the published interaction circuit and the MIG provide a complete design solution of the 2 MW 48 GHz gyroklystron.

II. PRINCIPLE AND OVERALL DESIGN OF GYROKLYSTRON

Fig. 1(a) shows a simple flowchart covering each section of the gyroklystron design. A high-voltage high-power modulator which is available from Scandinova [15] will be used to provide the required beam voltage and current. The high-power microwave radiation extracted through the output window will be fed into the SLAC Energy Development (SLED)-II type pulse compressor (with a power compression ratio of ∼7) and used to drive the linearizer [16]. Each of the boxed components
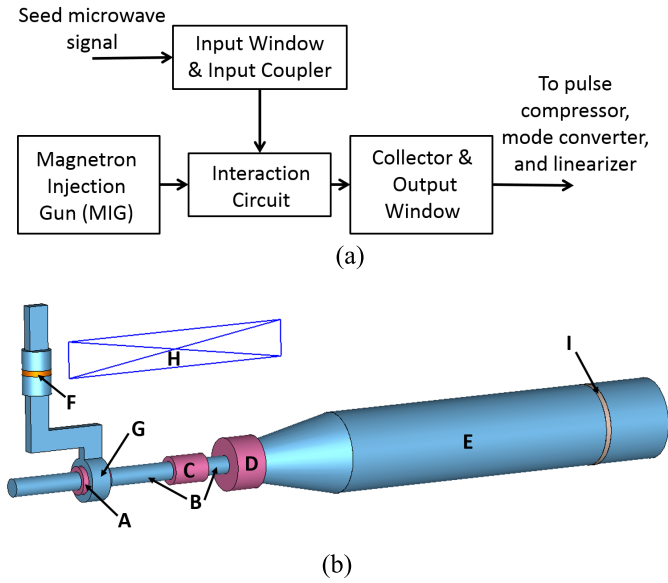
This article has been accepted for inclusion in a future issue of this journal. Content is final as presented, with the exception of pagination.

2   IEEE TRANSACTIONS ON ELECTRON DEVICES

(a)

(b)

Fig. 1. (a) Flowchart of the gyroklystron. (b) Components of the gyroklystron design (not to exact scale), cavities highlighted in pink. A–input cavity; B–drift tubes; C–intermediate cavity; D–output cavity; E–collector; F–pillbox-type coupler with input window; G–coaxial input coupler for first cavity; H–solenoid; and I–output window.

in Fig. 1(a) has been studied as part of this work and is presented in the following sections.

High-frequency gyroklystrons are sometimes designed to operate at the second harmonic to lower the magnetic field requirement at the cost of reduced efficiency [17], [18]. In this instance, a fundamental harmonic design was preferred as maximizing efficiency was a primarily goal. Additionally, highly stable operation was desired and magnetic field variations have a lesser impact on a fundamental harmonic device.

Fig. 1(b) shows a 3-D representation of the interaction circuit and input coupler. In the gyroklystron, microwave power is coupled into an input cavity to excite a $TE_{0,1,1}$ mode which applies phase-bunching forces to the electron beam. One or more intermediate cavities serve to reinforce the bunching effect, and then the bunched electrons transfer a portion of their energy to the field in the output cavity. The electron beam is generated by a MIG in which electrons emitted from a thermionic cathode are guided into the beam tunnel with the desired properties by an optimized arrangement of magnetic fields. Since only transverse momentum is lost during the interaction, the beam still has a large amount of power at the point of deposition and the thermal effect on the collector must be considered.

III. MIG AND INTERACTION CIRCUIT

The initial parameters of the MIG were estimated using the Baird tradeoff equations [19]. These estimates were then optimized by the finite element trajectory solver TRAK [20], using a multiobjective genetic algorithm considering 11 geometric and four field parameters. Further detail on the theory and methodology is presented in [14]. The optimized MIG achieved a spread of 8.9% in the transverse-to-axial velocity ratio α. The interaction circuit is a three-cavity configuration,
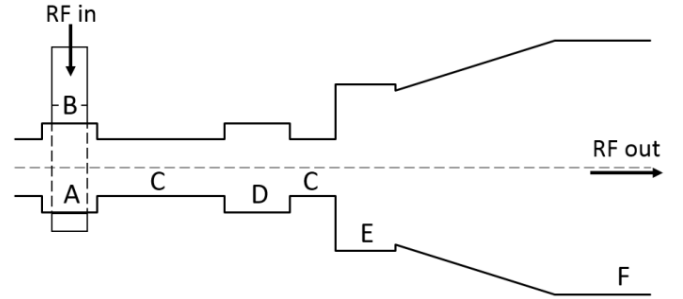

Fig. 2. Schematic of a three cavity gyroklystron interaction circuit. A–input cavity; B–input coupler; C–drift tubes; D–intermediate cavity; E–output cavity; and F–collector.

as shown in Fig. 2. The detailed design process has been presented in [13], summarized as follows.

1) Cavity sizes were estimated through consideration of eigenfrequency equations, cutoff frequency, and coupling coefficients.
2) The initial beam parameters and the estimated gain was obtained using gyroklystron linear theory [21].
3) The linear theory designs were refined using a self-consistent nonlinear model [22], [23].
4) The design was verified and reoptimized using particle-in-cell (PIC) simulation in MAGIC [24], and the performance was tested over various input parameter sets.

The main results described in [13] and [14] show that the gyroklystron's ideal-beam output power is 2.3 MW with a 37 A, 150 kV beam. With the optimized MIG's α-spread of 8.9%, the predicted output power of the gyroklystron is reduced to 2.0 MW. This meets the power requirement of the SLED-II pulse compressor and linearizer design. Confidence in the simulation results is high as MAGIC has been used in the design of several gyroklystron amplifiers and shown good agreement between simulation and experimental data [25]–[27]. The linearizer specification also places the demand that the phase stability of the amplifier should be no higher than 0.5° [11]. This can be calculated by (1) and the detailed derivation is presented in [28]

$$d\phi = \left(1+\alpha^2\right)^{\frac{1}{2}} \frac{\omega L}{c} \frac{\left(\gamma^2-1\right)^{\frac{1}{2}}}{\gamma+1} \left(1 + \frac{\Delta}{2} \frac{\alpha^2}{1+\alpha^2} \frac{\alpha^2-\gamma}{\gamma}\right) \frac{dV}{V}$$

(1)

where L is the length of the interaction circuit and Δ is the normalized detuning parameter. As most of the parameters in (1) are fixed based on the design of the interaction circuit, the primary influence on phase stability is the voltage stability of the high-power modulator. The phase stability over the device length was calculated to be 0.26° per 0.01% voltage stability of the modulator. Scandinova's K100 modulator can meet extreme stability specifications [15]. Therefore, the designed gyroklystron can meet the requirement of the typical linearizer system for the CompactLight XFEL.

IV. COAXIAL INPUT COUPLER

Initial simulations of the interaction circuit simply assume an ideal $TE_{0,1,1}$ mode being excited. In practice, it is not
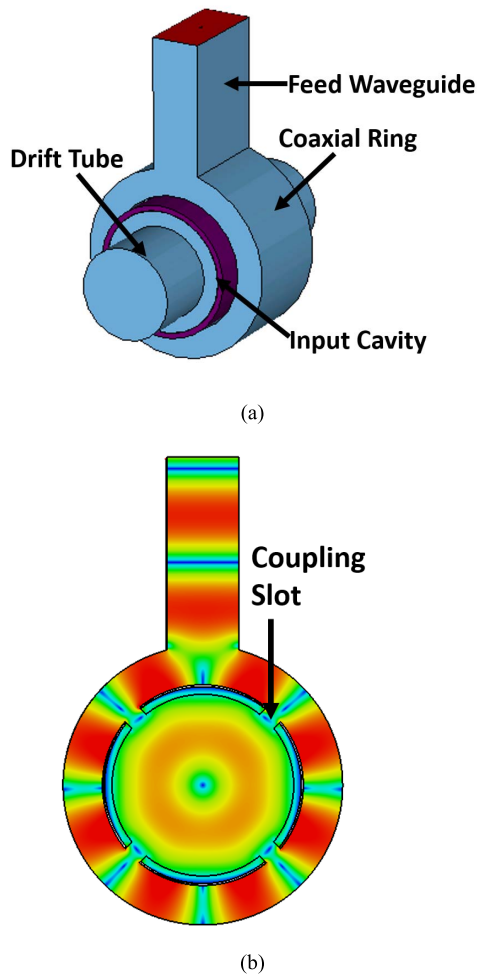
This article has been accepted for inclusion in a future issue of this journal. Content is final as presented, with the exception of pagination.

NIX *et al.*: DESIGN OF A 48 GHz GYROKLYSTRON AMPLIFIER

3

(a)

(b)

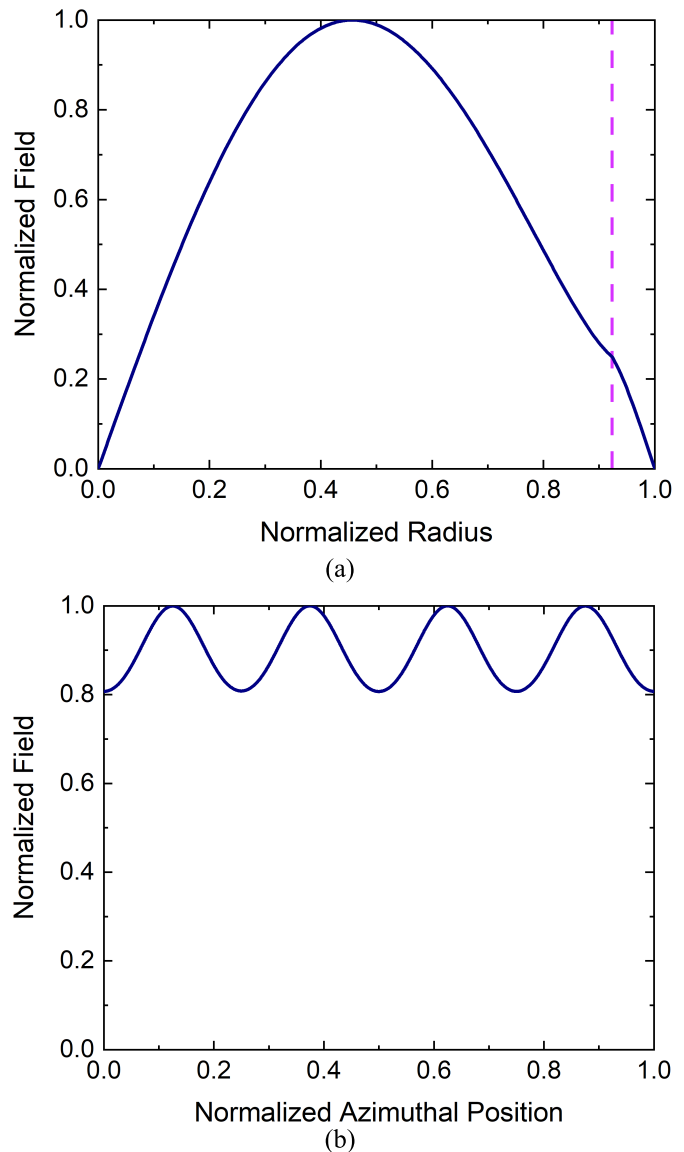Fig. 3. Coaxial coupler geometry. (a) 3-D model. (b) Cross section with field pattern.

(a)

(b)

Fig. 4. (a) Radial and (b) azimuthal field-profile in the input coupler. The dashed line in the top figure indicates the beginning of the dielectric wall-lining.

so trivial to excite the correct mode, and the design of the coupling system must be considered as part of the complete gyroklystron design. The seed microwave signal is supplied to the input cavity through a coaxial input coupler of the arrangement shown in Fig. 3.

A rectangular waveguide feeds into a coaxial cavity which encircles the gyroklystron input cavity. Four evenly spaced slots on the shared wall between the gyroklystron cavity and the coaxial ring allow energy to leak through and excite the desired mode.

By this structure, a rectangular $TE_{0,1}$ waveguide mode is converted to a $TE_{4,1,1}$ coaxial cavity mode and then to a $TE_{0,1,1}$ cylindrical cavity mode. The standard WR22 waveguide (5.69 mm × 2.84 mm) was selected for convenience of manufacture and the cavity dimensions are determined by the optimized interaction circuit [13]. The inner radius of the coaxial section (4 mm) is just larger than the cavity radius accounting for wall thickness. The remaining parameters to consider are therefore the outer radius of the coaxial region and the dimensions of the coupling slots. The outer radius of the coaxial region should be that which sets the eigenfrequency of the coaxial $TE_{4,1,1}$ mode to 48 GHz, which in this case was 5.57 mm. Finite-difference time-domain (FDTD) simulations

in CST Microwave Studio were then performed to analyze and optimize for the best achievable mode purity of the $TE_{0,1}$ mode in the input cavity. To demonstrate the feasibility of the design, a simplified model was computed, showing effective excitation of the desired mode in an unlined cavity. The actual cavity requires a dielectric layer on the outer wall to maintain the correct Q of 180. The dielectric properties used in this simulation were $\varepsilon_r = 12$ and $\tan(\delta) = 0.62$, which can be achieved with a BeO:SiC compound [29]. The simulated reflection parameter at the input port was exported and postprocessed with Q factors calculated by the method and program described in [30]. Initial simulations showed that this made it more difficult for the coupler to excite a pure mode. Parameter sweeps over the aperture dimensions were performed to improve mode coupling, resulting in the field-profile shown in Fig. 4. The optimized coupling slots were rectangular with dimensions of 2.3 mm × 0.8 mm.
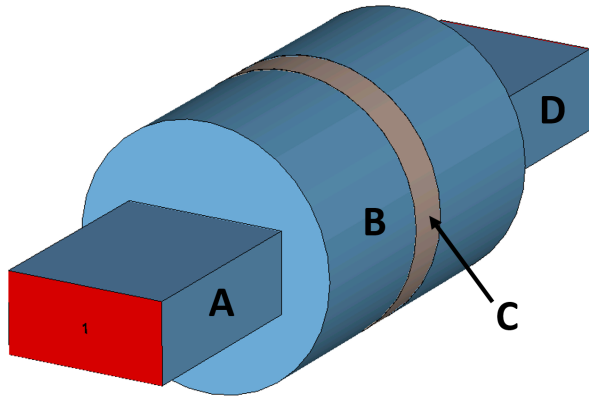
4

This article has been accepted for inclusion in a future issue of this journal. Content is final as presented, with the exception of pagination.

IEEE TRANSACTIONS ON ELECTRON DEVICES

Fig. 5. Geometry of the input window. A–waveguide from microwave source; B–cylindrical pillbox section; C–alumina disk; and D–feed waveguide to the input coupler.

Fig. 6. Reflection parameters of the input window.

The peak field along the radial line occurs at $0.45r_c$ rather than the optimal $0.48r_c$, though this offset is smaller than both the Larmor radius of electron orbits and the thickness of the beam and is hence not expected to significantly influence the device performance. In the azimuthal direction, the peak field magnitude varies 11% above and below its average value, which can be accounted for by a slight increase in input power to ensure that all electrons receive sufficient accelerating force. To investigate the mode purity, one end of the cavity was widened to allow the coupled wave to propagate into a waveguide structure where its composition was analyzed at an exit port. The output mode was an almost pure $TE_{0,1,1}$ mode and other modes were negligible.

V. VACUUM WINDOWS

The input and output windows of the gyroklystron have been designed. In addition to appropriate physical strength and vacuum sealing, the windows must have reflection coefficients as small as possible over the operating frequency band. Several types of window design exist, but the choice is partly limited by the geometry of the device. In this case, the input coupler (Section IV) features a rectangular waveguide. To avoid the need for additional steps or tapers, a pillbox-type structure [31] was selected for the input window as pictured in Fig. 5. For the output window, a single-disk circular window was selected as this could fit conveniently into the established output waveguide geometry. The rectangular sections of the input window arrangement are identical in dimension to those of the input coupler.

The optimal window thickness depends on the dielectric constant of the material and can be estimated by

$$d = N\left(\frac{\sqrt{\lambda_d}}{2}\right) \quad (2)$$

where N is an integer, and λ_d is the wavelength in the material calculated from the wavelength and relative permeability by

$$\lambda_d = \frac{\lambda}{\sqrt{\varepsilon_r'}}. \quad (3)$$

The choice of window material depends on the thermal, mechanical, and optical properties of the material. In this
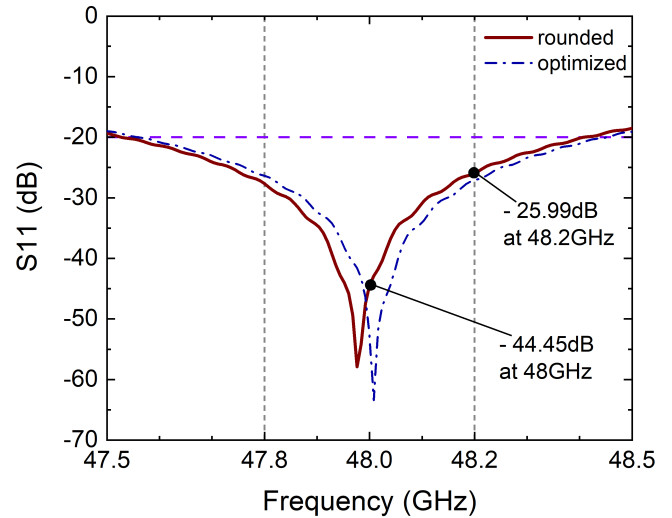
case, 95% Al_2O_3 was used, which has a relative permittivity of 9.4.

The radius of the input window's cylindrical section was estimated with consideration of the cutoff frequency. The thickness was estimated (2), but since the device has a bandwidth requirement, it is not as simple as choosing the ideal thickness at 48 GHz. Therefore, the dimensions were optimized in CST Microwave Studio to minimize reflection over the full range of the bandwidth. There is no fixed point that separates good and bad performance, so upper limits were set by the reasonable judgment of a suitable order of magnitude. The limits selected were -35 dB at the center frequency (48 GHz) and -20 dB within the gyroklystron's 3-dB bandwidth (47.8–48.2 GHz). The reflection was shown to be highly sensitive to geometry. An initial optimization sequence only specifying to move the minimum to 48 GHz displayed exceptional reflection of -58 dB at 48 GHz, but failed to meet the target values across the full bandwidth. The optimizer goals were reassessed, and it was instead considered that provided the reflection parameter at 48 GHz met the requirement, the exact position of the minimum value may be allowed to shift. This approach proved successful, as it allowed the maximum value within the specified frequency range to improve from -17 to -26 dB. The reflection at 48 GHz changed to -53 dB, which is still significantly better than the chosen target. A conservative estimate of 10 μm machining precision was assumed. With dimensions rounded to this level, the reflection parameters were -44 dB at 48 GHz and -26 dB within the bandwidth, which is still better than the chosen targets. Fig. 6 illustrates the difference between the optimized and rounded curves. The rounded dimensions were a pillbox radius of 4.64 mm, a pillbox length of 11.10 mm, and a disk thickness of 1.58 mm.

For the single-disk output window, boron nitride (BN) was selected as the window material as it offers excellent mechanical strength and thermal properties, at the same time is much cheaper than CVD diamond. While the high pulse repetition frequency required by the XFEL is high at 1000 Hz with 1.5 μs pulse duration, the average power is much lower

This article has been accepted for inclusion in a future issue of this journal. Content is final as presented, with the exception of pagination.

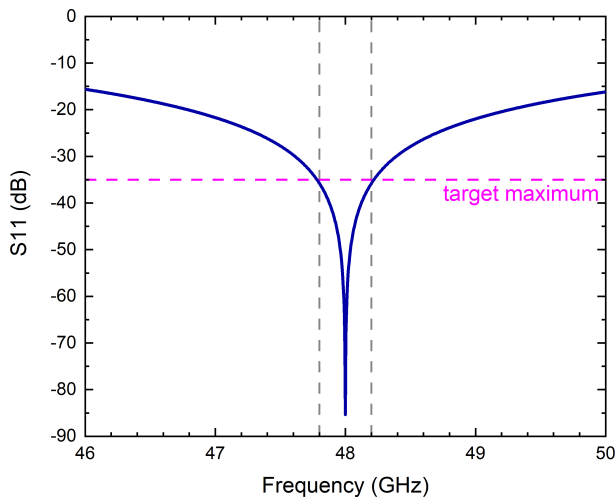NIX *et al.*: DESIGN OF A 48 GHz GYROKLYSTRON AMPLIFIER

5

Fig. 7. Reflection curve of the optimized output window, which meets the specified target reflection parameter across the bandwidth.

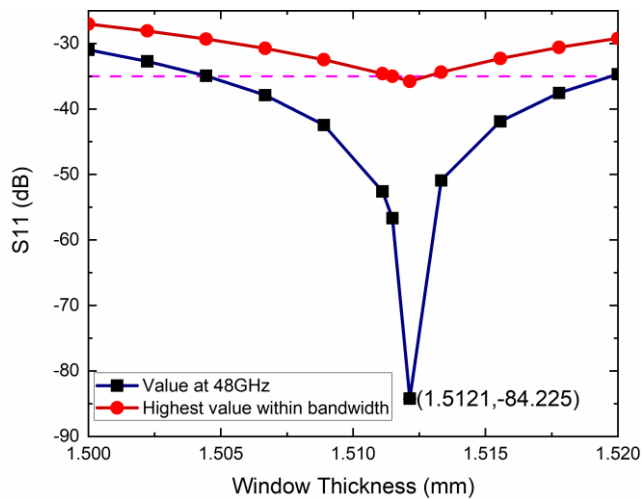Fig. 8. Variation of reflection parameter of the output window as window thickness is adjusted.
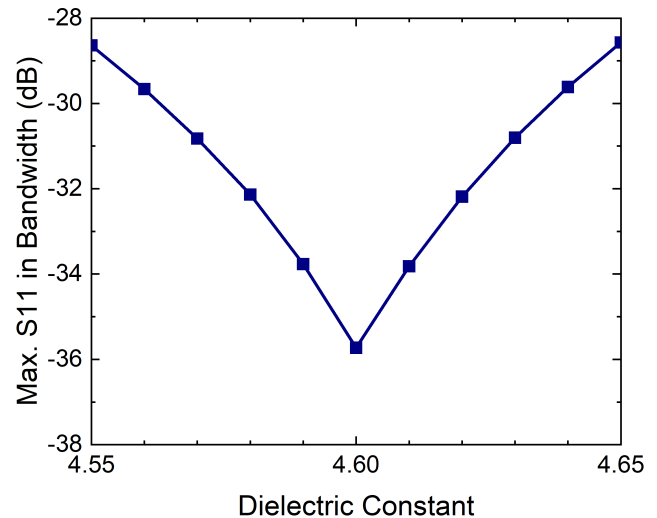

Fig. 9. Variation of reflection parameter of the output window as dielectric constant is adjusted.

measurement using a vector network analyzer. Fig. 9 shows the variation of the maximum reflection within the gyroklystron's 3-dB bandwidth for a range of dielectric constants at a fixed window width.

VI. COLLECTOR AND ITS THERMAL ANALYSIS

The optimal interaction efficiency was around 40%, thus leaving around 60% of the beam power present when it is deposited after the interaction. Although the short-pulsed operation leads to a much lower average power than a CW device, the loading is still large enough that thermal analysis and cooling systems are necessary. Here a two-stage process was used. First, the particle data from the PIC simulation was imported into CST's trajectory solver, which was used to calculate the paths of electrons through the collector region and determine deposition density. The trajectory solver result was then imported to CST's thermal analysis program as a heat source. Since the PIC simulations did not fully account for the pulsed operation, the power was reduced by setting a scaling factor on the imported heat source. For 1.5 μs pulses at a repetition rate of 1000 Hz, the scaling factor would be 0.0015. However, that factor assumes perfect square pulses and optimal interaction. It is an important precaution to design around the full beam power. A 2 μs linear rise (and fall) time was taken, though this was a conservative estimate, and a shorter rise is plausible with current modulator technology. The scaling factor used accounting for this rise time and the full beam power was 0.006. The rounding and approximations made in determining the scaling factor all provide a slight upward error, meaning that the simulation result is unlikely to result in underestimating the value.

The deposition heat source is a surface plot with no dependency on the external structure. Preliminary analysis of an 11.6 mm collector showed that peak deposition density would be very high. Minor adjustments to the magnetic field-profile were able to provide only small improvements. Including a tapered section or changing the collector radius increase the surface area of deposition and hence lowers maximum loading.

than a continuous wave (CW) device, and therefore a BN window can safely handle the power load. Reflection from the output window poses more risk to the performance than from the input window, as reflections here would travel back toward the interaction region and may interfere with the output mode. A stricter limit of −35 dB reflection was therefore set as the target maximum over the device bandwidth. The reflection curve is illustrated in Fig. 7.

The optimized dimensions displayed a maximum reflection of −36 dB within the bandwidth, but again there was high sensitivity to thickness. Fig. 8 illustrates the tolerance requirement of the window thickness. The optimal window thickness was 1.51 mm.

High machining precision of 10 μm is required to meet the specified target over the bandwidth range, while the value at 48 GHz remains suitably low for a larger thickness range. The true dielectric constant in the manufactured material may also differ from the assumed value slightly. It is therefore possible to construct a window that is slightly thicker than the calculated value and grind it to the correct value after

This article has been accepted for inclusion in a future issue of this journal. Content is final as presented, with the exception of pagination.

6   IEEE TRANSACTIONS ON ELECTRON DEVICES
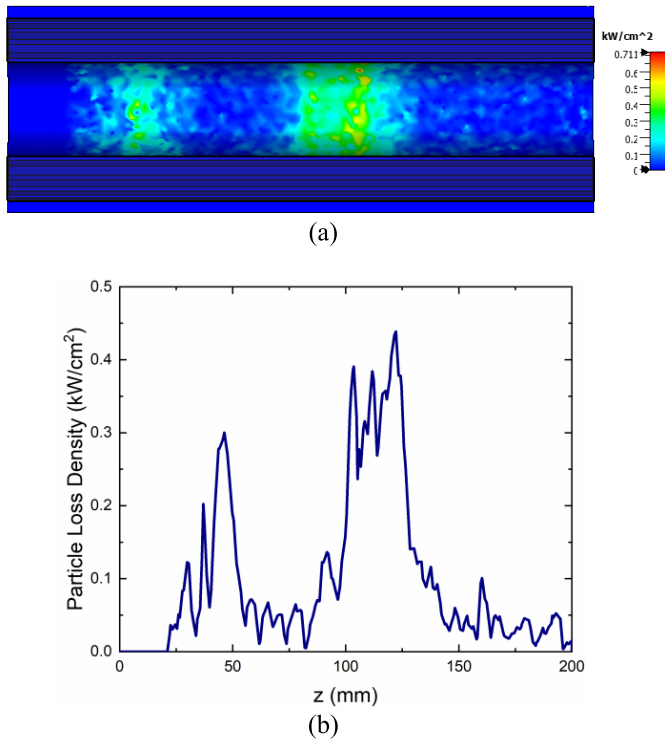
Fig. 10.   (a) Particle deposition density on a surface cross section and (b) along an arbitrary surface line in the collector region.

The surface area is maximized when the deposition takes place on a large-radius cylindrical wall. Since the particle import interface is far from the cavity region, there is space for tapering to occur before the deposition region, and safe performance is predicted to be possible with a 16 mm radius cylindrical collector region. Small, localized areas with a peak deposition density of around 0.71 kW/cm^2 were observed as shown in Fig. 10(a), while the vast majority of the surface saw loading under 0.5 kW/cm^2.

Fig. 10(b) shows the particle deposition density along a line following the surface in the axial direction, where $z = 0$ is the position of the import interface for electrons which was placed 140 mm from the output cavity aperture. The deposition is not perfectly symmetrical, but the peaks remain at the same position and roughly the same magnitude whichever line is chosen. Fig. 11 shows the electron trajectories in the collector region and an example temperature plot with a maximum temperature of 120 °C.

The thermal analysis was also considered in the full-beam zero-drive case as the beam profile would differ without bunching effects. The resulting peak temperature and surface loading values on the collector heating were observed to remain at safe levels in the event of input source failure.

A realistic collector typically requires a cooling system to ensure safe operation. The cooling system consists of a pumping system to provide a flow of pressurized cold water to carry heat away from the collector walls [32]–[34]. Grooves are included to increase the surface area of the contact surface between the copper and the water. Fig. 12 shows the groove geometry proposed for the collector structure. In the thermal analysis, the effect of water-cooling was approximated by
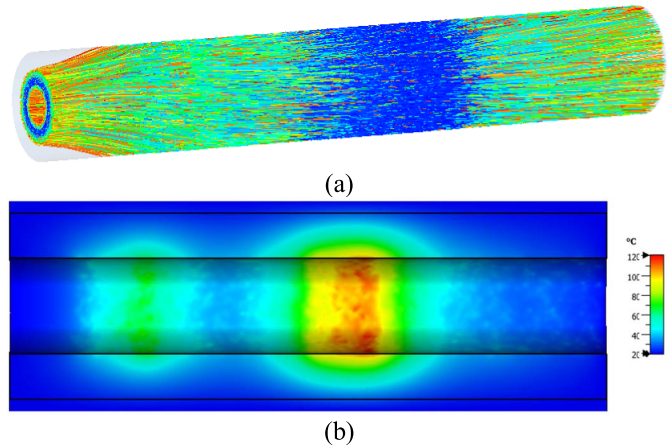

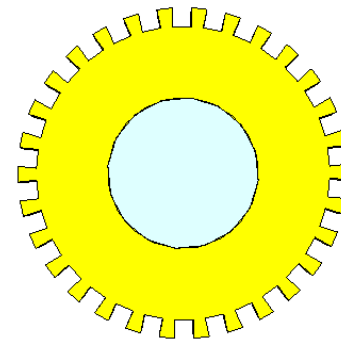Fig. 11.   (a) Electron trajectories and (b) temperature distribution in the collector region.

Fig. 12.   Cross section of proposed axial groove geometry to increase the surface area of the metal–water interface.
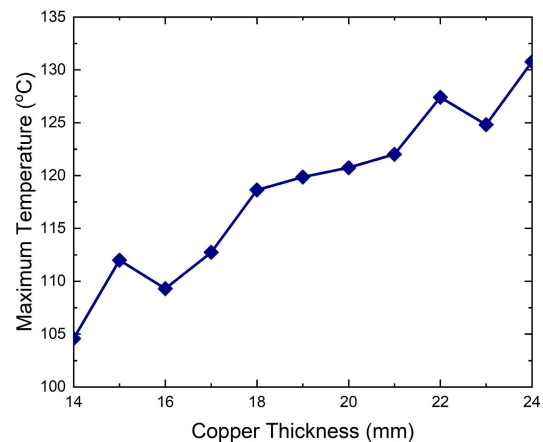

Fig. 13.   Variation of maximum temperature with increasing copper thickness.

applying a convective heat transfer coefficient of 3 W/cm^2/K to the surface [35].

If the thickness of copper between the deposition surface and the water-cooling surface is too large, the water cooling is not as effective, but if it is too thin, there is a risk of overheating the water and losing the effect. Hence a parameter sweep was carried out to show the variation of maximum temperature with copper thickness, as shown in Fig. 13. In all cases tested, the peak temperature remains within safe limits for copper and the surface temperature at the metal–water interface remains below boiling point.

This article has been accepted for inclusion in a future issue of this journal. Content is final as presented, with the exception of pagination.

NIX *et al.*: DESIGN OF A 48 GHz GYROKLYSTRON AMPLIFIER 7

Although practical testing would be required to finalize the cooling system design, the results discussed here demonstrate the feasibility of the collector, showing peak temperature and peak deposition density to be safely within the material limits of copper.

VII. CONCLUSION

In this article, the design of a 48 GHz gyroklystron amplifier has been presented. The preceding results presented in [13] and [14] have been summarized and expanded upon with additional discussion on the phase stability, which has been shown to meet the linearizer requirement if an appropriate modulator is used. The vacuum windows and input coupler have been designed. The input window comfortably met design targets, and the output window can meet design targets provided that the machining precision of the window material is sufficiently high. The input coupler was predicted to excite a $TE_{0,1,1}$ with a slight impurity that caused variations in the peak field by 11% around an azimuthal line. Finally thermal analysis of the beam deposition region was performed, demonstrating that the power loading and peak temperature in a 16-mm radius collector are safe at a very high repetition rate of 1000 Hz. The feasibility of the interaction circuit, MIG, vacuum windows, and collector has been demonstrated through detailed simulation work, and together these components form a viable design for a MW-level 48 GHz gyroklystron suitable for application in a linearizer for an XFEL.

REFERENCES

[1] J. L. Hirshfield and J. M. Wachtel, "Electron cyclotron maser," *Phys. Rev. Lett.*, vol. 12, no. 19, pp. 533–536, May 1964, doi: 10.1103/PhysRevLett.12.533.

[2] A. A. Tolkachev, B. A. Levitan, G. K. Solovjev, V. V. Veytsel, and V. E. Farber, "A megawatt power millimeter-wave phased-array radar," *IEEE Aerosp. Electron. Syst. Mag.*, vol. 15, no. 7, pp. 25–31, Jul. 2000, doi: 10.1109/62.854021.

[3] G. J. Linde, M. T. Ngo, B. G. Danly, W. J. Cheung, and V. Gregers-Hansen, "WARLOC: A high-power coherent 94 GHz radar," *IEEE Trans. Aerosp. Electron. Syst.*, vol. 44, no. 3, pp. 1102–1117, Jul. 2008, doi: 10.1109/TAES.2008.4655367.

[4] V. L. Granatstein and W. Lawson, "Gyro-amplifiers as candidate RF drivers for TeV linear colliders," *IEEE Trans. Plasma Sci.*, vol. 24, no. 3, pp. 648–665, Jun. 1996, doi: 10.1109/27.532948.

[5] W. Lawson, J. P. Calame, G. S. Nusinovich, and B. Hogan, "Reflections on the university of Maryland's program investigating gyro-amplifiers as potential sources for linear colliders," *THz Sci. Technol.*, vol. 10, no. 1, pp. 1–43, 2017.

[6] D. Sprehn *et al.*, "Latest results in SLAC 75 MW PPM klystrons," *AIP Conf. Proc.*, vol. 807, no. 1, pp. 137–144, 2006.

[7] T. I. Smith, "Production of intense low emittance beams for free electron lasers using electron linear accelerators," *Nucl. Instrum. Methods Phys. Res. A, Accel. Spectrom. Detect. Assoc. Equip.*, vol. 250, no. 1, pp. 64–70, 1986, doi: 10.1016/0168-9002(86)90861-2.

[8] A. Mak, P. Salén, V. Goryashko, and J. Clarke, "XLS deliverable D2.1, WP2: FEL science requirements and facility design," CompactLight Des. Rep., Accessed: May 2021. [Online]. Available: https://www.compactlight.eu/uploads/Main/D2.1_XLS_Specification.pdf

[9] J. C. Cai, I. Syratchev, and G. Burt, "Design study of a high-power Ka-band high-order-mode multibeam klystron," *IEEE Trans. Electron Devices*, vol. 67, no. 12, pp. 5736–5742, Dec. 2020, doi: 10.1109/TED.2020.3028348.

[10] L. Wang *et al.*, "Design of a Ka-band MW-level high efficiency gyroklystron for accelerators," *IET Microw., Antennas Propag.*, vol. 12, no. 11, pp. 1752–1757, 2018.

[11] A. Castilla *et al.*, "Development of 36 GHz RF systems for RF linearisers," presented at the 12th Int. Part. Accel. Conf. (IPAC), Campinas, Brazil, May 2021, Paper FRXB02.

[12] A. Castilla *et al.*, "Studies of a Ka-band lineariser for a compact light source," *Article Submitted Phys. Rev. Accel. Beams*, 2021.

[13] L. J. R. Nix *et al.*, "Demonstration of efficient beam-wave interaction for a MW-level 48 GHz gyroklystron amplifier," *Phys. Plasmas*, vol. 27, no. 5, May 2020, Art. no. 053101, doi: 10.1063/1.5144590.

[14] L. Zhang, L. J. R. Nix, and A. W. Cross, "Magnetron injection gun for high-power gyroklystron," *IEEE Trans. Electron Devices*, vol. 67, no. 11, pp. 5151–5157, Nov. 2020, doi: 10.1109/TED.2020.3025747.

[15] Scandinova. *Product Sheet: K-Series K100*. Accessed: Sep. 2020. [Online]. Available: https://scandinovasystems.com/products/k-series/k100/

[16] P. B. Wilson, Z. D. Farkas, and R. D. Ruth, "SLED II: A new method of RF pulse compression," in *Proc. Linear Accel. Conf.*, 1990, pp. 204–206.

[17] H. W. Matthews *et al.*, "Experimental studies of stability and amplification in a two-cavity second harmonic gyroklystron," *IEEE Trans. Plasma Sci.*, vol. 22, no. 5, pp. 825–833, 1994, doi: 10.1109/27.338298.

[18] S. X. Xu *et al.*, "A Ka-band second harmonic gyroklystron amplifier," *IEEE Trans. Plasma Sci.*, vol. 40, no. 8, pp. 2099–2104, Aug. 2012, doi: 10.1109/TPS.2012.2199522.

[19] J. M. Baird and W. Lawson, "Magnetron injection gun (MIG) design for gyrotron applications," *Int. J. Electron.*, vol. 61, no. 6, pp. 953–967, 1986, doi: 10.1080/00207218608920932.

[20] S. Humphries, Jr., "Numerical modeling of space-charge-limited charged-particle emission on a conformal triangular mesh," *J. Comput. Phys.*, vol. 125, no. 2, pp. 488–497, May 1996, doi: 10.1006/jcph.1996.0110.

[21] G. S. Nusinovich, B. G. Danly, and B. Levush, "Gain and bandwidth in stagger-tuned gyroklystrons," *Phys. Plasmas*, vol. 4, no. 2, pp. 469–478, Feb. 1997, doi: 10.1063/1.872115.

[22] M. S. Chauhan, M. V. Swati, and P. K. Jain, "Design and simulation of a gyroklystron amplifier," *Phys. Plasmas*, vol. 22, Mar. 2015, Art. no. 033111.

[23] T. M. Tran, B. G. Danly, K. E. Kreischer, J. B. Schutkeker, and R. J. Temkin, "Optimization of gyroklystron efficiency," *Phys. Fluids*, vol. 29, no. 4, pp. 1274–1281, 1986, doi: 10.1063/1.865876.

[24] B. Goplen, L. Ludeking, D. Smith, and G. Warren, "User-configurable MAGIC for electromagnetic PIC calculations," *Comput. Phys. Commun.*, vol. 87, nos. 1–2, pp. 54–86, May 1995, doi: 10.1016/0010-4655(95)00010-D.

[25] J. J. Choi *et al.*, "Experimental investigation of a high power, two-cavity, 35 GHz gyroklystron amplifier," *IEEE Trans. Plasma Sci.*, vol. 26, no. 3, pp. 416–425, Jun. 1998, doi: 10.1109/27.700773.

[26] M. S. Chauhan, M. V. Swati, and P. K. Jain, "PIC simulation study of a 35 GHz, 200 kW gyroklystron," *J. Microw. Optoelectron. Electromagn. Appl.*, vol. 12, no. 2, pp. 353–362, Dec. 2013.

[27] W. He, C. R. Donaldson, L. Zhang, K. Ronald, A. D. R. Phelps, and A. W. Cross, "Broadband amplification of low-terahertz signals using axis-encircling electrons in a helically corrugated interaction region," *Phys. Rev. Lett.*, vol. 119, no. 18, Oct. 2017, Art. no. 184801, doi: 10.1103/PhysRevLett.119.184801.

[28] G.-S. Park, V. L. Granatstein, P. E. Latham, C. M. Armstrong, A. K. Ganguly, and S. Y. Park, "Phase stability of gyroklystron amplifier," *IEEE Trans. Plasma Sci.*, vol. 19, no. 4, pp. 632–640, Aug. 1991, doi: 10.1109/27.90329.

[29] J. P. Calame and D. K. Abe, "Applications of advanced materials technologies to vacuum electronic devices," *Proc. IEEE*, vol. 87, no. 5, pp. 840–864, May 1999, doi: 10.1109/5.757257.

[30] D. Kajfez, *Q Factor Measurements Using MATLAB*. Norwood, MA, USA: Artech House, 2011.

[31] L. Zhang, C. R. Donaldson, A. W. Cross, and W. He, "A pillbox window with impedance matching sections for a W-band gyro-TWA," *IEEE Electron Device Lett.*, vol. 39, no. 7, pp. 1081–1084, Jul. 2018, doi: 10.1109/LED.2018.2834859.

[32] L. Savoldi *et al.*, "Towards the optimization of the thermal–hydraulic performance of gyrotron collectors," *Fusion Eng. Des.*, vol. 100, pp. 120–132, Nov. 2015, doi: 10.1016/j.fusengdes.2015.04.044.

[33] Y. Shen, W. Jiang, H. Fu, and Y. Luo, "Thermal-hydraulic design of collector cooling for high power gyro-TWT," in *Proc. Int. Conf. Microw. Millim. Wave Technol. (ICMMT)*, May 2018, pp. 1–3.

[34] R. Yan, D. Wang, H. Li, M. Mu, Y. Lian, and Y. Luo, "Design of collectors for high average/continuous-wave power gyro-devices," *IEEE Trans. Electron Devices*, vol. 66, no. 3, pp. 1512–1518, Mar. 2019, doi: 10.1109/TED.2018.2889722.

[35] K. Dong, R. Yan, and Y. Luo, "Optimal design and thermal analysis of undepressed collectors for 35-GHz gyro-TWTs," *IEEE Trans. Electron Devices*, vol. 62, no. 8, pp. 2652–2656, Jun. 2015.